



HAL
open science

Development of platinum based nanoparticles to enhance cancer cell killing by gamma rays and carbon ion radiation

Daniela Salado Leza

► **To cite this version:**

Daniela Salado Leza. Development of platinum based nanoparticles to enhance cancer cell killing by gamma rays and carbon ion radiation. Material chemistry. Université Paris-Saclay, 2016. English. NNT : 2016SACLS456 . tel-02458848

HAL Id: tel-02458848

<https://theses.hal.science/tel-02458848>

Submitted on 29 Jan 2020

HAL is a multi-disciplinary open access archive for the deposit and dissemination of scientific research documents, whether they are published or not. The documents may come from teaching and research institutions in France or abroad, or from public or private research centers.

L'archive ouverte pluridisciplinaire **HAL**, est destinée au dépôt et à la diffusion de documents scientifiques de niveau recherche, publiés ou non, émanant des établissements d'enseignement et de recherche français ou étrangers, des laboratoires publics ou privés.

NNT: 2016SACLS456

THESE DE DOCTORAT
DE
L'UNIVERSITE PARIS-SACLAY
PREPAREE A
L'UNIVERSITE PARIS SUD

ECOLE DOCTORALE N° 571

Sciences chimiques: molécules, matériaux, instrumentation et biosystèmes

Spécialité de doctorat: Chimie

Par

Daniela Edith Salado Leza

Development of platinum based nanoparticles to enhance cancer cell killing by
gamma rays and carbon ion radiation

Thèse présentée et soutenue à Orsay, le 25/11/2016

Composition du Jury:

M Simoni Eric	Professeur, Université Paris Sud	Président
M Roux Stéphane	Professeur, Université de Franche Comté	Rapporteur
Mme Hervé du Penhoat Marie-Anne	Maître de conférences, Université Pierre Marie Curie	Rapporteur
Mme Remita Hynd	Directeur de recherche, Université Paris Sud	Examinatrice
M Prise Kevin	Professeur, Queen's University	Examinateur
Mme Lacombe Sandrine	Professeur, Université Paris Sud	Directeur de thèse

Titre: Développement de nanoparticules à base de platine visant à améliorer la destruction de cellules cancéreuses par des rayons gamma et par ions carbone

Mots clés: nanoparticules de platine, radiosensibilisateurs, hadronthérapie, rayons gamma, nanomédecine

Résumé: La radiothérapie basée sur l'utilisation des photons de haute énergie (rayons X) est l'approche la plus courante dans le traitement du cancer. Toutefois, elle est limitée par la tolérance des tissus sains. Par conséquent, il est d'un intérêt majeur de développer des nouvelles techniques et protocoles pour améliorer le ciblage des effets de la radiation dans les tumeurs. Dans cette perspective, la hadronthérapie (irradiation de la tumeur par des protons ou des ions carbone de haute énergie) est considérée comme l'une des techniques oncologiques les plus prometteuses et efficace. Le dépôt d'énergie des ions est maximum en fin de parcours (pic de Bragg) sans dépôt d'énergie derrière la tumeur, ce qui permet de mieux cibler la tumeur. Pourtant, l'utilisation de cette modalité reste limitée du fait de la dose, petite mais significative, reçue par les tissus sains situés à l'entrée du faisceau, causant des effets secondaires.

Pour améliorer les performances des thérapies par radiation, une nouvelle stratégie basée sur la combinaison de nanoparticules métalliques (NPs) avec des rayonnements ionisants a été développée. Cette stratégie innovante a été largement étudiée par le groupe *Nanomédecine et Hadronthérapie* à l'Institut des Sciences Moléculaires d'Orsay, groupe que j'ai rejoint pour ma thèse de doctorat.

En effet, les nanoparticules ont une chimie de surface remarquable qui permet de les fonctionnaliser avec des ligands qui les

rendent plus futiles et moins reconnus par des macrophages. Cela permet une accumulation importante de nano-agents dans les tumeurs. Par conséquent, en utilisant des nano-agents, la sélectivité du traitement peut être améliorée, ce qui pourrait augmenter l'indice thérapeutique des médicaments anticancéreux classiques ou amplifier l'effet du rayonnement.

Le but de mon travail a été donc le développement de nouvelles nanoparticules non-toxiques à base de platine (Pt NPs) visant à améliorer la destruction des cellules cancéreuses par des rayons gamma et par ions carbone.

Une méthode originale de synthèse en une seule étape combinant la radiolyse et la PEGylation *in situ* a été optimisée. Cette méthode a permis d'obtenir des Pt NP stables et prêts-à-l'emploi avec une taille et forme homogène. Différents techniques ont été utilisées pour caractériser les propriétés physico-chimiques des nanoparticules. Les Pt NP consistent en petits noyaux métalliques sphériques (~ 3 nm) revêtus du poly (éthylène glycol), un polymère biocompatible bien connu et largement utilisé en nanomédecine. Les Pt NPs ont un diamètre hydrodynamique (d_H) moyen d'environ 9 nm. Ces caractéristiques physico-chimiques des Pt NP permettent de prédire le ciblage de la tumeur et la clairance *in vivo* ($d_H < 10$ nm).

L'impact biologique de ces nouvelles Pt NPs a été évalué sur deux lignées de cellules cancéreuses humaines; HeLa et U87-MG.

Les conditions non-toxiques ont été déterminées par survie clonogénique à différentes concentrations de Pt. Il a été observé que les Pt NPs ont un mode d'internalisation qui dépend fortement de la lignée cellulaire. Celles-ci sont, dans tous les cas, localisées exclusivement dans le cytoplasme. Les NPs de platine développés dans ce travail permettent d'amplifier significativement la destruction de cellules cancéreuses en utilisant des rayons gamma et un faisceau médical d'ions carbone (290 MeV / uma). Le facteur d'amplification (dénomé AF, Amplification Factor en anglais) des Pt NPs à 2 Gy est supérieur lorsque des ions carbone sont utilisés pour irradier des cellules HeLa. Le AF augmente de 14% (rayons gamma) à 44% en utilisant des ions C⁶⁺, un résultat très encourageant pour l'hadronthérapie.

Les mécanismes moléculaires à l'origine de cet effet ont été étudiés grâce à l'utilisation d'une nanosonde biologique (un plasmide d'ADN) et des rayons gamma. Ces expériences ont montré que les Pt NPs sont responsables de l'augmentation de dommages nanométriques (> 2 nm) *via* les effets directs et indirects du rayonnement.

Ces lésions de taille nanométrique sont d'une grande importance car elles peuvent être létales pour les cellules. Cet effet est attribué à des processus électroniques d'activation et de re-neutralisation de la NP qui engendre une forte perturbation dans le volume nanométrique qui l'entoure tel que la production groupée de radicaux libres fortement réactifs et toxiques. Les résultats suggèrent également l'effet du plasmon métallique des NPs dans le mécanisme d'amplification.

En conclusion, ce travail à l'interface de la physique, chimie et biologie montre les capacités des NPs à base de platine à améliorer l'éradication par radiation des cellules cancéreuses, en particulier, à améliorer les performances de l'hadronthérapie. De plus, les méthodes et protocoles mis en place dans ce travail permettent de développer des nouvelles nanoparticules multi-fonctionnelles dans le domaine de la thérapie guidée par imagerie, théranostic.

Title: Development of platinum based nanoparticles to enhance cancer cell killing by gamma rays and carbon ion radiation

Keywords: platinum nanoparticles, radiosensitization, radio-enhancement, hadrontherapy, gamma rays, nanomedicine

Abstract: Radiotherapy, based on the use of high-energy photons (X-rays), is the most common approach in cancer treatment. However, its implementation is limited by the tolerance of healthy tissue. Therefore, it is of major interest the development of new techniques and protocols to improve the selectivity of the radiation effects within the tumor. In this perspective, the hadrontherapy (tumor irradiation by high-energy protons or carbon ions) is considered, among others, as one of the most promising and effective oncological techniques. The energy deposition of ions in depth is maximum at the end of the track (Bragg peak) with no energy deposition behind the tumor. However, this modality remains restricted by the lower but significant damage induced to the normal tissue located at the entrance of the ion beam causing side effects.

To improve the performance of radiation therapies, a new strategy based on the combination of metallic nanoparticles (NPs) with ionizing radiations has been evaluated. This innovative strategy has been largely studied by the group *Nanomedicine and Hadrontherapy* from the Institute of Molecular Sciences in Orsay, group that I joined for my PhD. Indeed, NPs have a remarkable surface chemistry that allows their functionalization with ligands that make them less recognized by macrophages, which allows an important accumulation of the nano-agents selectively into the tumors (Enhanced Permeability and Retention (EPR) effect).

Hence, the treatment selectivity may be enhanced using nano-agents, which might increase the therapeutic index of conventional anti-cancer drugs or amplify the effect of radiation.

The goal of my work was thus to develop novel non-toxic platinum based nanoparticles (Pt NPs) to enhance cancer cell killing using γ -rays and carbon ions.

An optimized one-step method of synthesis, combining radiolysis with *in situ* PEGylation, was successfully established. This method enabled to obtain stable and ready-to-use Pt NPs with a uniform size and shape. Complementary techniques were used to characterize the physico-chemical properties of nanoparticles. The Pt NPs consist on small spherical metallic cores (~ 3 nm) coated with the well-known biocompatible poly (ethylene glycol), which is largely used in nanomedicine. The Pt NPs have an average hydrodynamic diameter (d_H) of about 9 nm. The physico-chemical characteristics of Pt NPs allow predicting tumor targeting and *in vivo* clearance ($d_H < 10$ nm).

The biological impact of Pt NPs was evaluated in two human cancer cell lines; HeLa and U87-MG. The non-toxic conditions were determined by performing clonogenic assays with different Pt concentrations. It has been observed that Pt NPs have an internalization pathway that strongly depends on the cell line. These are, in all cases, exclusively localized in the cytoplasm.

The Pt NPs developed in this work significantly enhanced cancer cell killing using γ -rays and medical carbon ions (290 MeV/uma). The amplification factor (AF) of Pt NPs at 2 Gy is greater when carbon ions are used to irradiate HeLa cells. The AF increases from 14% using γ -rays to 44% using C^{6+} ions, a very encouraging result for hadrontherapy.

The molecular mechanisms underlying this effect were investigated through the use of a bio-nanoprobe (plasmid DNA) and γ -rays. These experiments showed that Pt NPs are responsible for the increase of nanometric molecular damage (>2 nm) *via* the direct and indirect effects of radiation. Nanosize lesions are of great importance as they may be lethal to cells.

This effect is attributed to an electronic activation processes and to the re-neutralisation of NPs, which generates a strong perturbation in the surrounding nanometer volume producing highly reactive and toxic free radical clusters. The experimental results also suggested the effect of the NPs plasmon in the amplification mechanism.

In conclusion, this work at the interface of physics, chemistry and biology shows the potential of platinum NPs to improve the eradication of cancer cells by radiation, in particular, to improve the performance of hadrontherapy. In addition, the methods and protocols developed in this work allow synthesizing and evaluating novel multi-modal Pt NPs for theranostic.

Acknowledgments

Everything that has a beginning has an ending. This is not only the result of my work; this is the result of many people working with me side by side.

Firstly, I would like to thank Dr. José Luis Rodríguez because this professional and personal experience started when we met together and we spoke about dreams. Thanks Doc! I will never forget your support and help.

Sandrine, thanks for answering my e-mails from the other side of the world. Thanks for believing in me and for the opportunity. I learned a lot with you and I am keeping the best for the rest of my life. Hynd, I will never find the words but I hope I will find the way to show you my gratitude. I will never forget the way you used to introduce me to people in the lab. You taught me more than nanoscience. You made me feel at home in the difficulties. Thanks for everything *ma belle*.

Erika and Lenka, thank you for sharing with me your knowledge and experience. Thanks for every moment in the lab and for the friendship. It was always nice to do experiments with you, to learn from you and from my own mistakes that you kindly made me see. Your freshness and happiness were my motor in the hardest moments.

I would like to thank all my friends and colleagues from the lab. Sha, the time together is very precious for me and I am thankful with life for our friendship. Thanks for make me feel part of the group since the beginning. My girls Mar, Ala and Amina, the best moments in the office were with you. It was great that harmony between us, thank you. Leo, I will never forget that we firstly met when you just joined SERP-Chem and that later you became my favorite Filipino. Thank you for being there always to encourage me. Thanks Vlad for the time together in the cell culture, I wish you the best. I would also like to thank the ARGENT project managers coming to work with Sandrine; it was very nice to meet you and to share moments with you. Thanks to all the students coming to the lab for short periods, you brought me more motivation and invaluable knowledge.

Something very important in this successful story was the environment in the lab. I would like to thank all the researchers and students from ISMO, LCP, CLUPS, ICMMO, Institut Curie and to all the collaborators I had the pleasure to meet. Thank you for all that cups of coffee, cakes, enriching discussions and experiments together.

I thank CONACyT for the financial support, which allowed me to be trained as a highly qualified scientist and young researcher at the University of Paris Saclay.

I would like to thank all the members of the jury for accepting our invitation and for evaluating my work. I have very nice memories from my PhD thesis defense, from your questions and comments that help me to be a better researcher.

Finally, as my heart only speaks spanish I would like to take this space to let it speak freely.

Queridos padres, Héctor y Lupita, todo esto es gracias a ustedes. Recuerden que cada paso que doy en realidad lo estamos dando juntos. Muchas gracias por confiar en mi y dejarme volar. Gracias por todo su esfuerzo y por haber hecho de mi una mujer perseverante. Cualquier sacrificio es válido para mostrarles el maravilloso trabajo de amor que han realizado en mi. Siempre serán mi luz.

Queridos hermanos, Alejandra y Héctor, la peque no tiene palabras para agradecerles todo lo que hacen por ella. Ustedes son un gran ejemplo a seguir y me siento la persona más afortunada por tenerlos como hermanos. Ale, éstas son las líneas que de corazón te dedico, debes estar segura de que tu peque estará para ti en todo momento, antes que nada y que nadie. Gracias por tu presencia en los momentos más difíciles de la tesis. Héctor, simplemente eres muy chido y gracias por las hermosas demostraciones de cariño y apoyo. Soy lo que tu ejemplo me impulsa a ser.

Queridos Luis y Cristy, son los mejores nuevos hermanos que jamás hubiera pensado tener. Gracias por traer más felicidad a esta familia. Luis, fuiste el apoyo que necesité, llegaste en el momento justo. Jamás olvidaré tus consejos y cuidados. Cristy, siempre agradeceré que estuvieras allí para escucharme y que a pesar de la distancia nuestra amistad crecieran más y más.

Bebé Iker, tu llegada cambio mi vida y me hiciste muy feliz. Gracias a ti encontré la fuerza para seguir hasta el final. Eres un pequeño muy amado y tendrás en mi siempre un apoyo incondicional.

Quiero agradecer a todos mis amigos, aquellos que han caminado a mi lado y que ahora encuentran nuevos caminos, a los que llegaron para quedarse y a los que me dejaron enseñanzas invaluable. Lalo, lo logramos y juntos fue siempre mejor. Gracias por ser como un hermano para mi, por las pizzas y los memes, cuenta conmigo siempre. Mis niñas mexicanas, gracias por las sonrisas y tristezas compartidas, les deseo todo el éxito del mundo y espero poder seguir presente en sus vidas de una u otra manera. Lenka, sis, gracias por tu dulzura y cariño. Mar, mi ángel, nunca dudes que estaré para ti como tu estuviste para mi en todo momento, muchísimas gracias. ¡Qué guay tenerte en mi vida! Agradezco de corazón a la familia Julia Sotiropoulos, por el amor y la amistad que ha trascendido en los últimos años.

Así, agradezco a todos su presencia y apoyo. Aunque no alcance a mencionar cada nombre o cada institución, siempre estaré muy agradecida.

Esta tesis es el fruto de mucho esfuerzo y dedicación. Estuvo llena de matices y me siento muy contenta con el resultado final. Espero que esta tesis sea un pequeño-gran avance científico para mejorar el tratamiento y la calidad de vida de enfermos con cáncer a través de la nanomedicina. Una nueva etapa comienza en mi vida y estoy lista, MERCI.

OUTLINE

INTRODUCTION.....	1
CHAPTER I: NANOTECHNOLOGY FOR BIOMEDICAL APPLICATIONS State-of-the-art	
1 Nanotechnology.....	6
1.1 Methods for nanomaterials preparation.....	6
1.2 Applications of nanomaterials.....	14
2 Nanomedicine.....	15
2.1 Drug delivery.....	16
2.2 Medical imaging.....	17
2.3 Other advances.....	18
3 Radiation therapies.....	21
3.1 Conventional radiotherapy	21
3.2 Hadrontherapy: an alternative approach for targeted cancer treatment.....	21
4 Nanoparticles for radiation therapies.....	24
4.1 Photons.....	25
4.2 Ions.....	26
5 The choice of gold and platinum NPs.....	28
5.1 Physico-chemical properties, surface chemistry and applications of Au and Pt....	28
5.2 Optical properties of NPs.....	32
5.3 Impact in biological systems: metal compounds and NPs.....	34
6 Interaction of ionizing radiation with NPs.....	35
6.1 Activation processes by incident photons, ions and electrons.....	36
6.2 Plasmon excitation/relaxation.....	42
6.3 Relaxation processes	43
6.4 Electron capture by positively charged sites	46

7	Objectives of this work.....	47
8	References.....	48

CHAPTER II: MATERIALS AND METHODS

1.	Synthesis of platinum based nanoparticles.....	61
1.1	Monometallic PEGylated platinum nanoparticles.....	61
1.2	Mono- and bimetallic PEGylated gold-platinum nanoparticles.....	65
2.	Methods for nanoparticles characterization.....	66
2.1	UV-Visible spectroscopy.....	67
2.2	Transmission Electron Microscopy (TEM).....	67
2.3	Dynamic Light Scattering (DLS).....	68
2.4	Zeta potential (ζ -potential).....	69
2.5	X-ray Photoelectron Spectroscopy (XPS).....	70
2.6	Fourier Transform Infrared (FTIR) spectroscopy.....	71
3.	Radiation sources.....	73
3.1	Cobalt-60 gamma source.....	73
3.2	Caesium-137 gamma source.....	76
3.3	Medical carbon ions.....	77
4.	Biological models: description and methods.....	80
4.1	Cellular models.....	80
4.2	Bio-nanoprobe: pBR322 plasmid DNA.....	91
5.	References.....	95

Chapter III: RESULTS AND DISCUSSION PEGylated platinum nanoparticles

1.	Nanoparticles characterization.....	101
1.1	Characterization by spectrophotometry UV-Vis.....	102

1.2	Size distribution and morphology	104
1.3	Oxidation state and chemical composition by XPS.....	109
1.4	Functional characterization by FTIR	117
1.5	Stability in biological relevant media	123
1.6	Conclusion	126
2.	Biological impact of nanoparticles	128
2.1	Interaction of NPs with human cells – toxicity, uptake and localization	129
2.2	Effect of PtPEG-OH NPs on radiation induced cell-killing	143
2.3	Proof of principle: enhancement on the radio-induced nanosize damage.....	153
2.4	Conclusion: Multi-scale study	156
3.	References	158

Chapter IV: RESULTS AND DISCUSSION
Mono- and bimetallic PEGylated gold-platinum nanoparticles

1	Nanoparticles characterization.....	165
1.1	Characterization of by spectrophotometry UV-Vis, TEM and DLS	165
1.2	Chemical composition.....	179
1.3	Conclusion	191
2	Proof of principle: enhancement on the radio-induced nanosize damage	193
3	References.....	197
	CONCLUSIONS.....	201
	APPENDIX A.....	205
	APPENDIX B.....	217

LIST OF FIGURES

CHAPTER I: NANOTECHNOLOGY FOR BIOMEDICAL APPLICATIONS State-of-the-art

Figure I - 1. Schematic of the bottom-up and top-down approaches used in the synthesis of nanomaterials.	7
Figure I - 2. Scheme of the transient species produced during water radiolysis, without or in the presence of a diluted solute acting as a radical scavenger.	10
Figure I - 3. Illustration of chemical events that can be induced by high-energy radiation in polymers.....	13
Figure I - 4. Scheme of a multi-modal nanoparticle for molecular imaging, drug delivery and therapy.	15
Figure I - 5. Theranostic approach using nanoparticles.....	19
Figure I - 6. Principle: illustration of the dose deposition profile of X-rays (in blue) and ions at the rising Bragg peak (in black) and the Spread-out Bragg Peak (SOBP) (in red)...	22
Figure I - 7. Schematic comparison between the energy deposition of conventional radiotherapy and hadrontherapy to treat a brain tumor.....	23
Figure I - 8. Schematic of the amplification effect of nanoparticles at the nanoscopic scale.	27
Figure I - 9. Electron shell configuration diagram of gold.....	28
Figure I - 10. Electron shell configuration diagram of platinum.	30
Figure I - 11. Electronic structures of a gold atom, nanoparticle and solid.....	32
Figure I - 12. Scheme of the transition from discrete energy levels of atoms to electronic band structures.....	33
Figure I - 13. Schematic Surface Plasmon Resonance.	34
Figure I - 14. Photoelectric effect.	36
Figure I - 15. Compton effect.....	37
Figure I - 16. Electron-positron pair production.....	38
Figure I - 17. Processes involved in the interaction of photons with matter as function of the incident energy and atomic number of the target.....	39
Figure I - 18. Schematic representation of the energy loss by a charged particle interacting with the target electrons at a distance defined as the impact parameter.....	40
Figure I - 19. Interaction of secondary electrons by elastic and inelastic scattering.	42

Figure I - 20. Collective electronic excitation of the plasmon in a metallic nanoparticle...	43
Figure I - 21. Electronic relaxation <i>via</i> fluorescence.	44
Figure I - 22. Scheme of left: ionization, middle: electron emission, right: Auger de-excitation.	44
Figure I - 23. Fluorescence and Auger electron yields as a function of the atomic number for K shell vacancies.	45
Figure I - 24. Positively charged atom neutralizes <i>via</i> capture of electrons from surrounding water molecules.	46
Figure I - 25. Platinum based nanoparticles for radio-enhancement: perspective of improving hadrontherapy.	47

CHAPTER II: MATERIALS AND METHODS

Figure II - 1. Principle of the synthesis of PEGylated platinum nanoparticles by gamma rays water radiolysis and <i>in situ</i> PEGylation.	65
Figure II - 2. Nanoparticles samples for XPS analysis.	72
Figure II - 3. Schematic representation of the ⁶⁰ Co radioactive decay.	74
Figure II - 4. The cobalt-60 panoramic source used for NPs synthesis and plasmid DNA irradiation.	75
Figure II - 5. Dosimetry of the ⁶⁰ Co source measured at position 407.	76
Figure II - 6. Schematic representation of the ¹³⁷ Cs radioactive decay.	77
Figure II - 7. The caesium-137 GSR-D1 irradiator used for <i>in vitro</i> experimentation.	78
Figure II - 8. Illustration of the HIMAC facility in Chiba, Japan.	79
Figure II - 9. (a) Experimental set up used to irradiate cells by carbon ions at the HIMAC (NIRS, Chiba, Japan). (b) Scheme showing the conditions used to irradiate cells.	80
Figure II - 10. Schematic representation of the CFA protocol.	84
Figure II - 11. ICP principle and instrumentation of (a) the ICP-OES Varian 720 ES and (b) the GC-ICP-MS Thermo Scientific XSERIES 2.	86
Figure II - 12. Schematic representation of Nano SIMS principle.	87
Figure II - 13. The Cameca NanoSIMS 50 ion-probe for element analysis at the CMIB platform (Institut Curie).	88
Figure II - 14. Calibration of the Cameca NanoSIMS 50 by means of a Pt layer.	90

Figure II - 15. The JEOL 2200FS used at the PICT-IBiSA platform for cells imagery.....	91
Figure II - 16. Scheme of the three different plasmid conformations.	92
Figure II - 17. Scheme of the experimental protocol used for molecular experiments.	93

Chapter III: RESULTS AND DISCUSSION PEGylated platinum nanoparticles

Figure III - 1. (a) UV-vis absorption spectra of control solutions containing Pt(NH ₃) ₄ Cl ₂ (—) and PEG-OH (---) and samples consisting on diluted platinum containing solutions (10 ⁻³ mol.L ⁻¹) before (—) and after (—) irradiation (optical path= 2 mm). Inserted pictures correspond to an aqueous solution containing Pt(NH ₃) ₄ Cl ₂ and PEG-OH before and after irradiation (10 ⁻² mol.L ⁻¹ , D= 100 kGy). (b) Absorption spectra of samples shown in (a) but in a wavelength range from 200 to 400 nm.	102
Figure III - 2. TEM micrographs of PtPEG-OH NPs synthesized in water with an initial Pt ^{II} concentration of 10 ⁻² mol.L ⁻¹ and a PEG-OH:Pt molar ratio of <i>ca.</i> 100 measured at three magnifications. Scale bars: (a) 0.5 μm, (b) 50 nm and (c) 20 nm.	104
Figure III - 3. (a) Diameter distribution of the metallic core, (b) average hydrodynamic diameter and (c) electron diffraction pattern of PtPEG-OH NPs.	105
Figure III - 4. Schematic representation of a 3.2 nm platinum nanoparticle.	108
Figure III - 5. Survey XPS spectrum of PtPEG-OH NPs synthesized with a total gamma dose of 100 kGy.	109
Figure III - 6. XPS spectra corresponding to the Pt-4f core level region of platinum on (a) the platinum complex (—) and on a platinum solid sample (—) and (b) on PtPEG-OH NPs showing their bulk (—) and surface (—) components.	110
Figure III - 7. XPS spectra of (a) C-1s, (b) O-1s and (c) N-1s in pure PEG-OH, Pt(NH ₃) ₄ Cl ₂ and PtPEG-OH NPs.	112
Figure III - 8. FTIR spectra of (a) PEG-OH, (b) Pt ^{II} precursor salt, (c) Pt ^{II} precursor mixed with PEG-OH (without irradiation) and (d) PtPEG-OH NPs obtained after irradiation of the Pt ^{II} precursor and PEG-OH mixture.	117
Figure III - 9. Proposed Pt ^{II} -PEG conjugation before irradiation.....	120
Figure III - 10. Dehydrogenation of a primary alcohol to form an active primary aldehyde.	121
Figure III - 11. Formation of the intermediate specie before irradiation <i>via</i> amide linker.	121
Figure III - 12. Evolution of the hydrodynamic diameter (in blue) and ζ-potential (in red) versus pH for PtPEG-OH NPs suspensions at a Pt concentration of 5x10 ⁻⁴ mol.L ⁻¹	123

Figure III - 13. Evolution of the d_H of PtPEG-OH NPs in; water, PBS, NaCl and TE buffer, after 0, 1, 3, 6 and 22 h (Pt concentration of 5×10^{-4} mol.L $^{-1}$).....	125
Figure III - 14. Scheme of the novel radiolytic-PEGylation method to synthesize biocompatible PtPEG-OH NPs.....	127
Figure III - 15. Illustration of the resulting PtPEG-OH NPs conformation.....	127
Figure III - 16. Survival fraction of HeLa cells in the presence of water or incubated with PtPEG-OH NPs. The results are presented as means \pm Standard Deviation (SD), statistically analysed using one-way ANOVA (Turkey test: * $p < 0.05$ and ** $p > 0.05$).....	129
Figure III - 17. (a) Mass of the metal per cell and (b) density of internalized nanoparticles (NPs/ μm^3) in HeLa and U87-MG cells.	132
Figure III - 18. Mass spectra recorded by NanoSIMS from a platinum reference (—) and from HeLa cells loaded with PtPEG NPs (—).....	135
Figure III - 19. Nano-SIMS images of a HeLa cell loaded with PtPEG NPs. Panels a, b, and c correspond to CN $^-$, P $^-$ and $^{194}\text{Pt}^-$ respectively. Panel d is the merged image of $^{194}\text{Pt}^-$ and P $^-$. The arrows show an identified low concentration P $^-$ region in the cell cytoplasm.....	136
Figure III - 20. Illustration on the cellular uptake of particles.....	137
Figure III - 21. TEM images of cryo-fixed HeLa cells after incubation with 5×10^{-4} PtPEG-OH NPs for 6 hours. Panel (a) corresponds to a cell showing a vast cytoplasmic region while (b) and (c) are the magnified images of the squared regions 1 & 2 of panel (a).....	139
Figure III - 22. Diameter size histogram of the enclosed region 1 of Figure III-19c (inserted TEM image).....	139
Figure III - 23. TEM images of a control (a) and of a HeLa cells incubated with 5×10^{-4} mol.L $^{-1}$ PtPEG-OH NPs for 6 hours (b) prepared by chemical fixation. Panel (c) shows the size distribution of the squared aggregate shown in panel (b).....	140
Figure III - 24. TEM images of controls (a) and (b) and U87-MG cells incubated with 5×10^{-4} mol.L $^{-1}$ PtPEG-OH NPs for 6 hours (c) and (d) prepared by chemical fixation.	141
Figure III - 25. Suggested PtPEG-OH NPs uptake pathways in U87-MG and HeLa cells. ..	142
Figure III - 26. Survival curves of HeLa cells irradiated by γ -rays (●, ●) and carbon ions (■, ■) in controls and in presence of PtPEG-OH NPs. The horizontal and vertical black lines indicate the dose at 10% of survival.	143
Figure III - 27. Nanoparticles amplification factor as function of the γ -rays and carbon ions radiation dose.....	146
Figure III - 28. Survival curves of U87-MG cells irradiated by gamma rays in control (●) and in presence of PtPEG-OH NPs (●).....	149
Figure III - 29. Amplification factor of PtPEG-OH NPs as function of the dose.	151

Figure III - 30. Schematic representation of the radio-enhancing cell killing effect of PtPEG-OH NPs.....	152
Figure III - 31. Nanosize damage induced by γ -rays in plasmids loaded with PtPEG-OH NPs (■) and in the control (■) as function of the irradiation dose. DMSO effect in plasmids loaded with PtPEG-OH NPs (□) and in the control (□).	153
Figure III - 32. Multy-scale study: the radiation enhancing effect of PtPEG-OH NPs from the nanoscale to the cell.....	157

Chapter IV: RESULTS AND DISCUSSION

Mono- and bimetallic PEGylated gold-platinum nanoparticles

Figure IV - 1. UV-Vis absorption spectra (optical path= 2 mm) of control solutions containing 10^{-3} mol.L ⁻¹ Au ^{III} Cl ₄ ⁻ and PEG-2NH ₂ before irradiation (a). Panel (b) corresponds to the absorption spectra of samples shown in (a) but in a wavelength range from 250 to 400 nm.....	166
Figure IV - 2. UV-Vis absorption spectra (optical path= 2 mm) of samples containing 10^{-3} mol.L ⁻¹ Au ^{III} Cl ₄ ⁻ , PEG-2000 (a) or PEG-3000 (b) as function of the irradiation dose. Samples were prepared with a molar ratio PEG-2NH ₂ :Au of <i>ca.</i> 50. Inserted pictures show colloids after different irradiation doses.....	167
Figure IV - 3. TEM micrographs (a) of AuPEG-2000 NPs synthesized at 10^{-3} mol.L ⁻¹ with a PEG-2NH ₂ :Au molar ratio of <i>ca.</i> 50 with a total dose of 1 kGy. (b) Magnified image of AuPEG-2000 NPs. (c) Core size distribution.....	170
Figure IV - 4. TEM micrographs (a) of AuPEG-3000 NPs synthesized at 10^{-3} mol.L ⁻¹ with a PEG-2NH ₂ :Au molar ratio of <i>ca.</i> 50. (b). Magnified image of AuPEG-3000 NPs. The core size distribution is shown in (c).....	170
Figure IV - 5. (a) UV-Vis absorption spectra (optical path= 2 mm) of samples containing 10^{-3} mol.L ⁻¹ (Pt(NH ₃) ₄) ²⁺ and PEG-2000 as function of the irradiation dose. Samples were prepared with a molar ratio PEG-2NH ₂ :Pt of <i>ca.</i> 50. (b) Evolution of the absorbance at 450 nm as function of the irradiation dose.	171
Figure IV - 6. TEM micrograph of PtPEG-2NH ₂ NPs at 10^{-3} mol.L ⁻¹ prepared with a total dose of 2.5 kGy (a) and 10 kGy (b).....	172
Figure IV - 7. TEM micrographs at two different magnifications of PtPEG-2NH ₂ NPs synthesized at 5×10^{-3} mol.L ⁻¹ prepared with a total dose of 50 kGy (a) and (b). PtPEG-2NH ₂ NPs size distribution (c).	173
Figure IV - 8. Cross-linking process and structure of the poly (ethylene oxide) radical formed upon irradiation in aqueous solution.	174
Figure IV - 9. Schematic synthesis of PtPEG-2NH ₂ NPs (Pt NFs) by the proposed mechanism involving free Pt ^{II} ions in the presence of free PEG-2NH ₂ before irradiation (1), the radiolytic reduction of metal ions in competition with the polymer cross-linking process (2) and the homogenous formation of Pt NFs embedded into the PEG matrix (3).	175

Figure IV - 10. UV-Vis absorption spectra (optical path= 2 mm) of controls before irradiation (a) and samples containing 5×10^{-4} mol.L ⁻¹ Au ^{III} Cl ₄ ⁻ , 5×10^{-4} mol.L ⁻¹ Pt(NH ₃) ₄ ²⁺ and 5×10^{-2} PEG-2NH ₂ (Mw= 2000 g.mol ⁻¹) as function of the irradiation dose (b). Inserted pictures in (b) show colloids after different irradiation doses.....	176
Figure IV - 11. Schematic synthesis of Au:PtPEG-2NH ₂ NPs by the formation of an Au ^{III} -PEG-2NH ₂ complex (1), the radiolytic reduction of metal ions and early electron transfer from Pt to Au (2) and formation of Au _{core} -Pt _{shell} structured nanoparticles stabilized by PEG-2NH ₂ (3).....	177
Figure IV - 12. TEM micrographs of Au:PtPEG-2NH ₂ NPs synthesized at 10 ⁻³ mol.L ⁻¹ with a PEG-2NH ₂ :M _T molar ratio of <i>ca.</i> 50 (a). Magnified image of Au:PtPEG-2NH ₂ NPs (b), The core size distribution is shown in (c).....	178
Figure IV - 13. Survey XPS spectra of the as-synthesized PtPEG-2NH ₂ , AuPEG-2NH ₂ and Au:PtPEG-2NH ₂ NPs.....	179
Figure IV - 14. XPS spectra corresponding to the Au-4f core level region of gold on (a) a metallic gold film and (b) on AuPEG-2NH ₂ NPs.	179
Figure IV - 15. XPS spectra of AuPEG-2NH ₂ NPs at the C-1s (a), O-1s (b) and N-1s (c) regions.....	180
Figure IV - 16. XPS spectrum of PtPEG-2NH ₂ NPs at the Pt-4f core level region.....	182
Figure IV - 17. XPS spectra of a control consisting on pure PEG-2NH ₂ and PtPEG-2NH ₂ NPs at the C-1s (a), O-1s (b) and N-1s (c) regions.....	183
Figure IV - 18. XPS spectrum corresponding to the Au and Pt-4f core level region of bimetallic PEG-diamine nanoparticles.	186
Figure IV - 19. XPS spectra of Au:PtPEG-2NH ₂ NPs corresponding to the C-1s (a), O-1s (b) and N-1s (c) core levels regions.	187
Figure IV - 20. FTIR spectra of (a) PEG-2NH ₂ , (b) AuPEG-2NH ₂ NPs, (c) PtPEG-2NH ₂ NPs and (d) Au:PtPEG-2NH ₂ NPs obtained by radiolysis.....	189
Figure IV - 21. Proposed configuration of the radiolysis induced grafting polymerization of PEG-2NH ₂ chains.....	191
Figure IV - 22. Schematic representation of mono and bimetallic gold-platinum PEGylated nanoparticles.	192
Figure IV - 23. Induced molecular nanosize damage in the control (■) and in plasmids loaded with PtPEG-2NH ₂ NPs (■), AuPEG-2NH ₂ NPs (■) and Au:PtPEG-2NH ₂ NPs (■) as function of the irradiation dose. DMSO effect in the control (□) and in plasmids loaded with PtPEG-2NH ₂ NPs (□), AuPEG-2NH ₂ NPs (□) and Au:PtPEG-2NH ₂ NPs (□).....	193
Figure IV - 24. Yield enhancement from 1 nm metallic NPs. Dashed lines show the contribution of individual atomic excitations while solid lines show the resulting sum of the individual and plasmonic excitations.....	195

Figure IV - 25. The radiation enhancement mechanism of metallic nanoparticles. Representation of the early-stage physical processes: collective electronic excitation, follow by the chemical stage consisting on ROS production that ends with bond cleavage in biomolecules, which might induce cell death.....196

APPENDIX A: Characterization Techniques

Figure A - 1. Typical TEM configuration.....205

Figure A - 2. Schematic representation of the fundamental principle of DLS (a) and the hydrodynamic diameter of a metal nanoparticle (b).....207

Figure A - 3. Schematic representation of the fundamental principle of the zeta potential.208

Figure A - 4. Optical configuration of the Zetasizer Nano-ZS for zeta potential measurements.....209

Figure A - 5. XPS principle: energy band structure and emission process for a model atom.210

Figure A - 6. IR region and vibrational modes.....212

Figure A - 7. Schematically representation of a FTIR spectrometer and signal processing.213

Figure A - 8. Principle of ATR infrared213

APPENDIX B: Influence of platinum concentration

Figure B - 1. Amplification factor of nanosize damage by PtPEG NPs as function of concentration.218

LIST OF TABLES

CHAPTER I: NANOTECHNOLOGY FOR BIOMEDICAL APPLICATIONS

State-of-the-art

Table I - 1. Summary: characteristics and physical properties of gold and platinum.....	31
--	----

CHAPTER II: MATERIALS AND METHODS

Table II - 1. Bio-compatible and water soluble polymers used for <i>in situ</i> metal nanoparticles surface coating.....	62
---	----

Table II - 2. Methods for nanoparticles characterization.....	67
--	----

Table II - 3. Main information of HeLa and U87-MG cells from the ATCC.....	82
---	----

Table II - 4. Experimental protocol for the samples preparation with and without nanoparticles.....	94
--	----

Chapter III: RESULTS AND DISCUSSION

PEGylated platinum nanoparticles

Table III - 1. Influence of the PEG-OH:Pt molar ratio on the stability and size distribution of PtPEG-OH NPs.....	106
--	-----

Table III - 2. Summary of binding energy values reported in literature for the Pt-4f _{7/2} core level of different Pt phases.....	110
---	-----

Table III - 3. XPS reference table with C1s, O1s and N1s binding energies of the aliphatic species here investigated.....	112
--	-----

Table III - 4. XPS data summary: BE and FWHM of platinum, carbon, oxygen and nitrogen in different environments (Pt(NH ₃) ₄ Cl ₂ , Pt ⁰ solid, PEG-OH, and PtPEG-OH NPs).....	115
---	-----

Table III - 5. XPS and theoretical elemental composition of PtPEG-OH NPs and their precursors.....	116
---	-----

Table III - 6. Reference table of characteristic infrared absorption frequencies and vibrational assignments of selected organic functional groups.....	118
--	-----

Table III - 7. Main characteristics of the new PtPEG-OH NPs in comparison with Au-DTDTA NPs.....	126
---	-----

Table III - 8. Uptake of PtPEG-OH and Au-DTDTA NPs in HeLa and U87-MG cells after 6h incubation.....	130
---	-----

Table III - 9. Uptake of PtPEG-OH NPs in HeLa cells after 6 h and 24 h of incubation.....	132
--	-----

Table III - 10. α and β coefficients for HeLa cells irradiated by γ -rays or by carbon ions in the presence of PtPEG-OH NPs and in the controls.....	144
---	-----

Table III - 11. Radiation doses (γ -rays and carbon ions) to reach 10% of survival with and without PtPEG-OH NPs. DEF and dose enhancement (%).....	147
Table III - 12. RBE-D ¹⁰ , REF-2 Gy and NPs enhancement values of HeLa cells treated with γ -rays and carbon ions with or without PtPEG-OH NPs.....	148
Table III - 13. α and β coefficients for U87-MG cells irradiated by γ -rays in the presence of metallic NPs and in the controls.....	150
Table III - 14. Yields of controls and plasmids loaded with PtPEG-OH NPs with a NP:plasmid ratio close 4:1. DMSO was added in some experiments. The AFs are also reported.....	154

Chapter IV: RESULTS AND DISCUSSION

Mono- and bimetallic PEGylated gold-platinum nanoparticles

Table IV - 1. Ratio of absorbance of gold nanoparticles at the surface plasmon resonance peak (A_{SPR}) to the absorbance at 450 nm (A_{450}) as function of the particle diameter.	169
Table IV - 2. Nanoparticles size determination by the model reported by Haiss <i>et al.</i>	169
Table IV - 3. XPS data summary: binding energy, assignment and FWHM of AuPEG-2NH ₂ NPs.	181
Table IV - 4. XPS data summary: binding energy, assignment and FWHM of the control (pure PEG-2NH ₂) and PtPEG-2NH ₂ NPs.....	185
Table IV - 5. XPS data summary: binding energy, assignment and FWHM of Au:PtPEG-2NH ₂ NPs.....	187
Table IV - 6. Yields of the control and plasmids loaded with mono- and bimetallic gold-platinum NPs ([2:1] ratio). The AFs and DMSO effect are also reported.	194

APPENDIX B: Influence of platinum concentration

Table B - 1. The yields of controls and plasmids loaded with PtPEG NPs at different concentrations. DMSO was added in some experiments. The AFs are also reported.....	217
---	-----

List of abbreviations

AF	Amplification Factor
ATR	Attenuated Total Reflection
Au NPs	Gold nanoparticles
Au-DTDTPA NPs	Gold nanoparticles stabilized by dithiolated diethylene triamine pentaacetic acid
Au:PtPEG-2NH ₂ NPs	PEGylated bimetallic gold-platinum nanoparticles stabilized by PEG-2NH ₂
AuPEG-2NH ₂ NPs	PEGylated gold nanoparticles stabilized by PEG-2NH ₂
BE (also denoted as E _b)	Binding energy
CFA	Colony Formation Assay
CHO	Chinese Hamster Ovary cells
cis-Pt	cis-platinum anticancer drug
D	Radiation dose
DEF	Dose Enhancing Factor
d _H	Hydrodynamic diameter
DLS	Dynamic Light Scattering
DMEM	Dulbecco's Modified Eagle Medium
DMSO	Dimethyl sulfoxide
DSB	Double Strand Break
FBS	Fetal Bovine Serum
Fcc	face-centered cubic lattice
FDA	Food and Drug Administration (US)
FTIR	Fourier Transform Infrared
FWHM	Full width at half maximum
GBNs	Gadolinium based nanoparticles
HIMAC	Heavy Ion Medical Accelerator in Chiba
ICP-MS	Inductively Coupled Plasma Mass Spectrometry
ICP-OES	Inductively Coupled Plasma Optical Emission Spectrometry
IR	Infrared
LET	Linear Energy Transfer
LMCT	Ligand-to-Metal Charge Transfer absorption band
MRI	Magnetic Resonance Imaging
NE AA	Non-essential Amino Acids
NPs	Nanoparticles
PBS	Phosphate Buffered Saline solution
PdI	Polydispersity Index
PE	Plating Efficiency
PEG	Poly(Ethylene Glycol)
PEG-2NH ₂	Poly(Ethylene Glycol) diamine
PEG-OH	Standard Poly (Ethylene Glycol)
Pt NFs	PEGylated platinum nanoflowers stabilized by PEG-2NH ₂
Pt NPs	Platinum based nanoparticles
Pt-PAA NPs	Platinum nanoparticles stabilized by Poly(Acrylic Acid)
PtPEG-2NH ₂ NPs (also denoted as Pt NFs)	PEGylated platinum nanoparticles stabilized by PEG-2NH ₂
PtPEG-OH NPs	PEGylated platinum nanoparticles stabilized

PtPEG-OH NPs – X	by PEG-OH PEGylated platinum nanoparticles prepared with an X PEG- OH:Pt molar ratio
PZC	Point of zero charge
RBE	Relative Biological Effectiveness
REE	Radio-Enhancing Effect
REF	Relative Enhancing Factor
SF	Survival Fraction
SOBP	Spread out Bragg peak
SPR	Surface Plasmon Resonance
SSB	Single Strand Break
TEM	Transmission Electron Microscopy
UV-Vis	Ultraviolet – Visible
XPS	X-ray Photoelectron Spectroscopy
ζ-potential	Zeta potential

INTRODUCTION

General motivation

Cancer is the first cause of death in industrial societies. Around 50% of patients receive radiotherapy as part of their treatment. This modality can be used alone or in combination with chemotherapy or surgery. Conventional radiotherapy is based on the use of high-energy (1-20 MeV) X-rays. Thanks to the high penetration of X-rays in tissues, this modality is used to treat deeply sited tumors in a non-invasive way. Unfortunately this radiation is not tumor selective and severe side effects to patients are induced due to damage in healthy tissues. Hence, concentration of radiation effects in tumors is a major challenge in radiation therapies and new strategies have been proposed.

New radiation modalities such as Intensity-Modulated Radiation Therapy (IMRT), cyberKnife and hadrontherapy have been developed in this purpose. These approaches have been improved by taking into account the topological features of tumors and the physical properties of the ionizing beam. In particular, hadrontherapy is one of the promising modality, which is based on carbon ions radiation. The advantage of charged particles rests on their physical properties, to deposit the maximum energy at the end of their track (defined as the Bragg peak). Hence the dose deposited after the tumor is close to zero. This ballistic property is a strong advantage compared to other modalities, and hadron (or proton) therapy is currently used to treat tumors seated in badly sensitive organs, *e.g.* eyes, brain and neck. In spite of this superior property, this modality remains limited by the low but significant dose deposited at the entrance of the track, which also damages normal tissue.

In the last decades, a new strategy based on the combination of nanomedicine with radiotherapy has been developed to amplify the effect of ionizing radiations. In particular, nanoparticles containing heavy atoms (high-Z NPs), such as platinum and gold, have been proposed as potential nano-radio-enhancers. The versatility of nanoparticles surface chemistry opens the perspectives to functionalize NPs with tumor targeting molecules and contrast agents to concentrate them in the tumors. Thus this innovative strategy is expected to improve radiation effects selectively in the tumor.

Surprisingly, little has been proposed for the combination of NPs and hadrons. The group Nano-Hadron at the Institute of Molecular Sciences in Orsay (ISMO) was the first to propose this strategy (thesis of Erika Porcel 2008-11). They have shown that

nanostructured platinum atoms (Pt NPs) activated by carbon ions amplify the induction of nanometer size molecular damage. Unfortunately, these first Pt based nano-radio-enhancers were found toxic in cells.

Aim of the present work

The aim of my work was to develop stable, biocompatible and non-toxic, platinum based nanoparticles able to amplify radiation effects.

To this purpose, the nanoparticles synthesis was optimized using radiolysis, a singular but very advantageous sustainable method to synthesize small high-Z NPs. In order to assure biocompatibility and low toxicity, the Pt NPs were coated with poly(ethylene glycol) (PEG), a soluble biocompatible polymer widely used in nanomedicine.

This work includes: i) the synthesis and characterization of stable, biocompatible and sterile PEGylated platinum NPs, ii) their biological impact in cells (toxicity, uptake and localization), iii) the *in vitro* characterization of their properties to enhance radiation effects (photon and ion beam) and iv) the understanding of molecular scale mechanisms. Finally, a new type of platinum based bimetallic NPs have been also developed.

Description of the manuscript organization

In **Chapter I**, an overview of different nanotechnological developments for biomedical applications is presented. In addition, the state-of-the-art on nanomedicine and its combination with radiotherapies is shown together with the theoretical framework that allows a better understanding of the physical, chemical and biological processes taking place when ionizing radiations interact with a metallic nanoparticle. In **Chapter II**, the materials and methods used in this work are summarized. In **Chapter III**, the main results obtained for the PEGylated platinum nanoparticles, namely PtPEG-OH NPs, are presented and discussed. The potentiality of PtPEG-OH NPs to enhance the performance of hadrontherapy is particularly addressed in this chapter. The proposition of mono- and bimetallic gold-platinum nanoparticles as nano-radio-enhancers is shown in **Chapter IV**.

CHAPTER I: NANOTECHNOLOGY FOR BIOMEDICAL APPLICATIONS
State-of-the-art

1	Nanotechnology	6
1.1	Methods for nanomaterials preparation	6
1.1.1	Metallic NPs preparation <i>via</i> chemical synthesis.....	8
1.1.2	Metallic NPs preparation <i>via</i> water radiolysis	9
1.1.2.1	Water radiolysis	9
1.1.2.2	Redox properties of aqueous solutions.....	10
1.1.2.3	Radiolytic reduction and atom coalescence.....	11
1.1.2.4	Irradiation of polymers.....	13
1.2	Applications of nanomaterials	14
2	Nanomedicine	15
2.1	Drug delivery	16
2.2	Medical imaging.....	17
2.3	Other advances	18
2.3.1	Theranostic.....	18
2.3.2	Photothermal	20
2.3.3	Sensitization	20
3	Radiation therapies	21
3.1	Conventional radiotherapy.....	21
3.2	Hadrontherapy: an alternative approach for targeted cancer treatment.....	21
4	Nanoparticles for radiation therapies.....	24

4.1	Photons	25
4.2	Ions	26
5	The choice of gold and platinum NPs	28
5.1	Physico-chemical properties, surface chemistry and applications of Au and Pt	28
5.1.1	Gold	28
5.1.2	Platinum.....	29
5.2	Optical properties of NPs	32
5.2.1	Electronic structure: from the atom to the solid.....	32
5.2.2	The plasmon effect of metallic NPs.....	33
5.3	Impact in biological systems: metal compounds and NPs.....	34
6	Interaction of ionizing radiation with NPs.....	35
6.1	Activation processes by incident photons, ions and electrons.....	36
6.1.1	Activation by incident photons.....	36
6.1.2	Activation by incident ions	40
6.1.3	Activation by incident electrons.....	41
6.2	Plasmon excitation/relaxation	42
6.3	Relaxation processes	43
6.3.1	Fluorescence	43
6.3.2	Auger electron emission	44
6.3.3	Radiative versus non radiative de-exciation.....	45
6.4	Electron capture by positively charged sites	46

7	Objectives of this work.....	47
8	References.....	48

Chapter I: NANOTECHNOLOGY FOR BIOMEDICAL APPLICATIONS State-of-the-art

1 Nanotechnology

The revolutionary concept of nanotechnology started in 1959 when the physicist Richard Feynman (Nobel Prize in Physics - 1965) expressed that “the principles of physics, as far as I can see, do not speak against the possibility of manoeuvring things atom by atom”. However, it was until 1974 that the word “nanotechnology” was firstly employed by Professor Norio Taniguchi to define ultrahigh precision machines. In the 80’s, the modern nanotechnology era began with the development of the Scanning Tunnelling Microscope (STM) and the Atomic Force Microscope (AFM), in which scientists were able to observe and manipulate individual atoms and molecules. Therefore, nanoscience and nanotechnology are the study and application of extremely small objects (10^{-9} m) that involves the understanding of the fundamental physics, chemistry and biology of nanometre-scale objects.

1.1 Methods for nanomaterials preparation

In the *nano*-world, the properties of a material strongly depend on its size and shape. These characteristics define the applicability of *e.g.* plasmonic metallic nanostructures, quantum semiconductors and magnetic nanoparticles. There are two main approaches in the synthesis of nanomaterials known as the bottom-up and top-down approaches.

The top-down approach is based on the use of macroscopic materials that are modified through an externally-controlled process in order to reach nanometer size structures. This approach is commonly used in electronics to prepare integrated circuits within structures smaller than 100 nm (photolithography). The implementation of this method is generally complex and expensive due to its instrumentation.

On the other hand, the bottom-up approach is based on a self-assembly process that leads to the formation of nanostructures. In this process basic units such as atoms and molecules, are combined into larger stable structures. Common examples are quantum

dots [1] and nanoparticles (NPs) formation from colloidal initial suspensions [2]. The manufacturing cost mainly depends on the abundance and marketing competition of the primary units, as well as, on the final product design and synthetic route.

The described methods to synthesize NPs are illustrated in **Figure I - 1**.

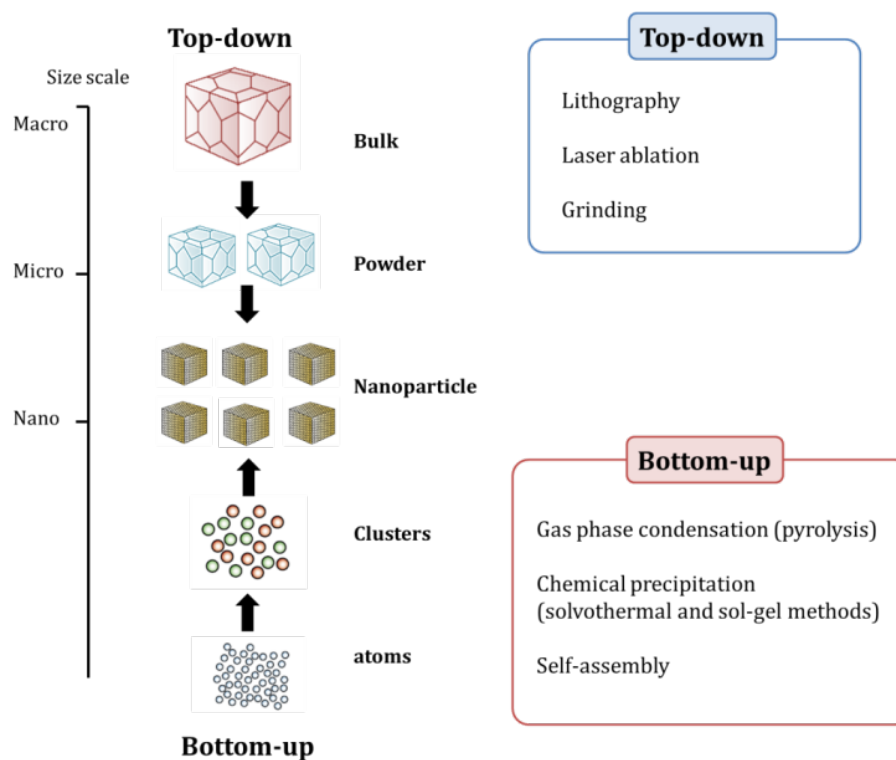


Figure I - 1. Schematic of the bottom-up and top-down approaches used in the synthesis of nanomaterials.

By comparing both manufacturing processes, the bottom-up method is more suitable in the synthesis of nanomaterials with a wider range of applications. This method is less expensive, more versatile and technologically simple to implement in academia and industry (scalability). The bottom-up approach is further classified into: i) gas phase (pyrolysis) and ii) liquid phase fabrication (*e.g.* solvothermal and sol-gel method). In the next section, we address the use of the liquid phase approach in the case of metallic NPs preparation.

[1] Liu R *et al.* (2011) *J. Am. Chem. Soc.* **133** 15221–3

[2] Sau T K and Rogach A L (2012) *Complex-shaped metal nanoparticles: Bottom-up syntheses and applications*

1.1.1 Metallic NPs preparation *via* chemical synthesis

Metallic nanoparticles are commonly prepared in liquid phase, through a method often denoted as chemical colloidal synthesis. This method involves the chemical or biological reduction of metal salts, photochemical or electrochemical pathways, or sonochemical/thermal decomposition of metal compounds in aqueous or organic solvents [2]. The process takes place in the presence of additives such as surfactants, ligands and polymers, which allows controlling the size and shape of nanoparticles. Colloids may be stabilized through electrostatic or steric forces. The first stabilization mechanism involves repulsive forces generated by an electric double layer formed at the nanoparticle surface (ions) while the second consists in a barrier created by adsorbed polymers/surfactants (brushes). Advantageously, these colloidal nanomaterials are suitable for further integration into more complex systems and devices, opening a great number of applications.

For instance, gold nanoparticles (Au NPs) are commonly prepared *via* chemical routes. The conventional method involves the reduction of HAuCl_4 by the action of citrate ions in water. This method is known as the Turkevich method [3] and leads to the formation of quasi-spherical Au NPs with an average core diameter of about 12 and 20 nm. The protocol has been optimized to enhance the size, shape homogeneity and stability of NPs [4] [5]. More interestingly, the use of thiol functionalized polymers allowed obtaining highly stable Au NPs [6], as gold may react with hydrogen sulphide [7] [8]. Thus, smaller Au NPs, with a diameter size ranging from 1.5 to 5.2 nm, can be successfully synthesized by means of thiol ligands [6]. In particular, the use of thiol-poly(ethylene glycol) derivatives are of great interest for the biomedical application of Au NPs [9] [10].

In this work, I evaluated the biological impact of advanced Au NPs. These nanoparticles were provided by Gloria Jiménez Sánchez, PhD student at the University of Franche-Comté (Besançon, France) supervised by Prof S. Roux. Briefly, these Au NPs were synthesized by

[3] Turkevich J *et al.* (1951) *Discuss. Faraday Soc.* **11** 55–75

[4] Frens G (1973) *Nat. Phys. Sci.* **241** 20–2

[5] Slot J W and Geuze H J (1981) *J. Cell Biol.* **90** 533–6

[6] Brust M *et al.* (1994) *Chem. Commun.* 801–2

[7] Woehrle G H *et al.* (2005) *J. Am. Chem. Soc.* **127** 2172–83

[8] Roux, S *et al.* *Int. J. Nanotechnology*

[9] Eck W *et al.* (2008) *ACS Nano* **2** 2263–72

[10] Wuelfing W P *et al.* (1998) *J. Am. Chem. Soc.* **120** 12696–7

reducing HAuCl_4 with NaBH_4 in a methanol/water mixture. The dithiolated derivate of the diethylenetriaminepentaacetic acid (DTPA), named DTDTPA, was used as ligand to ensure the quasi-irreversible grafting of gold nanoparticles, providing higher colloidal stability [11].

Platinum nanoparticles (Pt NPs) are also synthesized *via* chemical reduction of platinum ions in aqueous or organic solutions [12] [13]. These methods commonly use the K_2PtCl_4 precursor and reducing agents such as NaBH_4 . Thus, the main limitations of preparing metallic NPs *via* chemical methods are: i) the use of multi-step routes, ii) the addition of reducing agents, iii) the heating of the aqueous or organic solutions to initiate the reaction and iv) the necessity of purification and sterilization steps for biomedical concerns.

In this work, metallic nanoparticles were prepared in water *via* a photochemical method that involves the use of ionizing photons (γ -rays) to reduce metal salts and obtain purely metallic nanoparticles through a one-step method. The description of this method is presented in the next section.

1.1.2 Metallic NPs preparation *via* water radiolysis

1.1.2.1 Water radiolysis

The process of water radiolysis can be summarized by the following reactions occurring at different time scales (time by which each event is estimated to be complete) [14]:



Equation I - 1 represents the initial electronic excitation of a water molecule, which takes place on the time scale of an electronic transition. The positive radical H_2O^+ undergoes the ion-molecule reaction of **Equation I - 2** in $\sim 10^{-14}$ s. The excited H_2O^* state dissociates

[11] Alric C *et al.* (2013) *Nanoscale* **5** 5930–9

[12] Mironava T *et al.* (2013) *Toxicol. Vitr.* **27** 882–9

[13] Long N V *et al.* (2010) *Nanotechnology* **21** 035605

[14] Buxton G V (1987) *Radiation Chemistry: Principles and Applications* pp 321–49

as shown in **Equation I - 3** and the secondary electrons released to the medium are solvated in $\sim 10^{-12}$ s. Water radiolysis is illustrated in **Figure I - 2**.

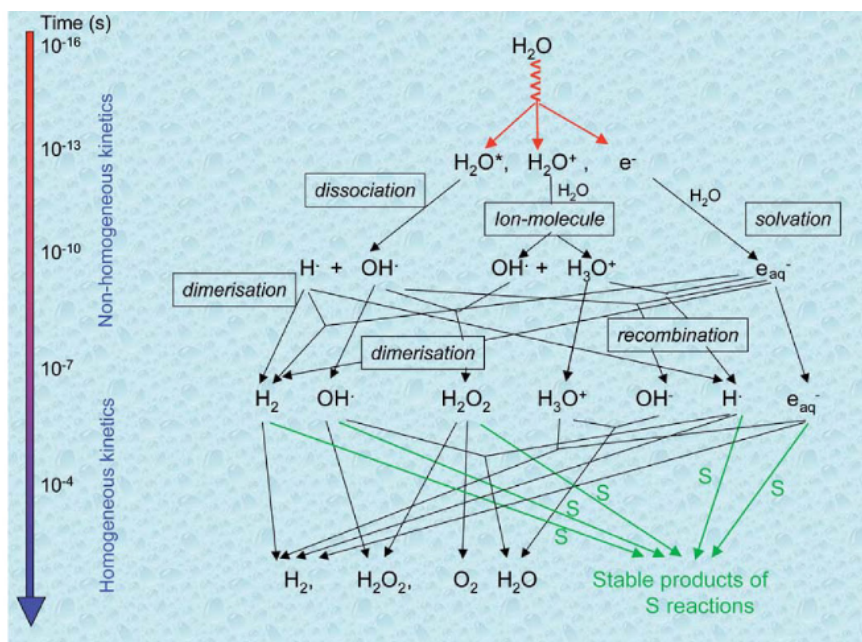


Figure I - 2. Scheme of the transient species produced during water radiolysis, without or in the presence of a diluted solute acting as a radical scavenger [15].

A fraction of the products in reactions **Equation I - 2** and **Equation I - 4** then diffuse to encounter another species and react to form molecular and secondary radical products.

1.1.2.2 Redox properties of aqueous solutions

In this work, metallic NPs were synthesized by water radiolysis in the perspective to produce ready-to-use biocompatible NPs. Water radiolysis generates free radicals acting as strong reducing or oxidizing agents. The redox properties of these primary radicals (see **Figure I - 2**) are:

- e_{aq}^- : a powerful reductant with a standard reduction potential of $E^\circ(\text{H}_2\text{O} / e_{aq}^-) = -2.87 \text{ V}$
- H^\cdot : a powerful reductant only in acidic conditions with a standard reduction potential of $E^\circ(\text{H}^+ / \text{H}^\cdot) = -2.31 \text{ V}$
- OH^\cdot : a powerful oxidant with a standard oxidation potential of

[15] Rodgers M A J (1987) *Radiation Chemistry: Principles and Applications*

$E^\circ(\text{OH}^\cdot/\text{OH}^-) = 1.90 \text{ V}$ in neutral solutions and

$E^\circ(\text{H}^\cdot, \text{OH}^\cdot/\text{H}_2\text{O}) = 2.72 \text{ V}$ in acidic solutions

The hydrated electron e_{aq}^- and the hydrogen atom H^\cdot atom react by attaching to a vacant orbital of an acceptor molecule such as a metal ion M_{aq}^{n+} by:



where n is the charge of the metal ion.

The hydroxyl radical OH^\cdot oxidizes inorganic ions by a simple one-electron transfer process:



where S is a diluted solute acceptor.

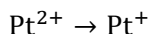
In radiation chemistry, the reduction or oxidation of the solute(s) are responsible for the production of new compounds. As water radiolysis induces approximately the same yields of reducing and oxidizing radicals one of these processes may be favored by the production of reactive or inert secondary radicals [16]. These secondary radicals are produced by: i) the irradiation of diluted organic solvents (as alcohols) or ii) by the irradiation of polymers. In this work the first strategy is not used and only the presence of polymers may modify the yields of the reducing and oxidizing reactions.

1.1.2.3 Radiolytic reduction and atom coalescence

The synthesis of metallic nanoparticles by radiolysis was a major challenge of my work. The method consists of reducing positive metal complexes (Pt^{II} for Pt NPs and Au^{III} for Au NPs) down to the metallic state *via* radiolysis. The metal ions are reduced by e_{aq}^- and H^\cdot as shown in **Equation I- 5** and **Equation I- 6**.

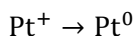
Multivalent ions, as Pt^{II} , are reduced down to the zero-valent state according to a multi-step reaction mechanism which involves intermediate species:

[16] Buxton G V (2008) An overview of the radiation chemistry of liquids *Radiation Chemistry*



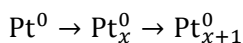
Equation I - 8

and



Equation I - 9

The uniform energy deposition into the irradiated medium leads to a homogeneous distribution of metal atoms and nucleation sites in the solution. Since the binding energy between two metal atoms is stronger than the atom–solvent or atom–ligand interaction energies, metal clusters are formed with a remarkable monodispersity through a multi-step coalescence process [17]:



Equation I - 10

where x is the number of Pt atoms forming the cluster (coalescence).

At high dose rate, as that used in this work (see source dosimetry in **Chapter II –Section 3.1.2**), all reducing species are produced and scavenged by the metal ions within a short time, following by coalescence of the well dispersed atoms [18]. The size of the atomic cluster (Pt_{x+1}^0) is delimited *in situ* by the presence of polymeric molecules which act as stabilizer. Polymers containing functional groups with good affinity to the metal ensure the anchoring of the molecules at the nanoparticle surface (see surface chemistry of Au and Pt in **Section 5.1**). Thus, the polymer chains stabilize the nanoparticle by electrostatic repulsion or steric hindrance. Moreover, the stabilizer does not chemically reduce the ions because this may induce the development of the atomic clusters (production of bigger NPs) [19].

Due to the remarkable reduction power of radicals, radiolysis is also a suitable method in the synthesis of clusters containing two or more metals [20], materials of great interest for various applications (*e.g.* catalysis [21]). It was shown by pulse radiolysis of mixed metallic solutions that electron transfer occurs from less noble atoms to the ions of the

[17] Remita H and Remita S (2010) Metal Clusters and Nanomaterials: Contribution of Radiation Chemistry *Recent Trends in Radiation Chemistry* p 607

[18] Belloni J and Mostafavi M (2001) *Stud. Phys. Theor. Chem.* **87** 411–52

[19] Belloni J and Remita H (2008) Metal clusters and nanomaterials *Radiation chemistry: from basics to applications in material and life sciences*

[20] Belloni J *et al.* (1998) *New J. Chem.* **22** 1239–55

[21] Mirdamadi-Esfahani M *et al.* (2010) *Gold Bull.* **43** 49–56

most noble metal, which leads to a favorable reduction of this last metal, resulting in a core-shell structure. Indeed, this process depends on the redox potential (tendency of chemical species to acquire electrons) of the complex metal ions used as precursors. The optical absorption band (see surface plasmon in **Section 5.2.2**) is progressively shifted in these mixtures [17]. At high dose rate (*e.g.* pulses of an electron beam with a few $\text{kGy}\cdot\text{s}^{-1}$) the reduction of all ions can be achieved rapidly without any inter-metal electron transfer. In this case, the coalescence takes place between the various atoms according to their abundance in the solution and independently on their potential. Thus, an alloyed structure may be formed by radiolysis [19].

1.1.2.4 Irradiation of polymers

The irradiation of polymers, used as stabilizers for colloidal NPs synthesis, leads to contrasting behaviors depending on its composition (repetition monomeric units). Possible effects of ionizing radiation in polymers are chain scission and cross-linking of polymeric chains [22]. The chemical changes induced by irradiating polymers are summarized in **Figure I - 3**. The effect of polymers irradiation in the synthesis of metallic nanoparticles is discussed in **Chapter III** and **IV** in relation with the NPs developed in this work.

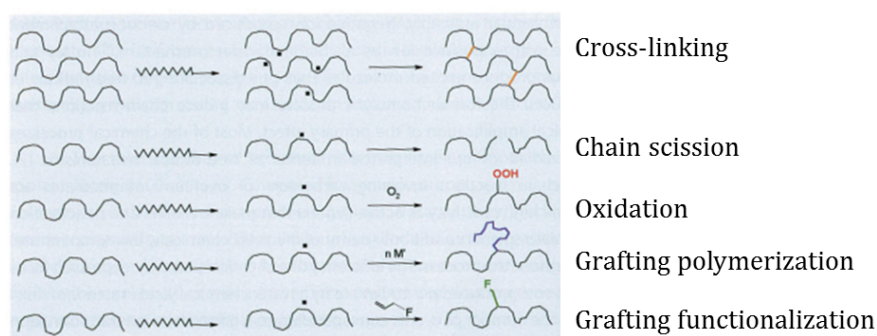


Figure I - 3. Illustration of chemical events that can be induced by high-energy radiation in polymers [22].

[17] Remita H and Remita S (2010) *Metal Clusters and Nanomaterials: Contribution of Radiation Chemistry Recent Trends in Radiation Chemistry* p 607

[19] Belloni J and Remita H (2008) *Metal clusters and nanomaterials Radiation chemistry: from basics to applications in material and life sciences*

[22] Coqueret X (2008) *Radiation chemistry: from basics to applications in material and life sciences* p 131

1.2 Applications of nanomaterials

Nowadays, nanoparticles are widely used in fields such as electronics, fuel cells, cosmetics, textile industry, car industry, self-cleaning surfaces, depollution, catalysis, photonics, biology and medicine.

Notably, in the last decades human has conducted nanoscience research to the imitation of nature and its perfect processes. For instance, we have been inspired from natural photosynthesis to enhance, by involving nanotechnology, electronic processes to efficiently produce clean energy [23] [24]. At the same time, we are constantly looking for the optimal use of the renewable natural resources, such as sunlight, for the benefit of society. Within this perspective, titanium dioxide can be doped with or metallic nanoclusters [25] [26] to enhance its photocatalytic activity in the spectral range of sunlight.

The *Fantastic Voyage*, a science fiction film directed by Richard Fleischer in 1966, tells us the story of a submarine crew who is reduced down to a microscopic size and venture into the body of an injured scientist to repair the damage to his brain. The perfect human machine sometimes needs to be “fixed” and this process may start at the nanoscale. Knowledge on the human body, its metabolic and enzymatic mechanisms, allowed scientists developing efficient nano-tool to detect (labs on chips) and to treat diseases. Today we are reaching the nano-robotic (self-propelled nanoparticles) era. A clear example is the shared Nobel Prize in Chemistry 2016, between Jean-Pierre Sauvage (France), J. Fraser Stoddart (UK), and Ben L. Feringa (Netherlands) for the “design and synthesis of molecular machines”, nanomachinery for a wide variety of applications, which will be a *Fantastic Voyage*.

This PhD project is the first stop in a voyage to developing efficient biocompatible platinum based nanoparticles (Pt NPs) to enhance radiation therapies. In the next section, an overview on the applicability of nanotechnology in medicine is presented.

[23] Kay A *et al.* (1994) *J. Phys. Chem.* **98** 952–9

[24] Ryu J *et al.* (2011) *Adv. Mater.* **23** 1883–8

[25] Méndez-Medrano M G *et al.* (2016) *J. Phys. Chem. C* **120** 5143–54

[26] Luna A L *et al.* (2016) *Appl. Catal. B Environ.* **191** 18–28

2 Nanomedicine

The application of nanotechnology in medicine with the perspective to prevent, diagnose and treat diseases is named nanomedicine. Due to the versatility of nanomaterials (surface chemistry), specific ligands such as antibodies, peptides and small molecules (fluorescent and targeting agents **Figure I - 4**) can be conjugated to develop selective diagnostic tools or therapeutic nano-agents, enhancing the physico-chemical properties and selectivity of conventional pharmaceutical drugs.

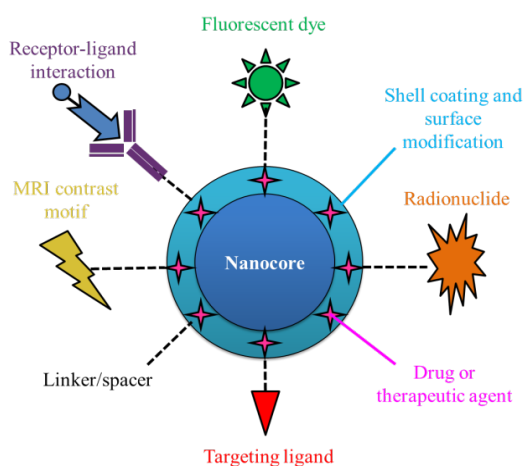


Figure I - 4. Scheme of a multi-modal nanoparticle for molecular imaging, drug delivery and therapy.

By regulation, all potential nano-therapeutics (organic (polymeric) or inorganic nanostructures) must exhibit a safe behavior after intravenous injection by preferential accumulation in the malignant side and easily renal elimination *in vivo*. The bio-distribution and clearance of nanoparticles are both influenced by: i) physiological factors such as bloodstream, opsonisation, endothelial permeability and ii) their physico-chemical properties such as size, shape, charge and surface chemistry. In particular, it is commonly considered that inorganic nanoparticles with sizes smaller than some tens of nanometers, do not accumulate in undesired organs, minimizing toxicity risks [27] [28]. The surface charge of nanoparticles also plays an important role in their uptake. For instance, positive charged nanoparticles adsorb plasma proteins by opsonisation, which causes their capture by phagocytes and further accumulation in the liver and spleen (with pores of about 100

[27]Choi H S *et al.* (2007) *Nat. Biotechnol.* **25** 1165–70

[28] Michelle L *et al.* (2008) *Nanomedicine (Lond)* **3** 703–17

nm) [29] [30]. In contrast, neutral or negatively charged nanoparticles circulate for longer time as the opsonisation phenomenon rarely occurs. Thus, all these properties must be carefully characterized in the development of potential nano-therapeutics.

2.1 Drug delivery

The most common approach in nanomedicine is the use of polymeric or inorganic nanoparticles containing encapsulated, dispersed, absorbed or conjugated therapeutic molecules as selective drug delivery systems. These nano-agents are known as nanocarriers.

The physico-chemical properties and biological performance of a nanocarrier is optimized in order to successfully release the active compound in the affected organ. The nanocarrier formulation and its conjugation with the drug is of great importance for a targeted therapy. Cell-specific targeting may be accomplished by using active or passive mechanisms. The active approach uses recognition ligands such as antibodies attached to the surface of the carrier, or by the use of physical controlled stimuli (*e.g.* temperature, pH or magnetism). The passive approach is a result of enhanced permeability and retention (EPR) effect, which occurs in leaky tissues of tumors [31].

Drug delivery systems are mainly used to treat infectious or genetic diseases and cancer. Nanocarriers are mainly found as liposomes and lipid nanoparticles (80 – 300 nm), dendrimers (1 – 10 nm), polymers (10 – 100 nm), silica (10 – 300 nm) or carbon nanomaterials (1 – 5 nm) [32].

Liposomes were the first to be investigated as drug carriers [33] [34]. Liposomes are vesicles composed by phospholipids and steroids (*e.g.* cholesterol) that increase the solubility of anticancer drugs and thus their therapeutic effect [35]. Smaller carriers are based on polymeric nanoparticles, made from biocompatible and biodegradable materials, which are considered as more promising drug carriers than liposomes [36] [37]. The first

[29] Alexis F *et al.* (2008) *Mol. Pharm.* **5** 505–15

[30] Albanese A *et al.* (2012) *Annu. Rev. Biomed. Eng.* **14** 1–16

[31] Acharya S and Sahoo S K (2011) *Adv. Drug Deliv. Rev.* **63** 170–83

[32] Wilczewska A Z *et al.* (2012) *Pharmacol. Reports* **64** 1020–37

[33] Bangham A D and Horne R W (1964) *J. Mol. Biol.* **8** 660–8

[34] Saunders L and Thomas I L (1958) *J. Chem. Soc.* 483

[35] dos Santos Giuberti C *et al.* (2011) *J. Liposome Res.* **21** 60–9

[36] You J *et al.* (2013) *J. Nanoparticle Res.* **15** 2123

developments were devised as polymeric carriers for vaccines and anticancer drugs [38]. For instance, the delivery of anticancer drugs that does not cross the blood-brain barrier, such as doxorubicin, has been enhanced by the use of polymeric nanoparticles [39]. Under the existing regulatory framework, medicinal products containing nanoparticles in form of liposomes (*e.g.* Caelyx, Myocet), polymer protein conjugates (*e.g.* PegIntron, Somavert), polymeric substances (*e.g.* Copaxone) or suspensions (*e.g.* Rapamune, Emend) have already been authorized in EU and the US.

Inorganic nanoparticles are important multifunctional platforms in nanomedicine. For instance, nanostructures composed of metal-organic frameworks (nanoMOFs) are stable biocompatible nano-agents with the ability of efficiently adsorb and release therapeutic molecules [40] [41]. Silica based nanoparticles are used as nanoreservoirs and nanocarriers of commonly prescribed drugs to enhance their tolerance and therapeutic efficiency [42] [43]. The sol-gel chemistry allows developing porous silica nanoparticles for drug delivery purposes. These carriers have been largely investigated in the treatment of Parkinson's disease [44]. An alternative silica composite containing titania is successfully used in clinics for the treatment of diabetic foot ulcers [45].

2.2 Medical imaging

Nanomedicine plays also a key role in medical imaging. In this context, different approaches have been investigated.

Among the optical approaches, nano-probes for fluorescence imaging consist in polymeric or inorganic based nanoparticles functionalized with near-infrared fluorescent markers (NIRF). The NIRF spectral window, from 650 up to 900 nm, allows imaging biological tissues with minimum auto-fluorescence overlapping [46]. The main advantages of NIRF dye-containing nanoparticles are: i) higher photostability and biocompatibility, ii) better

[37] Gref R *et al.* (2012) *Adv. Drug Deliv. Rev.* **64** 316–26

[38] Couvreur P *et al.* (1982) *J. Pharm. Sci.* **71** 790–2

[39] Gulyaev A E *et al.* (1999) *Pharm. Res.* **16** 1564–9

[40] Agostoni V *et al.* (2015) *Sci. Rep.* **5** 7925

[41] Baati T *et al.* (2013) *Chem. Sci.* **4** 1597–607

[42] López T *et al.* (2016) *J. Encapsulation Adsorpt. Sci.* **06** 47–55

[43] López Goerne T M *et al.* (2013) *J. Nanomater.* **2013**

[44] López T *et al.* (2015) *Mater. Lett.* **161** 160–3

[45] López T and Rodríguez C E (2015) *Rev. la Fac. Med. la UNAM* **58** 5–12

[46] He X *et al.* (2010) *Rev. Nanomedicine Nanobiotechnology* **2** 349–66

water solubility, iii) enhanced fluorescence signal and iv) higher versatility for bioconjugation [46].

Another approach is based on the intrinsic properties of nanoparticles. For instance, magnetic nanoparticles, such as iron oxide and gadolinium oxide, are used as contrast agents to improve the performance of the medical Magnetic Resonance Imaging (MRI) [47] [48]. More interestingly, magnetic nanoparticles can also be used as nanocarriers for targeted drug delivery [49] [50].

Finally, the radiolabeling of polymeric nanoparticles is an emerging field used to combine positron emission tomography (PET) or single photon computed tomography (SPECT) with drug delivery. Radiolabeling of PET isotopes with a very wide range of half-lives [51] enables therapy planning and monitoring by molecular imaging from the time of administration to several days or weeks.

2.3 Other advances

2.3.1 Theranostic

Multi-modal nanoparticles are particularly of great interest to achieve theranostic, an approach based in the use of a single hybrid-nano-agent for simultaneous targeted diagnostic and treatment (**Figure I - 5**).

The diagnosis is mainly achieved through the magnetic properties of the nanomaterial (MRI). The treatment may imply drug delivery systems [52] or the activation of nano-agents by an external stimulus (radiation).

[47] Sun C *et al.* (2008) *Adv. Drug Deliv. Rev.* **60** 1252–65

[48] Bridot J-L *et al.* (2007) *J. Am. Chem. Soc.* **129** 5076–84

[49] Dobson J (2006) *Drug Dev. Res.* **67** 55–60

[50] Tietze R *et al.* (2015) *Biochem. Biophys. Res. Commun.* **468** 463–70

[51] Stockhofe K *et al.* (2014) *Pharmaceuticals (Basel)*. **7** 392–418

[52] Fernandez-Fernandez A *et al.* (2011) *Appl. Biochem. Biotechnol.* **165** 1628–51

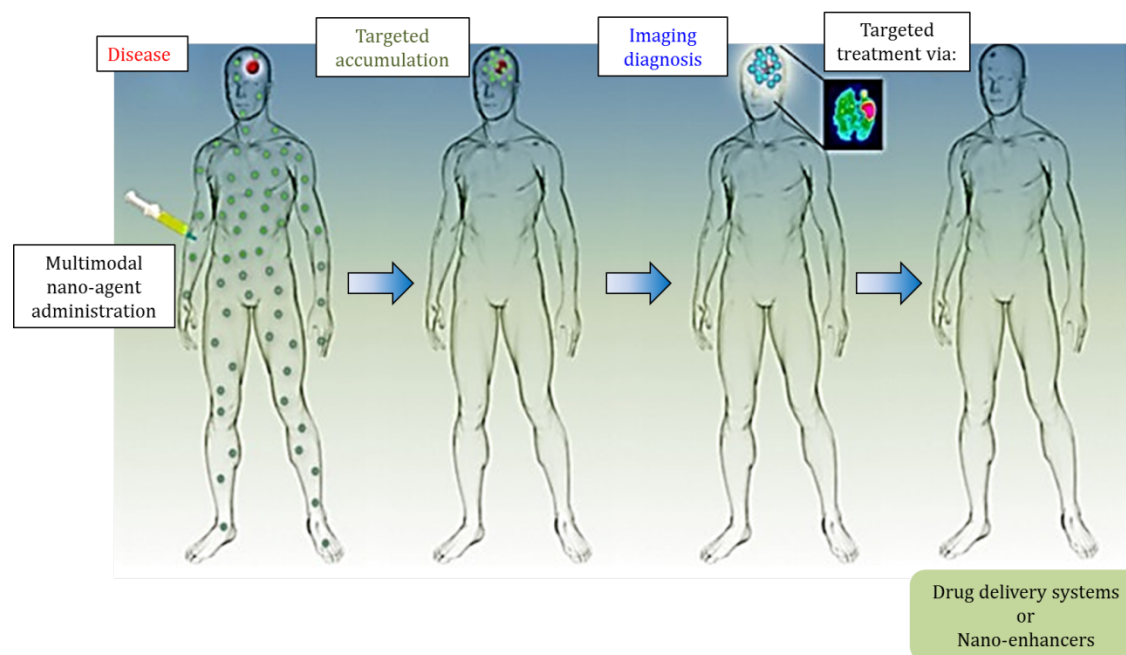


Figure I - 5. Theranostic approach using nanoparticles (adapted from [53]).

Many hybrid-nano-agents based on the magnetically active Fe_3O_4 have been proposed for imaging and therapeutic applications. [54]. These developments include the coating of Fe_3O_4 with Au NPs [55] and FePt alloy NPs [56], which combine the magnetic properties of iron oxide with the remarkable optical properties of metal nanoparticles. In particular, Au NPs are remarkable nano-agents in cancer diagnosis, as X-ray and computed tomography contrast agents, and treatment [57] [58].

On the other hand, lanthanide elements (with high atomic number) have a large range of properties that make them attractive as contrast and therapeutic agents [59]. For instance, gold nano-cores containing gadolinium chelates, are used not only as a contrast agent due to the presence of gadolinium (paramagnetic properties for MRI) but also for therapy due to the strong X-ray absorption of gold [60]. An extended study of the potentialities of gadolinium-based nanoparticles (GBNs) has provided encouraging results by combining imaging and therapy [59]. GBNs have been largely studied as a new range of agents for

[53] Ramos-Cabrer P and Campos F (2013) *Int. J. Nanomedicine* **8** 951–60

[54] Ho D *et al.* (2011) *Acc. Chem. Res.* **44** 875–82

[55] Heng Yu *et al.* (2005) *Nano Lett.* **5** 379–82

[56] Hong R *et al.* (2005) *Chem. Mater.* **17** 4617–21

[57] Hainfeld J F *et al.* (2006) *Br. J. Radiol.* **79** 248–53

[58] Butterworth K T *et al.* (2016) *Nanomedicine* **11** 2035–47

[59] Bridot J-L *et al.* (2009) *J. Mater. Chem.* **19** 2328

[60] Debouttière P-J *et al.* (2006) *Adv. Funct. Mater.* **16** 2330–9

theranostic, using different ionizing radiation sources as high-energy photons [61], neutrons [59] and carbon ions [62].

2.3.2 Photothermal

This modality is based on the surface plasmon phenomena of noble metal nanoparticles. When the metal nanoparticle, *e.g.* Au or Ag, is much smaller than the wavelength of light, coherent oscillation of the conduction band electrons are induced by interaction with the electromagnetic field. This resonance is called Surface Plasmon Resonance (SPR) (see the SPR effect of metallic NPs in **Section 5.2.2**) [63]. Thus, electromagnetic radiation at the frequency of the metal NP plasmon is efficiently absorbed and rapidly converted into heat [64]. This energy propagates into the medium to locally increase the temperature and kill targeted cells. The absorption band of NPs has to be located in the near-infrared region which is the wavelength range penetrating living tissue. Within this purpose, the size and shape of NPs has to be optimized. In this context, mainly gold based nanoparticles have been investigated, among them gold nanorods [65] and gold nanoshells [66] [67]. Less is known about the applicability of other metal based NPs, such as silver and platinum, in photothermal treatment. For instance, non-cytotoxic Pt NPs (5-6 nm core, stabilized with PVP) may generate a 9 °C increase in temperature when interacting with a near-IR 1064 nm laser leading to photothermal triggered cell death (Neuro 2A cancer cells) [68].

2.3.3 Sensitization

A sensitizer is a drug or biomolecule that makes cells more sensitive to a specific treatment. These agents mainly inhibit cells repairation pathways. For instance, a radiosensitizer is used in combination with radiation therapy to modify the biological response of cells to radiation. The vectorization of radiosensitizers is a new approach in the treatment of radio-resistant tumors. Polymeric nanoparticles are used within this purpose. The incorporation of short interfering DNA molecules (Dbait) with polymers impairs the repair of chromosomal damage, which makes cells more sensitive to the

[61] Miladi I *et al.* (2015) *Nanomedicine Nanotechnology, Biol. Med.* **11** 247–57

[62] Porcel E *et al.* (2014) *Nanomedicine* **10** 1601–8

[63] Eustis S and El-Sayed M A (2006) *Chem. Soc. Rev.* **35** 209–17

[64] Link S and El-Sayed M A (2000) *Int. Rev. Phys. Chem.* **19** 409–53

[65] Huang X *et al.* (2006) *J. Am. Chem. Soc.* **128** 2115–20

[66] Pattani V P and Tunnell J W (2012) *Lasers Surg. Med.* **44** 675–84

[67] Yang P *et al.* (2012) *Chemistry* **18** 9294–9

[68] Manikandan M *et al.* (2013) *Biomaterials* **34** 5833–42

effects of radiation. This strategy is known as nucleic acid-based cancer molecular therapies [69]. The combination of cholesterol and Dbait is a promising alternative in the field [70] [71].

3 Radiation therapies

3.1 Conventional radiotherapy

Radiotherapy is the most common approach to treat cancer, used in about 50% of the cases. Conventional radiotherapy based on the use of high energy photons (X-rays) is the most common approach in clinical settings. X-rays are generated by medical linear accelerators with energies in the order of few MeV (between 1 and 25 MeV). These ionizing beams have the ability to penetrate tissue, allowing the treatment of tumors in a non-invasive way. Unfortunately, high-energy photons present a significant lack of selectivity (see dose deposition profile in comparison with ions in **Figure I - 6**) and provoke damage not only in abnormal cells but also in healthy tissues, which induces side effects to patients. This effect is explained by the physical properties of photons and their interaction with biological matter at the energy of the treatment (see interaction of photons with matter in **Section 6.1.1**).

Therefore, the improvement of radiation therapy is a major challenge. In this perspective, new methods are explored to maximize the dose deposition in tumors through the development of more selective techniques such as Intensity-Modulated Radiation Therapy (IMRT), cyberknife and hadrontherapy.

3.2 Hadrontherapy: an alternative approach for targeted cancer treatment

Hadron beams for medical applications were first proposed by the physicist Robert R. Wilson in 1946 [72]. They were first tested by the Lawrence Berkeley National Laboratory (LBNL) in 1954 and more than 2500 patients were treated with proton, helium, carbon and neon ions. Despite the encouraging results, the LBNL's clinical treatment program was interrupted in 1993[73]. In 1994 the Heavy Ion Medical Accelerator (HIMAC), the first

[69] Dutreix M *et al.* (2010) *Mutat. Res.* **704** 182–9

[70] Berthault N *et al.* (2011) *Cancer Gene Ther.* **18** 695–706

[71] Schlegel A *et al.* (2012) *Mol. Ther. — Nucleic Acids* **1**

[72] Wilson R R (1946) *Radiology* **47** 487–91

[73] Berkeley Lab News Center

dedicated carbon-ion medical facility inspired by the work at Berkeley Lab, was built at NIRS in Chiba, Japan [74].

Hadrontherapy commonly uses protons (proton-therapy) and carbon ions (carbon-therapy) beams in the range from 70 to 400 MeV/a.m.u. Hadrontherapy is particularly suited to treat tumors seated in sensitive organs (*e.g.* head, neck and eyes) and childhood cancers (*e.g.* central nervous system tumors) due to the ballistic effect and efficiency of ions [75]. The physical processes taking place when ions interact with matter (in the case of NPs and biological systems) are addressed in **Section 6.1.2**.

Indeed, hadron beams enhance the tumor selectivity of conventional radiotherapy due to their dose deposition profile in tissue (see **Figure I - 6**).

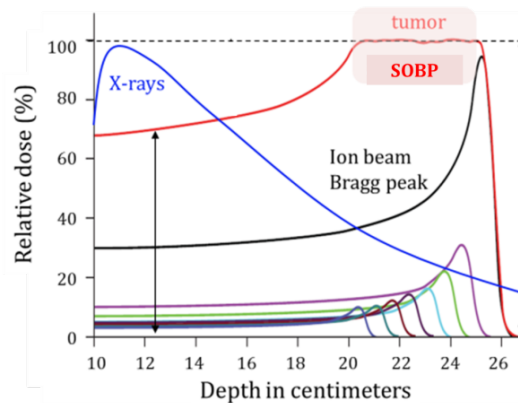


Figure I - 6. Principle: illustration of the dose deposition profile of X-rays (in blue) and ions at the rising Bragg peak (in black) and the Spread-out Bragg Peak (SOBP) (in red).

This unique characteristic allows the deposition of maximum energy into a relatively well-defined volume (Bragg peak) while sparing the surrounding healthy tissue. As hadron beams are stopped by penetrating tissues (over a few centimeters), a basically zero energy is deposited behind the tumor. In addition, fast ions (in particular carbon ions) experience less scattering in comparison with X-rays, which facilitates the delivery of high radiation doses to targets in close proximity to critical structures [76] (**Figure I - 7**). Thus, ions are biologically more efficient than X-rays (relative biological effectiveness, RBE), which allows increasing the therapeutic index of radiotherapies in the treatment of

[74] Hirao Y *et al.* (1992) *Nucl. Phys. A* **538** 541–50

[75] Laramore G E (2009) *Curr. Opin. Oncol.* **21** 224–31

[76] McDonald M W and Fitzek M M (2010) *Curr. Probl. Cancer* **34** 257–96

radioresistant tumors (*e.g.* glioblastoma and chordoma). These properties allow considering hadrontherapy as a more powerful oncological technique.

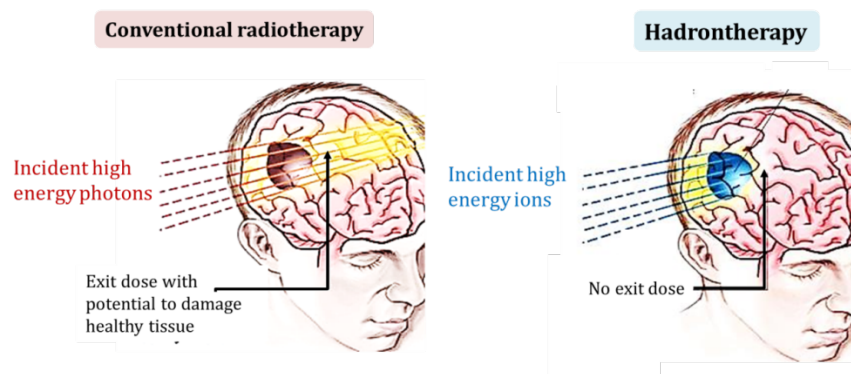


Figure I - 7. Schematic comparison between the energy deposition of conventional radiotherapy and hadrontherapy to treat a brain tumor (adapted from [77]).

Therefore, in spite of the high cost, since the early 1990s new hadron facilities have been built particularly in Europe and North America [78] [79]. New hadron-beam centers are under construction. France has two operating proton therapy centers, the Center of André Lacassagne in Nice and the Center of Protontherapy in Orsay. In addition, protontherapy treatments will be soon available in Toulouse at the Institut Claudius Regaud and one carbon facility, ARCHADE in Caen is in project. The experimental research using carbon beams is mainly conducted at GANIL, Caen [80].

During the treatment, ions may be delivered by: i) passive spreading or ii) active spreading [81]. In clinic, the most common delivery method is the passive spreading, which uses scattering materials to sufficiently broaden the Bragg Peak for total tumor coverage. This technique is known as spread-out of the Bragg peak (SOBP) (see red profile in **Figure I - 6**). Using this irradiation mode, the dose deposition at the entrance of the ion beam is accumulated and remains significant in front of the tumor, which induces side effects to the patients. Therefore, an innovative strategy combining metal based NPs with radiations has been evaluated. In this strategy, NPs will accumulate into the tumor to locally increase the effect of radiation and thus reduce the total dose.

[77] Proton therapy: The new weapon of choice against cancer is coming to Australia

[78] Schardt D (2016) Hadrontherapy *Basic Concepts in Nuclear Physics: Theory, Experiments and Applications*

[79] UniversitätsKlinikum Heidelberg: Therapy centers in the world

[80] France Hadron - Home

[81] Lomax A (2007) *Med. Phys.* **34** 2552

In this work, *in vitro* experiments were performed at the Heavy Ion Medical Accelerator (HIMAC) in Chiba using this SOBP strategy (see experimental conditions **Chapter III – Section 3.3.2**) with Pt NPs.

Thus, the main motivation of this work is the improvement of radiotherapies by combining the advantages of targeted nanomedicine with photons and carbon ions.

4 Nanoparticles for radiation therapies

Heavy atoms (high-Z, mostly metals) containing compounds have been used as a novel strategy to enhance the biological impact of radiations. The combination of chemotherapy, by means of cis-Pt, with photons (X-rays) showed encouraging *in vivo* results in the treatment of gliomas [82]. However, due to the high toxicity of cis-Pt (DNA cross-linking), the radio-enhancement of platinum atoms was not fully understood. The principle of combining high-Z atoms with irradiation was then elucidated in cells loaded with non-toxic molecular complexes [83]. The enhancement of radiobiological effects by heavy atoms was explained in terms of early physical events and Auger de-excitation processes [84]. In the perspective of targeted radiotherapy, this strategy failed by lack of tumor selectivity. An improved approach consisted on combining high-Z containing nano-agents with radiations [85].

Radiation dose enhancement by high-Z based nanoparticles, such as metallic nanoparticles, is a promising alternative in cancer therapeutics. Through an astute nanoparticle design, an efficient tumoral drug accumulation is achieved, which induces an increase of the local dose deposition (targeting) while preserving healthy tissues. Therefore, metal-based nanoparticles have been the object of intense experimental [86] and theoretical research [87] to better understand, from a physical, chemical and biological point of view, the enhancing effect of nanoparticles interacting with ionizing radiation. For instance, core-shell (metal-ligand) platinum nanoparticles and, more often,

[82] Biston M-C *et al.* (2004) *Cancer Res.* **64** 2317–23

[83] Usami N *et al.* (2008) *Int. J. Radiat. Biol.* **84** 603–11

[84] Kobayashi K *et al.* (2010) *Mutat. Res.* **704** 123–31

[85] Kong T *et al.* (2008) *Small* **4** 1537–43

[86] Retif P *et al.* (2015) *Theranostics* **5** 1030–44

[87] McMahon S J *et al.* (2011) *Radiother. Oncol.* **100** 412–6

nanostructured cis-Pt delivery systems are under study to enhance the therapeutic effect of platinum by minimizing its toxicity [88].

A molecular approach is commonly adopted to characterize the radiation enhancing effect of high-Z NPs. This approach consists in using plasmids (DNA-based molecular probes) [89] [90]. This allows evaluating the nanoparticles induced nanosize biological damage triggered by radiation, which has been demonstrated using photons and fast ions [89] [91] [62] [92] [93]. Experiments in the presence of a radical scavenger (DMSO), provide insights in the NPs radio-enhancement mechanism [91] [94], which has been also demonstrated in cells [95].

Au-core NPs are commonly used in combination with photons (see state-of-the-art in **Section 4.1**). Nevertheless, in 2010, our group opened new possibilities in combining Pt-core NPs with carbon ions to improve the performance of hadrontherapy [91] (see state-of-the-art in **Section 4.2**). This Pt-core NPs coated with poly (acrylic acid) were found toxic in cells and improvements were needed. This is the object of my work.

4.1 Photons

In the pioneer work of Hainfeld and co-workers, it was demonstrated *in vivo* that Au NPs (1.9 nm – glucose coating) prolonged the life of mice treated with 160 kV X-rays [96] [97]. Nowadays, beyond Au NPs that are considered as the most promising nano-radio-enhancers [98], nanostructures composed of other heavy elements such as hafnium (NBTXR3) [58] and gadolinium (AGuIX) [99] (developed respectively by the companies Nanobiotix, Paris, France and NH-TherAguix, Lyon-Grenoble, France) are currently tested in clinic.

-
- [58] Butterworth K T *et al.* (2016) *Nanomedicine* **11** 2035–47
[62] Porcel E *et al.* (2014) *Nanomedicine* **10** 1601–8
[88] Wang X and Guo Z (2013) *Chem. Soc. Rev.* **42** 202–24
[89] Porcel E *et al.* (2011) *J. Phys. Conf. Ser.* **261** 012004
[90] McMahon S J *et al.* (2011) *J. Phys. Chem. C* **115** 20160–7
[91] Porcel E *et al.* (2010) *Nanotechnology* **21** 85103
[92] Wyer J *et al.* (2009) *Phys. Med. Biol.* **54** 4705–21
[93] Schlatholter T *et al.* (2016) *Int. J. Nanomedicine* **11** 1549
[94] Sicard-Roselli C *et al.* (2014) *Small* **10** 3338–46
[95] Jain S *et al.* (2011) *Int. J. Radiat. Oncol. Biol. Phys.* **79** 531–9
[96] Hainfeld J F *et al.* (2004) *Phys. Med. Biol.* **49** N309–15
[97] Hainfeld J F *et al.* (2008) *J Pharm Pharmacol* **4** 977–85
[98] Her S *et al.* (2015) *Adv. Drug Deliv. Rev.*
[99] Verry C *et al.* (2016) *Nanomedicine* **11** 2405–17

The main metal-core NP used in radio-enhancement is Au-core NP, which notable features include their unique physical, chemical and optical properties (SPR). Extensive research work has been conducted *in vitro* [95] and *in vivo* [58] [see Review article 98]. For instance, the radio-enhancement of PEGylated gold nanoparticles under gamma irradiation was found size-dependent *in vitro* and *in vivo*. *In vitro* experiments (HeLa cell model) showed that NPs with sizes ranging from 5 to 50 nm, decrease cell survival by necrosis and apoptosis. *In vivo* tests demonstrated that these NPs sizes decrease the tumor volume and weight with size-dependent liver accumulation [100].

In clinic, the big challenge is the effective treatment of brain tumors. Current treatment approaches are limited in large part by the cumulative dose (conventional radiotherapy in sensitive organs) and the blood-brain barrier (BBB) that blocks the delivery of anticancer agents to the tumor tissue. The combination of PEGylated-gold nanoparticles with radiotherapy has been thus proposed as a remarkable improved protocol against glioblastoma [101].

Glioblastoma and other head-neck type of cancer can be more efficiently treated with hadron beams. The next section is an overview of recent results presenting the radio-enhancement of metal based NPs in combination with fast ions (protons and carbon ions).

4.2 Ions

Less is known about the biological impact of metal-core NPs combined with ions. The radio-enhancement of protons (40 MeV – single Bragg peak) by means of metallic nanoparticles (gold and iron) was firstly demonstrated by Kim and co-workers in 2010 [102]. They observed the amplification of cell-killing and enhancement of tumor regression in a CT26 mouse model. Even if the enhancing physico-chemical mechanism proposed in this work was controversial [103] [104], this work evidenced for the first time the radio-enhancement of protons by metallic NPs. As follow, the enhancing effect of particularly Au NPs has been largely studied in cellular and animal models [105].

[100] Zhang X-D *et al.* (2012) *Biomaterials* **33** 6408–19

[101] Joh D Y *et al.* (2013) *PLoS One* **8** e62425

[102] Kim J-K *et al.* (2010) *Nanotechnology* **21** 425102

[103] Le Sech C (2012) *Nanotechnology* **23**

[104] Dollinger G (2011) *Nanotechnology* **22**

[105] Terakawa A *et al.* (2011) *X-Ray Spectrom.* **40** 198–201

The improvement on the effect of carbon ions has been also evaluated [106] [107]. For instance, Kaur and co-workers proved *in vitro* (HeLa) the radiation enhancing effect of glucose capped Au NPs combined with carbon ions (62 MeV). However, the effect of cell uptake and cell line was not discussed. These two parameters, together with NPs localization, are crucial in the radio-enhancement process.

Nevertheless, this effect is not exclusive of gold. During my thesis work, the group showed that the activation of Pt-core NPs (as well as for GBNs in theranostic) leads to the amplification of the nanosize damage induced by fast protons (150 MeV) [93]. This enhancing effect has been explained as an electron emission (Auger and valence electrons) and ROS production amplification in the close vicinity of NPs, which reinforce the nanoscopic character of the biological perturbation (**Figure I - 8**).

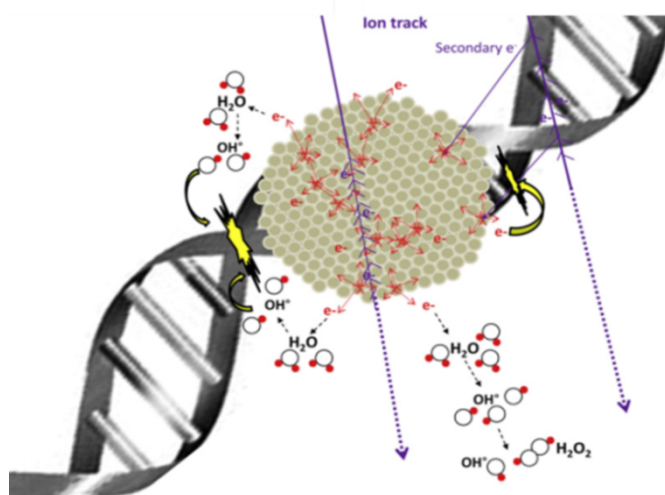


Figure I - 8. Schematic of the amplification effect of nanoparticles at the nanoscopic scale [91].

In summary, the use of Pt-core NPs for hadron therapy is an extremely interesting field of research, which is poorly exploited. This work is the first to show the radio-enhancement effect of Pt NPs in cells irradiated with photons and medical carbon ions.

[91] Porcel E *et al.* (2010) *Nanotechnology* **21** 85103

[93] Schlatholter T *et al.* (2016) *Int. J. Nanomedicine* **11** 1549

[106] Kaur H *et al.* (2013) *Nucl. Instruments Methods Phys. Res. Sect. B* **301** 7–11

[107] Liu Y *et al.* (2015) *Phys. Medica* **31** 210–8

5 The choice of gold and platinum NPs

Notably, metallic NPs have been largely used in combination with radiotherapies. This section aims to give an overview of the physico-chemical and electronic properties of gold and platinum, key properties on the biological impact and radiation enhancing effect of NPs.

5.1 Physico-chemical properties, surface chemistry and applications of Au and Pt

5.1.1 Gold

Gold (Au) is considered as the first metal discovered by man thousands of years ago. It is a rare metal with abundance in earth's crust of about 0.004 ppm (3.1×10^{-7} %) [108]. Gold is extremely malleable. It is an excellent thermal and electrical conductor, which strongly reflects infrared radiation.

From the chemical point of view, gold presents exceptional characteristics. It is the most noble of noble metals forming a huge variety of compounds. The nobility of the gold, as of other metals, rest on their large number of valence *d*-electrons which are available for bonding. The electron shell configuration of Au is shown in **Figure I - 9**.

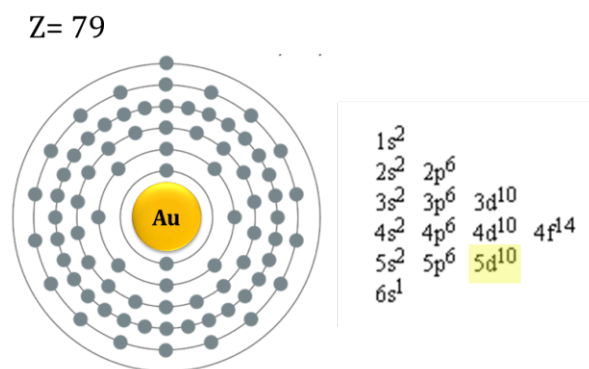


Figure I - 9. Electron shell configuration diagram of gold.

Gold compounds usually present oxidation states ranging from -1 to +5. However, Au^I and Au^{III} dominate gold chemistry. The reactivity of Au has been largely investigated [109]. For instance, Au^I (aurous ion) is the most common oxidation state within soft ligands compounds, which are typically linear. For instance, most drugs based on gold are Au^I

[108] It's Elemental - The Periodic Table of Elements

[109] Joost M (2015) *Synthesis and Original Reactivity of Copper and Gold Complexes*

derivatives [110]. The gold atom centred in Au^{III} complexes, *e.g.* gold chloride (Au₂Cl₆), are 8-electrons (*d*⁸) square planar compound with chemical bonds that have both covalent and ionic character [109]. In particular, Au^{III} complexes are largely used as precursors in the synthesis of Au NPs. In this work, I used as precursor the HAuCl₄ complex for the radiolytic synthesis of Au NPs (see method in **Chapter II – Section 1.2**).

Metallic gold (Au⁰) is an inert material as it is not attacked by oxygen (corrosion). It is unaffected by most acids. However, *aqua regia*, a 1:3 mixture of nitric acid and hydrochloric acid, dissolves gold oxidizing the metal to +3 ions.

The main applications of gold are: coinage, ornaments, jewellery, electronics, medicine and food. Particularly, due to the enhanced physical, chemical, optical, electronic and catalytic properties of Au NPs [111], which depend on their size, shape and surface chemistry, Au NPs are largely used as biosensors, catalysts and as optical devices [112] [113]. The surface chemistry (study of the chemical reactions at solid–liquid interface) of Au NPs has the potential to increase or decrease the stability and biological impacts of NPs. The surface of Au NPs is commonly capped with amine or thiol functional groups containing molecules or polymers such as polyallylamine hydrochloride (PAH), cetyltrimethylammonium bromide (CTAB), mercaptopropionic acid (MPA) [114], diethylenetriaminepentaacetic acid (DTPA) [11] and thiol-poly(ethylene glycol) (PEG) [115].

The most relevant characteristics of gold for this work are summarized (together with platinum) in **Table I - 1** (next section).

5.1.2 Platinum

Platinum (Pt) is a rare metal discovered in the sixteenth century in the Choco district of Columbia [116]. The occurrence of platinum group metals (Ru, Rh, Pd, Os, Ir and Pt) is less

[11] Alric C *et al.* (2013) *Nanoscale* **5** 5930–9

[110] Frank Shaw III C (1999) *Chem. Rev.* **99** 2589–600

[111] Haruta M *et al.* (1987) *Chem. Lett.* **16** 405–8

[112] Louis C and Pluchery O (2012) *Gold Nanoparticles for Physics, Chemistry and Biology*

[113] Granmayeh Rad A *et al.* (2011) *Phys. Procedia* **22** 203–8

[114] Bozich J S *et al.* (2014) *Environ. Sci. Nano* **1** 260–70

[115] Oh N and Park J-H (2014) *ACS Nano* **8** 6232–41

[116] McDonald D (1960) *History of Platinum*

than 2% by weight of the earth's crust and platinum abundance is estimated to be 0.005 ppm [117].

Platinum electrical and thermal properties are internationally used as the basics for calibration and reference (*e.g.* electrodes). In this context, the choice of platinum rests on its stability, inertness (as Pt⁰) and high purity. Pure platinum is a lustrous, ductile, and malleable material. The main characteristics of platinum considered in this work, together with gold, are summarized at the end of the section in **Table I - 1**.

The applicability of platinum depends on its nobility (number of valence *d*-electrons), bonding a range of simple substrates such as hydrogen, carbon, monoxide, olefins and acetylenes [118]. The electron shell configuration of Pt is shown in **Figure I - 10**.

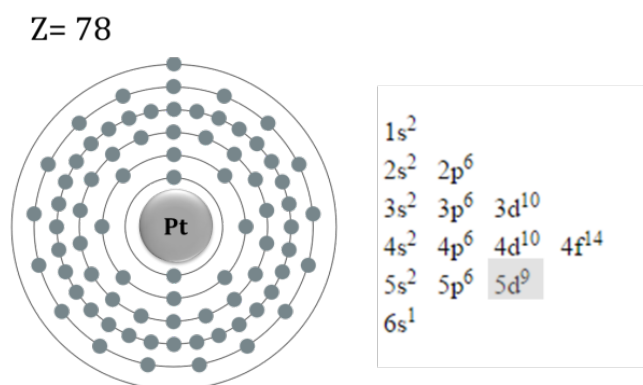


Figure I - 10. Electron shell configuration diagram of platinum.

Oxygen easily attacks platinum, which is commonly found in the +2 and +4 oxidation states. Elemental platinum is generally unreactive. However, when it is dissolved in *aqua regia*, it forms hexachloroplatinic acid (H₂PtCl₆) which is probably the most important platinum compound (Pt^{IV}) as it serves as the precursor for many others. The tetra-coordinated Pt^{II} complexes usually adopt 16-electron (*d*¹⁶) square planar geometries (*cis* or *trans*), which may be used in chemotherapy [119].

Thus, the applicability of platinum is based on its physico-chemical properties. Platinum is principally used in catalysis to: i) oxidize carbon monoxide, hydrogen and any unburnt

[117] Robson G G (1985) *Platinum 1985*

[118] Hartley F R (1991) *Chemistry of the platinum group metals : recent developments*

[119] McAuliffe C A *et al.* (1991) *Chemistry of the platinum group metals : recent developments*

hydrocarbons (automobilist industry) and ii) reduce the oxides of nitrogen [120]. In the chemical industry, platinum is widely used as catalyst in the oxidation of ammonia to nitric acid and in the selective hydrogenation and dehydrogenation (polymeric and pharmaceutical industries). Additionally, platinum is largely used in electronic devices due to its thermal properties.

At the nanoscale, Pt may be capped with molecules or polymers containing carboxylic (COO-) and hydroxyl (-OH) functional groups [121]. Indeed, colloidal Pt NPs are usually stabilized by covalent bonding, electrostatic interaction or chemisorption with these functional groups [121] [122]. Other good candidates to modify the surface chemistry of Pt NPs are thiol-containing polymers [56] resulting in an enhanced colloidal stability. The summary table of the metals is presented below.

Table I - 1. Summary: characteristics and physical properties of gold and platinum [123].

Property	Units	Au	Pt
Electronic configuration	-	[Xe] 4f ¹⁴ 5d ¹⁰ 6s ¹	[Xe]4f ¹⁴ 5d ⁹ 6s ¹
Atomic number	-	79	78
Atomic weight	g.mol ⁻¹	196.97	195.09
Atomic radius	nm	0.144	0.139
Ionization potentials - 1st	eV	9.2	9.0
2nd	eV	20.2	18.56
3rd	eV	30	28
4th	eV	44	41
Crystal structure	-	FCC	FCC
Lattice constant	nm	0.40782	0.39242
Fermi energy	eV	5.1	6.3
Standard potential	eV	+ 1.69 (Au ⁺ → Au ⁰) +1.50 (Au ³⁺ → Au ⁰)	+1.19 (Pt ²⁺ → Pt ⁰) +0.76 (Pt ⁴⁺ → Pt ⁰)
Electronegativity (Pauling scale)		2.54	2.28

- [56] Hong R *et al.* (2005) *Chem. Mater.* **17** 4617–21
 [120] Searles R A (1988) *Platin. Met. Rev.* **32** 123–9
 [121] Schrader I *et al.* (2015) *J. Phys. Chem. C* **119** 17655–61
 [122] Ono L K *et al.* (2011) *J. Phys. Chem. C* **115** 16856–66
 [123] The Photographic Periodic Table of the Elements

5.2 Optical properties of NPs

As already mentioned, materials at the nano-scale present remarkable physico-chemical properties that largely differ from the bulk. This is explained by the increased number of the surface atoms when decreasing the size of the NP. Indeed, electrons in a small conductive metallic NP flow freely due to their atomic confinement enhancing the electronic properties of the bulk. This effect is briefly described in the next section. More interestingly, this confinement results in the enhancement of the surface plasmon resonance (SPR) of metal (see description **Section 5.2.2**).

5.2.1 Electronic structure: from the atom to the solid

In solid-state physics, the band theory describes the electron band structure of bulk materials. Electrons in an atom occupy discrete energy levels (see for an example the electron shell configuration diagram of gold and platinum in **Section 5.1**). When these atoms are spaced close together, a large number of energy levels overlap resulting in energy bands; the so called valence and conduction band. A nanoparticle is in an intermediate state with an electron band structure between the atom and the bulk.

Figure I - 11. shows, for gold, the evolution of its electronic structure from the atom to the solid.

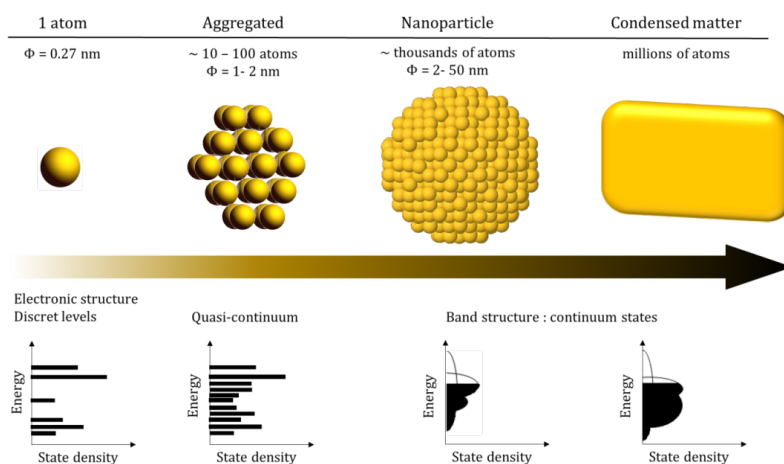


Figure I - 11. Electronic structures of a gold atom, nanoparticle and solid (adapted from [124]).

[124] Louis C and Pluchery O (2012) *Gold nanoparticles for physics, chemistry and biology*

In the particular case of gold, from the atom to the solid, the 6s and 6p bands hybridize. The 5d band, the highest fully occupied, is named valence band and the 6sp, the lowest vacant, is named conduction band. The Fermi level (E_F in **Figure I - 12**) represents the highest occupied energy level in the conduction band. The inter-band transitions from the *d* core electrons in the valence band to electronic levels in the conduction band, localized on top of the Fermi level (vacuum, white bands in **Figure I - 12**), take place from an energy threshold low enough to be reached with photons from the visible or near UV spectral region (see Fermi energy of gold and platinum in **Table I - 1**).

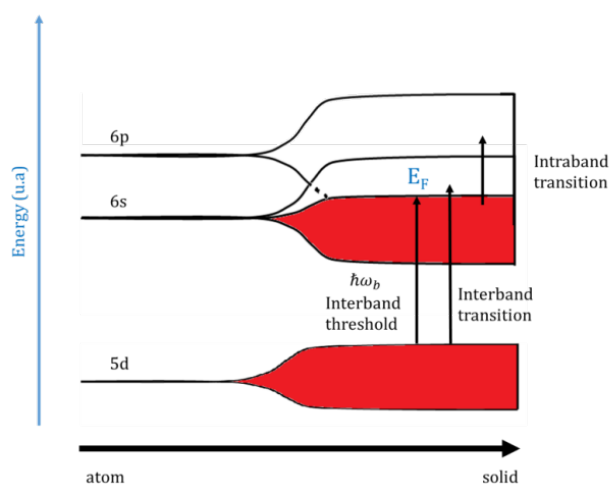


Figure I - 12. Scheme of the transition from discrete energy levels of atoms to electronic band structures (adapted from [124]).

Thus, the atomic confinement leads to an amplification of the absorption and the appearance of the plasmon, which is observed by absorption spectroscopy.

5.2.2 The plasmon effect of metallic NPs

When a metallic nanoparticle is much smaller than the wavelength of light, coherent oscillation of the conduction band electrons are induced by interaction with the electromagnetic field, this resonance is called Surface Plasmon Resonance (SPR) [63].

[63] Eustis S and El-Sayed M A (2006) *Chem. Soc. Rev.* **35** 209–17

[124] Louis C and Pluchery O (2012) *Gold nanoparticles for physics, chemistry and biology*

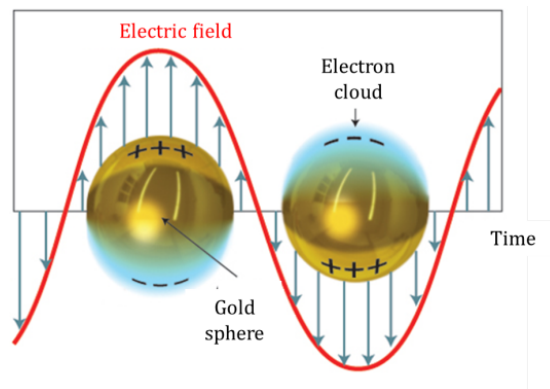


Figure I - 13. Schematic Surface Plasmon Resonance (adapted from [125]).

Plasmons are described as the oscillations of free electrons as consequence of the induction of a dipole moment in the material due to electromagnetic waves. These electrons migrate in the nanomaterial to restore its initial state. However, as the light waves oscillate, it leads to a constant shift in the dipole forcing the electrons to move at the same frequency as the light (see illustration in **Figure I - 13**).

This unique property of metallic nanoparticles made them the focus of several interdisciplinary researches, with applications including solar cells, catalysis, spectroscopy and signal enhancement for imaging and cancer treatment.

5.3 Impact in biological systems: metal compounds and NPs

Metal compounds have been used in medicine since the early 19th and 20th centuries to treat a wide variety of diseases [126] [110]. Since 1987, cisplatin (cis-Pt (Pt^{II})), the first platinum containing anti-cancer drug approved by the Food and Drug Administration [127], has been worldwide used in the treatment of various types of cancers. Since the discovery of cis-Pt, other platinum based drugs have been development for the treatment of endocrine-related cancers [128]. Moreover, by 1989, gold (I) and gold (III) containing molecules [110] were shown to have anti-cancer properties, results that inspired the future application of metal compounds against cancer. However, the main limitations to conventional cancer therapy in the chemo-modality include; harsh side effects, drug resistance and lack of solubility and selectivity. Cancer nanomedicine has the potential to

[110] Frank Shaw III C (1999) *Chem. Rev.* **99** 2589–600

[125] Juan M L *et al.* (2011) *Nat. Photonics* **5** 349–56

[126] Felson D T *et al.* (1990) *Arthritis Rheum.* **33** 1449–61

[127] Centre for Drug Evaluation and Research (1978) *FDA Oncol. Tools*

[128] Apps M G *et al.* (2015) *Endocr. Relat. Cancer* **22** R219–33

overcome these limitations by the use of nanostructured drug delivery systems [see Review article 88] and therapeutic agents [see Review article 129] for a targeted and more efficient medicine. In particular, by combining drugs or nano-agents containing heavy atoms with radiation, a significant treatment enhancement might be achieved [see Review articles 130 and 86].

Bulk Au⁰ is non-toxic and non-irritating when ingested, therefore it is sometimes used as a food decoration, *e.g.* in alcoholic drinks. At the same time, Au NPs are considered the less toxic metallic nanoparticles in biomedical concerns [131]. As already discussed the toxicity of metallic NPs depends on their surface functionalization [132] [133]. Due to the catalytic activity of platinum and its use in chemotherapy, the toxicity evaluation of Pt-core NPs has been a current object of research [134] [135] [136] [137], toxicity that mainly leads to DNA damage.

6 Interaction of ionizing radiation with NPs

Ionizing radiations are electromagnetic waves, ions or electrons that are energetic enough to remove electrons from atoms or molecules.

In this work, γ -rays and carbon ions were used. γ -rays from ⁶⁰Co and ¹³⁷Cs sources (see description in **Chapter II – Section 3.1**) were used to synthesize metallic NPs and to irradiate both, the bio-nanoprobe (a plasmid DNA based molecular probe) and cells. Carbon ions from the medical accelerator (HIMAC-Chiba, Japan) (see description in **Chapter II – Section 3.3**) were used in the irradiation of cells (HeLa). The interaction processes of ionizing photons, ions and electrons with condensed matter (NPs and biological matter) are described in this section.

-
- [86] Retif P *et al.* (2015) *Theranostics* **5** 1030–44
[88] Wang X and Guo Z (2013) *Chem. Soc. Rev.* **42** 202–24
[129] Bhattacharyya S, *et al.* (2011) *Pharm. Res.* **28** 237–59
[130] Kwatra D *et al.* (2013) *Transl. Cancer Res.* **2** 330–42
[131] Alkilany A M and Murphy C J (2010) *J. Nanopart. Res.* **12** 2313–33
[132] Książyk M *et al.* (2015) *Bull. Environ. Contam. Toxicol.* **94** 554–8
[133] Asharani P V *et al.* (2011) *Nanotoxicology* **5** 43–54
[134] Asharani P V *et al.* (2010) *Nanomedicine (Lond)* **5** 51–64
[135] Pelka J *et al.* (2009) *Chem Res Toxicol* **22** 649–59
[136] Elder A *et al.* (2007) *Adv. Mater.* **19** 3124–9
[137] Mironava T *et al.* (2013) *Toxicol. In Vitro* **27** 882–9

6.1 Activation processes by incident photons, ions and electrons

6.1.1 Activation by incident photons

Photons are elementary particles with zero mass and zero charge. Depending on its energy, the photon can interact with matter through different physical processes to activate NPs and induce biological damage. This interaction leads to a partial or total transfer of the photon energy to an electron.

Ionizing photons interact with matter by three different processes: photoelectric effect, Compton effect and electron-positron pair production.

- The photoelectric process, illustrated in **Figure I - 14**, takes place in the range of $10^2 < E_0 < 10^6$ eV (see **Figure I - 17** for targets such as H, C, N and O).

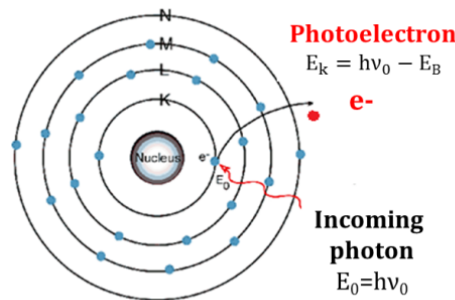


Figure I - 14. Photoelectric effect.

A photon is completely absorbed by an atom and an energetic photoelectron is ejected from one of the bound shells of the atom (mostly ionization of inner shell electrons) [138]. This process leads to the production of positive ionic species in the target. The photoelectron is ejected with a kinetic energy:

$$E_k = h\nu_0 - E_B \tag{Equation I - 11}$$

The photoelectric cross-section, the probability that this interaction occurs, increases with the mass of the targeted atom and decrease with the energy of the incident photon as follows:

[138] Blanc D and Portal G (1999) *Précis de physique nucléaire*

$$\sigma = cte \left(\frac{Z^4}{hv_0^3} \right)$$

Equation I - 12

- The Compton effect, illustrated in **Figure I - 15**, is characterized by the interaction of the incident photon with an outer shell electron. This process is dominant in the range of $10^5 < E_0 < 10^7$ eV (see **Figure I - 17** for targets such as H, C, N, O, Pt and Au).

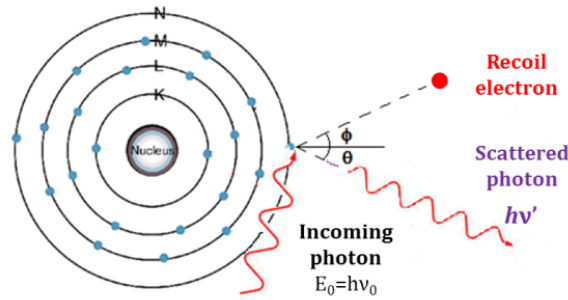


Figure I - 15. Compton effect.

The incoming photon with energy hv_0 is scattered at the angle θ (the scattering angle). The energy loss resulting from this interaction is transferred to an outer shell electron (also called recoiled electron), which is ejected from the atom. The energy hv' of the scattered photon is given by the following relation [139]:

$$hv' = \frac{hv_0}{1 + \alpha(1 - \cos\theta)}$$

Equation I - 13

where $\alpha = \frac{hv_0}{m_0c^2}$ and m_0 is the rest mass of the electron. The cross-section of the Compton effect only depends on the energy of the incident photon as shown in the Klein and Nishina following expression [140][139]:

$$\sigma_{KN} = 2\pi r_e^2 \left(\frac{1+\alpha}{\alpha^2} \left[\frac{2(1+\alpha)}{1+2\alpha} - \frac{\ln(1+2\alpha)}{\alpha} \right] + \frac{\ln(1+2\alpha)}{2\alpha} - \frac{1+3\alpha}{(1+2\alpha)^2} \right)$$

Equation I - 14

where r_e is the classical electron radius given by $r_e = \frac{e^2}{m_0c^2} = 2.819 \times 10^{-15}$ m.

[139] Mayles, P et al. (2007) *Handbook of radiotherapy physics. Theory and practice*
 [140] Klein O and Nishina Y (1929) *Z. Phys.* **52** 853–68

For $h\nu_0 > 0.5 \text{ MeV}$, the cross-section of the Compton effect is inversely proportional to $h\nu_0$ and slightly varies with the mass of the traversed material. Notably, this process is dominant for photons used in conventional radiotherapy [141].

- The electron-positron pair production, illustrated in **Figure I - 16**, takes place at energies higher than $1.02 \times 10^6 \text{ eV}$.

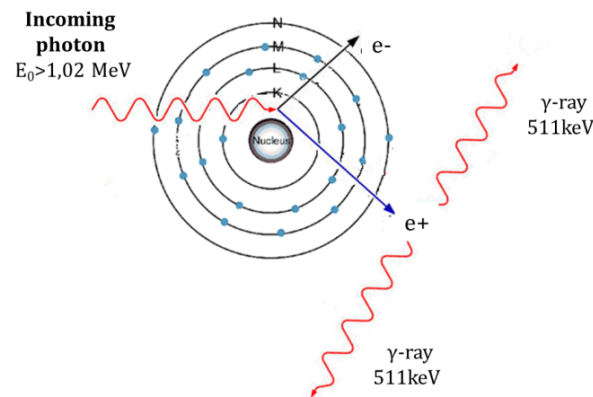


Figure I - 16. Electron-positron pair production.

In this mechanism the incoming photon is absorbed by the electric field of the atomic nucleus, which causes the creation of an electron (negatron)-positron pair emitted as the sum of their kinetic energies ($T^- + T^+$) by:

$$T^- + T^+ = h\nu_0 - 2m_0c^2$$

Equation I - 15

The two ejected particles (e^- and e^+) share the kinetic energy available and slow down through successive collisions with the surrounding medium. Once the positron is thermalized, it interacts with a low-energy electron from the surrounding medium. This reaction is known as annihilation. Momentum and energy are conserved in this process: two photons of 0.511 MeV are emitted at 180° from each other.

The cross section of the electron-positron pair production is proportional to the square of the atomic number of the target and becomes important at energies higher than $4m_0c^2$.

[141] Gazda M J and Coia L R (2005) Principles of radiation therapy *Cancer Management: a multidisciplinary approach*

In summary, **Figure I - 17** illustrates the relevance of the three interactions as function of the photon energy (in MeV) and atomic number of the target. Three regions can be distinguished:

- At low energy, up to 0.1 MeV, we observe that the photoelectric effect dominates. This effect vanishes when the incident photons have energies higher than 0.7 MeV. Notably, the photoelectric effect is more important in the presence of high-Z containing compounds such as gold and platinum (red and green horizontal lines, **Figure I - 17**) than in biological systems, which mainly contain carbon, hydrogen, oxygen and nitrogen atoms (blue lines, **Figure I - 17**).
- In the middle energy region, between 0.1 and 10 MeV, we observe that the Compton effect dominates. This effect characterizes the interaction of γ -rays. For instance, ^{60}Co γ -rays produce e^- of 0.6 MeV in average, which are energetic enough to induce further matter ionizations. The Compton process is nearly independent of the atomic number of the target (see $\sigma_{KN} = 2\pi r_e^2 \left(\frac{1+\alpha}{\alpha^2} \left[\frac{2(1+\alpha)}{1+2\alpha} - \frac{\ln(1+2\alpha)}{\alpha} \right] + \frac{\ln(1+2\alpha)}{2\alpha} - \frac{1+3\alpha}{(1+2\alpha)^2} \right)$ **Equation I - 14**).
- In the high energy region, higher than 7 MeV, the pair production becomes important and is dominant for energies above 10 MeV. It strongly depends on the atomic number of the target.

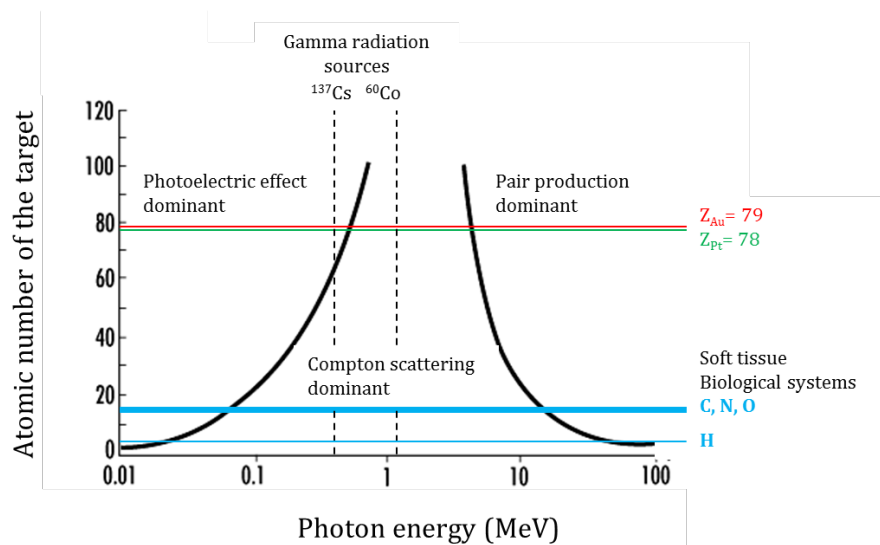


Figure I - 17. Processes involved in the interaction of photons with matter as function of the incident energy and atomic number of the target.

In conclusion, the photoelectric and Compton effect are the two main processes involve at the energy used to produce nanoparticles or to irradiate bio-systems (see vertical dotted lines in **Figure I - 17**).

6.1.2 Activation by incident ions

Fast ions mainly interact with the electrons of the targeted material (outer orbital electrons) through coulomb interaction. This interaction occurs at certain distance between the incident particle and the target electron, which is known as the impact parameter. In this process, illustrated in **Figure I - 18**, the incident ion transfers energy to the target to ionize and excite the atoms of the medium with a small deflection depending on the ion mass (momentum transfer).

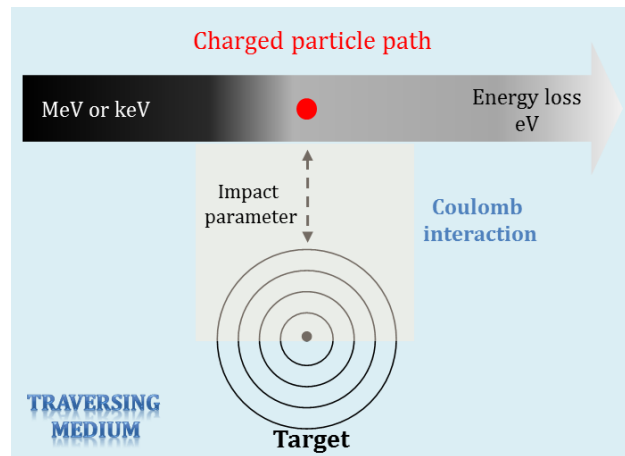


Figure I - 18. Schematic representation of the energy loss by a charged particle interacting with the target electrons at a distance defined as the impact parameter.

The energy transfer depends on the charge and velocity of the projectile, independently of its mass. Indeed, the inelastic collision with bound atomic electrons is the major process of energy loss at energies of interest in hadrontherapy.

Using non-relativistic collision theory, the second law of Newton and the Coulomb law describing the force between charged particles, the energy transfer Q is given by [139]:

$$Q = \frac{2k^2 z^2 e^4}{mb^2 v^2}$$

Equation I - 16

[139] Mayles, P et al. (2007) Handbook of radiotherapy physics. Theory and practice

where b is the impact parameter; m is the mass of the electron; z is the charge of the primary particle (in units of the electronic charge e); v is the velocity of the primary particle; and the constant $k = 8.9875 \times 10^9 \text{ Nm}^2 \text{ C}^{-2}$.

The maximum energy transfer Q_{\max} from an ion with mass M and kinetic energy T , to an electron with mass m (in rest) at $b = 0$ can be calculated by:

$$Q_{\max} = 4T \frac{mM}{(M+m)^2} \quad \text{Equation I - 17}$$

For instance, the interaction of carbon ions C^{6+} with $M = 12 \text{ u.m.a.}$ and a kinetic energy of 290 MeV/u.m.a. ($T = 12 \times 290 = 3480 \text{ MeV}$) might produce the emission of secondary electrons along the path ($m = 5.5 \cdot 10^{-4} \text{ u.m.a.}$) with kinetic energies ranging from 0 up to $Q_{\max} \sim 600 \text{ keV}$, electrons that are energetic enough to excite and ionize the surrounding medium and produce damage to biomolecules.

After inelastic collisions with electrons, incident particles slow down reaching energies below 100 keV (end of the track) allowing the interaction with the nucleus of the targeted atoms. The inelastic interactions with the nucleus result in the deflection of the incident particle associated with a nuclear reaction or bremsstrahlung, which energy deposition is negligible in clinical applications.

When a particle is almost at the end of its track, its capacity to ionize increases rapidly, giving rise to the Bragg peak (described in **Section 3.2**). The particle does not deposit any further energy beyond this point and thus the dose is practically zero after the tumor.

In conclusion, the energy loss of ions traversing a medium (*e.g.* tissue) is mainly due to interactions with electrons. Indeed, along the path of the incident ion, the electronic energy loss is three orders of magnitude higher than the loss of nuclear energy. Thus, NPs can be activated by the secondary electrons emitted on an ion path.

6.1.3 Activation by incident electrons

The Coulomb interaction of secondary electrons with the electrons of the medium can produce elastic or inelastic scattering.

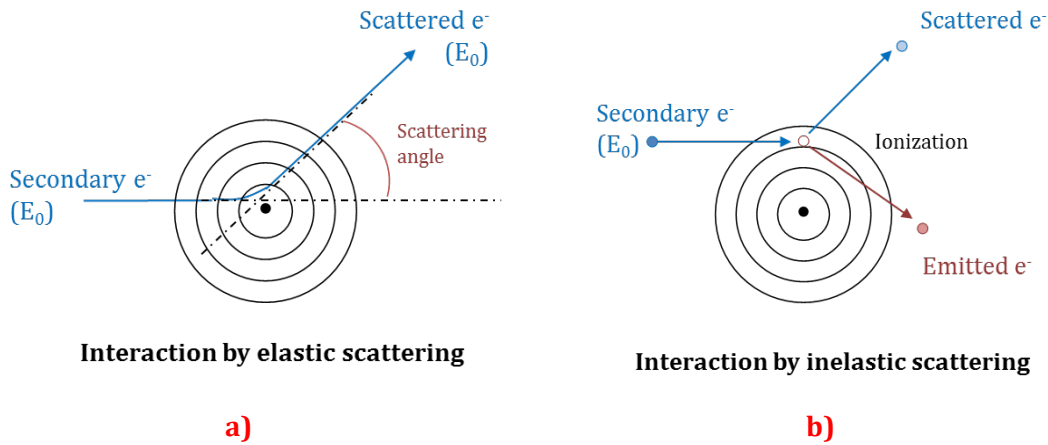


Figure I - 19. Interaction of secondary electrons by elastic and inelastic scattering.

By elastic scattering (**Figure I - 19a**), secondary electrons conserve their energy (E_0) but are strongly deviated. The probability of this process increases with the atomic number of the target (Z) and decrease with E_0 . Hence, this process is more important for low energy electrons, which only reach a few hundreds of eV.

By inelastic scattering (**Figure I - 19b**), secondary electrons transfer partially their kinetic energy to electrons in the medium. The cross-section of inelastic scattering is proportional to Z/E_0^2 . Hence, this process ionizes the medium through the scattering of the incoming secondary electron and an electron emission, which leads to the creation of atomic vacancies in the target.

Other interaction processes such as the Bremsstrahlung effect (radiative pathway) and the dissociative electron attachment [142] are negligible in the activation of NPs. Due to the atomic confinement in NPs, the activation *via* plasmon excitation/relaxation is of major interest in this work. This effect is described below.

6.2 Plasmon excitation/relaxation

Ionizing radiations as photons, ions and electrons may interact with a solid to excite and ionize the surrounding medium.

[142] Porcel E (2011) *Utilisation des nanoparticules pour améliorer les performances de la hadronthérapie*
Thèse de doctorat

In particular, metallic solids such as NPs are commonly considered, independently of their atomic structure, as a plasma of free electrons (previously described in **Section 5.2.2**). The interaction of ionizing radiation with free electrons leads to a collective electronic excitation, *i.e.* the excitation of the surface plasmon of the metal (**Figure I - 20**). The de-excitation of the plasmon may induce the emission of a photon (radiative process) or an electron (non-radiative process).

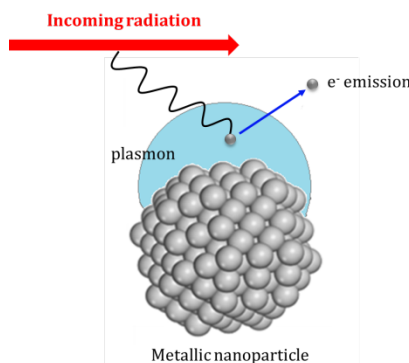


Figure I - 20. Collective electronic excitation of the plasmon in a metallic nanoparticle.

This process has been proposed as the major excitation/relaxation mechanism when metallic nanoparticles are activated by incident radiation [143].

6.3 Relaxation processes

After ionization the target is left in a highly excited state (positive charge). In particular, when inner shells are ionized, the electrons reorganize in order for the system to get back to its fundamental state. The excess energy associated with this phenomenon can be released through two possible processes: fluorescence (radiative process) or Auger de-excitation (non-radiative process). These two mechanisms are described below.

6.3.1 Fluorescence

When a vacancy is formed in the K-shell of the target atom, electronic de-excitation takes place and the excess energy is released through X-ray emission (radiative process). In this process, illustrated in **Figure I - 21**, the energy of the emitted X-ray photon is given by:

$$E = h\nu = E_K - E_{L2}$$

Equation I - 18

[143] Verkhovtsev A V *et al.* (2015) *J. Phys. Chem. C* **119** 11000–13

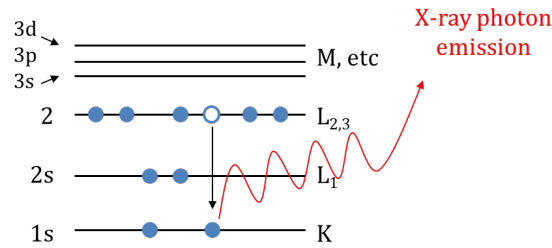


Figure I - 21. Electronic relaxation via fluorescence.

6.3.2 Auger electron emission

The Auger process was observed in 1922 by Lise Meitner and described in 1923 by Pierre Victor Auger [144]. Auger effects can take place when inner shells are ionized. The interactions of secondary electrons with the target may also ionize inner-shell electrons. The ionization of an inner shell is thus followed by Auger de-excitation and the emission of Auger electrons. This process is illustrated in Figure I - 22 in the case of a K L₁ L_{2,3} transition.

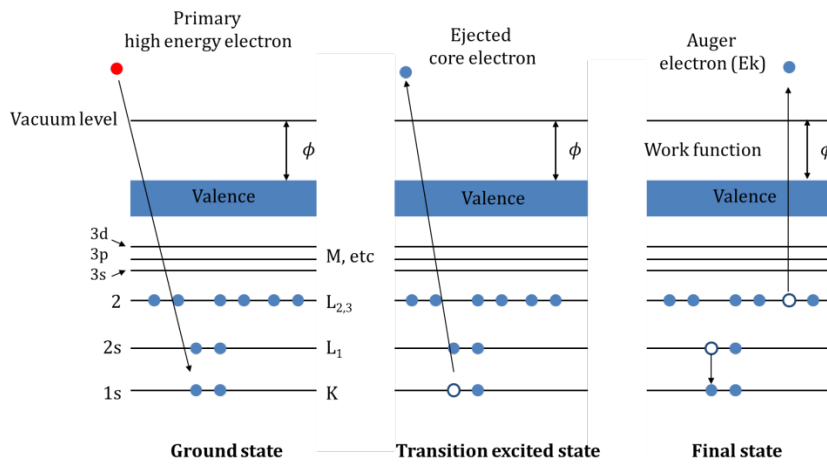


Figure I - 22. Scheme of left: ionization, middle: electron emission, right: Auger de-excitation.

The Auger electron is emitted with a kinetic energy (E_k):

$$E_k = E_1 - E_2 - E_3$$

Equation I - 19

[144] Hardouin Duparc O (2009) *Int. J. Mater. Res.* **100** 1162–6

with E_1 : energy of the incident photon (or secondary electron), E_2 : binding energy of the photoelectron (emitted from the K-shell orbital) and E_3 : binding energy of the Auger electron.

The Auger de-excitation process continues till the complete rearranging of the electron cloud is achieved (Auger cascade). This process leads to an amplified electron emission and to the production of a positively charged atom and thus positively charged NP.

6.3.3 Radiative versus non radiative de-exciation

The radiative and non-radiative de-excitation processes described above are in competition. The total transition rate is a sum of both processes. The Auger yield (ω_A) is related to the fluorescence (X-ray) yield (ω_X) by the following relation [145]:

$$\omega_A = 1 - \omega_X = 1 - \frac{W_X}{W_X + W_A} \quad \text{Equation I - 20}$$

where W_X is the X-ray transition probability and W_A is the Auger transition probability.

In the case of K-shell vacancies, the fluorescence yield increases with the atomic number of the target (**Figure I - 23**). The Auger effect is dominant for light elements such as C, N, O and P, the main constituents of biological systems.

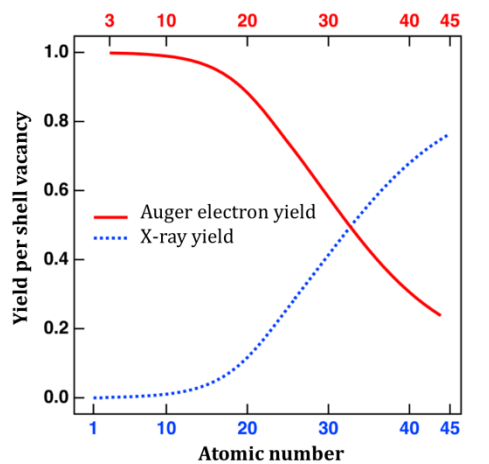


Figure I - 23. Fluorescence and Auger electron yields as a function of the atomic number for K shell vacancies. (https://en.wikipedia.org/wiki/Auger_electron_spectroscopy#/media/File:Auger_xray_wiki_in_png_format.png)

[145] Feldman L C and Mayer J W (1986) *Fundamentals of surface and thin film analysis*

For heavy elements, the Auger relaxation becomes dominant when L shell is ionized. For instance, in the case of Pt, following ionization of the K-shell, the atoms are relaxed in about only 4% by Auger emission. However, after ionization of the L-shell, platinum atoms relax in about 97% by the Auger de-excitation process [145].

6.4 Electron capture by positively charged sites

After relaxation processes by Auger cascades, atoms (or clustered atoms as nanoparticles) are left positively charged. For instance, when platinum is ionized in L-shell, the atoms de-excite with the emission of 10 Auger electrons. The platinum atom is thus left with ten positive charges. The atom neutralizes via capture of electrons from surrounding molecules (water), as shown in **Figure I - 24**.

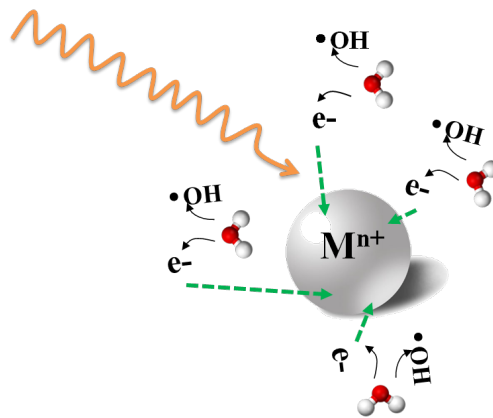
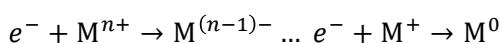


Figure I - 24. Positively charged atom neutralizes *via* capture of electrons from surrounding water molecules.



Equation I - 21

M= Pt, Au, Gd etc

This process was never mentioned before in the field of the radiobiology. In the present work, electron capture may take place between radiation induced activation of metallic nanoparticles and surrounding water molecules. This phenomenon has been recently described by Stumpf and co-workers in the case of semiconductors [146]

[146] Stumpf H (1971) *Phys. der Kondens. Mater.* **13** 101-17

7 Objectives of this work

The aim of my work is the development of small Pt based nanoparticles, stable, biocompatible and with properties of enhancing the effects of ionizing radiation (nano-radio-enhancement commonly called radiosensitization) by an optimized radiolytic route. This aims, as represented in **Figure I - 25**, as an end point at improving the performances of hadrontherapy.

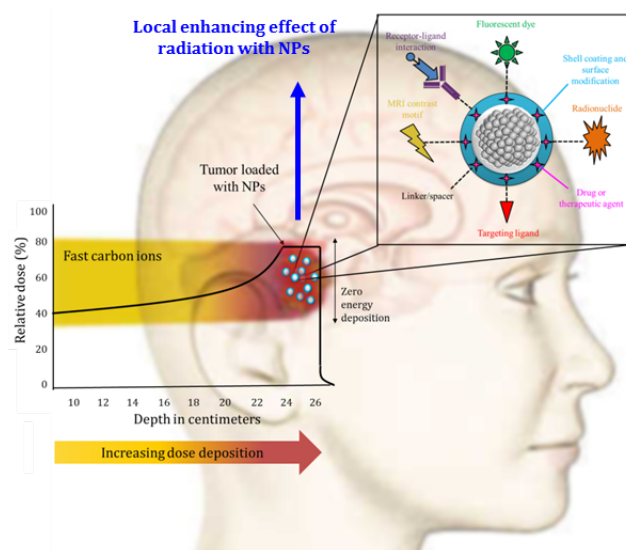


Figure I - 25. Platinum based nanoparticles for radio-enhancement: perspective of improving hadrontherapy.

The research objectives of this study are listed below:

- Improved synthesis of platinum based nanoparticles (small, stable and biocompatible).
- Physico-chemical characterization of Pt NPs (size, shape, composition and stability).
- Evaluation of Pt NPs biological impact (toxicity, uptake and localization).
- Characterization of the radio-enhancing properties of NPs under γ -rays and medical carbon ions.
- Understanding of molecular scale mechanisms.

8 References

- [1] Liu R, Wu D, Feng X and Müllen K 2011 Bottom-Up Fabrication of Photoluminescent Graphene Quantum Dots with Uniform Morphology *J. Am. Chem. Soc.* **133** 15221–3
- [2] Sau T K and Rogach A L 2012 *Complex-shaped metal nanoparticles: Bottom-up syntheses and applications* (WILEY-VCH Verlag GmbH & Co. KGaA)
- [3] Turkevich J, Stevenson P C and Hillier J 1951 A study of the nucleation and growth processes in the synthesis of colloidal gold *Discuss. Faraday Soc.* **11** 55–75
- [4] Frens G 1973 Controlled Nucleation for the Regulation of the Particle Size in Monodisperse Gold Suspensions *Nat. Phys. Sci.* **241** 20–2
- [5] Slot J W and Geuze H J 1981 Sizing of protein A-colloidal gold probes for immunoelectron microscopy. *J. Cell Biol.* **90** 533–6
- [6] Brust M, Walker M, Bethell D, Schiffrin D J and Whyman R 1994 Synthesis of Thiol-derivatised Gold Nanoparticles in *Chem. Commun.* 801–2
- [7] Woehrle G H, Brown L O and Hutchison J E 2005 Thiol-Functionalized, 1.5-nm Gold Nanoparticles through Ligand Exchange Reactions: Scope and Mechanism of Ligand Exchange *J. Am. Chem. Soc.* **127** 2172–83
- [8] Roux S, Tillement O, Billotey C, Coll J-L, Le Duc G and Marquette C Multifunctional nanoparticles : from the detection of biomolecules to the therapy Stéphane Roux *, Olivier Tillement * Claire Billotey Jean-Luc Coll Christophe Marquette Pascal Perriat *Int. J. Nanotechnology* 1–20
- [9] Eck W, Craig G, Sigdel A, Ritter G, Old L J, Tang L, Brennan M F, Allen P J and Mason M D 2008 PEGylated Gold Nanoparticles Conjugated to Monoclonal F19 Antibodies as Targeted Labeling Agents for Human Pancreatic Carcinoma Tissue *ACS Nano* **2** 2263–72
- [10] Wuelfing W P, Gross S M, Miles D T and Murray R W 1998 Nanometer gold clusters protected by surface-bound monolayers of thiolated poly(ethylene glycol) polymer electrolyte *J. Am. Chem. Soc.* **120** 12696–7
- [11] Alric C, Miladi I, Kryza D, Taleb J, Lux F, Bazzi R, Billotey C, Janier M, Perriat P, Roux S and Tillement O 2013 The biodistribution of gold nanoparticles designed for renal clearance. *Nanoscale* **5** 5930–9
- [12] Mironava T, Simon M, Rafailovich M H and Rigas B 2013 Platinum folate nanoparticles toxicity: Cancer vs. normal cells *Toxicol. Vitro.* **27** 882–9
- [13] Long N V, Chien N D, Hayakawa T, Hirata H, Lakshminarayana G and Nogami M 2010 The synthesis and characterization of platinum nanoparticles: a method of controlling the size and morphology *Nanotechnology* **21** 35605
- [14] Buxton G V. 1987 Radiation Chemistry of the liquid state: (1) Water and Homogeneous Aqueous Solutions *Radiation Chemistry: Principles and Applications* ed Farhataziz (Weinheim: VCH) pp 321–49
- [15] Rodgers M A J 1987 *Radiation Chemistry: Principles and Applications* ed Farhataziz (Weinheim: VCH)
- [16] Buxton G V 2008 An overview of the radiation chemistry of liquids *Radiation Chemistry* ed M Spothem-Maurizot, M Mostafavi, T Douki and J Belloni (Les Ulis Cedex: EDP Sciences)
- [17] Remita H and Remita S 2010 Metal Clusters and Nanomaterials: Contribution of Radiation Chemistry *Recent Trends in Radiation Chemistry* ed J F Wishart and B S Madhava Rao (World Scientific) p 607
- [18] Belloni J and Mostafavi M 2001 Radiation chemistry of nanocolloids and clusters *Stud. Phys. Theor. Chem.* **87** 411–52
- [19] Belloni J and Remita H 2008 Metal clusters and nanomaterials *Radiation chemistry: from basics to applications in material and life sciences* (Les Ulis Cedex: EDP Sciences) p 97

- [20] Belloni J, Mostafavi M, Remita H, Marignier J-L and Delcourt M-O 1998 Radiation-induced synthesis of mono- and multi-metallic clusters and nanocolloids *New J. Chem.* **22** 1239–55
- [21] Mirdamadi-Esfahani M, Mostafavi M, Keita B, Nadjó L, Kooyman P and Remita H 2010 Bimetallic Au-Pt nanoparticles synthesized by radiolysis: Application in electro-catalysis *Gold Bull.* **43** 49–56
- [22] Coqueret X 2008 Obtaining high performance polymeric materials by irradiation *Radiation chemistry: from basics to applications in material and life sciences* (Les Ulis Cedex: EDP Sciences) p 131
- [23] Kay A, Humphry-Baker R and Graetzel M 1994 Artificial Photosynthesis. 2. Investigations on the Mechanism of Photosensitization of Nanocrystalline TiO₂ Solar Cells by Chlorophyll Derivatives *J. Phys. Chem.* **98** 952–9
- [24] Ryu J, Lee S H, Nam D H and Park C B 2011 Rational Design and Engineering of Quantum-Dot-Sensitized TiO₂ Nanotube Arrays for Artificial Photosynthesis *Adv. Mater.* **23** 1883–8
- [25] Méndez-Medrano M G, Kowalska E, Lehoux A, Herissan A, Ohtani B, Bahena D, Briois V, Colbeau-Justin C, Rodríguez-López J L and Remita H 2016 Surface Modification of TiO₂ with Ag Nanoparticles and CuO Nanoclusters for Application in Photocatalysis *J. Phys. Chem. C* **120** 5143–54
- [26] Luna A L, Novoseltceva E, Louarn E, Beaunier P, Kowalska E, Ohtani B, Valenzuela M A, Remita H and Colbeau-Justin C 2016 Synergetic effect of Ni and Au nanoparticles synthesized on titania particles for efficient photocatalytic hydrogen production *Appl. Catal. B Environ.* **191** 18–28
- [27] Choi H S, Liu W, Misra P, Tanaka E, Zimmer J P, Itty Ipe B, Bawendi M G and Frangioni J V 2007 Renal clearance of nanoparticles *Nat. Biotechnol.* **25** 1165–70
- [28] Michelle Longmire, Peter L. Choyke, M.D., and Hisataka Kobayashi, M.D. P. 2008 Clearance Properties of Nano-sized Particles and Molecules as Imaging Agents: Consideration and Caveats *Nanomedicine (Lond)* **3** 703–17
- [29] Alexis F, Pridgen E, Molnar L K and Farokhzad O C 2008 Factors Affecting the Clearance and Biodistribution of Polymeric Nanoparticles *Mol. Pharm.* **5** 505–15
- [30] Albanese A, Tang P S and Chan W C W 2012 The effect of nanoparticle size, shape, and surface chemistry on biological systems. *Annu. Rev. Biomed. Eng.* **14** 1–16
- [31] Acharya S and Sahoo S K 2011 PLGA nanoparticles containing various anticancer agents and tumour delivery by EPR effect *Adv. Drug Deliv. Rev.* **63** 170–83
- [32] Wilczewska A Z, Niemirowicz K, Markiewicz K H and Car H 2012 Nanoparticles as drug delivery systems *Pharmacol. Reports* **64** 1020–37
- [33] Bangham A D and Horne R W 1964 Negative staining of phospholipids and their structural modification by surface-active agents as observed in the electron microscope. *J. Mol. Biol.* **8** 660–8
- [34] Saunders L and Thomas I L 1958 Diffusion studies with lysolecithin *J. Chem. Soc.* 483
- [35] dos Santos Giuberti C, de Oliveira Reis E C, Ribeiro Rocha T G, Leite E A, Lacerda R G, Ramaldes G A and de Oliveira M C 2011 Study of the pilot production process of long-circulating and pH-sensitive liposomes containing cisplatin. *J. Liposome Res.* **21** 60–9
- [36] You J, Li W, Yu C, Zhao C, Jin L, Zhou Y, Xu X, Dong S, Lu X and Wang O 2013 Amphiphilically modified chitosan cationic nanoparticles for drug delivery *J. Nanoparticle Res.* **15** 2123
- [37] Gref R, Domb A, Quéllec P, Blunk T, Müller R H, Verbavatz J M and Langer R 2012 The controlled intravenous delivery of drugs using PEG-coated sterically stabilized nanospheres *Adv. Drug Deliv. Rev.* **64** 316–26
- [38] Couvreur P, Kante B, Grislain L, Roland M and Speiser P 1982 Toxicity of Polyalkylcyanoacrylate Nanoparticles II: Doxorubicin-Loaded Nanoparticles *J. Pharm. Sci.* **71** 790–2

- [39] Gulyaev A E, Gelperina S E, Skidan I N, Antropov A S, Kivman G Y and Kreuter J 1999 Significant Transport of Doxorubicin into the Brain with Polysorbate 80-Coated Nanoparticles *Pharm. Res.* **16** 1564–9
- [40] Agostoni V, Horcajada P, Noiray M, Malanga M, Aykaç a., Jicsinszky L, Vargas-Berenguel a., Semiramoth N, Daoud-Mahammed S, Nicolas V, Martineau C, Taulelle F, Vigneron J, Etcheberry a., Serre C and Gref R 2015 A “green” strategy to construct non-covalent, stable and bioactive coatings on porous MOF nanoparticles *Sci. Rep.* **5** 7925
- [41] Baati T, Njim L, Neffati F, Kerkeni A, Bouttemi M, Gref R, Najjar M F, Zakhama A, Couvreur P, Serre C and Horcajada P 2013 In depth analysis of the in vivo toxicity of nanoparticles of porous iron(iii) metal-organic frameworks *Chem. Sci.* **4** 1597–607
- [42] López T, Álvarez M, Ramírez P, Jardón G, López M, Rodríguez G, Ortiz I and Novaro O 2016 Sol-Gel Silica Matrix as Reservoir for Controlled Release of Paracetamol: Characterization and Kinetic Analysis *J. Encapsulation Adsorpt. Sci.* **6** 47–55
- [43] López Goerne T M, López García M G, Rodríguez Grada G, Ortiz Pérez I, Gómez López E and Alvarez Lemus M A 2013 Obtaining of sol-gel ketorolac-silica nanoparticles: Characterization and drug release kinetics *J. Nanomater.*
- [44] López T, Esquivel D, Mendoza-Díaz G, Ortiz-Islas E, González R D and Novaro O 2015 L-DOPA stabilization on sol-gel silica to be used as neurological nanoreservoirs: Structural and spectroscopic studies *Mater. Lett.* **161** 160–3
- [45] López T and Rodríguez C E 2015 Uso de la nanopartícula de de úlceras en pie diabético : comunicación preliminar *Rev. la Fac. Med. la UNAM* **58** 5–12
- [46] He X, Wang K and Cheng Z 2010 In vivo near-infrared fluorescence imaging of cancer with nanoparticle-based probes *Wiley Interdiscip. Rev. Nanomedicine Nanobiotechnology* **2** 349–66
- [47] Sun C, Lee J S H and Zhang M 2008 Magnetic nanoparticles in MR imaging and drug delivery *Adv. Drug Deliv. Rev.* **60** 1252–65
- [48] Bridot J-L, Faure A-C, Laurent S, Rivière C, Billotey C, Hiba B, Janier M, Josserand V, Coll J-L, Elst L Vander, Muller R, Roux S, Perriat P and Tillement O 2007 Hybrid gadolinium oxide nanoparticles: multimodal contrast agents for in vivo imaging. *J. Am. Chem. Soc.* **129** 5076–84
- [49] Dobson J 2006 Magnetic nanoparticles for drug delivery *Drug Dev. Res.* **67** 55–60
- [50] Tietze R, Zaloga J, Unterweger H, Lyer S, Friedrich R P, Janko C, Pöttler M and Dürr S 2015 Magnetic nanoparticle-based drug delivery for cancer therapy *Biochem. Biophys. Res. Commun.* **468** 463–70
- [51] Stockhofe K, Postema J M, Schieferstein H and Ross T L 2014 Radiolabeling of Nanoparticles and Polymers for PET Imaging. *Pharmaceuticals (Basel).* **7** 392–418
- [52] Fernandez-Fernandez A, Manchanda R and McGoron A J 2011 Theranostic applications of nanomaterials in cancer: drug delivery, image-guided therapy, and multifunctional platforms. *Appl. Biochem. Biotechnol.* **165** 1628–51
- [53] Ramos-Cabrer P and Campos F 2013 Liposomes and nanotechnology in drug development: Focus on neurological targets *Int. J. Nanomedicine* **8** 951–60
- [54] Ho D, Sun X and Sun S 2011 Monodisperse Magnetic Nanoparticles for Theranostic Applications *Acc. Chem. Res.* **44** 875–82
- [55] Yu H, Chen M, Rice P M, Wang S X, White R L and Shouheng S 2005 Dumbbell-like Bifunctional Au–Fe₃O₄ Nanoparticles *Nano Lett.* **5** 379–82
- [56] Hong R, Fischer N O, Emrick T and Rotello V M 2005 Surface PEGylation and Ligand Exchange Chemistry of FePt Nanoparticles for Biological Applications *Chem. Mater.* **17** 4617–21
- [57] Hainfeld J F, Slatkin D N, Focella T M and Smilowitz H M 2006 Gold nanoparticles: a new X-ray contrast agent. *Br. J. Radiol.* **79** 248–53
- [58] Butterworth K T, Nicol J R, Ghita M, Rosa S, Chaudhary P, McGarry C K, McCarthy H O, Jimenez-Sanchez G, Bazzi R, Roux S, Tillement O, Coulter J A and Prise K M 2016

- Preclinical evaluation of gold-DTDTPA nanoparticles as theranostic agents in prostate cancer radiotherapy *Nanomedicine* **11** 2035–47
- [59] Bridot J-L, Dayde D, Rivière C, Mandon C, Billotey C, Lerondel S, Sabattier R, Cartron G, Le Pape A, Blondiaux G, Janier M, Perriat P, Roux S and Tillement O 2009 Hybrid gadolinium oxide nanoparticles combining imaging and therapy *J. Mater. Chem.* **19** 2328
- [60] Debouttière P-J, Roux S, Vocanson F, Billotey C, Beuf O, Favre-Réguillon a., Lin Y, Pellet-Rostaing S, Lamartine R, Perriat P and Tillement O 2006 Design of Gold Nanoparticles for Magnetic Resonance Imaging *Adv. Funct. Mater.* **16** 2330–9
- [61] Miladi I, Aloy M-T, Armandy E, Mowat P, Kryza D, Magné N, Tillement O, Lux F, Billotey C, Janier M and Rodriguez-Lafrasse C 2015 Combining ultrasmall gadolinium-based nanoparticles with photon irradiation overcomes radioresistance of head and neck squamous cell carcinoma *Nanomedicine Nanotechnology, Biol. Med.* **11** 247–57
- [62] Porcel E, Tillement O, Lux F, Mowat P, Usami N, Kobayashi K, Furusawa Y, Le Sech C, Li S and Lacombe S 2014 Gadolinium-based nanoparticles to improve the hadrontherapy performances. *Nanomedicine* **10** 1601–8
- [63] Eustis S and El-Sayed M A 2006 Why gold nanoparticles are more precious than pretty gold: Noble metal surface plasmon resonance and its enhancement of the radiative and nonradiative properties of nanocrystals of different shapes *Chem. Soc. Rev.* **35** 209–17
- [64] Link S and El-Sayed M A 2000 Shape and size dependence of radiative, non-radiative and photothermal properties of gold nanocrystals *Int. Rev. Phys. Chem.* **19** 409–53
- [65] Huang X, El-Sayed I H, Qian W and El-Sayed M A 2006 Cancer cell imaging and photothermal therapy in the near-infrared region by using gold nanorods *J. Am. Chem. Soc.* **128** 2115–20
- [66] Pattani V P and Tunnell J W 2012 Nanoparticle-mediated photothermal therapy: a comparative study of heating for different particle types. *Lasers Surg. Med.* **44** 675–84
- [67] Yang P, Xu Q-Z, Jin S-Y, Lu Y, Zhao Y and Yu S-H 2012 Synthesis of multifunctional Ag@Au@phenol formaldehyde resin particles loaded with folic acids for photothermal therapy. *Chemistry* **18** 9294–9
- [68] Manikandan M, Hasan N and Wu H-F 2013 Platinum nanoparticles for the photothermal treatment of Neuro 2A cancer cells *Biomaterials* **34** 5833–42
- [69] Dutreix M, Cosset J M and Sun J-S 2010 Molecular therapy in support to radiotherapy. *Mutat. Res.* **704** 182–9
- [70] Berthault N, Maury B, Agrario C, Herbette A, Sun J-S, Peyrieras N and Dutreix M 2011 Comparison of distribution and activity of nanoparticles with short interfering DNA (Dbait) in various living systems. *Cancer Gene Ther.* **18** 695–706
- [71] Schlegel A, Buhler C, Devun F, Agrario C, Urien S, Lokiec F, Sun J-S and Dutreix M 2012 Pharmacokinetics and Toxicity in Rats and Monkeys of coDbait: A Therapeutic Double-stranded DNA Oligonucleotide Conjugated to Cholesterol *Mol. Ther. — Nucleic Acids* **1** e33
- [72] Wilson R R 1946 Radiological use of fast protons. *Radiology* **47** 487–91
- [73] Anon The Promise of Ion Beam Cancer Therapy « Berkeley Lab News Center
- [74] Hirao Y, Ogawa H, Yamada S, Sato Y, Yamada T, Sato K, Itano A, Kanazawa M, Noda K, Kawachi K, Endo M, Kanai T, Kohno T, Sudou M, Minohara S, Kitagawa A, Soga F, Takada E, Watanabe S, Endo K, Kumada M and Matsumoto S 1992 Heavy ion synchrotron for medical use —HIMAC project at NIRS-Japan— *Nucl. Phys. A* **538** 541–50
- [75] Laramore G E 2009 Role of particle radiotherapy in the management of head and neck cancer. *Curr. Opin. Oncol.* **21** 224–31
- [76] McDonald M W and Fitzek M M 2010 Proton therapy. *Curr. Probl. Cancer* **34** 257–96

- [77] Proton therapy: The new weapon of choice against cancer is coming to Australia | Daily Telegraph
- [78] Schardt D 2016 Hadrontherapy *Basic Concepts in Nuclear Physics: Theory, Experiments and Applications* vol 182, ed J E García-Ramos, C. Alonso, M V Andrés and F Pérez-Bernal (Switzerland: Springer International Publishing) pp 55–86
- [79] Universitäts Klinikum Heidelberg: Therapy centers in the world
- [80] France Hadron - Home
- [81] Lomax A 2007 TU-C-BRA-01: An Overview of Proton Therapy *Med. Phys.* **34** 2552
- [82] Iston M-C, Joubert A, Adam J-F, Elleaume H, Bohic S, Charvet A, Estève F, Foray N and Balosso J 2004 Cure of Fisher Rats Bearing Radioresistant F98 Glioma Treated with cis-Platinum and Irradiated with Monochromatic Synchrotron X-Rays *Cancer Res.* **64** 2317–23
- [83] Usami N, Furusawa Y, Kobayashi K, Lacombe S, Reynaud-Angelin a, Sage E, Wu T-D, Croisy a, Guerquin-Kern J-L and Le Sech C 2008 Mammalian cells loaded with platinum-containing molecules are sensitized to fast atomic ions. *Int. J. Radiat. Biol.* **84** 603–11
- [84] Kobayashi K, Usami N, Porcel E, Lacombe S and Le Sech C 2010 Enhancement of radiation effect by heavy elements. *Mutat. Res.* **704** 123–31
- [85] Kong T, Zeng J, Wang X, Yang X, Yang J, Mcquarrie S, Mcewan A, Roa W, Chen J and Xing J Z 2008 Enhancement of Radiation Cytotoxicity in Breast-Cancer Cells by Localized Attachment of Gold Nanoparticles 1537–43
- [86] Retif P, Pinel S, Toussaint M, Frochet C, Chouikrat R, Bastogne T and Barberi-Heyob M 2015 Nanoparticles for Radiation Therapy Enhancement: the Key Parameters *Theranostics* **5** 1030–44
- [87] McMahon S J, Hyland W B, Muir M F, Coulter J A, Jain S, Butterworth K T, Schettino G, Dickson G R, Hounsell A R, O’Sullivan J M, Prise K M, Hirst D G and Currell F J 2011 Nanodosimetric effects of gold nanoparticles in megavoltage radiation therapy *Radiother. Oncol.* **100** 412–6
- [88] Wang X and Guo Z 2013 Targeting and delivery of platinum-based anticancer drugs *Chem. Soc. Rev.* **42** 202–24
- [89] Porcel E, Kobayashi K, Usami N, Remita H, Le Sech C and Lacombe S 2011 Photosensitization of plasmid-DNA loaded with platinum nano-particles and irradiated by low energy X-rays *J. Phys. Conf. Ser.* **261** 12004
- [90] McMahon S J, Hyland W B, Brun E, Butterworth K T, Coulter J a., Douki T, Hirst D G, Jain S, Kavanagh A P, Krpetic Z, Mendenhall M H, Muir M F, Prise K M, Requardt H, Sanche L, Schettino G, Currell F J and Sicard-Roselli C 2011 Energy Dependence of Gold Nanoparticle Radiosensitization in Plasmid DNA *J. Phys. Chem. C* **115** 20160–7
- [91] Porcel E, Liehn S, Remita H, Usami N, Kobayashi K, Furusawa Y, Le Sech C and Lacombe S 2010 Platinum nanoparticles: a promising material for future cancer therapy? *Nanotechnology* **21** 85103
- [92] Wyer J a, Butterworth K T, Hirst D G, Latimer C J, Montenegro E C, Shah M B and Currell F J 2009 Fragmentation and plasmid strand breaks in pure and gold-doped DNA irradiated by beams of fast hydrogen atoms. *Phys. Med. Biol.* **54** 4705–21
- [93] Schlatholter, Lacombe S, Eustache P, Porcel E, Salado D, Stefancikova L, Tillement O, Lux F, Mowat P, van Goethem M-J, Remita H and Biegun A 2016 Improving proton therapy by metal-containing nanoparticles: nanoscale insights *Int. J. Nanomedicine* **Volume 11** 1549
- [94] Sicard-Roselli C, Brun E, Gilles M, Baldacchino G, Kelsey C, McQuaid H, Polin C, Wardlow N and Currell F 2014 A New Mechanism for Hydroxyl Radical Production in Irradiated Nanoparticle Solutions *Small* **10** 3338–46
- [95] Jain S, Coulter J A, Hounsell A R, Butterworth K T, McMahon S J, Hyland W B, Muir M F, Dickson G R, Prise K M, Currell F J, O’Sullivan J M and Hirst D G 2011 Cell-specific radiosensitization by gold nanoparticles at megavoltage radiation energies. *Int. J.*

- Radiat. Oncol. Biol. Phys.* **79** 531–9
- [96] Hainfeld J F, Slatkin D N and Smilowitz H M 2004 The use of gold nanoparticles to enhance radiotherapy in mice *Phys. Med. Biol.* **49** N309–15
- [97] Hainfeld J F, Dilmanian F A, Slatkin D N and Smilowitz H M 2008 Radiotherapy enhancement with gold nanoparticles **4** 977–85
- [98] Her S, Jaffray D A and Allen C 2015 Gold nanoparticles for applications in cancer radiotherapy: Mechanisms and recent advancements *Adv. Drug Deliv. Rev.*
- [99] Verry C, Dufort S, Barbier E L, Montigon O, Peoc'h M, Chartier P, Lux F, Balosso J, Tillement O, Sancey L and Le Duc G 2016 MRI-guided clinical 6-MV radiosensitization of glioma using a unique gadolinium-based nanoparticles injection *Nanomedicine* **11** 2405–17
- [100] Zhang X-D, Wu D, Shen X, Chen J, Sun Y-M, Liu P-X and Liang X-J 2012 Size-dependent radiosensitization of PEG-coated gold nanoparticles for cancer radiation therapy. *Biomaterials* **33** 6408–19
- [101] Joh D Y, Sun L, Stangl M, Al Zaki A, Murty S, Santoiemma P P, Davis J J, Baumann B C, Alonso-Basanta M, Bhang D, Kao G D, Tsourkas A and Dorsey J F 2013 Selective Targeting of Brain Tumors with Gold Nanoparticle-Induced Radiosensitization ed M G Castro *PLoS One* **8** e62425
- [102] Kim J-K, Seo S-J, Kim K-H, Kim T-J, Chung M-H, Kim K-R and Yang T-K 2010 Therapeutic application of metallic nanoparticles combined with particle-induced x-ray emission effect. *Nanotechnology* **21** 425102
- [103] Le Sech C, Kobayashi K, Usami N, Furusawa Y, Porcel E and Lacombe S 2012 Comment on “Therapeutic application of metallic nanoparticles combined with particle-induced x-ray emission effect”. *Nanotechnology* **23**078001; author reply 078002
- [104] Dollinger G 2011 Comment on “Therapeutic application of metallic nanoparticles combined with particle-induced x-ray emission effect”. *Nanotechnology* **22**248001; discussion 248002
- [105] Terakawa A, Ishii K, Yamazaki H, Matsuyama S, Kikuchi Y, Ito Y, Tagawa A, Yasunaga S, Kawamura T, Takahashi Y, Hatori Y, Hamada N, Fujiki K, Ito N, Wada S, Funaki Y and Sera K 2011 PIXE analysis of a murine solid tumor treated with proton therapy combined with cisplatin *X-Ray Spectrom.* **40** 198–201
- [106] Kaur H, Pujari G, Semwal M K, Sarma A and Avasthi D K 2013 In vitro studies on radiosensitization effect of glucose capped gold nanoparticles in photon and ion irradiation of HeLa cells *Nucl. Instruments Methods Phys. Res. Sect. B Beam Interact. with Mater. Atoms* **301** 7–11
- [107] Liu Y, Liu X, Jin X, He P, Zheng X, Dai Z, Ye F, Zhao T, Chen W and Li Q 2015 The dependence of radiation enhancement effect on the concentration of gold nanoparticles exposed to low- and high-LET radiations *Phys. Medica* **31** 210–8
- [108] Anon It's Elemental - The Periodic Table of Elements
- [109] Joost M 2015 *Synthesis and Original Reactivity of Copper and Gold Complexes: σ -Bond coordination, oxidative addition, migratory insertion* (Springer)
- [110] Frank Shaw III C 1999 Gold-Based Therapeutic Agents *Chem. Rev.* **99** 2589–600
- [111] Haruta M, Kobayashi T, Sano H and Yamada N 1987 Novel Gold Catalysts for the Oxidation of Carbon Monoxide at a Temperature far Below 0 °C *Chem. Lett.* **16** 405–8
- [112] Louis C and Pluchery O 2012 *Gold Nanoparticles for Physics, Chemistry and Biology* (Imperial College Press)
- [113] Granmayeh Rad A, Abbasi H and Afzali M H 2011 Gold Nanoparticles: Synthesising, Characterizing and Reviewing Novel Application in Recent Years *Phys. Procedia* **22** 203–8
- [114] Bozich J S, Lohse S E, Torelli M D, Murphy C J, Hamers R J and Klaper R D 2014 Surface chemistry, charge and ligand type impact the toxicity of gold nanoparticles to *Daphnia magna* *Environ. Sci. Nano* **1** 260–70

- [115] Oh N and Park J-H 2014 Surface chemistry of gold nanoparticles mediates their exocytosis in macrophages. *ACS Nano* **8** 6232–41
- [116] McDonald D 1960 *A History of Platinum* (UK: Johnson Matthey)
- [117] Robson G G 1985 *Platinum 1985* (Johnson Matthey)
- [118] Hartley F R 1991 *Chemistry of the platinum group metals: recent developments* (Elsevier)
- [119] McAuliffe C A, Sharma H I and Tinker N D 1991 Cancer chemotherapy involving platinum and other platinum group complexes *Chemistry of the platinum group metals: recent developments* ed F R Hartley (Elsevier) p 642
- [120] Searles R A 1988 Car exhaust pollution control *Platin. Met. Rev.* **32** 123–9
- [121] Schrader I, Warneke J, Neumann S, Grotheer S, Swane A A, Kirkensgaard J J K, Arenz M and Kunz S 2015 Surface Chemistry of “Unprotected” Nanoparticles: A Spectroscopic Investigation on Colloidal Particles *J. Phys. Chem. C* **119** 17655–61
- [122] Ono L K, Croy J R, Heinrich H and Roldan Cuenya B 2011 Oxygen Chemisorption, Formation, and Thermal Stability of Pt Oxides on Pt Nanoparticles Supported on SiO₂/Si(001): Size Effects *J. Phys. Chem. C* **115** 16856–66
- [123] The Photographic Periodic Table of the Elements
- [124] Louis C and Pluchery O 2012 *Gold nanoparticles for physics, chemistry and biology* (London: Imperial College Press)
- [125] Juan M L, Righini M and Quidant R 2011 Plasmon nano-optical tweezers *Nat. Photonics* **5** 349–56
- [126] Felson D T, Anderson J J and Meenan R F 1990 The comparative efficacy and toxicity of second-line drugs in rheumatoid arthritis. Results of two metaanalyses. *Arthritis Rheum.* **33** 1449–61
- [127] (Centre for Drug Evaluation and Research) 1978 Approval summary for cisplatin for metastatic ovarian tumors *FDA Oncol. Tools*
- [128] Apps M G, Choi E H Y and Wheate N J 2015 The state-of-play and future of platinum drugs. *Endocr. Relat. Cancer* **22** R219–33
- [129] Bhattacharyya S, Kudgus R A, Bhattacharya R and Mukherjee P 2011 Inorganic nanoparticles in cancer therapy. *Pharm. Res.* **28** 237–59
- [130] Kwatra D, Venugopal A and Anant S 2013 Nanoparticles in radiation therapy: a summary of various approaches to enhance radiosensitization in cancer *Transl. Cancer Res.* **2** 330–42
- [131] Alkilany A M and Murphy C J 2010 Toxicity and cellular uptake of gold nanoparticles: what we have learned so far? *J. Nanopart. Res.* **12** 2313–33
- [132] Książyk M, Asztemborska M, Stęborowski R and Bystrzejewska-Piotrowska G 2015 Toxic effect of silver and platinum nanoparticles toward the freshwater microalga *Pseudokirchneriella subcapitata*. *Bull. Environ. Contam. Toxicol.* **94** 554–8
- [133] Asharani P V, Lianwu Y, Gong Z and Valiyaveetil S 2011 Comparison of the toxicity of silver, gold and platinum nanoparticles in developing zebrafish embryos. *Nanotoxicology* **5** 43–54
- [134] Asharani P V, Xinyi N, Hande M and Valiyaveetil S 2010 DNA damage and p53-mediated growth arrest in human cells treated with platinum nanoparticles *Nanomedicine (Lond)* **5** 51–64
- [135] Pelka J, Gehrke H, Esselen M, Tu M, Crone M, Muller T, Blank H, Send W, Zibat V, Brenner P, Schneider R, Gerthsen D and Marko D 2009 Cellular Uptake of Platinum Nanoparticles in Human Colon Carcinoma Cells and Their Impact on Cellular Redox Systems and DNA Integrity *Chem Res Toxicol* **22** 649–59
- [136] Elder A, Yang H, Gwiazda R, Teng X, Thurston S, He H and Oberdörster G 2007 Testing Nanomaterials of Unknown Toxicity: An Example Based on Platinum Nanoparticles of Different Shapes *Adv. Mater.* **19** 3124–9
- [137] Mironava T, Simon M, Rafailovich M H and Rigas B 2013 Platinum folate nanoparticles toxicity: cancer vs. normal cells. *Toxicol. In Vitro* **27** 882–9

- [138] Blanc D and Portal G 1999 *Précis de physique nucléaire* (Dunod)
- [139] Mayles, P.; Nahum, A. and Rosenwald J 2007 *Handbook of radiotherapy physics. Theory and practice* (Taylor & Francis Group)
- [140] Klein O and Nishina Y 1929 Scattering of radiation by free electrons on the new relativistic quantum dynamics of Dirac *Z. Phys.* **52** 853–68
- [141] Gazda M J and Coia L R 2005 Principles of radiation therapy *Cancer Management: a multidisciplinary approach* (SCP Oncology Group)
- [142] Porcel E 2011 Utilisation des nanoparticules pour améliorer les performances de la hadronthérapie
- [143] Verkhovtsev A V., Korol A V. and Solov'yov A V. 2015 Electron Production by Sensitizing Gold Nanoparticles Irradiated by Fast Ions *J. Phys. Chem. C* **119** 11000–13
- [144] Hardouin Duparc O 2009 Pierre Auger – Lise Meitner: Comparative contributions to the Auger effect *Int. J. Mater. Res.* **100** 1162–6
- [145] Feldman L C and Mayer J W 1986 *Fundamentals of surface and thin film analysis* (P T R Prentice Hall)
- [146] Stumpf H 1971 On the theory of electronic processes in ionic crystal semiconductors *Phys. der Kondens. Mater.* **13** 101–17

CHAPTER II: MATERIALS AND METHODS

1. Synthesis of platinum based nanoparticles	61
1.1 Monometallic PEGylated platinum nanoparticles	61
1.1.1 Description of the synthesis	62
1.1.1.1 Radiolysis	63
1.1.1.2 In situ PEGylation.....	63
1.1.2 Experimental protocol.....	64
1.2 Mono- and bimetallic PEGylated gold-platinum nanoparticles.....	65
2. Methods for nanoparticles characterization	67
2.1 UV-Visible spectroscopy	68
2.1.1 Instrumentation	68
2.1.2 Samples preparation	68
2.2 Transmission Electron Microscopy (TEM).....	68
2.2.1 Instrumentation	68
2.2.2 Samples preparation	68
2.3 Dynamic Light Scattering (DLS)	69
2.3.1 Instrumentation	69
2.3.2 Samples preparation	69
2.4 Zeta potential (ζ -potential).....	70
2.4.1 Instrumentation	70
2.4.2 Samples preparation	70

2.5	X-ray Photoelectron Spectroscopy (XPS).....	71
2.5.1	Instrumentation.....	71
2.5.2	Samples preparation.....	72
2.6	Fourier Transform Infrared (FTIR) spectroscopy.....	72
2.6.1	Instrumentation.....	73
2.6.2	Samples preparation.....	73
3.	Radiation sources.....	74
3.1	Cobalt-60 gamma source.....	74
3.1.1	Description.....	74
3.1.2	The source and its dosimetry.....	74
3.2	Caesium-137 gamma source.....	77
3.2.1	Description.....	77
3.2.2	The source and its dosimetry.....	77
3.3	Medical carbon ions.....	78
3.3.1	Description: the irradiation facility.....	78
3.3.2	Irradiation conditions.....	79
4.	Biological models: description and methods.....	81
4.1	Cellular models.....	81
4.1.1	Cell lines description.....	81
4.1.2	Cell culture conditions.....	82
4.1.3	Cytotoxicity evaluation of PtPEG-OH NPs by clonogenic assay.....	83

4.1.3.1	Principle of the method.....	83
4.1.3.2	Experimental protocol: samples preparation.....	83
4.1.3.3	Statistical evaluation: ANOVA.....	84
4.1.4	Cell survival experiments with irradiation.....	85
4.1.5	Intracellular nanoparticles characterization: methods and protocols.....	85
4.1.5.1	Inductively Coupled Plasma (ICP) spectroscopy.....	86
4.1.5.2	Ion Microscopy: NanoSIMS Imaging.....	87
4.1.5.3	Transmission Electron Microscopy.....	90
4.2	Bio-nanoprobe: pBR322 plasmid DNA.....	92
4.2.1	Samples preparation and irradiation.....	92
4.2.2	Radio-induced nanosize damage: analysis and quantification.....	94
5.	References.....	96

CHAPTER II: MATERIALS AND METHODS

All the experimental protocols and analytical methods used in this work are described in this chapter.

In **Section 1**, the method and experimental conditions used to synthesize PEGylated metallic nanoparticles are presented.

In **Section 2**, the characterization techniques and samples preparation protocols used to determine the physico-chemical features of nanoparticles are described.

In **Section 3** we present and describe the radiation sources used in this work for the synthesis of nanoparticles and to irradiate biological samples.

Finally, in **Section 4** we show the biological models, from cells to biomolecules, used to evaluate the *in vitro* impact of nanoparticles.

1. Synthesis of platinum based nanoparticles

In this section, the experimental conditions used to prepare mono- and bimetallic platinum based nanoparticles are presented. I optimized a radiolytic method to obtain soluble, biocompatible and non-toxic Pt NPs using only US Food and Drug Administration (FDA) approved polymers. Radiolysis is a well-known reproducible and clean method to obtain dispersed and homogenous metallic NPs [1] [2] [3]. The optimization of the method was carried out in collaboration with Dr. Hynd Remita at the Laboratoire de Chimie Physique (Université Paris-Saclay, UMR8000 CNRS).

1.1 Monometallic PEGylated platinum nanoparticles

The first platinum nanoparticles produced by radiolysis with biomedical purposes were developed in the thesis of Dr. Erika Porcel under the direction of Prof. Sandrine Lacombe and in collaboration with Dr. Hynd Remita [4]. These nanoparticles consisted on 3 nm platinum core particles stabilized with poly (acrylic acid) (Pt-PAA NPs) [5]. They were toxic for cells at low concentrations ($<1.2 \times 10^9$ Pt-PAA NPs for CHO cells), which limited their use for radiotherapy concerns. Hence, the aim of my work was to improve the Pt NPs formulation to decrease their cytotoxicity and to open perspectives of tumor targeting.

In order to decrease the cytotoxicity of Pt-core NPs several biocompatible, biodegradable and water-soluble polymers were proposed [6] and tested. **Table II - 1** summarizes the polymers used in this work.

[1] Belloni J *et al.* (1998) *New J. Chem.* **22** 1239–55

[2] Henglein A (1989) *Chem. Rev.* **89** 1861–73

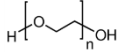
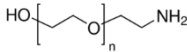
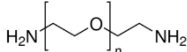
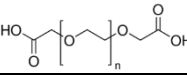
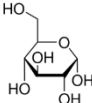
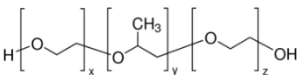
[3] Remita H and Remita S (2010) *Recent Trends in Radiation Chemistry* (World Scientific)

[4] Porcel E (2011) *Thèse de Doctorat* (Université Paris-Sud 11)

[5] Porcel E *et al.* (2010) *Nanotechnology* **21** 85103

[6] Marin E *et al.* (2013) *Int. J. Nanomedicine* **8** 3071–91

Table II - 1. Bio-compatible and water soluble polymers used for *in situ* metal nanoparticles surface coating.

Name and structural chemical formula		Molecular Weight (g.mol ⁻¹)
Poly (ethylene glycol) PEG-OH		600
		1000
		3000
O-(2-aminoethyl) poly(ethylene glycol)		3000
Poly(ethylene glycol) diamine PEG-2NH₂		2000
		3000
Poly(ethylene glycol) bis(carboxymethyl) ether		600
D-(+)-Glucose		180.16
Poly(vinyl alcohol) Mowiol® 8-88		~67 000
Poly (ethylene glycol)- <i>block</i> -poly (propylene glycol)- <i>block</i> -poly (ethylene glycol) Pluronic F-68		8350

In particular, poly (ethylene glycol) (PEG) is widely used in the field of polymer-based drug delivery and nanomedicine. It is nontoxic and has been approved by the FDA and the EU for internal consumption [7].

In a very early stage of this work, two main PEG derivatives, PEG-OH and PEG-2NH₂, were found to be the most promising biocompatible polymers for nanoparticles developments by radiolysis in water. I developed two types of monometallic platinum nanoparticles using PEG coatings; the PEGylated platinum nanoparticles, named as PtPEG-OH NPs, using the standard PEG-OH (Mw= 1000 g.mol⁻¹, n ~ 22.3 repeating units) and PtPEG-2NH₂ NPs using the homobifunctional PEG-2NH₂ (Mw= 2000 g.mol⁻¹, n ~ 44.6 repeating units). In the next sections, the experimental method and protocols used to synthesize PEGylated platinum nanoparticles are described.

1.1.1 Description of the synthesis

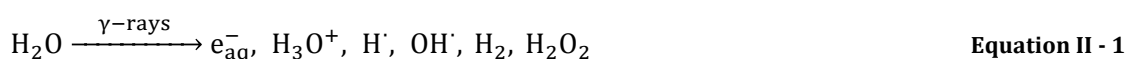
In this work, the synthesis of biocompatible metallic nanoparticles was optimized by combining radiolysis with *in situ* PEGylation. The principles of this method are described in this section.

[7] Knop K *et al.* (2010) *Angew. Chemie - Int. Ed.* **49** 6288–308

1.1.1.1 Radiolysis

Radiolysis is a well-known method to prepare colloidal metallic nanoparticles (see the theoretical framework in **Chapter I – Section 1.1.2**). The radiolytic synthesis of nanoparticles is performed at room temperature and atmospheric pressure. It leads to homogeneous reduction and nucleation in the bulk.

The physico-chemical processes taking place during the radiolytic reduction of metal ions in aqueous solution have been already described [8] [9] [3] (see detailed description in **Chapter I – Section 1.1.2.1**). Briefly, the irradiation of deoxygenated water with high-energy radiation (X-rays, γ -rays, electrons or ions) induces the excitation and ionization of water molecules, which leads to the production of radiolytic molecular and radical species (**Equation II - 1**). Those species that are homogeneously distributed in the bulk act as strong reducing or oxidizing agents.



Solvated electrons e_{aq}^- and hydrogen atoms $\text{H}\cdot$ are strong reducing agents with the respective redox potentials: $E^\circ(\text{H}_2\text{O} / \text{e}_{\text{aq}}^-) = -2.87 \text{ V}$ and $E^\circ(\text{H}^+ / \text{H}\cdot) = -2.31 \text{ V}$, that efficiently reduce dissolved metal ions down to the zero-valent state. In the case of a free or complexed monovalent metal ion M^{n+} , the reduction proceeds through **Equation I - 5** and **Equation I - 6** (see **Chapter I – Section 1.1.2.2**):

Multivalent ions, as Pt^{II} , are reduced down to the zero-valent state according to a multi-step reaction mechanism which involves intermediate valences, $\text{Pt}^{\text{II}} \rightarrow \text{Pt}^{\text{I}}$ and $\text{Pt}^{\text{I}} \rightarrow \text{Pt}^0$ (see **Chapter I – Section 1.1.2.3**).

The uniform energy deposition into the irradiated total medium leads to homogeneous distribution of metal atoms and nucleation sites in the solution and thus the formation of metal clusters with remarkable monodispersity.

1.1.1.2 In situ PEGylation

The PEGylation term refers to the decoration and stabilization of a particle surface by covalently grafting or entrapping and adsorption of PEG chains. The *in situ* term indicates

[8] Treguer M *et al.* (1998) *J. Phys. Chem. B* **102** 4310–21

[9] Remita H *et al.* (2005) *Radiat. Phys. Chem.* **72** 575–86

that the surface coating takes place at the time the nanoparticle is synthesized, in a one-step synthetic route.

The *in situ* surface coating of platinum nanoparticles was accomplished by performing the radiolytic reaction in the presence of PEG. PEG limits the nucleation and growth steps in order to obtain homogenous colloidal nanoparticles. The main advantages of using radiolysis are that: i) no reducing chemical agent is added, as the reducing species are induced by water radiolysis and ii) the nanoparticles can be synthesized in water. PEGylation takes place during the radiolytic synthesis, thus metallic nanoparticles stabilized by PEG are obtained in a bio-compatible solvent. Moreover, the colloidal solutions sterilized by the irradiation can be directly used in biological samples.

1.1.2 Experimental protocol

In the synthesis of PEGylated platinum nanoparticles, tetraammine platinum (II) chloride ($\text{Pt}(\text{NH}_3)_4\text{Cl}_2$) was used as precursor. This compound is non-toxic and can be safely handled. Moreover, it contains less chloride than other potential precursors. Chloride ions (Cl^-) are radical scavenger, which may reduce the yield of the synthesis.

Briefly, aqueous solutions containing $\text{Pt}(\text{NH}_3)_4\text{Cl}_2$ and PEG (PEG-OH or PEG-2NH₂) were deaerated by nitrogen bubbling (*ca.* 15 min) and then irradiated by γ -rays ($E = 1.33$ MeV, $\text{LET} = 0.2$ keV. μm^{-1}) with a dose rate of *ca.* 95.5 Gy. min^{-1} (see dose rate determination in **Section 3.1**). Inert atmospheric conditions (N_2) were used to avoid recombination of solvated electrons with solvated oxygen and back oxidations of very small metal clusters. Approximately 10 kGy at 95.5 Gy. min^{-1} were used to completely reduce 10^{-3} mol.L⁻¹ of Pt^{II} (see XPS results in **Chapter III - Section 1.3**).

Figure II - 1 shows the synthesis of PEGylated platinum nanoparticles by radiolysis and *in situ* PEGylation. It illustrates a colloidal aqueous solution containing a) 10^{-3} mol.L⁻¹ of the Pt^{II} complex prior irradiation and b) 10^{-3} mol.L⁻¹ PtPEG-OH NPs obtained after irradiation. Thus, the concentration of PtPEG-OH NPs is always expressed in moles of Pt per liters of solvent (water, typically $V_{\text{water}} = 10$ ml).

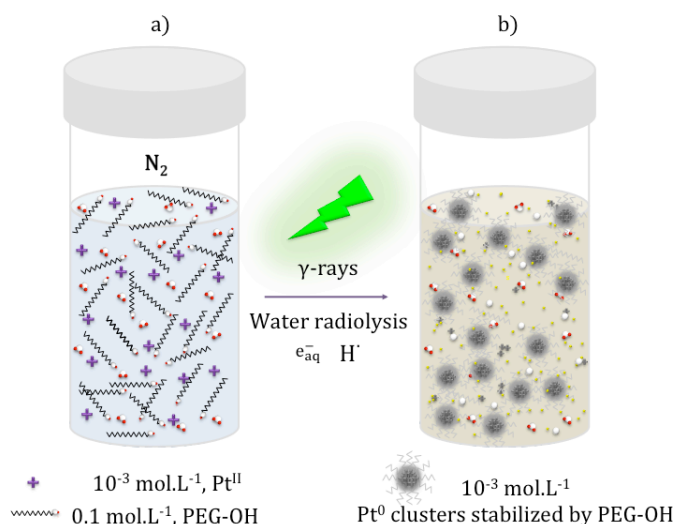


Figure II - 1. Principle of the synthesis of PEGylated platinum nanoparticles by gamma rays water radiolysis and *in situ* PEGylation.

The synthesis was optimized by varying the PEG-OH:Pt molar ratio from *ca.* 1 up to 100. The PEG-OH molar concentration was estimated from H (OCH₂CH₂)_nOH with n= 1 and thus Mw= 62 g.mol⁻¹ (monomeric unit).

The NPs prepared using PEG-OH with a PEG-OH:Pt molar ratio of *ca.* 100 were the most stable (see results in **Chapter III – Section 1.2.1**). They were particularly characterized as radio-enhancers in living cells and at molecular level (bio-nanoprobe) (see results in **Chapter III – Section 2.3**).

1.2 Mono- and bimetallic PEGylated gold-platinum nanoparticles

The new radiolytic-PEGylation method was applied to the synthesis of bimetallic nanoparticles. The *in situ* PEGylation was performed in the presence of the homobifunctional PEG-2NH₂ (Mw= 2000 g.mol⁻¹). In particular, for monometallic gold nanoparticles, we evaluated the effect of the PEG chain length using PEG-2NH₂ of different molecular weight (2000 and 3000 g.mol⁻¹).

Briefly, mono and bimetallic nanoparticles were synthesized at 10⁻³ mol.L⁻¹ using the Pt(NH₃)₄Cl₂ and HAuCl₄ precursors. Bimetallic nanoparticles were prepared using a Pt:Au molar ratio of 1. The PEG-2NH₂ was used with a molar ratio PEG:M_T (M_T= total metal content) of *ca.* 50. The PEG-2NH₂ molar concentration was estimated from H₂N (OCH₂CH₂)_nCH₂CH₂NH₂ with n= 1 and thus Mw= 104 g.mol⁻¹.

The solutions containing the precursor(s) and PEG-2NH₂ were deaerated by nitrogen bubbling and irradiated with increasing doses, from 0.5 kGy up to 10 kGy, to follow the reduction of the metal ions (Au^{III} and Pt^{II}) and nanoparticles formation by UV-visible spectroscopy. These solutions were irradiated at the maximum of dose rate (*ca.* 95.5 Gy.min⁻¹).

The radiation enhancing effect of mono- and bimetallic nanoparticles on the induction of nanosize damage was evaluated at molecular level using the bio-nanoprobe (see results **Chapter IV - Section 2**).

2. Methods for nanoparticles characterization

The physico-chemical characterization of the as-synthesized nanoparticles, term used to refer to fresh nanoparticles after synthesis, includes:

- **Structure:** crystallinity, size and shape
- **Composition:** purity, elemental analysis, surface chemistry and coating density
- **Stability:** agglomeration-sedimentation effects in relevant physiological media

Table II - 2 enlists the different techniques used in this work to characterize the nanoparticles. We also enlisted the methods used to elucidate the novel properties of these potential nano-radio-enhancers. The instrumentation and samples preparation protocols are presented in the section indicated in the first column. The fundamental principle of each technique is described in the **Appendix A**.

Table II - 2. Methods for nanoparticles characterization.

Section	Characterized feature	Method	Sample preparation
2.1	Metal ions reduction and NPs formation	UV-Visible spectroscopy	Diluted colloidal NPs
2.1	Size, shape and crystallinity	TEM	NPs dried under atmospheric conditions
2.3	Hydrodynamic size Stability and level of aggregation	DLS	Diluted colloidal NPs
2.4	Surface charge	Zeta potential	Diluted colloidal NPs
2.5	Chemical composition	XPS	NPs dried under atmospheric conditions
2.6	Functional composition	FTIR	NPs dried under atmospheric conditions
4.1.3	Cytotoxicity	Clonogenic assay	Human cancer cell lines in culture
4.1.5.1	Uptake quantification	ICP-OES ICP-MS	Cell pellets after NPs incubation in human cancer cell cells
4.1.5.1 4.1.5.1	Localization in cells	NanoSIMS TEM	Fixed cells
4.1.4	Cell killing radio-enhancement	Clonogenic assay	Irradiation of living cells with γ -rays and medical carbon ions
4.2	Molecular damage radio-enhancement	Agarose gel electrophoresis	γ -rays irradiation of the bio-nanoprobe (plasmid DNA)

2.1 UV-Visible spectroscopy

2.1.1 Instrumentation

The main characterization technique, used to follow the reduction of the metal ions and nanoparticles formation, was the ultraviolet-visible spectroscopy. All measurements were performed at the Laboratoire de Chimie Physique (Université Paris-Saclay, UMR8000 CNRS) using an Agilent 8453 UV-visible Spectroscopy System.

2.1.2 Samples preparation

The as-synthesized nanoparticles, if prepared at 10^{-2} mol.L⁻¹, were diluted in ultrapure water to a final concentration of 10^{-3} mol.L⁻¹ and measured at room temperature in a quartz cell (Hellma Analytics, $l = 0.2$ cm). A blank consisting in ultrapure water was measured before sampling (see results **Chapter III** for PtPEG-OH NPs and **Chapter IV** for mono- and bimetallic PEG-2NH₂ NPs).

2.2 Transmission Electron Microscopy (TEM)

2.2.1 Instrumentation

Two TEM facilities were used in collaboration to characterize the metallic core size, crystallinity and morphology of the as-synthesized nanoparticles. The fundamental principle of TEM is described in the **Appendix A-1**.

A JEOL 100CXII microscope at an accelerating voltage of 100 kV operated by Dr. Patricia Beaunier at the Laboratoire de Réactivité de Surfaces (Université Paris VI, in collaboration with Dr. Hynd Remita) was used for the imaging and crystallographic determination of metallic NPs.

A JEOL 2200FS microscope at an accelerating voltage of 200 kV was used at the IBiSA platform (Institut Curie, Orsay) in collaboration with Dr. Marco Sergio and Dr. Sylvain Trepout to determine the size and morphology of NPs before incubation within cells.

2.2.2 Samples preparation

Drops of as-synthesized nanoparticles were deposited on copper grids specially treated by Dr. Beaunier or on commercial carbon-formvar copper grids (200 mesh, Agar Scientific Ltd) and observed after natural drying under the JEOL 100CXII or JEOL 2200FS respectively. The nanoparticles size distribution histograms were built by analyzing more

than 2000 particles using the ImageJ 1.46r software. In the case of PtPEG-OH NPs, results are presented and discussed in **Chapter III – Section 1.2**. For the mono- and bimetallic PEGylated gold-platinum nanoparticles, results can be found in **Chapter IV – Section 1.1**.

2.3 Dynamic Light Scattering (DLS)

The hydrodynamic diameter (d_H) indicates the size of colloidal particles including the metal core (determined by TEM), the particle coating (polymer/ligand) and the solvation shell (surrounding solvent, water). The fundamental principle of DLS is described in the **Appendix A-2**.

Knowledge on the d_H size of nanoparticles in suspension provides important clues about possible interactions with biological systems. It is commonly accepted that nanomaterials with sizes smaller than some tens of nanometers, do not accumulate in undesired organs and are more easily eliminated by renal clearance, minimizing toxicity risks [10] [11].

2.3.1 Instrumentation

In this work, the d_H of the as-synthesized nanoparticles was determined by DLS. We used a Zetasizer Nano-ZS (laser He-Ne, 633 nm) from Marven Instrument Ltd, in collaboration with Dr. Laure Catala at the Institut de Chimie Moléculaire et des Matériaux d'Orsay (ICMMO - UMR8182 CNRS).

2.3.2 Samples preparation

Firstly, we analyzed the d_H of the as-synthesized nanoparticles. These nanoparticles were diluted in ultrapure water to a final concentration of 5×10^{-4} mol.L⁻¹ and measured at room temperature in a semi-micro polystyrene (PS) cuvette. The size distribution is shown by number as the mean of three independent NPs batches. Results on the PtPEG-OH NPs are presented and discussed in **Chapter III – Section 1.2**. For the mono- and bimetallic PEGylated gold-platinum nanoparticles, results can be found in **Chapter IV – Section 1.1**.

Secondly, we investigate the stability of particularly PtPEG-OH NPs in different media by measuring the d_H of nanoparticles suspensions. We studied the influence of time (time post dilution preparation). Diluted samples (5×10^{-4} mol.L⁻¹) in ultrapure water, phosphate

[10] Choi H S *et al.* (2007) *Nat. Biotechnol.* **25** 1165–70

[11] Michelle L *et al.* (2008) *Nanomedicine (Lond)* **3** 703–17

saline buffer (PBS), NaCl, Tris-EDTA buffer (TE) and Dulbecco's Modified Eagle's Medium (DMEM) were analyzed, in a semi-micro PS disposable cuvette, immediately and 1, 3, 6 and 22 h after dilution preparation at 37°C. The size distribution is presented by intensity (see results in **Chapter III – Section 1.5**).

2.4 Zeta potential (ζ -potential)

The ζ -potential of nanoparticles developed with medical purposes is another important feature that must be well characterized. In particular, a positive or a negative ζ -potential may determine the interaction and uptake of nanoparticles by living organisms [12]. The fundamental principle of the ζ -potential measurements is described in the **Appendix A-3**.

The ζ -potential strongly depends on the composition of the particles suspensions, which is mainly affected by:

- ionic concentration
- type of ions
- presence of surfactants or polyelectrolytes
- pH

For instance, homogeneously highly charged particles ($> +30$ mV or > -30 mV) will resist flocculation and aggregation for longer periods making such samples more stable. In this work, we firstly evaluated the ζ -potential of the as-synthesized nanoparticles and then their stability as function of pH.

2.4.1 Instrumentation

We determined the ζ -potential of colloidal nanoparticles using the Zetasizer Nano-ZS already described (**Section 2.3.1**).

2.4.2 Samples preparation

Firstly, we analyzed the ζ -potential of the as-synthesized nanoparticles (pH ~ 6), which were diluted in ultrapure water to a final concentration of 10^{-3} mol.L⁻¹ and measured at room temperature. A disposable folded capillary cell was used with this purpose.

[12] Zhang Y *et al.* (2008) *Biomed. Microdevices* **10** 321–8

In particular, we evaluated the influence of pH in the ζ -potential of the PtPEG-OH NPs. Nanoparticles were diluted in aqueous solutions containing NaCl [0.01 mol.L⁻¹] to a final concentration 10⁻³ mol.L⁻¹ and then adjusted to the desired pH ranging from 3 up to 11. The isoelectric point of nanoparticles was thus determined. This point indicates the pH at which nanoparticles carries no net electrical charge, *i.e.* $\zeta = 0$ mV (point of zero charge (PZC)). All values reported in **Chapter IV - Section 1.5.1** are the mean \pm standard derivation of triplicate measurements.

2.5 X-ray Photoelectron Spectroscopy (XPS)

X-ray Photoelectron Spectroscopy, also known as Electron Spectroscopy for Chemical Analysis (ESCA), is widely used to analyse the chemical composition of surfaces. Its ability to explore the first few atomic layers, 1-10 nm, and assign the elemental composition (empirical formula), chemical state and electronic state of the elements within a material, makes XPS a powerful technique in emerging nanoscience developments. The fundamental principle of XPS is described in the **Appendix A-4**.

In this work, we used XPS to evaluate the purity, elemental composition, electronic state and chemical conformation of as synthesized, mono and bimetallic platinum based nanoparticles.

2.5.1 Instrumentation

XPS measurements were performed in collaboration with Dr. Diana Dragoë (ICMMO - UMR8182 CNRS). We used a K Alpha XPS spectrometer (Thermo Fisher Scientific) working with a pressure in the low 10⁻⁹ mbar range. This XPS spectrometer is equipped with a monochromatic aluminum source (Al K α , 1486.7 eV).

The XPS analyses were performed fixing a spot size of 400 μ m, which corresponds to an irradiated zone of approximately 1 mm². The hemispherical analyzer was operated at 0° take off angle in the Constant Analyser Energy (CAE) mode. Pass energy of 200 eV and a step of 1 eV were used for the acquisition of survey scans. Pass energy of 50 eV and a step of 0.1 eV were used for the acquisition of narrow windows. Charge compensation was done by means of a “dual beam” flood gun. The recorded spectra were processed by means of the Avantage software, using a peak-fitting routine with Shirley background and

symmetrical 70%-30% mixed Gaussian-Lorentzian peak shapes. In particular, a Doniach-Sunjic type function [13] was used to fit the Pt⁰ asymmetric peaks.

All the results discussed in **Chapter III – Section 1.3** and **Chapter IV – Section 1.2.1** were reproducibly obtained over at least three independent NPs synthesis.

2.5.2 Samples preparation

XPS analysis was performed in dried samples. Commonly, 30 µl of colloidal suspensions containing the as-synthesized NPs were deposited on cover glasses (Menzel-Glaser) and dried under atmospheric conditions 72h prior analysis.

Figure II - 2 shows the picture of the sample holder with nanoparticles and a control (PEG-OH) (on the left) and a magnified picture that shows different points used for XPS analysis (on the right).

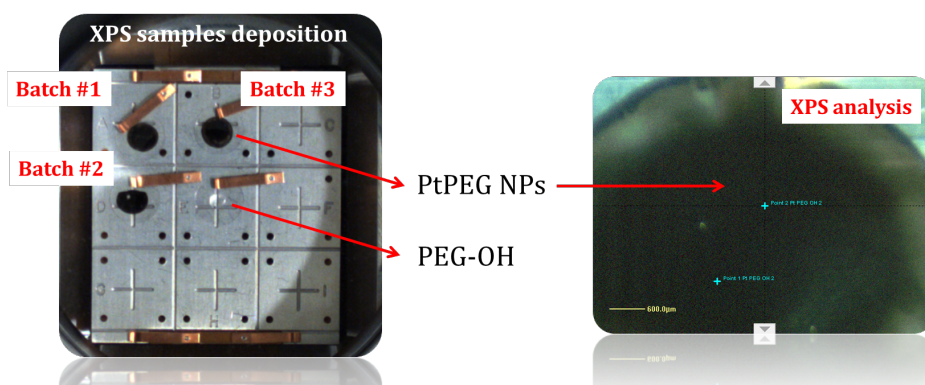


Figure II - 2. Nanoparticles samples for XPS analysis.

2.6 Fourier Transform Infrared (FTIR) spectroscopy

Infrared (IR) spectroscopy, also called vibrational spectroscopy, is an analytical tool largely used to determine the chemical structure and functional groups present in organic and inorganic compounds. The fundamental principle of FTIR is described in the **Appendix A-5**.

FTIR spectroscopy was used in this work to characterize the functional groups of the NPs coating.

[13] Olivero J J and Longbothum R L (1977) *J. Quant. Spectrosc. Radiat. Transfer* **17** 233–6

2.6.1 Instrumentation

In this work, an Alpha FTIR Spectrometer (Bruker Optik GmbH) was used at the laboratory of Nanosciences et Innovation pour les Matériaux, la Biomédecine et l'Énergie (CEA – Saclay) to characterize the PEGylation of metallic nanoparticles. NPs were characterized using the attenuated total reflection (ATR) module of the FTIR spectrometer.

2.6.2 Samples preparation

A small drop of the as-synthesized colloidal nanoparticles was deposited on the ATR module and dried with air. The transmittance FTIR spectra were measured from 4000 to 375 cm^{-1} (OPUS software, spectral resolution of $\sim 4 \text{ cm}^{-1}$). Three independent batches of as-synthesized metallic nanoparticles were analysed. The resulting FTIR spectra are the average of 60 scans. Control samples consisting on the pure Pt^{II} complex and PEGs were also measured. In the case of PtPEG-OH NPs, results are presented and discussed in **Chapter III – Section 1.4**. For the mono- and bimetallic PEGylated gold-platinum nanoparticles, results can be found in **Chapter IV – Section 1.2.2**.

3. Radiation sources

In this section, we present the different radiation sources used in this work. Gamma rays were used to synthesize nanoparticles and to irradiate biological samples (cells and the bio-nanoprobe). Medical carbon ions were particularly used to study the efficiency of nanoparticles to improve the performance of hadrontherapy.

3.1 Cobalt-60 gamma source

Cobalt-60 (^{60}Co) is a widely used source of highly penetrating γ -rays (MeV). In this work, the panoramic cobalt-60 source, managed by the Laboratoire de Chimie Physique, was used in the radiolytic synthesis of nanoparticles (see experimental protocol in **Section 1**) and in all molecular scale experiments (see experimental protocol in **Section 4.2**).

3.1.1 Description

^{60}Co is a synthetic radioactive isotope of cobalt with a half-life of *ca.* 5.3 years. It is produced artificially in nuclear reactors. ^{60}Co decays by beta $^-$ decay to the metastable excited isotope nickel-60 ($^{60}\text{Ni}^*$). The excited nickel nucleus emits then two gamma rays with energies of 1.17 and 1.33 MeV (LET= 0.2 keV. μm^{-1}) to stabilize (**Figure II - 3**).

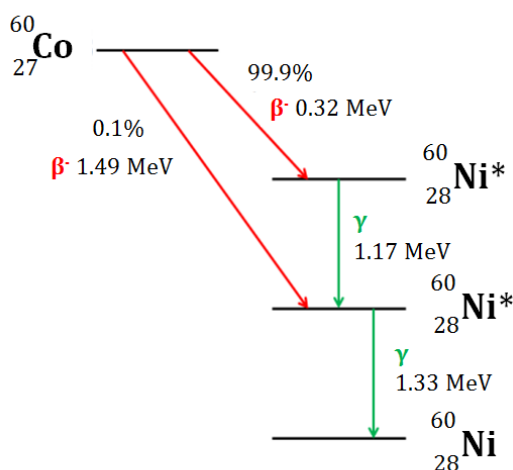


Figure II - 3. Schematic representation of the ^{60}Co radioactive decay.

3.1.2 The source and its dosimetry

The dose rate of a ^{60}Co source depends on its activity and decreases with the square of the distance from the source. In this work and for each individual application, the dose rate of

gamma rays was determined by Fricke dosimetry [14]. The dose rate at the position of samples irradiation was determined once per year. **Figure II - 4** shows the ^{60}Co source and the used experimental positions used.



Figure II - 4. The cobalt-60 panoramic source used for NPs synthesis and plasmid DNA irradiation.

Briefly, the reaction involved in the Fricke dosimeter is the radiolytic oxidation of ferrous ions to ferric ions ($\text{Fe}^{2+} \rightarrow \text{Fe}^{3+}$) at low pH and in the presence of oxygen. The standard dosimeter solution contains $10^{-3} \text{ mol.L}^{-1}$ of ferrous sulphate (FeSO_4) in a $0.4 \text{ mol.L}^{-1} \text{ H}_2\text{SO}_4$ solution (pH ~ 0.46). Water radiolysis (see mechanism in **Chapter I - Section 1.1.2.1**) in presence of Fe^{2+} ions and oxygen leads to the following reactions:



[14] Hardwick T J (1951) *Can. J. Chem.* **30** 17-22



Equation II - 7

When O_2 is present, the yield of Fe^{3+} is calculated by:

$$G(\text{Fe}^{3+}) = 2G(\text{H}_2\text{O}_2) + G(\text{OH}^\cdot) + 3G(\text{H}^\cdot)$$

Equation II - 8

As the $G(\text{Fe}^{3+})$ depends on the molecular yields of primary radicals, it mainly varies with pH and LET. For instance, the yield of Fe^{3+} using a ^{60}Co gamma source ($\text{LET} = 0.2 \text{ keV} \cdot \mu\text{m}^{-1}$) is equal to $16.2 \times 10^{-6} \text{ mol} \cdot \text{J}^{-1}$. The formation of Fe^{3+} generates a spectral signal at 304 nm which can be easily measured by absorption spectrophotometry. The dose response is linear up to *ca.* 400 Gy. The absorbed dose (D) is then determined by using the follow relationship:

$$D(\text{Gy}) = \frac{A}{\epsilon \cdot l \cdot G}$$

Equation II - 9

where A = absorbance, ϵ = molar absorption coefficient = $2204 \text{ l} \cdot \text{mol}^{-1} \cdot \text{cm}^{-1}$ and l = optical path = 1 cm. Thus, the dose rate is finally determined by plotting the absorbed dose D as function of the irradiation time.

Figure II - 5 shows the dose as function of time at one of the irradiation positions. The linear response has a slope of about $8.4 \text{ Gy} \cdot \text{min}^{-1}$ ($R^2 = 0.997$), which represents the average dose rate. At positions closer to the source (positions 7, 8 and 9 in **Figure II - 4**), we obtained an average dose rate of $95.5 \text{ Gy} \cdot \text{min}^{-1}$.

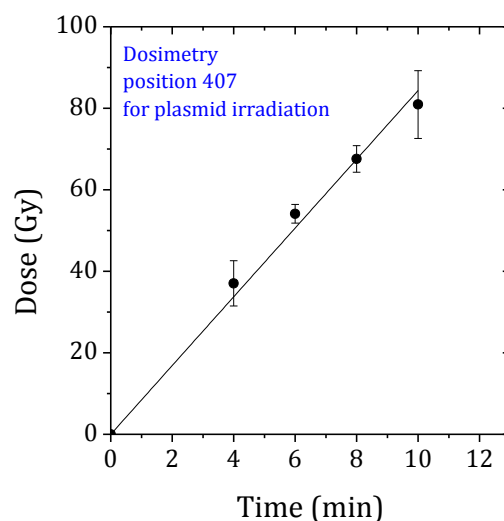


Figure II - 5. Dosimetry of the ^{60}Co source measured at position 407.

3.2 Caesium-137 gamma source

In this work, a Caesium-137 source was used to irradiate *in vitro* cells (see cell line description in **Section 4.1.4**). This source, which has a dose rate lower than that of the cobalt-60 source, is more adapted to the irradiation of living cells.

3.2.1 Description

Caesium-137 is a radioactive isotope of caesium formed by the nuclear fission of uranium-235. ^{137}Cs has a half-life of about 30.17 years. It decays in about 95% by beta- emission to a metastable nuclear isotope of barium ($^{137}_{56}\text{Ba}^*$). The remainder (*ca.* 5%) directly populates the ground state of the barium-137. The metastable Ba-137 has a half-life of about 153 seconds and completely decays by the emission of gamma rays with energy of about 0.662 MeV (LET= 0.2 keV. μm^{-1}) (**Figure II - 6**).

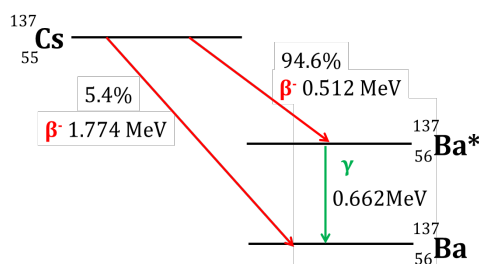


Figure II - 6. Schematic representation of the ^{137}Cs radioactive decay.

3.2.2 The source and its dosimetry

Living cells were irradiated with a GSR-D1, a common ^{137}Cs gamma rays irradiator used in radiobiology (**Figure II - 7**). This source located at the Institut Curie - Orsay, France, is used in collaboration with Dr. Evelyne Sage.

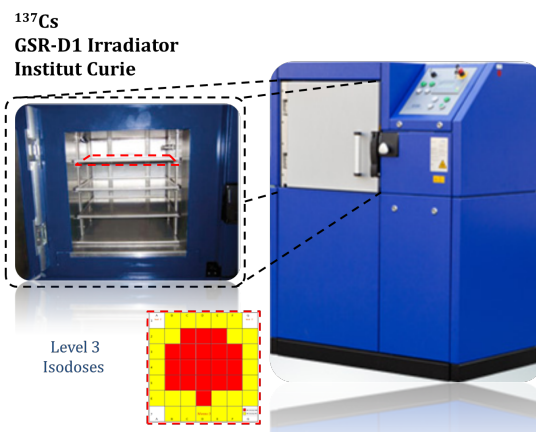


Figure II - 7. The caesium-137 GSR-D1 irradiator used for *in vitro* experimentation.

The dose rate was determined considering the deactivation of ¹³⁷Cs. It was calculated using a programmed macro furnished by the radioprotection professionals from Institute Curie. A dose difference of <10% is achieved by considering the isodoses describing each level of the irradiator chamber (in red **Figure II - 7**). Cells were irradiated with an average dose rate of 1 Gy.min⁻¹ and doses ranging from 0 up to 5 Gy. The experimental protocol used to irradiate cells is presented in **Section 4.1.4**. The results are presented and discussed in **Chapter III - Section 2.2**.

3.3 Medical carbon ions

These experiments were performed at the Heavy Ion Medical Accelerator (HIMAC) in Chiba, Japan in collaboration with Dr. Ryoichi Hirayama (NIRS, Chiba, Japan) and Dr. Noriko Usami from the High Energy Accelerator Research Organization (KEK, Japan). Only the effect of the PtPEG-OH NPs activated by carbon ions was evaluated on HeLa cells. The results are presented and discussed in **Chapter III - Section 2.2.1**.

3.3.1 Description: the irradiation facility

The HIMAC is considered as the first specialized heavy ion cancer treatment facility worldwide. It mainly consists of a primary accelerator (synchrotron) that accelerates carbon beams and other heavy particle beams, from He²⁺ to Xe⁵⁴⁺, to 800 MeV of energy per nucleus, an injector (linear accelerator) and treatment rooms for patients [15] (see illustration in **Figure II - 8**).

[15] <http://www.nirs.go.jp/ENG/core/ace/index.html>

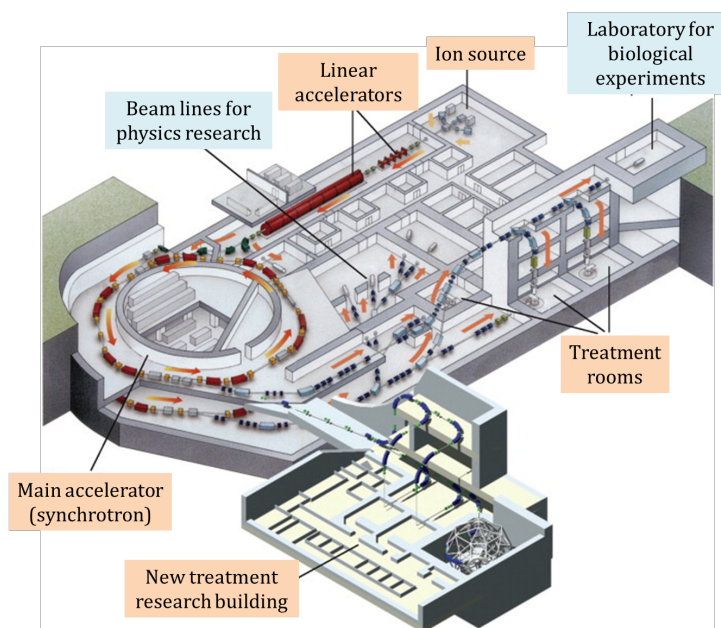


Figure II - 8. Illustration of the HIMAC facility in Chiba, Japan
(<http://www.nirs.go.jp/ENG/core/ace/index.html>)

Fortunately, the HIMAC has special experimental rooms exclusively dedicated to research in biology and physics. The radiation enhancing effect (REE) of platinum nanoparticles in combination with carbon ions was firstly elucidated by the group using bio-nanoprobes in 2010. Since then this project focused on the evaluation of different high-Z based nanoparticles, such as gold and gadolinium based nanoparticles, with the perspective to develop applications in hadrontherapy.

3.3.2 Irradiation conditions

HeLa cells were prepared as described in **Section 4.1.4** and exposed to C^{6+} ions using an experimental setup specifically dedicated to irradiate cells (as shown in the picture and scheme of **Figure II - 9**).

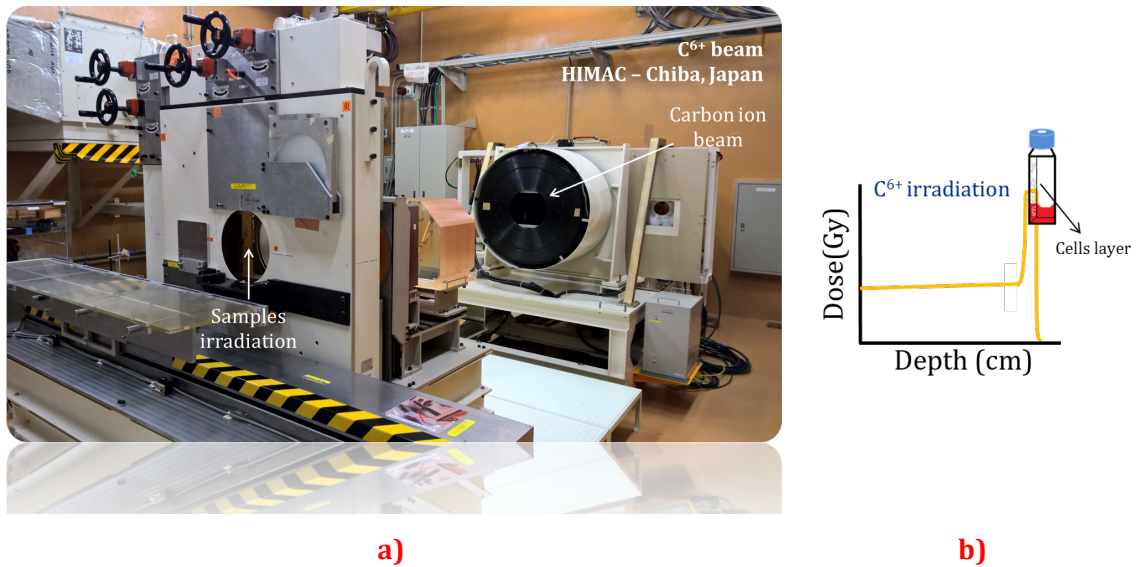


Figure II - 9. (a) Experimental set up used to irradiate cells by carbon ions at the HIMAC (NIRS, Chiba, Japan). (b) Scheme showing the conditions used to irradiate cells.

Cells were placed vertically to the beam and irradiated at the middle of the Spread Out Bragg Peak (SOBP) within an average LET of $110 \text{ keV}\cdot\mu\text{m}^{-1}$ and a dose rate of approximately $15 \text{ Gy}\cdot\text{min}^{-1}$. The SOBP had a size of 5 mm. The energy of the incident particles was $290 \text{ MeV}/\text{uma}$. The beam delivered a uniform flux within 2% variation in a 10 cm diameter circle [see more details in 4]. Cells were irradiated at doses ranging from 0 up to 2.5 Gy.

[4] Porcel E (2011) Thèse de Doctorat (Université Paris-Sud 11)

4. Biological models: description and methods

In this work, we adopted a multi-scale approach to characterize the impact and the action mechanisms of NPs on bio systems. The REE of nanoparticles was evaluated in living cells. The nanoscale impact of NPs was investigated on plasmid DNA used as a molecular bio-nanoprobe.

In this section we present the biological models, as well as, the methods and experimental protocols optimized during my thesis.

The cell lines and culture conditions, the methods used to determine the toxicity and REE of NPs in living cells, as well as, the techniques used to quantify the cell uptake and evaluate the intracellular localization of NPs are presented in **Section 4.1**. This study has been performed only for the PtPEG-OH NPs.

In **Section 4.2** we present the quasi-standardized method used in the group to quantify the radio-induced nanometer size molecular damages, which allows elucidating the physico-chemical processes and radio-enhancement mechanism.

4.1 Cellular models

The biological impact of PtPEG-OH NPs was evaluated using two human immortalized cell lines, HeLa and U87-MG.

4.1.1 Cell lines description

HeLa cells were derived from cervical cancer in 1951. They are widely used in radiobiology and cancer research due to their remarkable durability and proliferation [16]. They have a doubling time of about 24 hours and a plating efficiency of about 60%. In this work, we particularly evaluated the toxicity and REE of PtPEG-OH NPs in HeLa cells irradiated by gamma rays and medical carbon ions.

Glioblastoma is the most common and aggressive malignant primary brain tumor in humans [17], which cannot be efficiently treated by conventional therapeutic modalities. In this work, we used the U87-MG cell line, which was derived from malignant gliomas in

[16] Rahbari R *et al.* (2009) *Biotechniques* **46** 277–84

[17] Clark M J *et al.* (2010) *PLoS Genet.* **6**

1966, to evaluate the toxicity of PtPEG-OH NPs and their REE only under gamma radiation. U87-MG cells have a doubling time of about 36 hours and plating efficiency of ~10%.

HeLa and U87 MG cells were obtained from the American Type Culture Collection (ATCC).

Table II - 3 summarizes the main characteristics of each cell line.

Table II - 3. Main information of HeLa and U87-MG cells from the ATCC (<https://www.lgcstandards-atcc.org/>)

HeLa (ATCC® CCL-2™)	Organism	<i>Homo sapiens</i> , human
	Tissue	Cervix
	Disease	Adenocarcinoma
	Morphology	Epithelial
	Growth properties	Adherent
U87-MG (ATCC® HTB-14™)	Organism	<i>Homo sapiens</i> , human
	Tissue	Brain
	Disease	Glioblastoma - astrocytoma
	Morphology	Epithelial
	Growth properties	Adherent

4.1.2 Cell culture conditions

Cells were grown in monolayer using Dulbecco's Modified Eagle Medium (DMEM). The DMEM was enriched with 10% Fetal Bovine Serum (FBS), 1% antibiotics (100 units/ml penicillin + 100 µg/ml streptomycin) and 1% glutamine. In the particular case of U87-MG cells, 1% of non-essential amino acids (NE AA) was added. Cells were cultured at 37°C in a humidified 95% air / 5% CO₂ atmosphere.

Commonly, when cells were 70 - 90% confluent, they were split into new culture vessels. For this, the culture medium was removed and discarded, the cell layer was rinsed twice with phosphate buffered saline (PBS) solution (pH 7.4) and 0.05% trypsin solution was then added to the culture flask. Trypsin cleaves peptide chains mainly at the carboxyl side of the amino acids, which allows the detachment of the cells monolayer. Thus, trypsin was incubated for about 5 minutes at 37°C, 5% CO₂ until the cell layer was detached from the substratum and dispersed. Complete growth medium was then added and cells were collected by gently pipetting. Appropriate aliquots of the cell suspensions were placed into new culture vessels for further culture.

4.1.3 Cytotoxicity evaluation of PtPEG-OH NPs by clonogenic assay

The cytotoxicity of the as-synthesized PtPEG-OH NPs was evaluated in HeLa and U87-MG cells by clonogenic assay.

4.1.3.1 Principle of the method

Clonogenic assay or colony formation assay (CFA) is an *in vitro* cell survival assay based on the ability of a single cell to grow and proliferate to form a colony. The method was developed by T.T. Puck and coworkers from the University of Colorado in 1955 [18]. We used the CFA to evaluate the cytotoxicity of PtPEG-OH NPs in HeLa and U87-MG cells, and to determine the impact of NPs on cells survival after radiation treatment (Section 4.1.4).

4.1.3.2 Experimental protocol: samples preparation

Exponentially grown cells (2×10^5) were plated in T25 culture flasks and maintained overnight in a 5% CO₂ atmosphere at 37°C. Cells were then incubated for 6 h with enriched culture medium containing PtPEG-OH NPs at two different Pt concentrations, 5×10^{-4} and 10^{-3} mol.L⁻¹. The control samples consisted in cells incubated with enriched medium containing a water volume equivalent to that of the nanoparticle suspension. After incubation, cells were trypsinized and re-seeded into 10 cm petri dishes at different densities in order to achieve *ca.* 100 colonies per dish 14 days after. For each condition 6 petri dishes were prepared.

Colonies were fixed and stained with a 0.5% methylene blue - methanol solution (50% v/v). Those colonies containing more than 50 cells were scored. The results presented in Chapter III - Section 2.1.1 correspond to the plating efficiency (PE) of the control and cells incubated with NPs. The PE was calculated as follows:

$$PE = \frac{\text{Number of colonies counted}}{\text{Number of cells seeded}} \times 100 \quad \text{Equation II - 10}$$

The experimental protocol is illustrated in Figure II - 10.

[18] Puck T T *et al.* (1955) *J. Exp. Med.* **103** 273–84

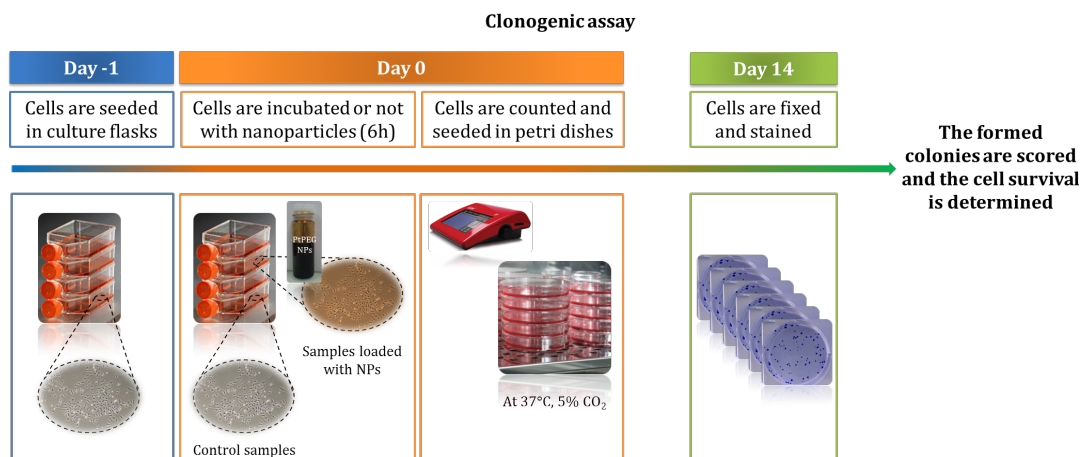


Figure II - 10. Schematic representation of the CFA protocol.

4.1.3.3 Statistical evaluation: ANOVA

The analysis of variance (ANOVA) is a commonly used statistical method in biology. It is used to determine whether there are any statistical significant differences between the means of three or more independent groups. It was developed by the statistician and biologist Ronald Fisher in 1921 [19]. ANOVA is the extension of the t-test, which is limited to the analysis of two independent groups.

Specifically, ANOVA tests the null hypothesis (H_0):

$$H_0: \mu_1 = \mu_2 = \mu_3 = \dots \mu_k$$

Equation II - 11

where μ = group mean and k = number of groups. The key output of ANOVA test is the p-value that is compared to a significance level (α). If the p-value is less than or equal to the significance level ($p \leq \alpha$), the null hypothesis is rejected concluding that not all the population means are equal. If the p-value is greater than the significance level ($p > \alpha$), there is not enough evidence to reject the null hypothesis concluding that the means of all populations are equal. Often α is set to 0.05, implying that it is acceptable to have a 5% of error rejecting the H_0 .

In this work, each group is defined as: a different NPs treatment applied to the same cell line. The mean of each group is the PE of three independent CFA, which correspond to 9 countable petri dishes. Here, we applied the ANOVAOneWay method from OriginPro 8.5

[19] Fisher R A S (1921) *Fish. Collect. Pap. Relat. to Stat. Math. theory Appl.* 3–32

(OriginLab, Northampton, USA) using a significance level of 0.05. The results are presented in **Chapter III – Section 2.1.1**.

4.1.4 Cell survival experiments with irradiation

The REE of PtPEG-OH NPs was evaluated by means of CFA in HeLa and U87-MG cells. Comparative studies were performed using gold nanoparticles (Au-DTDTPA NPs) (see results **Chapter III – Section 2.2**).

Cell survival was assessed by a standard 14 days colony formation assay. Exponentially grown cells (2×10^5) were plated in T25 culture flasks and maintained overnight in a 5% CO₂ atmosphere at 37°C. Cells were then incubated 6 h with enriched culture medium containing PtPEG-OH NPs at a final Pt concentration of 5×10^{-4} mol.L⁻¹. An equivalent water volume was added into control samples. Cells were then irradiated in fresh enriched medium under atmospheric conditions at room temperature.

The impact of NPs on γ -rays (¹³⁷Cs) effects was performed with HeLa and U87-MG cells. The impact of NPs on carbon ion beams was probed on HeLa cells only. The survival fraction (SF) of the control was calculated as follows:

$$SF = \frac{\text{Colonies counted}}{\text{Cells seeded} \times \frac{PE}{100}} \quad \text{Equation II - 12}$$

The results are presented in **Chapter III– Section 2.2.1** and **2.2.2** as the normalized SF of cells with regard to the SF of the control.

4.1.5 Intracellular nanoparticles characterization: methods and protocols

We quantified the uptake of nanoparticles by Inductively Coupled Plasma (ICP) using an Optical Emission Spectrophotometer (OES) and a Mass Spectrometer (MS) (**Section 4.1.5.1**).

The intracellular localization of PtPEG-OH NPs was investigated by Ion Microscopy (NanoSIMS) and TEM (**Sections 4.1.5.2** and **4.1.5.3**).

4.1.5.1 Inductively Coupled Plasma (ICP) spectroscopy

a) Instrumentation

An ICP-OES Varian 720 ES (**Figure II - 11a**) was used to quantify the uptake of platinum and gold nanoparticles in HeLa and U87-MG cells with a detection limit of $20 \mu\text{g}\cdot\text{L}^{-1}$ ($0.1 \mu\text{g}/\text{sample}$).

A GC-ICP-MS Thermo Scientific XSERIES 2 (**Figure II - 11b**) was also used to evaluate the uptake of PtPEG-OH NPs in HeLa cells with higher precision (detection limit of $0.001 \mu\text{g}/\text{sample}$). This analysis was performed by the company Ultra Traces Analyses Aquitaine in Pau, France.

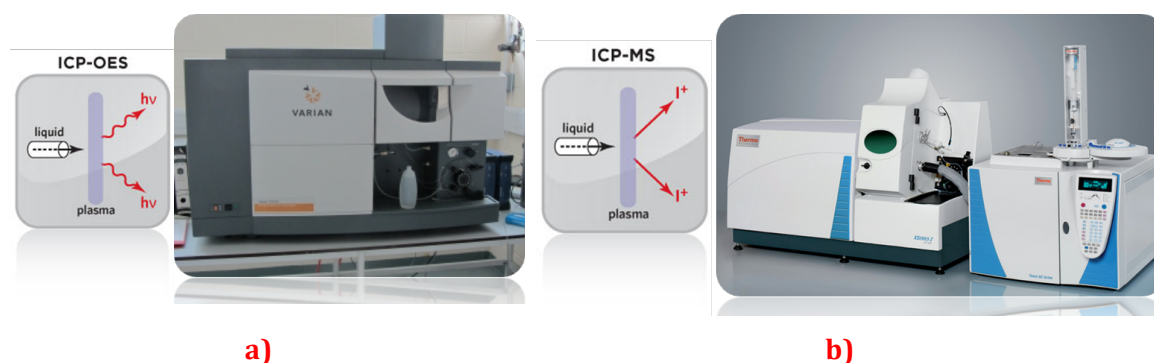


Figure II - 11. ICP principle and instrumentation of (a) the ICP-OES Varian 720 ES and (b) the GC-ICP-MS Thermo Scientific XSERIES 2.

b) Samples preparation

For ICP-OES analysis, close to 2×10^6 HeLa and U87-MG cells were incubated for 6 h with platinum (PtPEG-OH NPs) or gold (Au-DTDTPA NPs) at a final concentration of $5 \times 10^{-4} \text{ mol}\cdot\text{L}^{-1}$ in the culture medium. After incubation, the medium was removed, cells were rinsed with 1x PBS and collected by trypsination. Cells were then counted and centrifuged (7 min at 1200 rpm). The cells pellets were dissolved in *aqua regia* (a mixture of nitric acid and hydrochloric acid in a molar ratio of 1:3) and diluted in ultrapure water ($V_T = 5 \text{ ml}$) for the analysis. The results from one replicate are presented and discussed in **Chapter III - Section 2.1.2.1**.

For ICP-MS analysis, around 2×10^6 HeLa cells were incubated for 6 and 24 hours with PtPEG-OH NPs at a final concentration of $5 \times 10^{-4} \text{ mol}\cdot\text{L}^{-1}$. Cells pellets were sent at -80°C to

Pau, France, for further analysis. Results from one replicate are presented in **Chapter III – Section 2.1.2.2.**

4.1.5.2 Ion Microscopy: NanoSIMS Imaging

Ion microscopy is an alternative method to fluorescent microscopy, which does not require the presence of any fluorescent tag. Its use for the characterization of the intracellular distribution of free-labelled PtPEG-OH NPs in HeLa cells was developed in my thesis for the first time.

a) Fundamental principle

Introduced in the early sixties by Castaing and Slodzian [20], ion microscopy is a technique optimized for the composition analysis of solid surfaces and thin films. **Figure II - 12** illustrates the fundamental principle of a typical ion microscope.

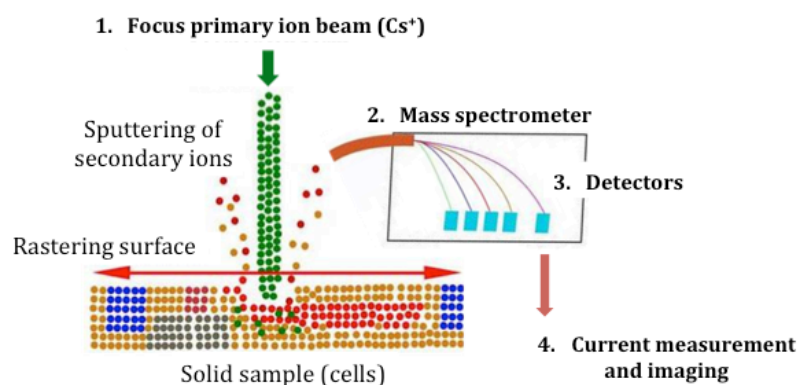


Figure II - 12. Schematic representation of Nano SIMS principle (adapted from [21]).

In brief, the phenomenon of secondary ion emission results from the collision of high energy particles (focused ion beam) with a solid sample. Under the impact, the energy of the primary ion beam dissipates into the sample inducing a collision cascade which breaks most chemical bonds. The atoms or combinations of atoms (fragments of molecules) are released (sputtering process) from a few atomic layers of the sample surface, in a neutral or charged form (ions). These ions are then focused and guided to a mass spectrometer. The mass/charge ratio analysis of secondary ions allows measuring the ion current and imaging the elemental composition of the sample. Imaging is achieved by scanning the

[20] Castaing R and Slodzian G (1962) *J. Microsc. (Paris)*. **1** 395–410

[21] Jiang H *et al.* (2014) *J. Lipid Res.* **55** 2156–66

focused primary ion beam across the sample and by recording the number of secondary ions for each pixel of the scan (raster).

b) Instrumentation

The experiments have been performed with the CAMECA NanoSIMS 50™ (instrument developed by G. Slodzian, Professor of Université Paris-Sud, Orsay (France), the French Space Agency ONERA, B. Daigne and the CAMECA company) in collaboration with Dr. Jean-Luc Guerquin-Kern and Dr. Ting-Di Wu at Institut Curie – Orsay (France) (**Figure II - 13**).

The NanoSIMS 50™ contains a source of primary ions (Cs^+ or O^{2+} , O^- , *etc.*), a mass spectrometer and a detection device. The whole system works under ultra-high vacuum, ranging from 10^{-10} Torr (analysis chamber) to 10^{-8} Torr (detector compartment). Its main characteristics are [22]:

- High lateral resolution (≤ 50 nm in caesium, ≤ 150 nm in oxygen).
- Ability to measure up to 5 masses (ions) in parallel, from the same micro-volume, and ensuring perfect isotopic ratio from the same small volume or perfect image superimposition.
- Very good transmission even at high mass resolution (60% at $M/\Delta M = 5000$).
- Direct optical observation of the sample within the ionization chamber, allowing fast selection of the area of interest.
- Charge compensation for insulating samples (in secondary negative ion mode).



Figure II - 13. The Cameca NanoSIMS 50 ion-probe for element analysis at the CMIB platform (Institut Curie).

[22] Guerquin-Kern J-L *et al.* (2005) *Biochim. Biophys. Acta - Gen. Subj.* **1724** 228–38

c) Samples preparation: cryo-fixation

This preparation protocol is long and involves several steps. Each step is critical for the good preservation of biological specimens and their post-analysis.

In brief, about 35 000 HeLa cells, in a 60 μl volume, were plated on 1 cm^2 Melinex film support (Agar Scientific Ltd., Stansted, Essex, UK) and let to attach at 37°C in a humidified 5% CO_2 atmosphere for 2 h. After attachment, wells containing the Melinex supports were filled with enriched culture medium. Cells were grown overnight and then incubated for 6 hours with 5×10^{-4} mol.L^{-1} PtPEG-OH NPs (conditions used for irradiation). After incubation, those non-internalized NPs were removed, by washing twice with 1x PBS, and new enriched medium was added.

The Melinex supports were then cut in small squares (9 mm^2) and cells were fixed by slam freezing on a metal mirror precooled with liquid nitrogen to -180°C. This fixation method was used to avoid chemical interference during NanoSIMS analysis. The cryofixation was performed in a Leica EM CPC system. Samples were dehydrated following a two weeks freeze drying protocol which started at -130°C. By reaching 0°C dehydrated samples were embedded in resin and polymerized at 60°C for 8 h. After polymerization several sections of *ca.* 0.2 μm were deposited on a silicon holder and analysed.

d) Analysis

The primary incident ion beam was generated from a caesium source with energy of 16 keV and a probe size of *ca.* 50 nm in diameter. The magnetic field was set to detect Pt, the heaviest element ($m_{\text{Pt}} = 195$) on one of the largest detectors while the other movable detectors were positioned to analyze CN^- and P^- . The mass spectrometer was calibrated with a control sample consisting of a platinum layer deposited on a gold film. **Figure II - 14** shows the count rates (count per second, cps) as function of the ions mass (a.m.u.). We clearly observe the peaks corresponding to the main platinum isotopes with their respective proportions; 33% ^{194}Pt and ^{195}Pt , 25% ^{196}Pt and 7% ^{198}Pt . The small signal at 197 a.m.u. corresponds to the gold support.

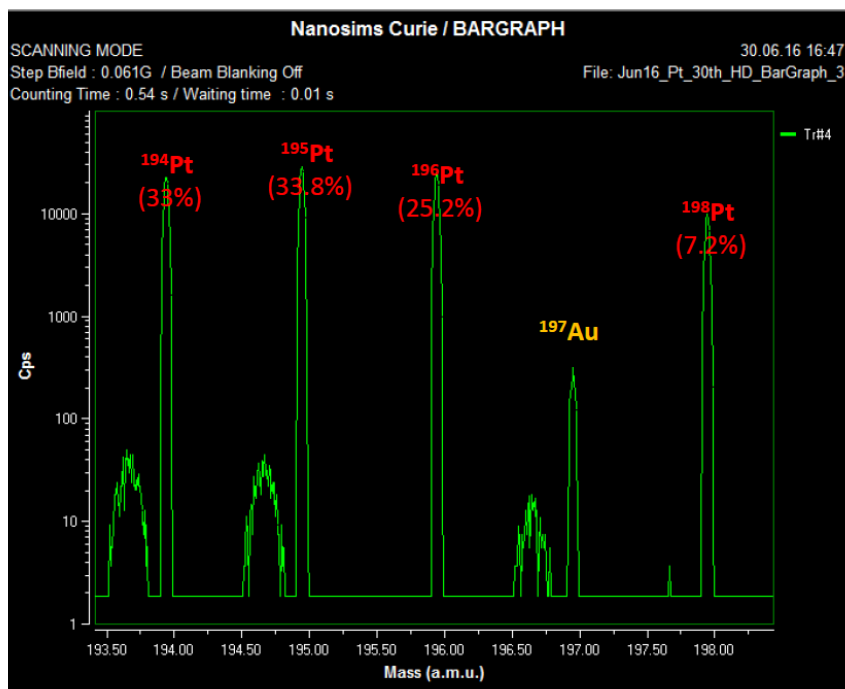


Figure II - 14. Calibration of the Cameca NanoSIMS 50 by means of a Pt layer.

The spatial analysis was performed as follows: firstly the CN^- emission was analysed over a large area ($240 \mu\text{m} \times 720 \mu\text{m}$) and secondly, a complete analysis (CN^- , P $^-$ and ^{194}Pt) was performed for two selected cells. In **Chapter III- Section 2.1.3.1**, we present the complete analysis performed in one HeLa cell loaded with PtPEG-OH NPs. It is important to highlight that these measurements were performed close to the end of this project and a complementary statistical analysis is in process.

4.1.5.3 Transmission Electron Microscopy

TEM was used to better elucidate the localization and uptake mechanism(s) of PtPEG-OH NPs in HeLa and U87-MG cells.

TEM has a better spatial resolution (atomic resolution $\leq 10^{-9}$ m) in comparison with NanoSIMS (50 nm). TEM is commonly used to image biological specimens ranging from intact eukaryotic cells to individual proteins >150 kDa.

a) Instrumentation

The localization of PtPEG-OH NPs in HeLa and U87-MG cells was performed in collaboration with Dr. Sergio Marco and Dr. Sylvain Trepout at the BioImaging Cell and

Tissue Core Facility from Institut Curie –Orsay, France (PICT-IBiSA platform), with a JEOL 2200FS microscope (**Figure II - 15**).



Figure II - 15. The JEOL 2200FS used at the PICT-IBiSA platform for cells imagery.

b) Samples preparation: chemical fixation

About 60 000 HeLa and U87-MG cells were plated on microscopic slides (Menzel-Glaser, $\phi = 20$ mm) placed in a 6 wells-plate and let to attach at 37°C in a humidified 5% CO₂ atmosphere for 2 h. After attachment, wells containing the slides were filled with enriched culture medium. Cells were grown overnight and then incubated for 6 h with 5×10^{-4} mol.L⁻¹ PtPEG-OH NPs. Control samples were incubated at same conditions but using pure water instead of nanoparticles. The slides were then rinsed with PBS 1X and fixed for 35 min at 4°C in a mixture of 2.5% glutaraldehyde and 4% paraformaldehyde prepared in the same buffer solution. Cells were then rinsed 3 times with PBS to remove all reagents traces. After rinsing with PBS, the cells were dehydrated using ethanol in gradient concentrations, from 40% to pure ethanol, and embedded step by step in Epon resin [23]. Samples were then polymerized at 60°C. From selected areas consisting on a homogenous cells layer, resin blocks were formed. They were finally cut into ultrathin (~100 nm) square sections using an ultramicrotome. The obtained slices were deposited on 200 mesh copper grids (Agar scientific) and observed.

Measurements were performed for close to 20 HeLa and 20 U87-MG cells, including control and PtPEG-OH NPs loaded samples. They correspond to 3 different slices regions.

[23] Luft J H (1961) *J. Biophys. Biochem. Cytol.* **9** 409–14

In **Chapter III – Section 2.1.3.2**, we show the most representative images obtained in this study. Notably, a robust statistical analysis is in process at the PICT-IBiSA platform.

4.2 Bio-nanoprobe: pBR322 plasmid DNA

In this work, we used a molecular probe to quantify the radiation induced complex (nanometer size) damage in the presence of nanoparticles. This probe is the pBR322 plasmid DNA, which is a circular double-stranded DNA of 4361 base pairs (2.83×10^6 Da). It is commercially supplied (Thermo Scientific) in solution at $0.5 \mu\text{g} \cdot \mu\text{L}^{-1}$ in a TE buffer consisting on $10 \text{ mmol} \cdot \text{L}^{-1}$ Tris-HCl (pH=7.6) and $1 \text{ mmol} \cdot \text{L}^{-1}$ ethylenediaminetetraacetic acid (EDTA).

Depending on its degradation level, plasmid DNA presents the advantage of having three different conformations namely supercoiled, relaxed and linear (see **Figure II - 16**), which can be easily separated and quantified.



Figure II - 16. Scheme of the three different plasmid conformations.

The native morphology consists of the supercoiled conformation for more than 95% and *ca.* 5% of the relaxed conformation, which corresponds to the plasmid with single strand break (SSB). The linear conformation that corresponds to the plasmid with two breaks in two strands separated by less than ten base pairs (DSB) is not present in the native product.

4.2.1 Samples preparation and irradiation

In this work, a protocol developed before (thesis of Dr. Erika Porcel) was used and adapted to evaluate the nanoscale effect of nanoparticles on the induction of simple breaks

(SSB) and complex breaks (DSB) by radiation [5]. An illustration of the experimental protocol is presented in **Figure II - 17**.

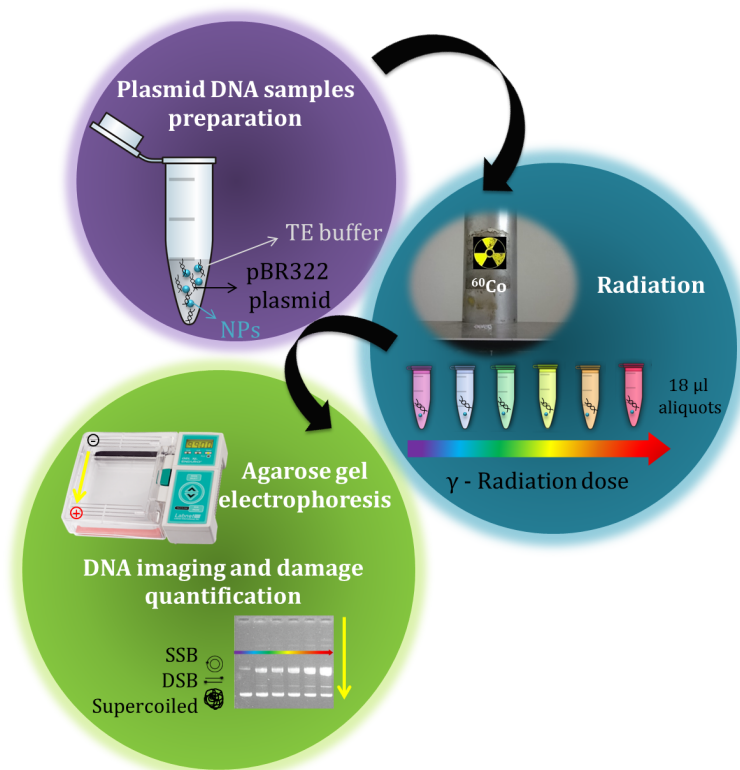


Figure II - 17. Scheme of the experimental protocol used for molecular experiments.

Briefly, initial samples consisted on 5 µg plasmid DNA diluted in 10 µl of 1x TE buffer solution. In this buffer, we assured a constant counter ions concentration, an important parameter to keep the plasmid conformation unchanged. The as-synthesized NPs were diluted in ultrapure water to reach a Pt concentration of $4.23 \times 10^{-5} \text{ mol.L}^{-1}$. For instance, this concentration corresponds to the addition of one PtPEG-OH NP (around 1000 Pt atoms, see estimation **Chapter III -Section 1.2.2**) per 2 plasmids [5]. This ratio was used in all the experiments (evaluation of mono- and bimetallic PEGylated nanoparticles). Control samples were prepared by adding 47 µL of ultrapure water to the plasmid in order to mimic the effect of the water added with NPs.

For each condition, 6 aliquots (18 µL) were prepared and irradiated at doses ranging from 0 up to 250 Gy with a dose rate of *ca.* 8.4 Gy/min. The dose rate of the panoramic ^{60}Co source was determined by Fricke dosimetry (**Section 3.1.2**).

[5] Porcel E et al. (2010) *Nanotechnology* 21 85103

In some samples, the contribution of indirect effects to the radiation induced damage was evidenced by adding dimethylsulfoxide (DMSO) [24] to the samples at a final concentration of 1.0 mol.L⁻¹ (see results **Chapter III - Section 2.3.3** for PtPEG-OH NPs and **Chapter IV - Section 2** for mono-and bimetallic PEG-2NH₂ NPs). DMSO is known to possess important radioprotective properties which are generally associated with its rapid reaction with OH· radicals. In the radiolysis of aqueous systems, the rate constant of this reaction is 4.2x10⁹ M⁻¹.s⁻¹ (neutral pH) [25]. In **Table II - 4** we present a model protocol used to prepare samples of pure plasmid DNA, plasmid DNA in presence of DMSO, plasmid DNA loaded with nanoparticles and plasmid DNA loaded with nanoparticles in presence of DMSO.

Table II - 4. Experimental protocol for the samples preparation with and without nanoparticles.

Sample	Plasmid (μl)	1x TE buffer (μl)	NPs (μl)	H ₂ O (μl)	DMSO 7.8 mol.L ⁻¹ (μl)	Total Volume (μl)
Control	10	123	0	47	0	180
Control + DMSO	10	123	0	24	23	180
DNA+NPs	10	123	24	23	0	180
DNA+NPs+DMSO	10	123	24	0	23	180

A complementary study on the effect of NP concentration was evaluated by changing the ratio of PtPEG-OH NPs over plasmids (between 0 up to 8 NPs per plasmid). The results are presented in **Appendix B**.

4.2.2 Radio-induced nanosize damage: analysis and quantification

After irradiation, the radiation-induced damage was analysed by agarose gel electrophoresis. The three plasmid DNA conformations were separated in a 1% agarose gel. It was prepared by dissolving 1.5 g of agarose powders in 150 mL of 1x Tris Acetate EDTA buffer solution (TAE). Samples were then gently mixed with a DNA gel loading buffer consisting of 0.21% bromophenol blue, 0.21% xylene cyanol FF, 0.2 M EDTA, pH 8.0 and 50% glycerol (5-PRIME). These final mixtures were carefully deposited into the agarose gel immersed in a 1x TAE solution for electrophoresis migration.

[24] Chapman J D *et al.* (1979) *Radiat. Environ. Biophys.* **16** 29–41

[25] Meissner G *et al.* (1967) *Zeitschrift für Naturforsch.* **22** 13–9

The migration was performed at 4°C for about 2 hours 20 minutes at 80 V. DNA was stained after migration in a 0.02% ethidium bromide (EtBr) aqueous bath (30 min) and rinsed with pure water prior imaging. The EtBr is an intercalating agent commonly used as a fluorescent tag for nucleic acids stain. It is classified as a mutagen because it intercalates DNA (*i.e.*, inserts itself between the DNA strands breaks) which affects DNA biological processes as its replication and transcription [26]. For this reason, it is treated as hazardous waste. Hence, EtBr was strictly handled and disposed according to regulations.

After staining, the lines corresponding to plasmids with different conformations were revealed under UV light at 302 nm and recorded with a CCD camera. The ImageQuant 5.0 software was used to quantify the intensity of the different DNA conformations (densitometry).

The supercoiled plasmids (S) bind 1.47 times less EtBr than the relaxed (R) and the linear (L) conformations. The intensity of S is then multiplied by 1.47 and the intensities are normalized by:

$$\text{Total} = 1.47 \times S + R + L \quad \text{Equation II - 13}$$

$$S' = \frac{1.47 \times S}{\text{Total}} \quad \text{Equation II - 14}$$

$$L' = \frac{L}{\text{Total}} \quad \text{Equation II - 15}$$

$$R' = \frac{R}{\text{Total}} \quad \text{Equation II - 16}$$

From S' and L' , the yields of single and double strand breaks are calculated according to a Poisson law, which is time independent and finds applicability for low probabilities as in here [27]. The SSB and DBS (nanosize damage) yields were calculated by:

$$\text{SSB yield (breaks per plasmid)} = \ln \left(\frac{1-L'}{S'} \right) \quad \text{Equation II - 17}$$

$$\text{DSB yield (breaks per plasmid)} = \frac{L'}{1-L'} \quad \text{Equation II - 18}$$

The dose-response curves were thus obtained by plotting the yields as function of the irradiation dose. The results for mono- and bimetallic nanoparticles are presented and discussed in **Chapter III** and **IV**.

[26] Waring M J (1965) *J. Mol. Biol.* **13** 269–82

[27] Spothheim-Maurizot M *et al.* (1990) *Int. J. Radiat. Biol.* **57** 301–13

5. References

- [1] Belloni J, Mostafavi M, Remita H, Marignier J and Delcourt M-O 1998 Radiation-induced synthesis of mono- and multi-metallic clusters and nanocolloids *New J. Chem.* **22** 1239–55
- [2] Henglein A 1989 Small-particle research: physicochemical properties of extremely small colloidal metal and semiconductor particles *Chem. Rev.* **89** 1861–73
- [3] Remita H and Remita S 2010 Metal Clusters and Nanomaterials: Contribution of Radiation Chemistry *Recent Trends in Radiation Chemistry* ed J F Wishart and B S Madhava Rao (World Scientific) p 607
- [4] Porcel E 2011 *Utilisation des nanoparticules pour améliorer les performances de la hadronthérapie* (Université Paris-Sud 11)
- [5] Porcel E, Liehn S, Remita H, Usami N, Kobayashi K, Furusawa Y, Le Sech C and Lacombe S 2010 Platinum nanoparticles: a promising material for future cancer therapy? *Nanotechnology* **21** 85103
- [6] Marin E, Briceño M I and Caballero-George C 2013 Critical evaluation of biodegradable polymers used in nanodrugs *Int. J. Nanomedicine* **8** 3071–91
- [7] Knop K, Hoogenboom R, Fischer D and Schubert U S 2010 Poly(ethylene glycol) in drug delivery: Pros and cons as well as potential alternatives *Angew. Chemie - Int. Ed.* **49** 6288–308
- [8] Treguer M, de Cointet C, Remita H, Khatouri J, Mostafavi M, Amblard J, Belloni J and de Keyzer R 1998 Dose Rate Effects on Radiolytic Synthesis of Gold–Silver Bimetallic Clusters in Solution *J. Phys. Chem. B* **102** 4310–21
- [9] Remita H, Lampre I, Mostafavi M, Balanzat E and Bouffard S 2005 Comparative study of metal clusters induced in aqueous solutions by γ -rays, electron or C6+ ion beam irradiation *Radiat. Phys. Chem.* **72** 575–86
- [10] Choi H S, Liu W, Misra P, Tanaka E, Zimmer J P, Itty Ipe B, Bawendi M G and Frangioni J V 2007 Renal clearance of nanoparticles *Nat. Biotechnol.* **25** 1165–70
- [11] Michelle Longmire, Peter L. Choyke, M.D., and Hisataka Kobayashi, M.D. P . 2008 Clearance Properties of Nano-sized Particles and Molecules as Imagen Agents: Consideration and Caveats *Nanomedicine (Lond)* **3** 703–17
- [12] Zhang Y, Yang M, Portney N G, Cui D, Budak G, Ozbay E, Ozkan M and Ozkan C S 2008 Zeta potential: a surface electrical characteristic to probe the interaction of nanoparticles with normal and cancer human breast epithelial cells. *Biomed. Microdevices* **10** 321–8
- [13] Olivero J J and Longbothum R L 1977 Empirical fits to the voigt line width: a brief review *J. Quant. Spectrosc. Radiat. Transfer* **17** 233–6
- [14] Hardwick T J 1951 The oxidation of ferrous sulphate solutions by y-rays-the absolute yield *Can. J. Chem.* **30** 17–22
- [15] Dept. of Accelerator and Medical Physics | Center and Research core | National Institute of Radiological Science
- [16] Rahbari R, Sheahan T, Modes V, Collier P, Macfarlane C and Badge R M 2009 A novel L1 retrotransposon marker for HeLa cell line identification *Biotechniques* **46** 277–84
- [17] Clark M J, Homer N, O'Connor B D, Chen Z, Eskin A, Lee H, Merriman B and Nelson S F 2010 U87MG decoded: The genomic sequence of a cytogenetically aberrant human cancer cell line *PLoS Genet.* **6**
- [18] Puck T T, Marcus P I and Cieciora S J 1955 Clonal growth of mammalian cells in vitro *J. Exp. Med.* **103** 273–84
- [19] Fisher R A S 1921 On the “probable error” of a coefficient of correlation deduced from a small sample *Fish. Collect. Pap. Relat. to Stat. Math. theory Appl.* 3–32
- [20] Castaing R and Slodzian G 1962 Microanalyse par Émission Ionique Secondaire *J. Microsc. (Paris).* **1** 395–410

- [21] Jiang H, Goulbourne C N, Tatar A, Turlo K, Wu D, Beigneux A P, Grovenor C R M, Fong L G and Young S G 2014 High-resolution imaging of dietary lipids in cells and tissues by NanoSIMS analysis. *J. Lipid Res.* **55** 2156–66
- [22] Guerquin-Kern J-L, Wu T-D, Quintana C and Croisy A 2005 Progress in analytical imaging of the cell by dynamic secondary ion mass spectrometry (SIMS microscopy) *Biochim. Biophys. Acta - Gen. Subj.* **1724** 228–38
- [23] Luft J H 1961 Improvements in epoxy resin embedding methods *J. Biophys. Biochem. Cytol.* **9** 409–14
- [24] Chapman J D, Doern S D, Reuvers A P, Gillespie C J, Chatterjee A, Blakely E A, Smith K C and Tobias C A 1979 Radioprotection by DMSO of mammalian cells exposed to X-rays and to heavy charged-particle beams *Radiat. Environ. Biophys.* **16** 29–41
- [25] Meissner G, Henglein A and Beck G 1967 Pulsradiolytische Untersuchung von Dimethylthioäther und Dimethylsulfoxyd in wässriger Lösung *Zeitschrift für Naturforsch.* **22** 13–9
- [26] Waring M J 1965 Complex formation between ethidium bromide and nucleic acids *J. Mol. Biol.* **13** 269–82
- [27] Spothem-Maurizot M, Charlier M and Sabattier R 1990 DNA Radiolysis by Fast Neutrons *Int. J. Radiat. Biol.* **57** 301–13

Chapter III: RESULTS AND DISCUSSION PEGylated platinum nanoparticles

1. Nanoparticles characterization.....	101
1.1 Characterization by spectrophotometry UV-Vis	102
1.2 Size distribution and morphology.....	104
1.2.1 Influence of the PEG-OH:Pt ratio on the stability and size of NPs.....	105
1.2.2 Estimation on the number of Pt atoms per NP.....	107
1.3 Oxidation state and chemical composition by XPS	109
1.3.1 Qualitative elemental composition.....	109
1.3.2 Platinum core oxidation state.....	109
1.3.3 Insights on the interaction of PEG molecules with the Pt ⁰ core.....	112
1.3.4 Quantitative elemental composition.....	115
1.4 Functional characterization by FTIR.....	117
1.5 Stability in biological relevant media.....	123
1.5.1 Influence of pH in NaCl	123
1.5.2 Stability in different solvents.....	124
1.6 Conclusion.....	126
2. Biological impact of nanoparticles	128
2.1 Interaction of NPs with human cells – toxicity, uptake and localization.....	129
2.1.1 Cytotoxicity evaluation	129
2.1.2 Cell uptake.....	130
2.1.2.1 Quantification of the cell uptake	130

2.1.2.2	Influence of the incubation time on the cell uptake	132
2.1.3	Intracellular distribution of NPs	134
2.1.3.1	NanoSIMS analysis.....	134
2.1.3.2	TEM imaging.....	137
2.1.3.3	Conclusion	142
2.2	Effect of PtPEG-OH NPs on radiation induced cell-killing	143
2.2.1	HeLa cells irradiation experiments.....	143
2.2.1.1	Cells survival curves.....	143
2.2.1.2	Cell survival analysis: direct versus sub-lethal damages.....	144
2.2.1.3	Quantification of the amplification efficiency	145
2.2.2	U87-MG cells irradiation experiments	149
2.2.2.1	Cells survival curves.....	149
2.2.2.2	Cell survival analysis: direct versus sub-lethal damages.....	150
2.2.2.3	Quantification of the amplification efficiency	150
2.2.3	Conclusion.....	151
2.3	Proof of principle: enhancement on the radio-induced nanosize damage.....	153
2.3.1	Effect of PtPEG-OH NPs on the induction of nanometer size damages	153
2.3.2	Amplification efficiency of molecular nanosize damage	154
2.3.3	Insight in mechanisms: the effect of OH · radicals	155
2.4	Conclusion: Multi-scale study	156
3.	References.....	158

Chapter III: RESULTS AND DISCUSSION PEGylated platinum nanoparticles

In this chapter we present and discuss the characterization and biological impact of the novel PEGylated platinum nanoparticles (PtPEG-OH NPs). The physico-chemical characterization of these nanoparticles is shown in **Section 1**. Their biological impact in two different human cancer cell lines is then presented in **Section 2.1** while their nanoscale effect using the bio-nanoprobe already described is finally presented in **Section 2.3**.

1. Nanoparticles characterization

During my thesis, I developed a unique one-step green method to synthesize ready-to-use (sterilized) biocompatible Pt NPs for biomedical applications. I performed the characterization of these nano-agents by using complementary techniques. In this perspective I contributed to bring new methods to the group.

The radiolytic reduction of the Pt^{II} precursor and thus nanoparticles formation were firstly characterized by spectrophotometry UV-Vis (**Section 1.1**). The size and shape of the as-synthesized PtPEG-OH NPs were characterized by TEM and DLS, these results are shown in **Section 1.2**. In **Section 1.3** the oxidation state and chemical composition of PtPEG-OH NPs determined by XPS is presented. The functional characterization using FTIR is shown and discussed in **Section 1.4**. Finally, the stability of PtPEG-OH NPs in different relevant media was investigated by DLS and is presented in **Section 1.5**.

1.1 Characterization by spectrophotometry UV-Vis

The PtPEG-OH NPs were synthesized by means of γ -rays water radiolysis. For these measurements, NPs synthesized in water containing 10^{-2} mol.L $^{-1}$ of Pt(NH $_3$) $_4$ Cl $_2$ and 1 mol.L $^{-1}$ of PEG-OH ($M_w = 1000$ g.mol $^{-1}$) (PEG-OH:Pt molar ratio of *ca.* 100) were diluted to 10^{-3} mol.L $^{-1}$ (in Pt) and used.

Metallic nanoparticles display strong optical absorption due to the excitation of the surface plasmon resonance of the metal (SPR) [1]. The reduction of Pt II and the formation of platinum nanoparticles were followed by UV-visible absorption spectroscopy. **Figure III - 1a** shows the UV-visible absorption spectra of an aqueous solution containing Pt(NH $_3$) $_4$ Cl $_2$ and PEG-OH before irradiation (in blue) and the same solution after irradiation (in red) (see experimental conditions **Chapter II - Section 1.1.2**).

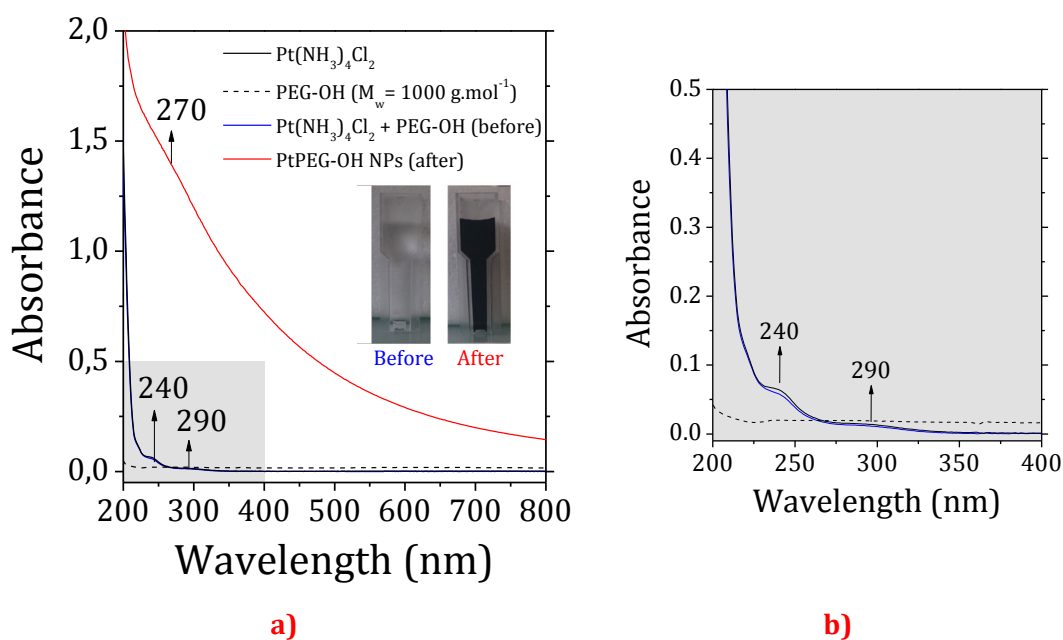


Figure III - 1. (a) UV-vis absorption spectra of control solutions containing Pt(NH $_3$) $_4$ Cl $_2$ (—) and PEG-OH (---) and samples consisting on diluted platinum containing solutions (10^{-3} mol.L $^{-1}$) before (—) and after (—) irradiation (optical path = 2 mm). Inserted pictures correspond to an aqueous solution containing Pt(NH $_3$) $_4$ Cl $_2$ and PEG-OH before and after irradiation (10^{-2} mol.L $^{-1}$, $D = 100$ kGy). (b) Absorption spectra of samples shown in (a) but in a wavelength range from 200 to 400 nm.

In **Figure III - 1**, the black and blue absorption spectra reveal that, before irradiation, the aqueous solutions composed of Pt(NH $_3$) $_4$ Cl $_2$ or Pt(NH $_3$) $_4$ Cl $_2$ in the presence of PEG-OH have a main absorption peak close to 240 nm and a small shoulder around 290 nm, which

[1] Mie G (1908) *Ann. Phys.* **330** 377-445

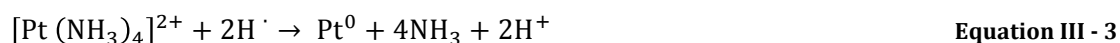
correspond to the ligand-to-metal charge transfer (LMCT) band between $(\text{NH}_3)_4^{2+}$ and Pt^{II} ions [2]. The absorption spectrum of the PEG-OH alone (---), does not display any signal in the UV-visible region. After irradiation, we observe the disappearance of the two initial absorption peaks and the appearance of a stretched absorption spectrum with a single broad peak centered around 270 nm. This new spectrum is attributed to platinum-PEG colloids. Notably, the spectrum of PtPEG-OH NPs remains unchanged during several months, which indicates the complete reduction of platinum ions and formation of stable nanoparticles. These observations are in good agreement with previous works where the optical properties of colloidal platinum nanoparticles synthesized by radiolysis were studied [2] [3]. The inserted pictures in **Figure III - 1a** show the color change, from colorless before irradiation to dark brown after gamma rays treatment. This color is characteristic of the formation of platinum nanoparticles.

The formation of metallic platinum nanoparticles from the radiolytic reduction of $\text{Pt}(\text{NH}_3)_4\text{Cl}_2$ in aqueous solution takes place through the following mechanisms [2]:

1. The $\text{Pt}(\text{NH}_3)_4\text{Cl}_2$ platinum complex in solution dissociates into $[\text{Pt}(\text{NH}_3)_4]^{2+}$ cations and 2Cl^- anions.



2. The solvated electrons e_{aq}^- and hydrogen radicals H^\cdot produced by water radiolysis efficiently reduce Pt^{2+} ions to Pt^0 atoms.



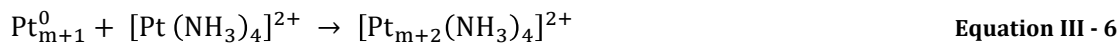
3. The coalescence of the neutral atoms leads to the formation of the metal atomic clusters.



[2] Gharibshahi E and Saion E (2012) *Int. J. Mol. Sci.* **13** 14723–41

[3] Remita H *et al.* (2005) *Radiat. Phys. Chem.* **72** 575–86

4. During the radiolytic process, the Pt_{m+1}^0 clusters can also be re-combined with $[\text{Pt}(\text{NH}_3)_4]^{2+}$ ions to form $[\text{Pt}_{m+2}(\text{NH}_3)_4]^{2+}$. These recombined ions might form larger Pt_{m+2}^0 nanoparticles which agglomerate until a complete reduction is achieved.



To obtain stable and homogenous clusters, the coalescence must be limited by the presence of ligands such as polymeric molecules. In the present case, PEG-OH molecules were used as stabilizer (see synthesis in **Chapter II – Section 1.1.2**).

1.2 Size distribution and morphology

The brownish color of the platinum colloidal solution after irradiation (inserted picture **Figure III - 1a**) was the first indication of nanoparticles formation. **Figure III - 2** shows TEM micrographs of PtPEG-OH NPs synthesized with an initial platinum concentration of $10^{-2} \text{ mol.L}^{-1}$, a PEG-OH:Pt molar ratio of *ca.* 100 and a total radiation dose of 100 kGy. These micrographs were obtained with the JEOL 2200FS microscope at the PICT-IBiSA platform.

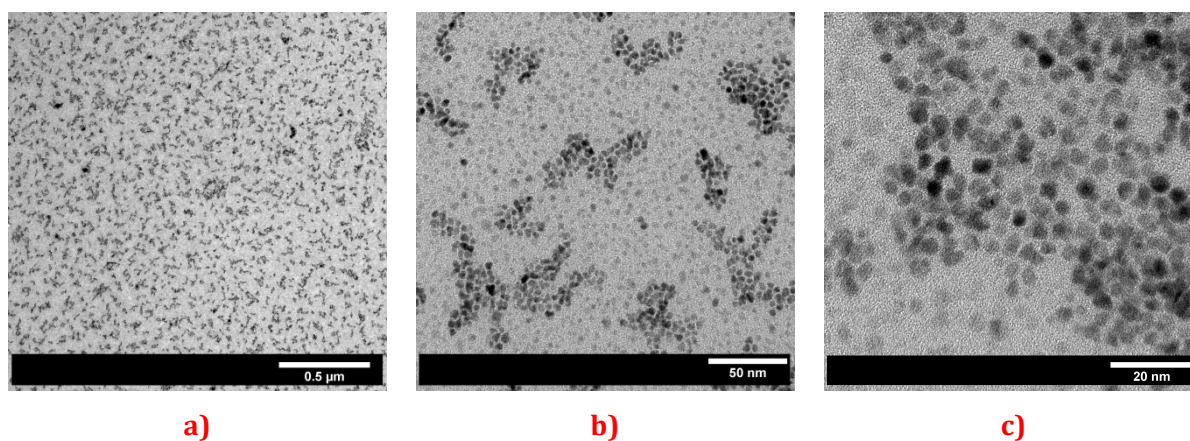


Figure III - 2. TEM micrographs of PtPEG-OH NPs synthesized in water with an initial Pt^{II} concentration of $10^{-2} \text{ mol.L}^{-1}$ and a PEG-OH:Pt molar ratio of *ca.* 100 measured at three magnifications. Scale bars: (a) 0.5 μm , (b) 50 nm and (c) 20 nm.

At the three different magnifications, we clearly observe homogeneity in size and shape. This measurement shows that PtPEG-OH NPs are mainly spherical with an average metallic core diameter of $3.2 \pm 0.8 \text{ nm}$ (**Figure III - 3a**). DLS measurements showed that these NPs have an average d_{H} of $8.8 \pm 3.1 \text{ nm}$ ($\text{Pdl} = 0.238 \pm 0.004$) (**Figure III - 3b**). In

agreement with other works [4] [5], the -OH end-group of PEG conferred to platinum nanoparticles an average negative ζ -potential of -16.6 ± 5.1 mV in water (pH $\sim 6 - 7$, synthesis conditions). **Figure III - 3c** shows the electron diffraction pattern of these PtPEG-OH NPs. This tells that the platinum core have a crystal structure (ordered arrangement of atoms).

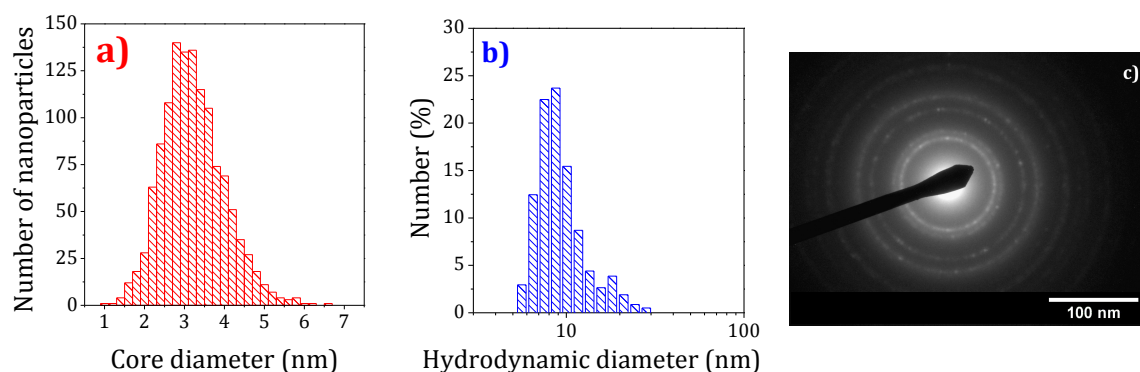


Figure III - 3. (a) Diameter distribution of the metallic core, (b) average hydrodynamic diameter and (c) electron diffraction pattern of PtPEG-OH NPs.

PtPEG-OH NPs synthesized with platinum concentrations ranging from 10^{-3} up to 10^{-2} mol.L $^{-1}$ (PEG-OH:Pt molar ratio of *ca.* 100) are very similar in size and shape. Nanoparticles remain stable for several months when stored at 4 °C (verified by TEM, DLS, and spectrophotometry).

1.2.1 Influence of the PEG-OH:Pt ratio on the stability and size of NPs

Colloidal PtPEG-OH NPs were also synthesized with PEG-OH:Pt molar ratios of *ca.* 1, 5, 10, 25 and 50. The PtPEG-OH NPs with a PEG-OH:Pt molar ratio of *ca.* 1 precipitated immediately after irradiation while the other colloids were stable for longer time. PEG-OH:Pt molar ratio of *ca.* 5 precipitated in a week and thus no further investigation was carried out. Therefore, colloids containing PEG-OH:Pt molar ratio of *ca.* 10, 25 and 50 were further characterized. **Table III - 1** summarizes the stability, core diameter and hydrodynamic diameter of fresh PtPEG-OH NPs synthesized at different PEG-OH:Pt molar ratios.

[4] Doane T L *et al.* (2012) *Acc. Chem. Res.* **45** 317–26

[5] Gilles M *et al.* (2014) *Colloids Surfaces B Biointerfaces* **123** 770–7

Table III - 1. Influence of the PEG-OH:Pt molar ratio on the stability and size distribution of PtPEG-OH NPs.

PEG-OH:Pt	Colloidal stability*	Core diameter (nm)	Hydrodynamic diameter (nm)
1	non	-	-
5	weak	-	-
10	medium	3.0 ± 0.6	17.7 ± 5.5
25	medium	2.8 ± 0.8	14.7 ± 6.1
50	good	2.8 ± 1.0	11.8 ± 2.8
100	good	3.2 ± 0.8	8.8 ± 3.1

*The stability corresponds to a qualitative determination by the presence of turbidity or colloids precipitates when the solutions are stored at 4°C.
 weak= colloids precipitation in a week,
 medium= colloids precipitation in less than 3 weeks,
 good= colloids are stable for more than 6 week up to 3 months.

In **Table III - 1**, we observe that the platinum core diameter was constant for colloids containing PtPEG-OH NPs with a PEG-OH:Pt molar ratio of *ca* 10, 25, 50 and 100. On the other hand, the d_H of fresh colloids increased from 8.8 nm (PtPEG-OH NPs - 100) to 17.7 nm (PtPEG-OH NPs -10) indicating the presence of small NPs aggregates.

In particular, the PtPEG-OH NPs prepared with a PEG-OH:Pt molar ratio of *ca*. 50 exhibited good colloidal stability and identical morphological characteristics as those NPs synthesized with a PEG-OH:Pt molar ratio of *ca*. 100 (see **Figure III - 1**).

In summary, the PEG-OH:Pt molar ratios of *ca*. 50 and 100 are the best conditions to prepare well stable biocompatible PtPEG-OH NPs.

The impact of the PtPEG-OH NPs in biological systems (**Section 2**) was evaluated using nanoparticles synthesized with a PEG-OH:Pt molar ratio of about 100, which were considered as the most stable nano-agents for biomedical concerns.

1.2.2 Estimation on the number of Pt atoms per NP

Commonly, platinum atoms are organized in a face-centered cubic lattice (fcc) [6]. The platinum fcc crystal structure have 4 atoms per unit cell and a lattice constant of 3.912 Å (0.3912 nm). By considering the approach that there is an outer shell of atoms surrounding the spherical core of the nanoparticle, with finite thickness that corresponds to half of the lattice constant (0.1956 nm), we calculated the configuration of platinum atoms in the 3.2 nm nanocrystal as follow:

The volume of the inner platinum core is:

$$V_{\text{core}} = \frac{4\pi r^3}{3} = \frac{4\pi (1.6 - 0.1956)^3}{3} = 11.60 \text{ nm}^3$$

The total volume of a 3.2 nm diameter NP is:

$$V_{\text{tot}} = \frac{4\pi(1.6)^3}{3} = 17.15 \text{ nm}^3$$

The volume of the shell is the difference between the total volume and the volume of the core:

$$V_{\text{shell}} = V_{\text{tot}} - V_{\text{core}} = 17.15 - 11.60 = 5.55 \text{ nm}^3$$

Since the lattice constant of the Pt unit cell is 0.3912 nm the volume of a single unit cell is:

$$V_{\text{unit}} = (0.3912)^3 = 0.0599 \text{ nm}^3$$

Thus, we determine the number of unit cells making up the shell from:

$$\text{Unit cells}_{\text{shell}} = \frac{V_{\text{shell}}}{V_{\text{unit}}} = \frac{5.55}{0.0599} \approx 93$$

Considering 4 atoms per unit cell, the total number of platinum atoms in the surface is:

$$\text{Pt atoms}_{\text{surface}} = (93)(4) = 372 \text{ atoms}$$

[6] Davey W P (1925) *Phys. Rev.* 25 753-61

Then, the total number of atoms in the entire particle is calculated with the total number of unit cells as:

$$\text{Unit cells}_{\text{tot}} = \frac{V_{\text{tot}}}{V_{\text{unit}}} = \frac{17.15}{0.0599} \approx 286 \text{ atoms}$$

$$\text{Pt atoms}_{\text{tot}} = (286)(4) = 1144 \text{ atoms}$$

We find the fraction of surface atoms as:

$$f = \frac{\text{Pt atoms}_{\text{surface}}}{\text{Pt atoms}_{\text{tot}}} = \frac{372}{1144} \approx 0.33$$

As illustrated in **Figure III - 4**, one 3.2 nm platinum nanoparticle contains around 1000 atoms and ~33% of them are on the surface.

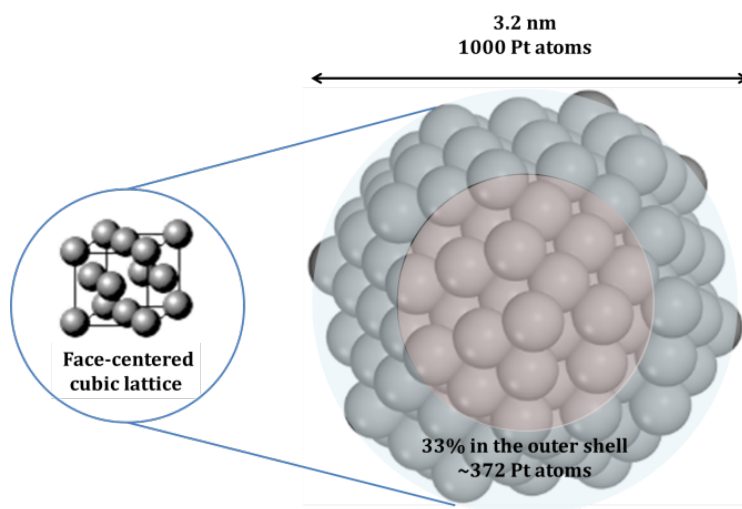


Figure III - 4. Schematic representation of a 3.2 nm platinum nanoparticle.

1.3 Oxidation state and chemical composition by XPS

In this work, we investigated the elemental composition, oxidation state and chemical structure of the as-synthesized PtPEG-OH NPs nanoparticles by XPS. The PtPEG-OH NPs synthesized at 10^{-2} mol.L⁻¹ (PEG-OH:Pt molar ratio of *ca.* 100) with a total dose of 100 kGy were analyzed.

1.3.1 Qualitative elemental composition

The survey XPS spectrum of PtPEG-OH NPs is shown in **Figure III - 5**. Only peaks characteristic of Pt, C, O, N and Cl were observed. This confirms that the PtPEG-OH NPs are composed of these elements only.

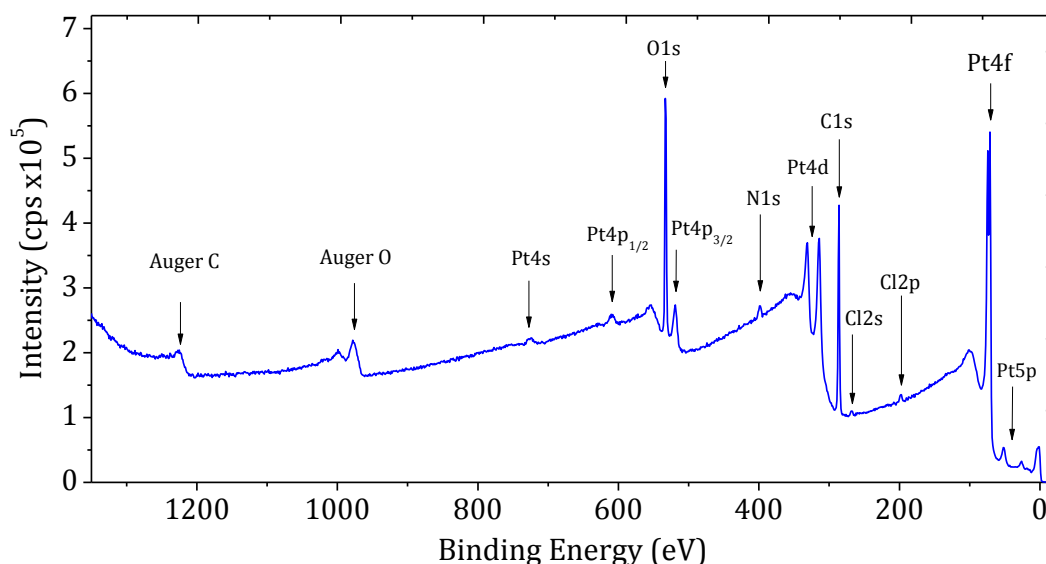


Figure III - 5. Survey XPS spectrum of PtPEG-OH NPs synthesized with a total gamma dose of 100 kGy.

1.3.2 Platinum core oxidation state

Figure III - 6a shows the high-resolution XPS spectra of the platinum complex ($\text{Pt}(\text{NH}_3)_4^{2+}$) powder (in black). For comparison we also measured the spectrum of a platinum solid sample (in blue). **Figure III - 6b** corresponds to the high-resolution XPS spectrum of PtPEG-OH NPs.

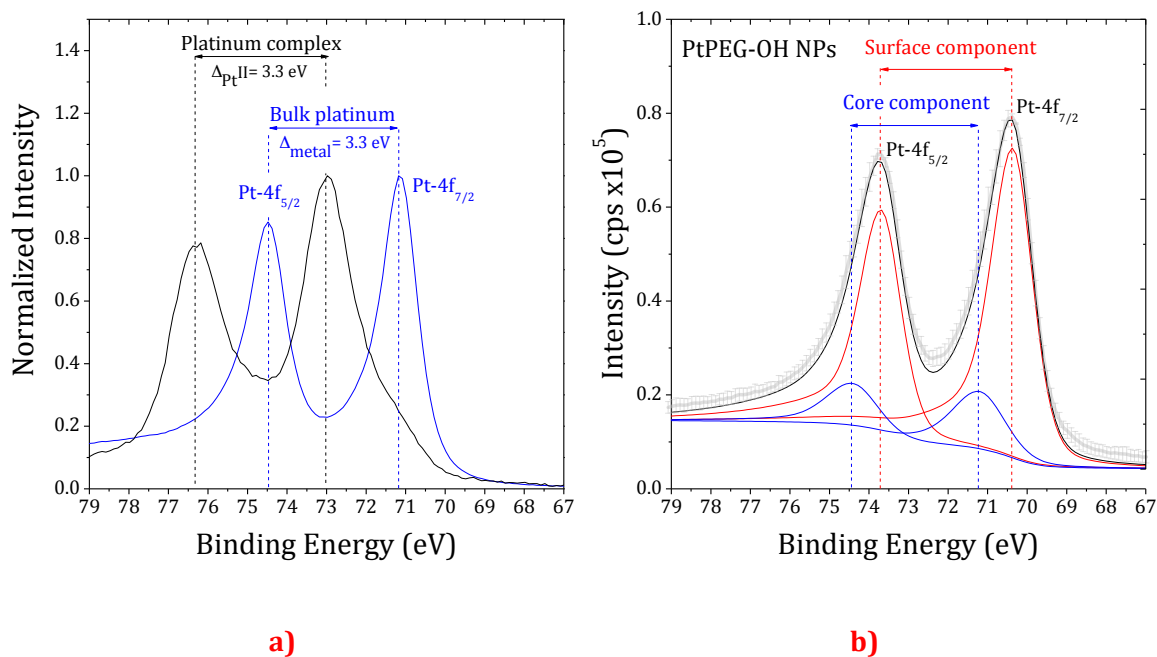


Figure III - 6. XPS spectra corresponding to the Pt-4f core level region of platinum on (a) the platinum complex (—) and on a platinum solid sample (—) and (b) on PtPEG-OH NPs showing their bulk (—) and surface (—) components.

In order to identify the oxidation state of the PtPEG-OH NPs, we selected from the literature the BE of different platinum samples that resemble the most to our case. The data correspond to bulk-like Pt species in single crystals and films, and oxidized Pt nanoparticles. The BE values are reported below.

Table III - 2. Summary of binding energy values reported in literature for the Pt-4f_{7/2} core level of different Pt phases.

4f _{7/2} BE (eV)		Sample	Reference
Pt ⁰	PtO		
70.7	73.3	Pt film	Kim K S <i>et al.</i> (1971) <i>J. Am. Chem. Soc.</i> 93 6296-7
70.9 (bulk) 70.5 (surf.)	-	Pt (111)	Puglia C <i>et al.</i> (1995) <i>Surf. Sci.</i> 342 119-33
71.2 - 71.5	72.2 - 72.5	Pt film (400 nm)/glass	Abe Y <i>et al.</i> (1999) <i>Jpn. J. Appl. Phys.</i> 38 4872
71.5	74.4	PtO (<2 nm)powder	Fleisch T H <i>et al.</i> (1986) <i>J. Phys. Chem.</i> 90 5317-20
Pt ₁ = 73.2 Pt ₆ = 72.5	-	Pt _n /SiO ₂ /Si (n=1 - 6)	Eberhardt W <i>et al.</i> (1990) <i>Phys. Rev. Lett.</i> 64 780
71.2	72.3	Pt (4 nm)/La ₂ O ₃ -ZrO ₂	Pitchon V <i>et al.</i> (1999) <i>J. Catal.</i> 186 64-74

71.1	72.8	Pt (3 nm)/MWCN	Tian Z Q <i>et al.</i> (2006) <i>J. Phys. Chem. B</i> 110 (11) 5343-50
72.0	73.4	Pt (10 nm)/ODA	Kumar A <i>et al.</i> (2004) <i>J. Chem. Sci.</i> 116 293-300

The precursor compound presented a peak at 73.0 eV (**Figure III - 6a**). From the table, we attribute this signal to the characteristic Pt-4f_{7/2} BE of platinum with a +2 oxidation state [7] [8]. Knowing that the distance between the Pt-4f_{7/2} and Pt-4f_{5/2} spin-orbit components is 3.33 eV, we confirm the attribution of the second peak. Note that the shoulder observed at lower BE is originated by the *in situ* reduction of the Pt^{II} ions during measurements. In the blue spectrum shown in **Figure III - 6a**, the well separated Pt-4f_{7/2} and Pt-4f_{5/2} spin-orbit components are observed at 71.1 and 74.5 eV respectively, which is specific to metallic Pt [9].

In **Figure III - 6b**, the spectrum of PtPEG-OH NPs at the Pt-4f core level is displayed in black. Its deconvolution shows two contributions: the contribution of the core component (double peak at 71.2 and 74.4 eV), commonly referred as bulk component, and the contribution of the main surface component (double peak at 70.4 and 73.7 eV). This measurement is in good agreement with other works performed in metallic Pt films [10] and Pt NPs [11] confirming the complete reduction of Pt^{II} ions into Pt⁰. Moreover, in the XPS summary table (see

Table III - 4 at the end of this section) we observe that the full width at half maximum (FWHM) of PtPEG-OH NPs, at the Pt-4f core level, increased by about 33%. This broadening suggests that there is a strong interaction between the metal surface and the PEG molecules [12].

The same result was found for three independent experiments performed with different NPs batches (within the error margin of the experimental set up (± 0.2 eV)), which demonstrates the accuracy and the reproducibility of the synthesis method.

[7] Kim K S *et al.* (1971) *J. Am. Chem. Soc.* **93** 6296-7

[8] Contour J P *et al.* (1977) *J. Catal.* **48** 217-28

[9] Barr T L (1978) *J. Phys. Chem.* **82** 1801-10

[10] Puglia C *et al.* (1995) *Surf. Sci.* **342** 119-33

[11] Liu F *et al.* (2009) *J. Surf. Anal.* **15** 271-3

[12] Fu X *et al.* (2001) *J. Colloid Interface Sci.* **243** 326-30

1.3.3 Insights on the interaction of PEG molecules with the Pt⁰ core

The arrangement of the PEG molecules at the surface of a Pt⁰ core was investigated by measuring the BE at the C-1s, O-1s and N-1s core levels. The C-1s, O-1s and N-1s XPS spectra of PEG-OH, Pt(NH₃)₄Cl₂ and PtPEG-OH NPs are shown in **Figure III - 7**.

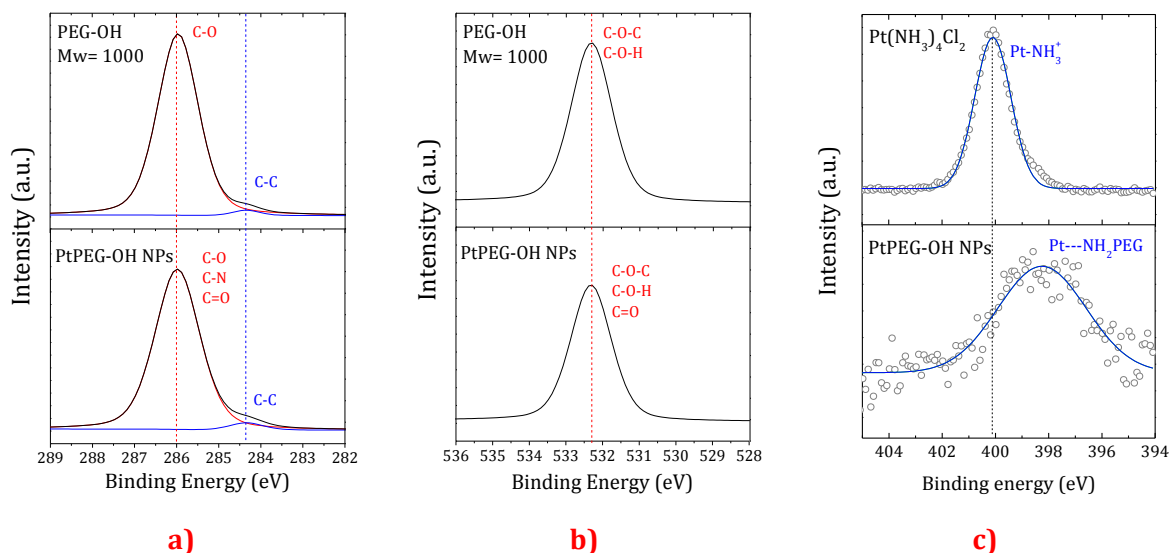


Figure III - 7. XPS spectra of (a) C-1s, (b) O-1s and (c) N-1s in pure PEG-OH, Pt(NH₃)₄Cl₂ and PtPEG-OH NPs.

In order to identify the C-1s, O-1s and N-1s peaks, we selected from the literature the BE of different aliphatic species that resemble the most to our study. The data are shown in **Table III - 3**.

Table III - 3. XPS reference table with C1s, O1s and N1s binding energies of the aliphatic species here investigated.

Atomic core level	Binding energy (eV)	Assignment	Reference
C-1s	286.2-286.7	C-O	Truica-Marasescu F <i>et al.</i> (2008) <i>Plasma Processes and Polymers</i> 5 44
	285.7-286.0	C-N	Shard A G <i>et al.</i> (2004) <i>Journal of Physical Chemistry B</i> 108 12472 F. Pippig <i>et al.</i> (2007) <i>Applied Surface Science</i> 253 6817
	287.6-288.3	C=O	Truica-Marasescu F <i>et al.</i> (2008) <i>Plasma Processes and Polymers</i> 5 44 Briggs D <i>et al.</i> (2003) <i>Surface and Interface Analysis</i> 35 156 Shard A G <i>et al.</i> (2004) <i>Journal of Physical Chemistry B</i> 108 12472
	286	C=O	Jansen R J J and van Bekkum H (1995) <i>Carbon N. Y.</i> 33 1021-7
	286.5	-C-CN	Deniau G <i>et al.</i> (2006) <i>Surf. Sci.</i> 600 675-84

O-1s	532.7	C-O-C H-O-C	López G P <i>et al.</i> (1991) <i>Surf. Interface Anal.</i> 17 267-72
	532.7	C=O	Whelan C M <i>et al.</i> (2004) <i>Thin Solid Films</i> 464 388-92
N-1s	397.8 – 399.0	N=C	Truica-Marasescu F <i>et al.</i> (2008) <i>Plasma Processes and Polymers</i> 5 44 Rangan S <i>et al.</i> (2005) <i>Journal of Physical Chemistry B</i> 109 12899
	399.1-399.6	NH ₂	Truica-Marasescu F <i>et al.</i> (2008) <i>Plasma Processes and Polymers</i> 5 44
	400.3-400.7	NHC=O	Chowdhury A K M S <i>et al.</i> (1999) <i>Surface and Coatings Technology</i> 112 133-139
	400.9-401.7	-NH ₂ /-NH ₃ ⁺	

Polymers with only alcohol- or ether-type oxygens, such as PEG-OH, exhibit C-O BEs ranging from 286.1 to 286.5 eV at the C-1s region and from 532.3 to 533.1 eV at the O-1s spectral region [13] [14] [15]. PEG-OH (**Figure III - 7a** and **b** – upper spectra) presented a C-1s peak centred at 286 eV with a small shoulder at lower binding energy. The peak around 286 eV is characteristic of carbon adjacent to oxygen in an ether environment (CH₂-O) [13]. The small shoulder observed at lower BE may be interpreted as the carbon-carbon bonding from the PEG chain [16]. We observed that the appearance of this small signal depends on the sample preparation (powders or drop casting) and substratum. The O-1s BE of PEG was found at 532.3 eV, which corresponds to C-O-C (ether) and C-O-H (hydroxyl) oxygens [13].

The PtPEG-OH NPs (**Figure III - 7a** and **b** – lower spectra) presented identical XPS signals at the C-1s and O-1s regions compared to those of PEG-OH alone. The slight increases (≤ 0.2 eV) observed in the FWHM at the C-1s and O-1s core levels of nanoparticles (see summary in

Table III - 4) are attributed to a commonly encountered charge compensation difficulty when measuring polymers [17] [18]. In addition, from the reference table the position of aminated carbons (C-N, -C-CN) is found at 286.0 ± 0.5 eV [19] [20] and double-bonded oxygen atoms (C=O) are found at 286 eV (C-1s) and 532.7 eV (O-1s) [21]. An overlapping between the C-N and C=O binding energies and the characteristic C-1s and O-1s peaks may

[13] López G P *et al.* (1991) *Surf. Interface Anal.* **17** 267-72

[14] Truica-Marasescu F and Wertheimer M R (2008) *Plasma Process. Polym.* **5** 44-57

[15] Contarini S *et al.* (1991) *Appl. Surf. Sci.* **51** 177-83

[16] Hong R *et al.* (2005) *Chem. Mater.* **17** 4617-21

[17] Drummond I W *et al.* (1993) *Fresenius. J. Anal. Chem.* **346** 200-4

[18] Pijpers A P *et al.* (1993) *Fresenius. J. Anal. Chem.* **346** 104-9

[19] Jansen R J J and van Bekkum H (1995) *Carbon N. Y.* **33** 1021-7

[20] Deniau G *et al.* (2006) *Surf. Sci.* **600** 675-84

[21] Whelan C M *et al.* (2004) *Thin Solid Films* **464** 388-92

suggest the presence of these chemical structures but the assignment cannot be confirmed considering only XPS data.

The precursor $\text{Pt}(\text{NH}_3)_4\text{Cl}_2$ (**Figure III - 7c** – upper spectrum) presents at 400.2 eV the typical signal of Pt-NH_3^+ [8]. It is well known that nitrogen-containing molecules are not stable during XPS measurement [19], which explains the small shoulder observed at lower BE.

Note that the signal of nitrogen (N-1s) in the case of PtPEG-OH NPs was much lower than C-1s and O-1s (**Figure III - 5**), this is because of the composition of the sample (at similar geometrical cross section). The low nitrogen content made difficult the measurements of the narrow windows. However, in order to decrease radiation damage and related changes in the nitrogen conformation, the average of a few high resolution XPS scans (16) at the N-1s region was used to determine the N-1s BE of the PtPEG-OH NPs. We observe (**Figure III - 7c** – lower spectrum) that the Pt-NH_3^+ BE vanished, indicating an important change on the chemical structure of nitrogen in the surface of the NPs. The PtPEG-OH NPs have a broadening N-1s peak at lower binding energy centered at 398.2 eV. The broadening may indicate the presence of several amine species. The assignment of this peak is very difficult due to the lack of available information. One study interpreted the N-1s chemical shift to lower BE as the direct interaction of nitrogen-containing functional groups with metal surfaces (Fe, Cu and Ni) [22]. Thus, these measurements at the N-1s core level suggest that amine groups strongly interact in proximity of Pt^0 surface, which confers good colloidal stability to NPs. The nature of this interaction (covalent or electrostatic) cannot be completely defined by XPS (see discussion **Section 1.4** – Infrared spectroscopy).

In summary, the XPS data at the C-1s, O-1s and N-1s energy ranges show that Pt^0 NPs are grafted with PEG molecules and suggest a key role of the precursor $-\text{NH}_3^+$ complex ligand in the stability and strength of this Pt-PEG interaction. In addition, some studies addressed the interpretation of the unchanged C-1s and O-1s core levels to PEG molecules that dominate a monolayer configuration at the nanoparticle surface [16] [23] [24] and the unchanged FWHM to a perpendicular grafting of PEG molecules [22]. For instance, with

[8] Contour J P *et al.* (1977) *J. Catal.* **48** 217–28

[16] Hong R *et al.* (2005) *Chem. Mater.* **17** 4617–21

[19] Jansen R J J and van Bekkum H (1995) *Carbon N. Y.* **33** 1021–7

[22] Crispin X *et al.* (2001) *J. Electron Spectros. Relat. Phenomena* **121** 57–74

[23] Forbes L M *et al.* (2011) *J. Mater. Chem.* **21** 15788

[24] Forbes L M *et al.* (2013) *J. Mater. Chem. A* **1** 10267–73

PEG molecules grafted parallel (flat) to the surface, we would expect a broadening of the photopeaks as due to the interaction of carbon and oxygen atoms with the metal (chemisorption) [22].

The XPS studies (binding energies and FWHM) of the PtPEG-OH NPs in comparison with the $\text{Pt}(\text{NH}_3)_4\text{Cl}_2$ precursor, the pure PEG-OH ligand and a Pt^0 solid samples are summarized and presented below (

Table III - 4).

Table III - 4. XPS data summary: BE and FWHM of platinum, carbon, oxygen and nitrogen in different environments ($\text{Pt}(\text{NH}_3)_4\text{Cl}_2$, Pt^0 solid, PEG-OH, and PtPEG-OH NPs).

Compound	Atomic core level	BE (eV)	Assignment	FWHM (eV)
$\text{Pt}(\text{NH}_3)_4\text{Cl}_2$	Pt-4f _{7/2}	73.0	Pt ^{II}	1.7
	Pt-4f _{5/2}	76.3	Pt ^{II}	1.7
	N-1s	400.2	Pt-NH ₃ ⁺	1.6
Pt^0 solid	Pt-4f _{7/2}	71.1	Pt ⁰	1.2
	Pt-4f _{5/2}	74.5	Pt ⁰	1.2
PEG-OH	C1s	286.0	C-O	1.2
	C1s	284.4	C-C	0.8
	O1s	532.3	C-O-H C-O-C	1.3
PtPEG-OH NPs	Pt-4f _{7/2} surf.	70.4	Pt ⁰	1.3
	Pt-4f _{5/2} surf.	73.7	Pt ⁰	1.3
	Pt-4f _{7/2} core	71.2	Pt ⁰	1.6
	Pt-4f _{5/2} core	74.4	Pt ⁰	1.6
	C-1s	286.0	C-O C-N C=O	1.3
		284.3	C-C	1.0
		532.3	C-O-H C-O-C C=O	1.3
	N-1s	398.2	Pt --- NH ₂ ⁻	3.9

1.3.4 Quantitative elemental composition

From the high resolution spectra previously presented, the semi-quantitative XPS elemental composition ($\pm 10\%$) of the PtPEG-OH NPs and their precursors, $\text{Pt}(\text{NH}_3)_4\text{Cl}_2$

and PEG-OH, was determined (**Table III - 5**). The elemental composition was calculated as follow:

$$\% \text{ Element} = \frac{A_E}{A_T} \times 100 \quad \text{Equation III - 8}$$

where A_E is the normalized area of the XPS peak for a given element and A_T is the sum of all the normalized areas. The data were treated applying the respective atomic sensitivity factors and by using the Avantage software (see spectra processing in **Chapter II - Section 2.5.1**).

Table III - 5. XPS and theoretical elemental composition of PtPEG-OH NPs and their precursors.

Sample	% Pt	% N	% Cl	% C	% O	C/O		PEG/Pt	
						XPS	Theoretical	XPS	Theoretical
Pt (NH ₃) ₄ Cl ₂	17	49	34	-	-	-	-	-	-
PEG-OH Mw= 1000 g.mol ⁻¹	-	-	-	66	34	2.00	2.00	-	-
PtPEG-OH NPs	14	<1	<1	57	29	1.96	2.00	6.08	6.20

The measurements are in good agreement with the theoretical evaluation of the composition (from the stoichiometry of the compounds).

1.4 Functional characterization by FTIR

Figure III - 8 shows the FTIR spectra of (a) the native PEG-OH ($M_w = 1000 \text{ g}\cdot\text{mol}^{-1}$), (b) the $\text{Pt}(\text{NH}_3)_4\text{Cl}_2$ complex, (c) the mixture of $\text{Pt}(\text{NH}_3)_4\text{Cl}_2$ with PEG-OH (PEG-OH:Pt molar ratio of *ca.* 100) and (d) the as-synthesized PtPEG-OH NPs obtained after irradiation. We highlight in red new IR bands and in blue those remarkable functional shifts appearing in spectra (c) and (d).

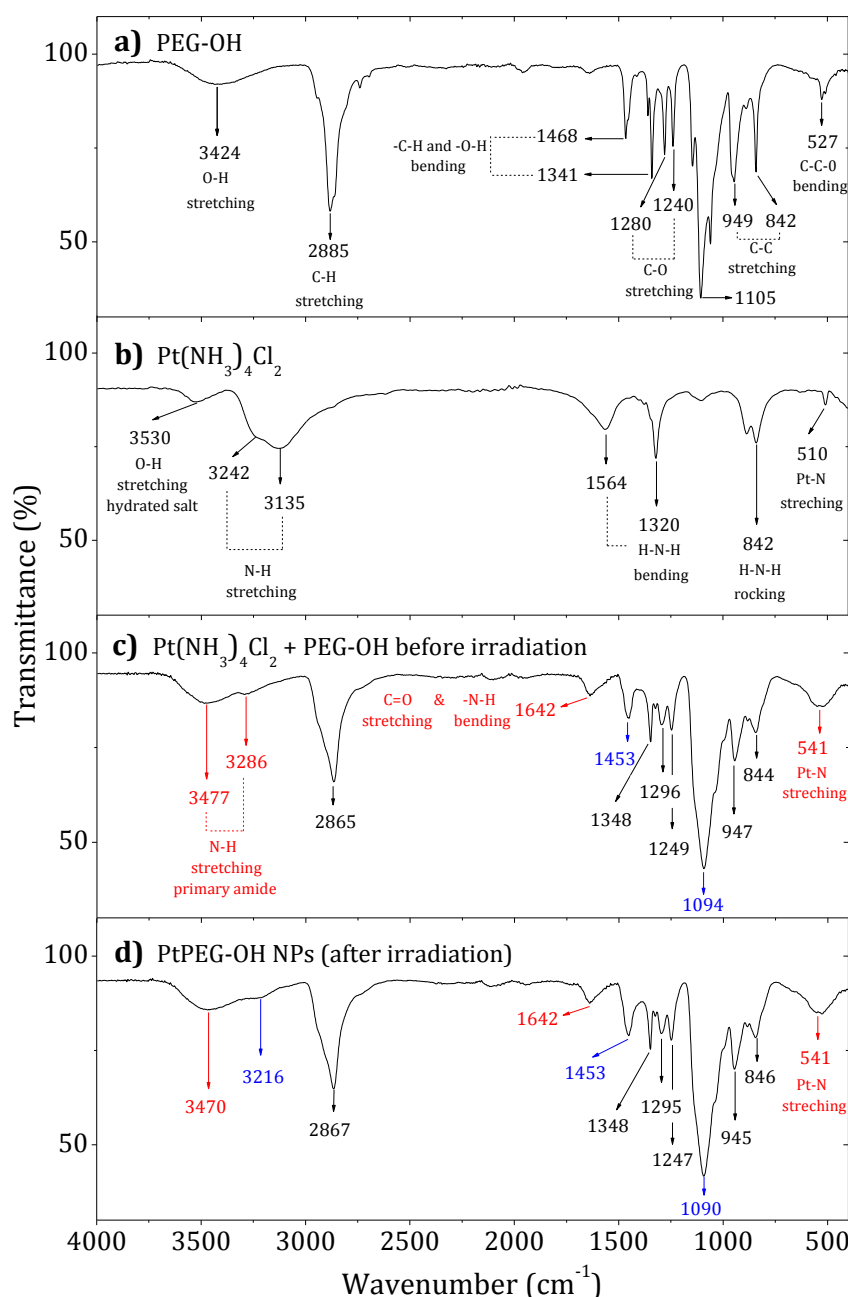
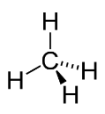
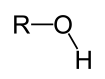
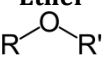
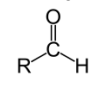
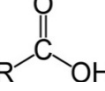
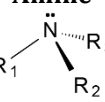


Figure III - 8. FTIR spectra of (a) PEG-OH, (b) Pt^{II} precursor salt, (c) Pt^{II} precursor mixed with PEG-OH (without irradiation) and (d) PtPEG-OH NPs obtained after irradiation of the Pt^{II} precursor and PEG-OH mixture.

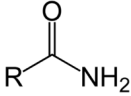
In order to identify the IR bands shown in **Figure III - 8**, the infrared frequencies and vibrational assignments of various functional groups used in this work are summarized in **Table III - 6**.

Table III - 6. Reference table of characteristic infrared absorption frequencies and vibrational assignments of selected organic functional groups. From [25] [26].

Functional Group	Stretching Vibrations			Bending Vibrations		
	Range (cm ⁻¹)	*Int.	Assignment	Range (cm ⁻¹)	*Int.	Assignment
Alkane 	2840-3000	str	C-H CH ₃ , CH ₂ & CH 2 or 3 bands	1350-1480	med	-C-H CH ₂ & CH ₃ deformation
				1370-1390	med	CH ₃ deformation
				720-725	wk	CH ₂ rocking
Alcohol 	3584-3700	var	O-H non-hydrogen-bonded usually sharp	1330-1420	med	-O-H in- plane
	3200-3600	str	O-H H-bonded usually broad	650-770	var	-O-H out-of-plane
	1000-1260	str	C-O			
	800-900		C-C aliphatic alcohol			
Ether 	1000-1300	str	C-O			
	1070-1150	str	C-O aliphatic ether			
Aldehyde 	2695-2830 2 bands	med	=C-H	1350-1360	str	-C-H α-CH ₃
	1720-1740	str	C=O	1400-1450	str	-C-H α-CH ₂
Carboxyl acid 	2500-3300 overlap C-H	str	O-H very broad	1395-1440	med	C-O-H
	1705-1720	str	C=O H-bonded	590-700	str	O-C=O
	1210-1320	med-str	C-O			
Amine 	3400-3500 dil. soln.	wk	N-H primary amines 2 bands	1580-1650	var	-N-H primary amines scissoring
	1020-1250	med	C-N	660-910	var	-N-H NH ₂ & NH wagging shifts with H-bonding

[25] Silverstein R M *et al.* (1991) *Spectrometric identification of organic compounds* (Wiley)

[26] Lambert J B (1987) *Introduction to organic spectroscopy* (Macmillan)

<p style="text-align: center;">Amide</p> 	1630-1690 overlap -N-H	str	C=O	535-615	str	C=O out-of-plane
	3100-3500 overlap O-H	med	N-H primary amides two peaks	1620-1655	med	-N-H NH ₂ and NH
	1400-1420	med	C-N primary amides	660-800	med	-N-H broad out-of-plane wagging

*Intensity: strong (str), variable (var) and weak (wk)

Figure III - 8a shows the IR spectrum of the native PEG-OH, it is in agreement with the literature [27]. Briefly, the signal observed at 3424 cm⁻¹ corresponds to the hydroxyl stretching mode $\nu_{\text{O-H}}$ of the bonded hydrogen in PEG chains. The peak centered at 2885 cm⁻¹ is characteristic of the alkyl stretching mode ν_{CH_2} . The peaks in the region from 1000 to 1300 cm⁻¹ are characteristic of the stretching vibrational modes of ether ($\nu_{\text{C-O}}$).

Figure III - 8b corresponds to the infrared spectrum of the Pt(NH₃)₄Cl₂ precursor. It displays bands at 3242 and 3135 cm⁻¹ attributed to the asymmetric and symmetric vibrational N-H stretching modes ν_{NH_3} . From 1564 to 842 cm⁻¹ the bending and rocking vibrational modes δ_{HNNH} and ρ_{NH_3} are observed. The IR band at 510 cm⁻¹ is due to the Pt-N stretching mode [28].

Figure III - 8c displays the IR spectrum of a mixture containing Pt(NH₃)₄Cl₂ and PEG-OH before irradiation (colorless solution **Figure III - 1a**). This spectrum is different from the addition of the spectra (a) and (b). All the NH₃⁺ vibrational modes of the platinum complex disappeared and new IR bands appeared. This indicates that a reaction between the two precursors took place. Briefly:

- The two new peaks observed at 3477 and 3286 cm⁻¹ are characteristic of the N-H stretching mode ν_{NH} of an amide functional group (see **Table III - 6**).
- In addition, we observe an IR band at 1642 cm⁻¹, which may be attributed to the C=O stretching vibrational mode of primary amides [25]. This signal overlaps the 1620 to 1655 cm⁻¹ region which corresponds to the N-H bending vibrational mode of this functional group.

[25] Silverstein R M *et al.* (1991) *Spectrometric identification of organic compounds* (Wiley)

[27] Krishnan K and Krishnan R S (1966) *Proc. Indian Acad. Sci. - Sect. A* **64** 111-22

[28] Nakamoto K (2009) *Infrared and Raman spectra of inorganic and coordination compounds*. (Wiley)

- Finally the IR signal at 1453 cm^{-1} may be attributed to the C-N stretching mode ν_{CN} of primary amides although it is shifted by 11 cm^{-1} . This can be explained by the overlap with the CH_2 bending mode δ_{HCH} of PEG at 1468 cm^{-1} .

Hence, all these new features converge and indicate the formation of a primary amide functional group. This statement is confirmed by the observation of the peak centered at 541 cm^{-1} corresponding to the Pt-N bond [29]. This peak is broadened due to overlapping the $535 - 615\text{ cm}^{-1}$ region of the C=O bending vibrational mode of amide.

In summary, this IR analysis demonstrates the reaction of the two precursors by conjugation of the PEG-OH chains with $(\text{Pt}(\text{NH}_3)_4)^{2+}$ to form an amide linker. The resulting intermediate species, formed before irradiation, is illustrated in **Figure III - 9**.

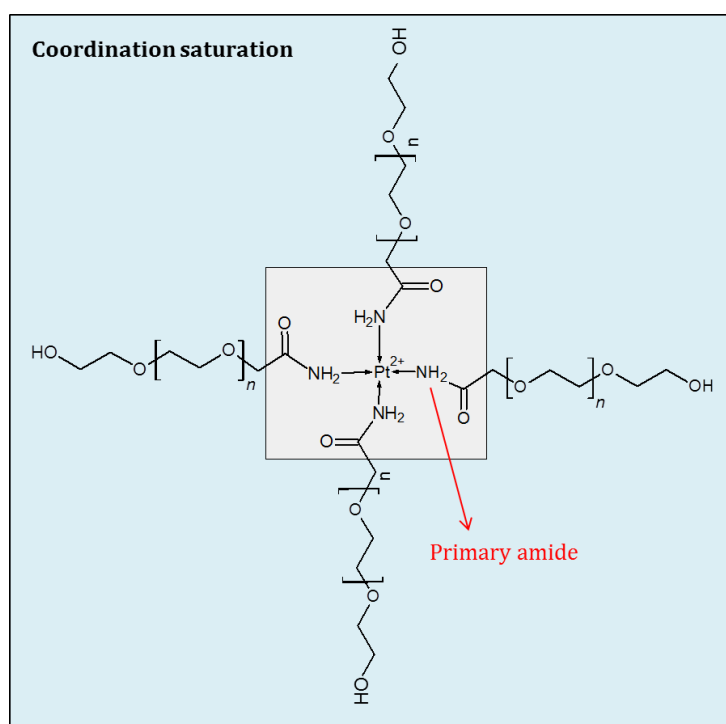


Figure III - 9. Proposed Pt^{II}-PEG conjugation before irradiation.

To explain the way the precursors react to form an amide linker, we propose the hypothesis that PEG-OH must be activated before reacting with the $-\text{NH}_3^+$ ligand of the platinum precursor. The simplest method to form an amide is by coupling a carboxyl group (C=O) with an amine group ($-\text{NR}_2$). In the present case:

[29] Wysokiski R et al. (2006) *J. Mol. Structure THEOCHEM* 758 169-79

- PEG-OH is initially activated forming an aldehyde-end group (-CHO). In the presence of oxygen, this activation takes place due to the dehydrogenation (oxidation) of the hydroxyl-end group of PEG by:

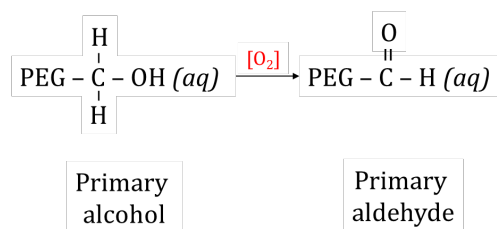


Figure III - 10. Dehydrogenation of a primary alcohol to form an active primary aldehyde.

The oxidation of alcohols and thus of PEG-OH is thermodynamically favorable [30]. However, in this work we suggest that the reaction is catalyzed at room temperature by platinum [31] [32] [33]. Primary alcohols can be oxidized to aldehydes or further to carboxylic acids (-COOH), which may react with the platinum precursor. However, little is known about the proportion of these species after PEG-OH oxidation.

- The formed PEG aldehyde-end group then reacts preferentially with ammonium [34] to form a primary amide as follows:

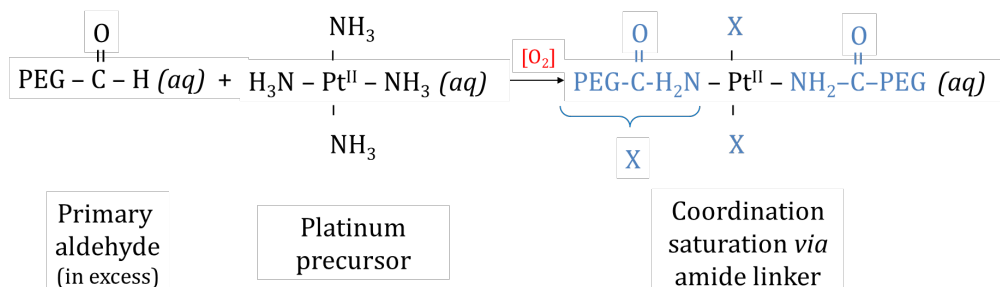


Figure III - 11. Formation of the intermediate specie before irradiation *via* amide linker.

Hence, an initial conjugation shell is formed through **Figure III - 10** and **Figure III - 11**.

When the above-illustrated intermediate species are irradiated, we obtain the IR spectrum of **Figure III - 8d** that corresponds to the spectrum of the as-synthesized PtPEG-OH NPs

[30] Glastrup J (1996) *Polym. Degrad. Stab.* **52** 217–22

[31] Chibani S *et al.* (2013) *Catal. Sci. Technol.* **3** 339–50

[32] Mallat T and Baiker A (1994) *Catal. Today* **19** 247–83

[33] Anderson R *et al.* (2003) *Adv. Synth. Catal.* **345** 517–23

[34] Cox Gad S (2007) *Handbook of Pharmaceutical Biotechnology* (John Wiley & Sons, Inc.)

(brownish solution **Figure III - 1a**). Only minor changes are observed after irradiation because the bonds visible by IR remain unchanged (*e.g.* C-O, C=O, O-H and N-H).

In conclusion, this is the first evidence that PEGylated platinum NPs are successfully produced by radiolysis. Very interestingly, we demonstrated that the controlled nucleation and growth take place *via* the formation of stable PEGylated intermediate species. These IR results are in good agreement with XPS measurements, addressing a strong Pt⁰-PEG interaction, which may depend on the -OH end-group activation and the reactivity of the platinum complex ligand (-NH₃⁺). Recently, Wand *et al.* suggested that the functionalization of small Pt NPs with amines may occur preferentially by Pt-H-N moieties or electrostatic interactions [35] (see proposed interactions in **Figure III - 15** adapted from [35]), which supports our spectroscopic findings (broadened N-1s XPS peak and Pt-N IR signal).

[35] Wand P *et al.* (2016) *J. Colloid Interface Sci.* **478** 72–80

1.5 Stability in biological relevant media

Firstly, we studied the stability of PtPEG-OH NPs (PEG-OH:Pt *ca.* 100) by measuring at room temperature the d_H and ζ -potential of nanoparticles at pH ranging from 3 up to 11 (**Section 1.5.1**). Then, the influence of time post dilution preparation was investigated in different solvents by measuring the d_H (**Section 1.5.2**) of NPs at 37°C. Thus, the stability of PtPEG-OH NPs was determined by d_H , ζ -potential and visual observation of turbidity.

1.5.1 Influence of pH in NaCl

PtPEG-OH NPs were diluted in NaCl as described in **Chapter II – Section 2.3.2** at a final Pt concentration of 5×10^{-4} mol.L⁻¹. **Figure III - 12** shows the evolution of the d_H (blue) and ζ -potential (red) of PtPEG-OH NPs as function of pH.

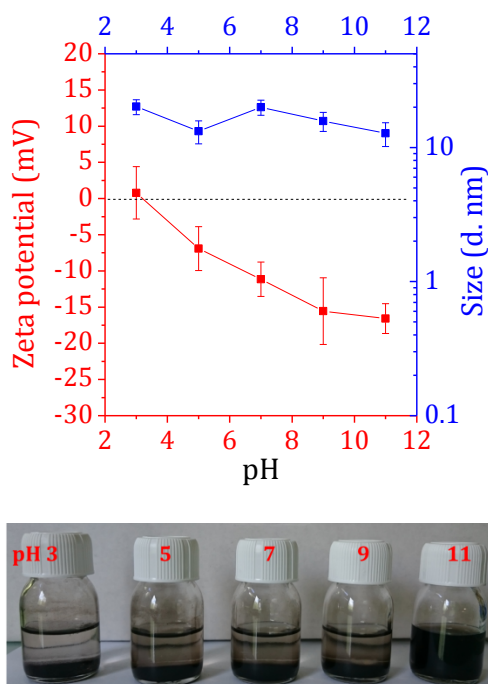


Figure III - 12. Evolution of the hydrodynamic diameter (in blue) and ζ -potential (in red) versus pH for PtPEG-OH NPs suspensions at a Pt concentration of 5×10^{-4} mol.L⁻¹.

We observe that the d_H of the nanoparticles remained almost constant in the entire pH range (in blue), with values ranging from 12 up to ~20 nm.

The PZC or isoelectric point is observed at pH 3 (in red). These results reflect the good stability of PtPEG-OH NPs at the pH of intracellular fluids (usually from 6.8 to 7.4). The negative ζ -potential is attributed to the -OH functional end-group of the PEG coating (pKa

=16) [36]. The PEG coating favours steric repulsion between particles, reducing thus their aggregation state. More interesting, the observation of a negative ζ -potential for all pH values, together with the size analysis, shows that the PEG molecules remain thereby grafted at all pH.

It is worth mentioning that the solutions did not present any turbidity. However, nanoparticles stored at room temperature precipitated one month later with exception of the nanoparticles suspension at pH 11, which corresponds to the most negatively charged and thus more stable suspension (red curve picture **Figure III - 12**).

These measurements show that in the proximity of cells, where the pH decreases from about 7 to 6, the ζ -potential of these PtPEG-OH NPs may vary slightly (-10 to -12mV) by keeping their d_H constant. This is different from the work of W. Rima *et al.* showing that gadolinium based NPs, with a PZC of ~ 6.6 , are strongly influenced at the proximity of the cell membrane [37], property that strongly defines the internalization pathway of NPs.

1.5.2 Stability in different solvents

The stability of PtPEG-OH NPs with a Pt concentration of $5 \times 10^{-4} \text{ mol.L}^{-1}$ was evaluated over time by measuring the d_H of NPs immediately and 1, 3, 6 and 22 h after samples preparation. This was studied for PtPEG-OH NPs (PEG-OH:Pt *ca.* 100) diluted in water, PBS buffer, NaCl and TE buffer. The measurements were performed at 37°C to mimic biological conditions. **Figure III - 13** shows the variation of d_H as function of time.

[36] Benyettou F *et al.* (2012) *J. Bioanal. Biomed.* **4** 39–44

[37] Rima W *et al.* (2013) *Biomaterials* **34** 181–95

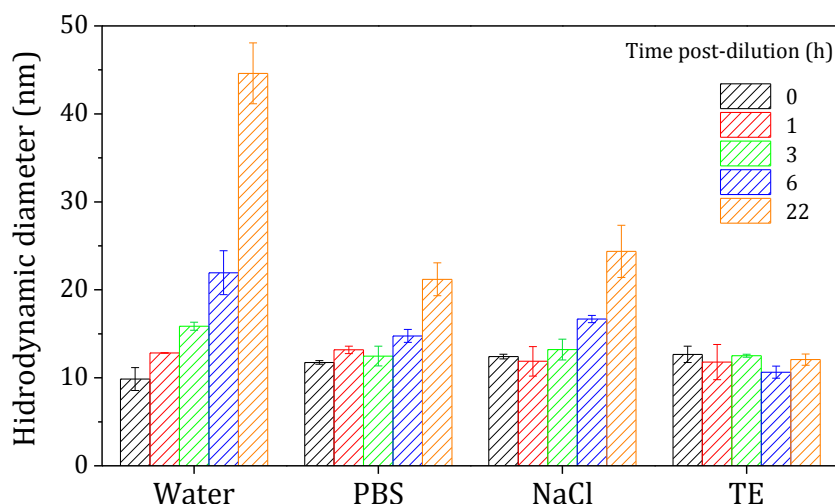


Figure III - 13. Evolution of the d_H of PtPEG-OH NPs in; water, PBS, NaCl and TE buffer, after 0, 1, 3, 6 and 22 h (Pt concentration of 5×10^{-4} mol.L $^{-1}$).

Firstly, we observe that NPs diluted in water at 37°C are not stable for more than 3h (increase of their d_H from ~ 10 up to 15 nm and 45 nm after 22 h). However, they are more stable in buffers such as PBS, NaCl and TE. NPs are very stable in TE. Indeed their d_H remains unchanged for more than 22h at 37°C. This, due to a screening effect between the NPs and molecules that compose the buffer (Tris and EDTA) [38].

Non-significant variation of the PDI value was observed (from 0.21 to 0.33 ± 0.01), exhibiting the homogeneity of solutions.

We performed the same experiment using enriched DMEM as buffer in order to reproduce the conditions that are used in cell studies. However, aggregates were found after 6 hours with similar results found for DMEM alone, showing the limitation of the technique to characterize NPs suspensions in complex media.

[38] Pfeiffer C et al. (2014) *J. R. Soc. Interface* **11** 20130931–20130931

1.6 Conclusion

In this chapter, I presented the advantageous and unique synthetic route to prepare non-toxic and sterilized solutions of PEGylated platinum nanoparticles, ready-to-use for biomedical applications. In addition, I described the new approach and methods that I established in the group to characterize NPs. These methods will be further used in the group for the development of novel potential nano-agents.

Table III - 7 summarizes the main characteristics of the new PtPEG-OH NPs. To compare with other NPs tested by the group as potential nano-radioenhancer to improve the effects of hadrontherapy, the main features of PtPEG-OH NPs are presented together with those of Au-DTDTPA NPs. The data presented here for Au-DTDTPA NPs were obtained and transmitted by our collaborator Gloria Jiménez Sánchez, PhD student at the University of Franche-Comté (Besançon, France) supervised by Prof S. Roux.

Table III - 7. Main characteristics of the new PtPEG-OH NPs in comparison with Au-DTDTPA NPs.

	PtPEG-OH NPs	Au-DTDTPA NPs
Plasmon resonance wavelength (nm)	Shoulder centered at 270	Shoulder 510-530
TEM diameter (nm)	3.2 ± 0.8	2.4 ± 0.5
Metallic surface atoms	372 ± 224	~233
Hydrodynamic diameter (nm)	8.8 ± 3.1	6.6 ± 3.1
Zeta potential (mV)	$-16.6 \pm 5.1^*$	-31.4**
pH PZC	3	3
Anchoring ligand	-NH ₃	-SH
Linking group	-OH	-COOH
Surface ligand	PEG	DTDTPA

*measured at pH 6.20 (the as-synthesized conditions in water)

**measured at pH 7.22

In conclusion, I succeeded in the synthesis of small metallic platinum NPs grafted with PEG-OH. **Figure III - 14** summarizes the novel radiolytic-PEGylation method developed in this work, which together with **Figure III - 15** illustrates the NPs I obtained.

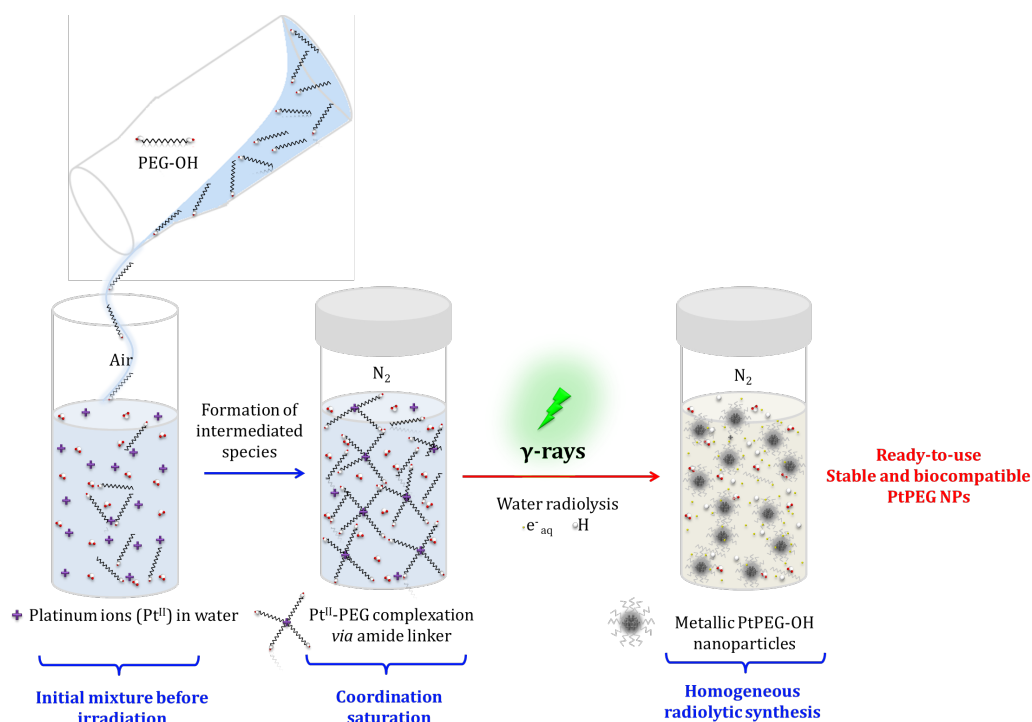


Figure III - 14. Scheme of the novel radiolytic-PEGylation method to synthesize biocompatible PtPEG-OH NPs.

Figure III - 15 shows a model deduced from the physico-chemical characterization of NPs. Concerning the mechanisms of synthesis, my study established that Pt^{II} is coordinated with PEG-OH prior to irradiation. However, this is the water radiolysis that is used to initiate the reduction, nucleation and growth steps of the NPs in the entire reactive volume. At the end, ready-to use, stable and biocompatible PtPEG-OH NPs are prepared by a simple, reproductive and environmentally friendly method.

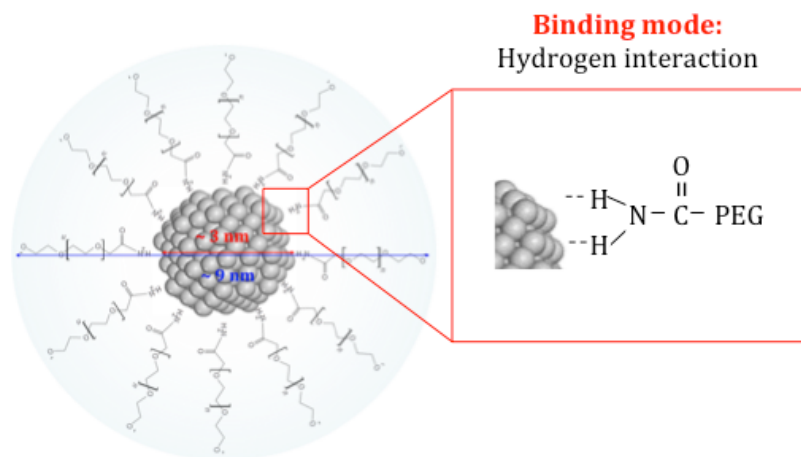


Figure III - 15. Illustration of the resulting PtPEG-OH NPs conformation.

2. Biological impact of nanoparticles

A multi-scale approach was used to evaluate the capacity of the PtPEG-OH NPs to enhance radiation toxicity (called radio-enhancement effect - REE). In this approach, cellular and molecular models were used (see materials and methods in **Chapter II – Section 4**) to describe not only the biological impact of radiation activated NPs but also the physico-chemical processes that take place in a nanometric volume.

In **Section 2.1**, we present for the first time the impact of PtPEG-OH NPs with living cells. It shows the cytotoxicity of PtPEG-OH NPs in **Section 2.1.1** followed by the uptake and intracellular localization of NPs in **Section 2.1.2** and **2.1.3**. The effect of nanoparticles on the radiation induced cell killing is discussed in **Section 2.2**.

In **Section 2.3**, we present the effect of PtPEG-OH NPs to amplify the induction of nanosize damages using the bio-nanoprobe (plasmid DNA).

2.1 Interaction of NPs with human cells – toxicity, uptake and localization

2.1.1 Cytotoxicity evaluation

We evaluated the cytotoxicity of PtPEG-OH NPs in HeLa and U87-MG cells by CFA (see methodology **Chapter II – Section 4.1.3**). We performed these studies at two different PtPEG-OH NPs concentrations.

Figure III - 16 shows the PE of HeLa cells without NPs (control) and of cells incubated for 6 h with 5×10^{-4} and 10^{-3} mol.L⁻¹ PtPEG-OH NPs. Since NPs are diluted in water, we disentangled the influence of water from the effect of NPs by measuring the PE of cells incubated with water (10 % of the total volume).

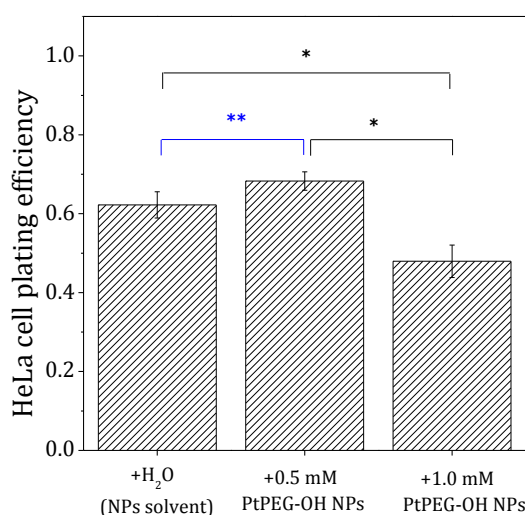


Figure III - 16. Survival fraction of HeLa cells in the presence of water or incubated with PtPEG-OH NPs. The results are presented as means \pm Standard Deviation (SD), statistically analysed using one-way ANOVA (Turkey test: * $p < 0.05$ and ** $p > 0.05$).

By comparing the PE of the control (+H₂O) with the PE of cells incubated with 5×10^{-4} mol.L⁻¹ PtPEG-OH NPs, we observed similar PE values ($\sim 65\%$). This indicates that at this concentration there is not toxicity associated to the addition of PtPEG-OH NPs ($p = 0.4227$). However, a significant cytotoxicity ($\sim 23\%$ less PE) was found at 10^{-3} mol.L⁻¹ ($p = 0.02113$).

Similarly, we found that 5×10^{-4} mol.L⁻¹ PtPEG-OH NPs are non-toxic for U87-MG cells. The PE of U87-MG cells in the control and in the presence of PtPEG-OH NPs was $\sim 5\%$.

The non-toxic conditions (PtPEG-OH NPs 5×10^{-4} mol.L⁻¹; 6h incubation time) were thus used in all the experiments that follow.

2.1.2 Cell uptake

We quantified the uptake of 5×10^{-4} mol.L⁻¹ PtPEG-OH NPs in HeLa and U87-MG cells, by ICP-OES and ICP-MS, and we investigated the influence of the incubation time on the cell uptake. For comparison, we also measured the uptake of Au-DTDTPA NPs (provided by Gloria Jiménez Sánchez, PhD student with Prof. Stéphane Roux at the University of Franche-Comté, Besançon, France).

2.1.2.1 Quantification of the cell uptake

ICP spectroscopies measure the quantity of defined elements in a sample. These measurements were performed on cells gently rinsed with PBS after NPs incubation (see samples preparation in **Chapter II – Section 4.1.5.1**). Thus, the quantified metal comes from NPs internalized or at least strongly attached to the cell membrane. The internalization of NPs is confirmed by performing cellular imaging (see intracellular distribution in **Section 2.1.3**).

Table III - 8 shows the quantitative data obtained by ICP-OES for PtPEG-OH and Au-DTDTPA NPs incubated 6h with HeLa and U87-MG cells.

Table III - 8. Uptake of PtPEG-OH and Au-DTDTPA NPs in HeLa and U87-MG cells after 6h incubation.

Cell line	Metal NP	Mass (µg)	pg/cell	mol/cell (x10 ⁻¹⁶)	NPs/cell (x10 ⁵)	NPs/µm ³
HeLa	Pt	0.495	0.168	8.601	5.178	241
	Au	0.100	0.044	2.226	3.261	152
U87-MG	Pt	1.225	0.742	38.06	22.91	750
	Au	0.291	0.113	5.716	8.372	274

The measurement gives the mass of metal contained in *ca.* 2×10^6 cells (see column 3 in **Table III - 8**). Hence, we calculated the concentration of metal (mass and mole) per cell (columns 4 and 5).

The NPs are composed of 1000 Pt atoms (~ 3.2 nm) and 411 Au atoms (~ 2.4 nm) respectively (see values **Table III - 7**). The number of NPs per cell was then determined as follows:

$$\frac{\# \text{ NPs}}{\text{cell}} = \frac{\text{mol NPs}}{\text{cell}} \times N_A$$

Equation III - 9

where N_A is the Avogadro constant ($6.022 \times 10^{23} \text{ mol}^{-1}$). The data are reported in column 6 **Table III - 8**.

The diameter of cells in suspension was measured with a LUNA cell counter (trypan blue staining). HeLa cells presented an average diameter of $16 \mu\text{m}$ and U87-MG of $18 \mu\text{m}$. Thus, we determined the density of NP per volume unit (see column 7 in **Table III - 8**) as follows:

$$\text{Density} \left[\frac{\text{NPs}}{\mu\text{m}^3} \right] = \frac{\# \text{ NPs}}{\text{cell}} \times \frac{3}{4\pi r_{\text{cell}}^3}$$

Equation III - 10

Note that the rate of platinum internalized in cells (0.495 and $1.225 \mu\text{g}$ in HeLa and U87-MG cells respectively) is very low (0.06 to 0.153% of the initial $798 \text{ Pt } \mu\text{g}$). These low values may be explained as: i) an effect of the experimental incubation conditions (2D culture, volume of medium and number of cells) and ii) the remarkable stability of NPs suspensions (pH PZC ~ 3). Interestingly, these values are higher than the cell uptake rate found for Au-DTDTPA NPs (0.006 to 0.018%). This comparison shows that, for the same experimental conditions, the uptake efficiency of PtPEG-OH NPs is *ca.* 10 times higher than the uptake of Au-DTDTPA NPs.

In **Figure III - 17a** we observe that the internalization of nanoparticles in U87-MG is higher than that in HeLa cells. Indeed, close to 4.4 times more Pt per cell is detected in U87-MG cells, compared to 2.6 times for Au.

Stated differently the NPs density (see **Figure III - 17b**), defined by the number of internalized NPs per μm^3 , is about 1.6 times higher for PtPEG-OH NPs than for Au-DTDTPA NPs in HeLa and 2.7 in U87-MG cells.

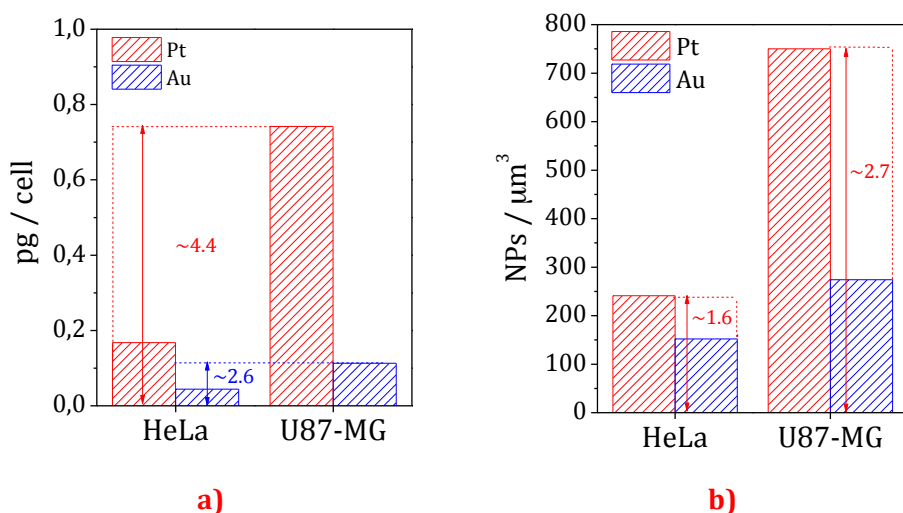


Figure III - 17. (a) Mass of the metal per cell and (b) density of internalized nanoparticles (NPs/ μm^3) in HeLa and U87-MG cells.

In summary, we established that the uptake of NPs is strongly cell line dependent. This experiment also shows the strong dependence of the uptake as a function of the NP type and their surface composition (coating ligand and ζ -potential). Finally, the higher uptake found for PtPEG-OH NPs suggests that these NPs are promising and test *in vivo* should be envisaged. A study is currently in progress in the group to further explore the uptake of metallic NPs in several cell lines.

2.1.2.2 Influence of the incubation time on the cell uptake

We performed ICP-MS measurements in HeLa cells incubated with $5 \times 10^{-4} \text{ mol.L}^{-1}$ PtPEG-OH NPs for 6 h and 24 h. The samples were prepared as presented in **Chapter II – Section 4.1.5**. The results are shown in **Table III - 9**.

Table III - 9. Uptake of PtPEG-OH NPs in HeLa cells after 6 h and 24 h of incubation.

Inc. time (h)	Mass (μg)	Cells ($\times 10^6$)	pg/cell	mol/cell ($\times 10^{-16}$)	NPs/cell ($\times 10^5$)	NPs/cell μm^3
6	5.06 ± 0.04	3.16	1.60	81.82	49.26	2297
24	5.71 ± 0.01	4.64	1.23	63.22	38.06	1775

Surprisingly, the mass measured with ICP-MS for $5 \times 10^{-4} \text{ mol.L}^{-1}$ PtPEG-OH NPs incubated during 6h with HeLa cells is *ca.* 10 times higher than the values obtained with ICP-OES (**Table III - 8**). With ICP-MS we found 0.45% of the total initial platinum content. This difference may be due to the technique sensitivity or to difference in the HeLa cell culture

(cell generation). Nonetheless, the comparison between the ICP-MS results obtained at 6 and 24 h of incubation indicates that the NPs uptake does not increase significantly with the incubation time.

2.1.3 Intracellular distribution of NPs

The intracellular distribution of NPs was investigated by NanoSIMS and TEM (see experimental conditions in **Chapter II – Section 4.1.5**). NanoSIMS has a lower spatial resolution but it allows chemical analysis of the elements. TEM analysis has better spatial resolution but it requires high quality and accuracy of sample preparation. The two methods have been explored.

2.1.3.1 NanoSIMS analysis

NanoSIMS experiment for the detection of platinum in cells was optimized before in the group [39]. In the present study, the cells were prepared by cryo-fixation. Only HeLa cells loaded with PtPEG-OH NPs were analyzed.

The first step consisted on the calibration of the mass spectrometer and the identification of the platinum isotopes (see method in **Chapter II – Section 4.1.5.2**). In this case, the stable isotope platinum-194 with its natural occurrence (33%) was used as the isotopic marker of PtPEG-OH NPs. The *in situ* calibration was performed by measuring the mass spectrum of a pure platinum surface used as reference. The mass spectrum of HeLa cells loaded with PtPEG-OH NPs (prepared as described in **Chapter II – Section 4.1.5.2**) was performed and compared to the reference.

Figure III - 18 shows the mass spectrum of the reference (black) and the HeLa Pt-containing sample (blue).

[39] Usami N *et al.* (2008) *Int. J. Radiat. Biol.* **84** 603–11

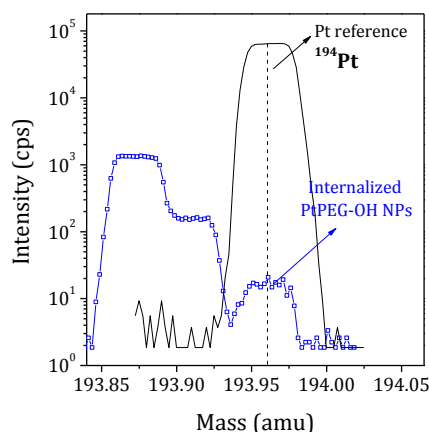


Figure III - 18. Mass spectra recorded by NanoSIMS from a platinum reference (—) and from HeLa cells loaded with PtPEG-OH NPs (—).

These measurements clearly demonstrate the presence of the ¹⁹⁴Pt isotopic marker in HeLa. The species at lower atomic masses were not characterized. These species did not interfere with the ¹⁹⁴Pt band found in the cell.

After calibration and identification of platinum in the cells, we investigated the intracellular distribution of PtPEG-OH NPs through the imaging mode of the NanoSIMS.

Figure III - 19 shows the Nano-SIMS imaging analysis performed on a HeLa cell loaded with PtPEG-OH NPs. Images were collected for the CN⁻, P⁻ and ¹⁹⁴Pt⁻ ions. It is noteworthy to mention that the images were collected simultaneously from the same sputtered micro volume of a square frame of 50 μm x 50 μm.

The morphological cell structure was derived from the CN⁻ and P⁻ images. **Figure III - 19a** shows the distribution of carbon and nitrogen containing molecules, an indication of organic matter such as nucleic acids and proteins. **Figure III - 19b** shows the phosphorus distribution. It is used to distinguish the cell nucleus due to its high phosphorus content (DNA). **Figure III - 19c** shows the distribution of platinum compounds (¹⁹⁴Pt⁻). Finally, **Figure III - 19d** presents the merged image of ¹⁹⁴Pt and P⁻.

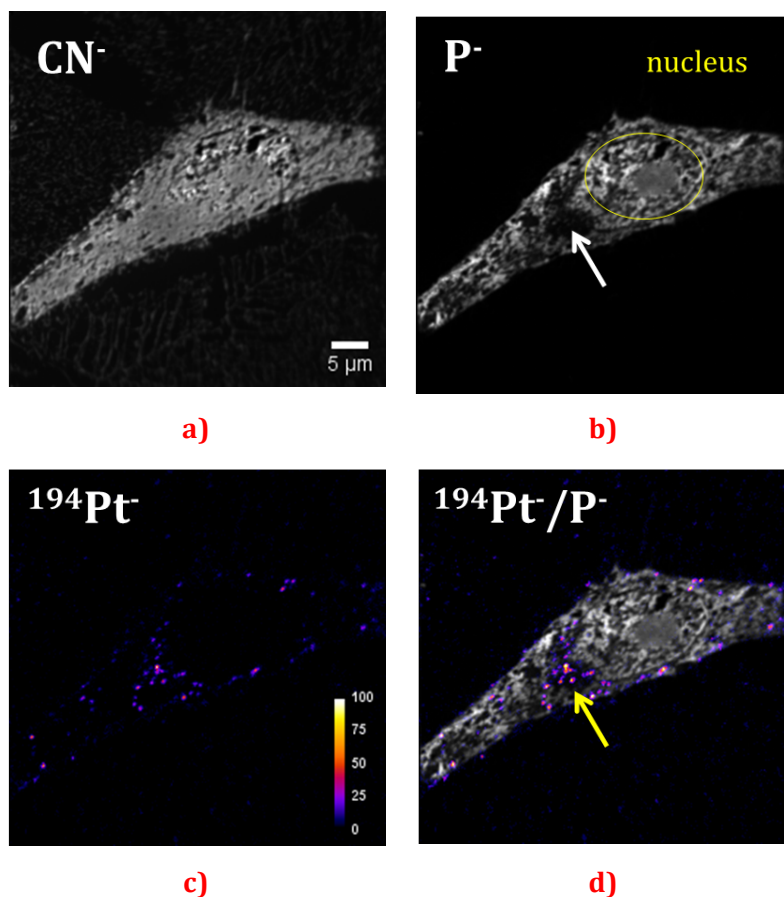


Figure III - 19. Nano-SIMS images of a HeLa cell loaded with PtPEG NPs. Panels a, b, and c correspond to CN⁻, P⁻ and ¹⁹⁴Pt⁻ respectively. Panel d is the merged image of ¹⁹⁴Pt⁻ and P⁻. The arrows show an identified low concentration P⁻ region in the cell cytoplasm.

This analysis clearly demonstrated the presence of platinum inside the cell. In particular, we observe that PtPEG-OH NPs are localized in the cytoplasm (**Figure III - 19d**) and not observed in the nucleus. This is in agreement with other works performed by the group with platinum complexes [39] and other studies with metal-containing NPs [40] [41] [42]. The analysis also showed that PtPEG-OH NPs are preferentially accumulated at cytoplasmic sites found low in phosphorus concentration (region pointed with an arrow). This has been already observed in other works where ¹⁵N-labeled peptide vectors co-localize HeLa cytoplasmic zones with low phosphorous concentration [43].

-
- [39] Usami N *et al.* (2008) *Int. J. Radiat. Biol.* **84** 603–11
 [40] Rima W *et al.* (2013) *Biomaterials* **34** 181–95
 [41] Jain S *et al.* (2011) *Int. J. Radiat. Oncol. Biol. Phys.* **79** 531–9
 [42] Shah N B *et al.* (2011) *Mol. Pharm.* **8** 176–84
 [43] Romer W *et al.* (2006) *Appl. Surf. Sci.* **252** 6925–30

We found some difficulties on the embedding process during samples preparation and thus as already discussed in **Chapter II – Section 4.1.5.2**, complementary statistical studies are in process.

2.1.3.2 TEM imaging

We performed TEM imaging to provide intracellular distribution of PtPEG-OH NPs with better resolution. Moreover, TEM allows elucidating the NPs uptake mechanism(s). HeLa cells samples were prepared by cryo-fixation or by chemical fixation. U87-MG cells samples were only prepared by chemical fixation (see samples preparation **Chapter II – Section 4.1.5**).

For a better understanding on the possible uptake mechanisms, **Figure III - 20** introduces different pathways involved in the internalization of nano-agents with variable physico-chemical characteristics.

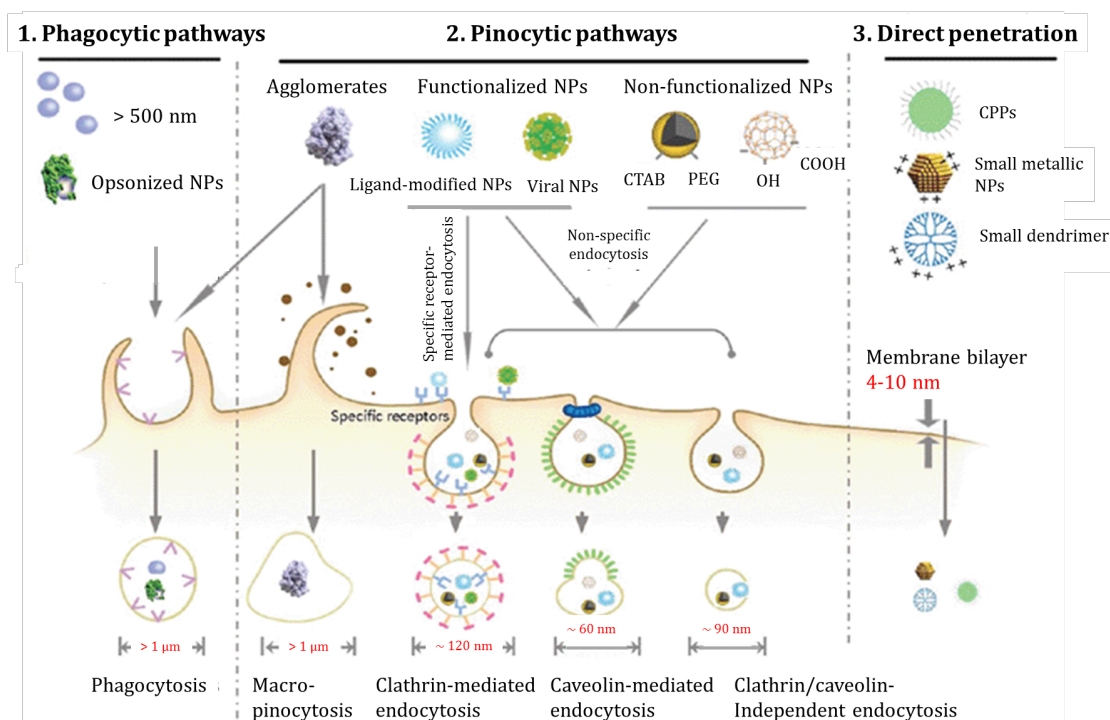


Figure III - 20. Illustration on the cellular uptake of particles. Adapted from [44]

Briefly, big (>500 nm) and opsonized NPs (deposition of immunoglobulins on the NP surface [45]) can be internalized by phagocytosis (#1 in **Figure III - 20**), which is the

[44] Mao Z *et al.* (2013) *Biomater. Sci.* **1** 896–911

[45] Bandyopadhyay A *et al.* (2015) *Nanoparticles in Lung Cancer Therapy - Recent Trends*

process by which cells internalize matter larger than around 1 μm in diameter. The pinocytic pathways are divided into: i) macro-pinocytosis, ii) clathrin-, iii) caveolin-mediated and iv) independent endocytosis (#2 in **Figure III - 20**). These processes involve the uptake of matter with a size of ~ 100 nm in diameter [46], such as NPs aggregates, functionalized and non-functionalized NPs. The macropinocytosis is the invagination of the cell membrane to form a pocket, which then pinches off into the cell to form a vesicle (0.5–5 μm in diameter) filled with a large volume of extracellular fluid and molecules. It can be mediated by pseudopodial extensions [47]. An endosome may be found in two main states: as an early endosome, which by being the first state of the endocytic pathway is often located in the periphery of the cell, and as a late endosome that travels into the cytosol and fuses with lysosomes. Lysosomes are the last compartment of the endocytic pathway. They are acidic (pH ~ 4.8) with a diameter of about 1 to 2 μm [48]. The last uptake mechanism (#3 in **Figure III - 20**) is the direct penetration, commonly named as passive diffusion. It involves the internalization of external substances across the cell membrane without need of energy input. This mechanism depends on the permeability of the cell membrane (lipid bilayer), size and charge of the substances. This pathway dominates in the uptake of small NPs.

a) [TEM imaging of HeLa cells after cryo-fixation](#)

Figure III - 21 shows some representative TEM images recorded from HeLa samples prepared as for NanoSIMS analysis. Panel **(a)** shows a HeLa cell at a magnification that allows observation of the cytoplasm. The weak contrast here found did not permit a clear identification of the nucleus. However, we analyzed regions close to the cells membrane to elucidate the nanoparticles internalization pathway(s). For instance, panels **(b)** and **(c)** correspond respectively to magnifications of the squared regions (1 & 2) in panel **(a)**. In panel **(b)**, we particularly observe cell membrane projections, known as pseudopods, which are commonly involved in the process of nutrients ingestion. Here, we observe that the pseudopods do not interfere with the uptake of the electron dense objects. Hence, we hypothesize that the NPs uptake takes place *via* passive diffusion. Interestingly, panel **(c)** shows isolated electron dense objects and some aggregates in the cell cytoplasm.

[46] Marsh M and Marsh M (2001) *Endocytosis* (Oxford University Press)

[47] Falcone S *et al.* (2006) *J. Cell Sci.* **119** 4758–69

[48] Gruenberg J and Maxfield F R (1995) *Curr. Opin. Cell Biol.* **7** 552–63

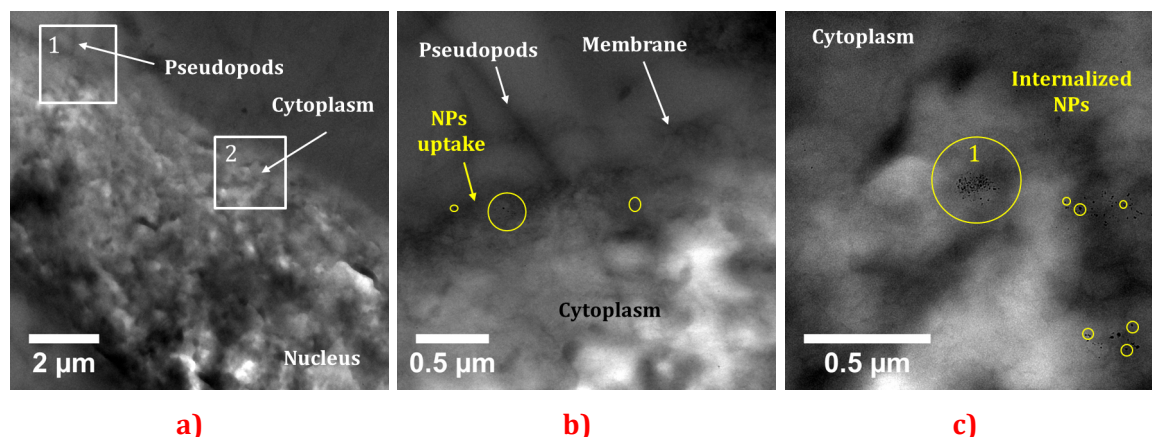


Figure III - 21. TEM images of cryo-fixed HeLa cells after incubation with 5×10^{-4} PtPEG-OH NPs for 6 hours. Panel (a) corresponds to a cell showing a vast cytoplasmic region while (b) and (c) are the magnified images of the squared regions 1 & 2 of panel (a).

In **Figure III - 22**, we show the enclosed aggregate of **Figure III - 21c**. We clearly observe that the internalized electron dense objects have a size distribution and morphology comparable to PtPEG-OH colloids. Thus, internalized PtPEG-OH NPs have been identified.

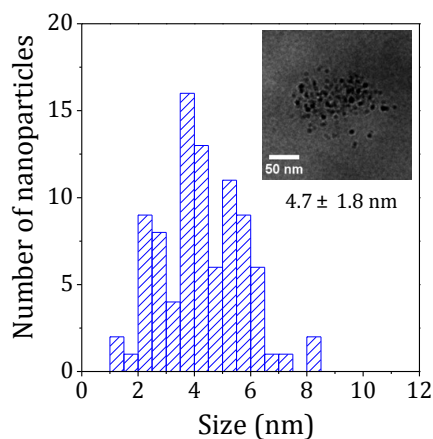


Figure III - 22. Diameter size histogram of the enclosed region 1 of Figure III-19c (inserted TEM image).

The size distribution histogram was built by measuring around 100 objects. We complemented these results by imaging HeLa cells after chemical fixation (next section).

b) TEM imaging of HeLa cells after chemical fixation

Figure III - 23 shows TEM images of a control HeLa cell (without NPs treatment) **(a)** and of a HeLa cell loaded with PtPEG-OH NPs **(b)** prepared by chemical fixation. **Figure III - 23c** displays the diameter size distribution of the squared electron dense region 1 (inserted TEM image) shown in **Figure III - 23b**. With this fixation protocol, we gained in contrast and we were able to differentiate the nucleus from the cytoplasm.

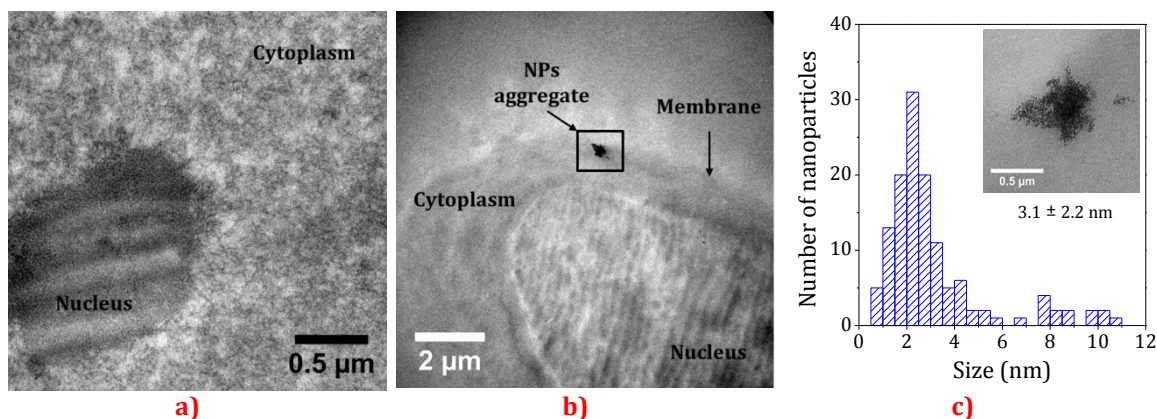


Figure III - 23. TEM images of a control (a) and of a HeLa cells incubated with $5 \times 10^{-4} \text{ mol.L}^{-1}$ PtPEG-OH NPs for 6 hours (b) prepared by chemical fixation. Panel (c) shows the size distribution of the squared aggregate shown in panel (b).

In **Figure III - 23a** non-electron dense objects were observed. **Figure III - 23b** confirms the presence of electron dense aggregates localized exclusively in the cytoplasm, which is in good agreement with NanoSIMS and TEM imaging after cryo-fixation. The diameter size distribution of internalized PtPEG-OH NPs (**Figure III - 23c**) fits with the size distribution of colloidal nanoparticles ($3.1 \pm 2.2 \text{ nm}$), identifying the aggregates to PtPEG-OH NPs.

By analyzing close to 10 TEM image, no membranes surrounding NP aggregates were observed. In conclusion, the absence of vesicles surrounding NPs aggregates strengthens the hypothesis that PtPEG-OH NPs are internalized by HeLa cells *via* passive diffusion (see pathway 3, **Figure III - 20**). For instance, as stated in **Section 1.5.1**, colloidal PtPEG-OH NPs are negatively charged at pH of extra- and intracellular fluids ($\text{PZC}_{\text{PtPEG-OH NPs}} = 3$), property that suggests direct NPs penetration. Hence, we hypothesize that PtPEG-OH NPs might aggregate inside the cell by the action of hydrolytic enzymes in the cytoplasm [49].

c) [TEM imaging of U87-MG cells after chemical fixation](#)

Figure III - 24 shows TEM images of controls and PtPEG-OH NPs loaded U87-MG cells prepared after chemical fixation.

[49] Fernandez S *et al.* (2007) *Biochim. Biophys. Acta - Mol. Cell Biol. Lipids* **1771** 633–40

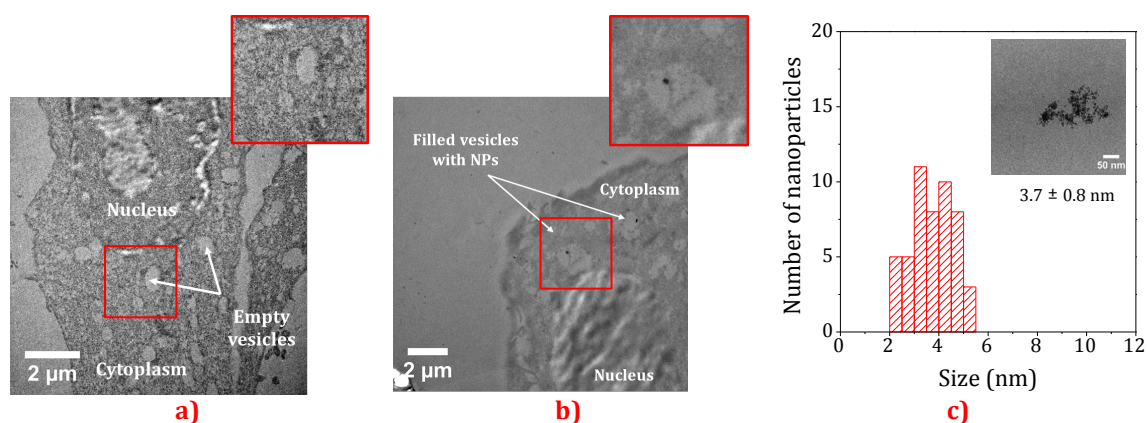


Figure III - 24. TEM images of controls (a) and (b) and U87-MG cells incubated with 5×10^{-4} mol.L⁻¹PtPEG-OH NPs for 6 hours (c) and (d) prepared by chemical fixation.

We distinguish the different compartments (nucleus and cytoplasm) of the cells. In the control (**Figure III - 24a**), we observe empty cytoplasmic vesicles and no electron dense objects. In **Figure III - 24b**, corresponding to a U87-MG cell loaded with NPs, the image displays also vesicles in the cytoplasm. In this case, the vesicles are filled with electron dense objects. **Figure III - 24c** shows the diameter size distribution of the electron dense objects, which fits again with the size distribution of colloidal nanoparticles (3.7 ± 0.8 nm), attributing the aggregates to PtPEG-OH NPs.

From the analysis performed in more than 10 U87-MG cells, we observed that the size of the NPs aggregates and vesicles differ. These findings are enlisted below:

- Highly concentrated NPs aggregates contained in small vesicles of about $0.5 \mu\text{m}$ were observed close to the cell membrane. They were attributed to early endosomes [50].
- Low concentrated NPs aggregates were observed in bigger vesicles of about $1 \mu\text{m}$ containing a large amount of cellular fluid. We attributed this structure to late endosomes, which are formed by fusion with lysosomes. [50].
- Highly concentrated NPs aggregates in vesicles of about $1 \mu\text{m}$ were also observed. This was attributed to the digestion path *via* macro-pinocytosis, which generally occurs for the uptake of micro-size nutrients or particles agglomerates [51] (see pathway 2, **Figure III - 20**). In addition, this was confirmed by observation of pseudopodial extensions.

[50] Kou L *et al.* (2013) *Asian J. Pharm. Sci.* **8** 1–10

[51] Leys S P and Eerkes-Medrano D I (2006) *Biol. Bull.* **211** 157–71

In summary, TEM analysis strongly suggests that the uptake of PtPEG-OH NPs by U87-MG cells occurs *via* non-mediated endocytosis and macro-pinocytosis. This result is in good agreement with our previous results, which established that gadolinium based nanoparticles are internalized in U87-MG cells by endocytosis [52].

2.1.3.3 Conclusion

The major result of this complementary NanoSIMS and TEM analysis is that PtPEG-OH NPs uptake is cell line dependent. In all the cases, internalized NPs were found in the cytoplasm with evidence of no penetration in the cell nucleus. HeLa cells internalize PtPEG-OH NPs by passive diffusion while U87-MG cells by endocytosis and macro-pinocytosis, which may explain ICP results (see **Section 2.1.2**). The scheme shown in **Figure III - 25** summarizes these results.

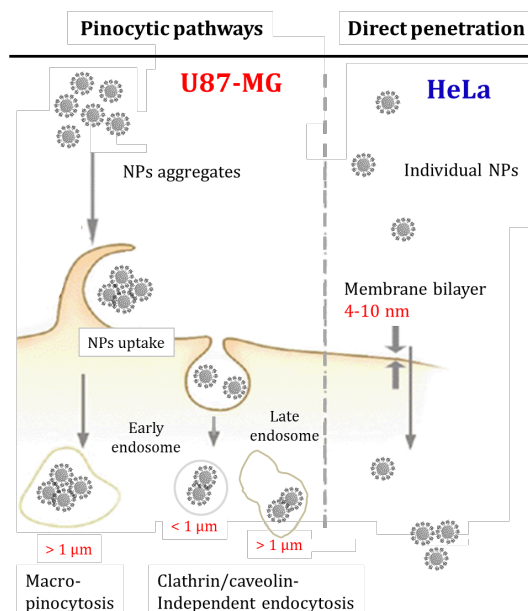


Figure III - 25. Suggested PtPEG-OH NPs uptake pathways in U87-MG and HeLa cells.

[52] Stefančíková L *et al.* (2014) *Cancer Nanotechnol.* 5 6

2.2 Effect of PtPEG-OH NPs on radiation induced cell-killing

The impact of PtPEG-OH NPs on the radiation induced cell-killing was evaluated in HeLa and U87-MG cells. Control cells and cells incubated with 5×10^{-4} mol.L⁻¹ PtPEG-OH NPs for 6 hours were irradiated by γ -rays and carbon ions in the conditions described in **Chapter II – Section 3.2.2** and **3.3.2**. The effect of nanoparticles was determined by performing clonogenic assays (see method in **Chapter II – Section 4.1.4**). Comparative studies were performed using Au-DTDTA NPs activated by gamma irradiation.

2.2.1 HeLa cells irradiation experiments

2.2.1.1 Cells survival curves

Figure III - 26 shows the survival curves of controls (dashed lines) and of cells incubated with PtPEG-OH NPs (solid lines). The cells SF were determined for doses ranging from 0 up to 5 Gy and from 0 up to 2.5 Gy for γ -rays and carbon ions respectively. The surviving fractions of cells are plotted on a logarithmic scale as function of the increasing radiation dose plotted on a linear scale.

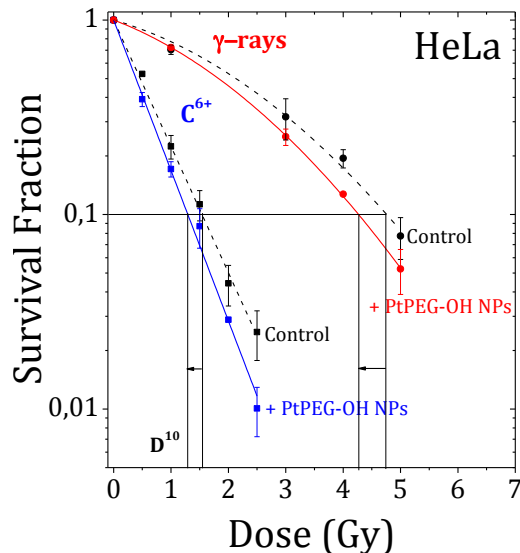


Figure III - 26. Survival curves of HeLa cells irradiated by γ -rays (●, ●) and carbon ions (■, ■) in controls and in presence of PtPEG-OH NPs. The horizontal and vertical black lines indicate the dose at 10% of survival.

We observe that the survival curves of carbon ions are below those of γ -rays. It confirms that cell-killing increases with the linear energy transfer (LET) of the incident beam. In this work, carbon ions had a LET of about $110 \text{ keV} \cdot \mu\text{m}^{-1}$ and γ -rays of $0.2 \text{ keV} \cdot \mu\text{m}^{-1}$ (see radiation sources **Chapter II – Section 3.2** and **3.3**).

We also observe that the decrease of the survival fraction is amplified in cells loaded with PtPEG-OH NPs (red and blue curves **Figure III - 26**) for the two irradiation modes. We highlight the doses at 10% of survival, which will be further discussed in the quantification of nanoparticles efficiency.

2.2.1.2 Cell survival analysis: direct versus sub-lethal damages

A plot of a biological effect observed (*e.g.* cell response) against the dose given is called as a dose response curve. In general, by increasing the dose, the effect increases.

Three types of dose response relationship are known:

- linear
- linear quadratic
- sigmoid.

In this work, we simulated the SF of the cell response curves using the following linear quadratic (LQ) model:

$$SF(D) = e^{-(\alpha D + \beta D^2)} \quad \text{Equation III - 11}$$

where the α parameter is attributed to the induction of directly lethal damage and β to the additive sub-lethal lesions leading to cell death [53] [54]. This mathematical model is commonly used in radiobiology to study the response of eukaryotic cells to radiation. The values of α and β determined after data fitting are reported in **Table III - 10**.

Table III - 10. α and β coefficients for HeLa cells irradiated by γ -rays or by carbon ions in the presence of PtPEG-OH NPs and in the controls.

Radiation	Sample	α (Gy ⁻¹)	β (Gy ⁻²)	α / β (Gy)	R ²
γ -rays	Control	0.15±0.07	0.071±0.016	2.11±0.42	0.997
	+PtPEG-OH NPs	0.26±0.01	0.066±0.003	3.94±0.02	0.999
C ⁶⁺	Control	1.50±0.02	-	-	0.999
	+PtPEG-OH NPs	1.78±0.03	-	-	0.998

This analysis shows that PtPEG-OH NPs induced an increase of α , from 0.15 to 0.26 for γ -rays and from 1.50 to 1.78 for carbon ions irradiation. We also observe that β decreased from 0.071 to 0.066 for γ -rays irradiation. The negligible β value for carbon ions

[53] Tubiana M, Dutreix J and Wambersie A (1986) *Radiobiologie* Chapitre IV pp 73-104

[54] Douglas B G and Fowler J F (1976) *Radiat. Res.* **66** 401-26

irradiation is in agreement with the linear dose response of high LET irradiations. In particular, the absence of sub-lethal of sub-lethal damages is one of the main advantages for hadrontherapy [55].

In order to evaluate the enhancement of the lethality of combining the radiation treatment with NPs, we also reported the α/β ratio, which describes the curvature of a cell survival curve. The α/β ratio gives the dose at which the linear and quadratic components of cell-killing are equal. The higher it is, the more linear the cell response is (cell death mainly due to directly lethal lesions). In this work, we observe that the α/β ratio increased from 2.11 to 3.94 in presence of PtPEG-OH NPs for gamma irradiation.

The α/β ratio also characterizes the effects of dose-per-fraction and cell repopulation (damage repair) in fractionated radiotherapy [53]. The enhancement of the α/β ratio with PtPEG-OH NPs opens the perspective of increasing the dose-per-fraction in the treatment because of the linear trend of the survival curve. This is of great interest in clinics.

The increase of carbon radiation effect as due to the increase of directly lethal damages by PtPEG-OH NPs is a major finding. To our knowledge, this is here the first evidence that core platinum nanoparticles increase the lethality of medical carbon beams.

2.2.1.3 Quantification of the amplification efficiency

The efficiency of PtPEG-OH NPs to amplify cancer cell-killing, *i.e.* the REE of NPs, was quantified by calculating different indicators including:

i) The Amplification Factor (AF)

The amplification factor is indicative of the cell-killing enhancement due to the presence of nanoparticles at a defined dose point. It is equivalent to the radiation sensitizing enhancement ratio (SER), which is commonly used to describe the cell-specific radiosensitization effect [41]. The AF is calculate as follows:

$$AF = \frac{SF_{\text{control}}^{\text{fitted curve}} - SF_{\text{PtPEG NPs}}^{\text{fitted curve}}}{SF_{\text{control}}^{\text{fitted curve}}} \times 100 [=] \%$$

Equation III - 12

[41] Jain S *et al.* (2011) *Int. J. Radiat. Oncol. Biol. Phys.* **79** 531–9

[53] Tubiana M, Dutreix J and Wambersie A (1986) *Radiobiologie* Chapitre **IV** pp 73–104

[55] Suzuki M *et al.* (2000) *Int. J. Radiat. Oncol.* **48** 241–50

Figure III - 27 shows the variation of the AF for carbon ions (in blue) and γ -rays (in red) as function of the dose.

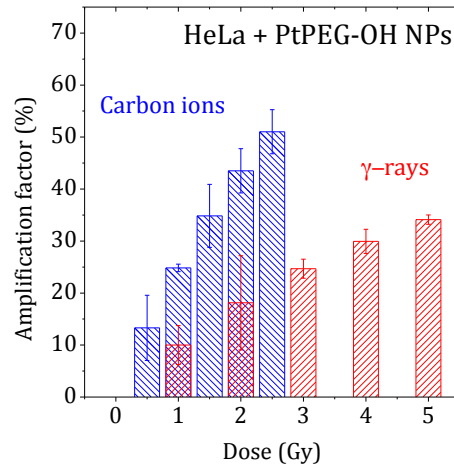


Figure III - 27. Nanoparticles amplification factor as function of the γ -rays and carbon ions radiation dose.

Firstly, we observe that the AF increases with the radiation dose. Very interestingly, the REE of PtPEG-OH NPs is stronger when carbon ions are used as incident radiation. In principle, this graph gives new insights into the reduction of the total dose of irradiation. For instance, at 2 Gy (dose fractionation regimen commonly used in clinic), the irradiation dose to use in the presence of PtPEG-OH NPs could be reduced by 44% and 14% for incident carbon ions and γ -rays respectively [56]

ii) The Dose Enhancing Factor (DEF)

The DEF is commonly used to evaluate the properties of nanoparticles to amplify/enhance the radiation effect [57]. This approach is used to assess the enhancement of *in vitro* radiotherapy from survival curves. The DEFs for γ -rays and carbon ions irradiations was determined from the simulated curves at 10% of survival (**Figure III - 26**) as follows:

$$\text{DEF} = \frac{D^{10}_{\text{control}}}{D^{10}_{\text{with NPs}}}$$

Equation III - 13

where D^{10} corresponds to the dose at 10% of survival.

Table III - 11 shows D^{10} for controls and HeLa cells loaded with PtPEG-OH NPs.

[56] Nogier T and Regaud C (1914) *Compt. Rend. Acad. Sci. Paris* **58** 1711-4

[57] Taggart L E et al. (2014) *Cancer Nanotechnol.* **5** 5

Table III - 11. Radiation doses (γ -rays and carbon ions) to reach 10% of survival with and without PtPEG-OH NPs. DEF and dose enhancement (%).

Radiation	Sample	D ¹⁰ (Gy)	DEF	Dose enhancement (%)
γ -rays	Control	4.75	-	-
	+PtPEG-OH NPs	4.26	1.11	10.3
C ⁶⁺	Control	1.54	-	-
	+PtPEG-OH NPs	1.29	1.19	16.2

These results show a dose enhancement of about 16% and 10% respectively for carbon ions and γ -rays irradiations (at 10% of survival). This again confirms that the cell-killing is more pronounced by combining PtPEG-OH NPs with incident carbon ions.

iii) The Relative Biological Effectiveness (RBE)

In radiation biology, the RBE value is used to quantify differences in the biological and clinical effects of radiations. The RBE is an unambiguous and commonly used concept in radiobiology [58]. It is the ratio of two absorbed doses delivered by two different radiation qualities (different LET). It compares the absorbed dose of a reference radiation (photons, predominately ⁶⁰Co γ -rays) to that of another radiation (protons, carbon ions, *etc.*), which results in the same biological effect under identical conditions [59]. It varies with the radiation quality, biological system and effect. The RBE is a key parameter used by oncologists and medical physicists to adapt the dose delivery according to a novel therapeutic approach.

In this work, we determined the RBE of carbon ions (in the absence and presence of NPs) using ¹³⁷Cs γ -rays as reference. The RBE was evaluated at 10% of survival by:

$$RBE_{\text{control}} = \frac{D_{\gamma\text{rays control}}^{10}}{D_{\text{C}^{6+} \text{ control}}^{10}} \quad \text{Equation III - 14}$$

and

$$RBE_{\text{NPs}} = \frac{D_{\gamma\text{rays control}}^{10}}{D_{\text{C}^{6+} \text{ with NPs}}^{10}} \quad \text{Equation III - 15}$$

[58] International Commission on Radiological Protection (1963) *Health Phys.* **9** 357–86
 [59] IAEA and ICRU (2008) Relative Biological Effectiveness in Ion Beam Therapy **461**

We obtained a RBE value of 3.09 for HeLa cells treated only with radiation (control). This result is in good agreement with other works [60]. On the other hand, in the presence of PtPEG-OH NPs, the RBE value increased in about 19% ($RBE_{NPs} = 3.68$) (see **Table III - 12** below).

iv) The Relative Enhancing Factor (REF)

By analogy with the RBE value, we evaluated the REF of PtPEG-OH NPs comparing the SF of the control with the SF in the presence of NPs at 2 Gy as follows:

$$REF_{\text{control}} = \frac{SF_{\text{y-rays control}}^2 \text{ Gy}}{SF_{\text{C}^{6+} \text{ control}}^2 \text{ Gy}} \quad \text{Equation III - 16}$$

and

$$REF_{NPs} = \frac{SF_{\text{y-rays control}}^2 \text{ Gy}}{SF_{\text{C}^{6+} \text{ with NPs}}^2 \text{ Gy}} \quad \text{Equation III - 17}$$

Table III - 12. RBE-D¹⁰, REF-2 Gy and NPs enhancement values of HeLa cells treated with γ -rays and carbon ions with or without PtPEG-OH NPs.

Sample	RBE(D ¹⁰)	REF(2 Gy)	Enhancement (%)	
			RBE	REF
Control	3.09	10.5	-	-
+PtPEG-OH NPs	3.68	18.7	19	44

The RBE(D¹⁰), REF(2 Gy) and respective NPs enhancement are summarized above in **Table III - 12**. Interestingly, the REF value increased by approximately 44% at 2 Gy, which confirmed the high potential of PtPEG-OH NPs to improve cancer cell-killing in fractionation regimens.

In summary, we demonstrated the REE of PtPEG-OH NPs. Hence, the combination of PtPEG-OH NPs with radiations may be considered as a very promising alternative to improve the biological effect of radiotherapies. In this cellular model, we observed that PtPEG-OH NPs have the unique property to enhance the lethality of radiations. More important, platinum nanoparticles strongly improved the effect of medical carbon ions.

[60] Kaur H *et al.* (2013) *Nucl. Instruments Methods Phys. Res. Sect. B Beam Interact. with Mater. Atoms* **301** 7–11

2.2.2 U87-MG cells irradiation experiments

The radio-enhancement effect of PtPEG-OH and Au-DTDTPA NPs was also investigated in U87-MG cells treated by gamma irradiation only. U87-MG cell samples were prepared and irradiated at the same conditions used for HeLa cells irradiation experiments (see method in **Chapter II – Section 4.1.4**).

2.2.2.1 Cells survival curves

The dose response curves of individually PtPEG-OH and Au-DTDTPA NPs treated U87-MG cells were found very similar. Hence, the survival curves of the control and of cells loaded with PtPEG-OH NPs exposed to γ -rays are shown in **Figure III - 28**.

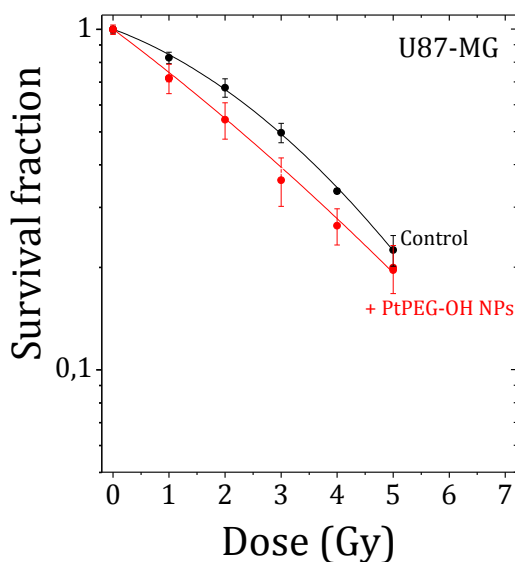


Figure III - 28. Survival curves of U87-MG cells irradiated by gamma rays in control (●) and in presence of PtPEG-OH NPs (●).

We observe that the exponential decrease of the survival curves was amplified in cells loaded with PtPEG-OH NPs. We obtained very similar effect using Au-DTDTPA NPs. Indeed, the survival curves for Pt and Au NPs overlap. More interestingly, the shape of the cell response curves changed from quadratic in the control to linear shape in the presence of metallic NPs between 0 and 5 Gy.

2.2.2.2 Cell survival analysis: direct versus sub-lethal damages

The values of α and β coefficients determined after data fitting are reported below in **Table III - 13**.

Table III - 13. α and β coefficients for U87-MG cells irradiated by γ -rays in the presence of metallic NPs and in the controls.

Sample	α (Gy ⁻¹)	β (Gy ⁻²)	α/β (Gy)	R ²
Control	0.14±0.01	0.032±0.002	4.37±0.03	0.999
+ PtPEG-OH NPs	0.34±0.01	-	-	0.997

Surprisingly, the PtPEG-OH NPs (and Au-DTDTPA NPs) enhanced the induction of directly lethal damages only. Indeed, α increased by a factor of two, from 0.14 to 0.34 in the presence of metallic NPs. As major result, we passed from a linear quadratic relation ($\alpha/\beta \sim 4$) to a linear relation with a negligible β value.

This result is of a major interest; it demonstrates that the combination of metallic nanoparticles with γ -rays produces a radiobiological effect that is similar to the effect induced by high LET radiations (linear survival curves). This result suggests a highly local ionizing effect of NPs as already proposed by McMahon *et al.* [61] [62]. Very importantly, this effect is cell line dependent, as it was only observed in U87-MG and not in HeLa cells.

2.2.2.3 Quantification of the amplification efficiency

Figure III - 29 shows the variation of the AF as function of the dose. In this case, the AF does not increase with the increasing dose (as observed with HeLa). In particular, at 2 Gy PtPEG-OH NPs amplify by about 23 % the biological effect of γ -rays. This behavior of the AF may be explained as due to: i) the absence of the β component or ii) a saturation effect due to the higher uptake of NPs in U87 as to compare with HeLa. To better elucidate the REF of NPs in U87-MG cells, irradiation experiments are being performed at higher irradiation doses to reach a SF of at least 0.01.

[61] McMahon S J *et al.* (2011) *Radiother. Oncol.* **100** 412-6

[62] McMahon S J *et al.* (2011) *Sci. Rep.* **1** 18

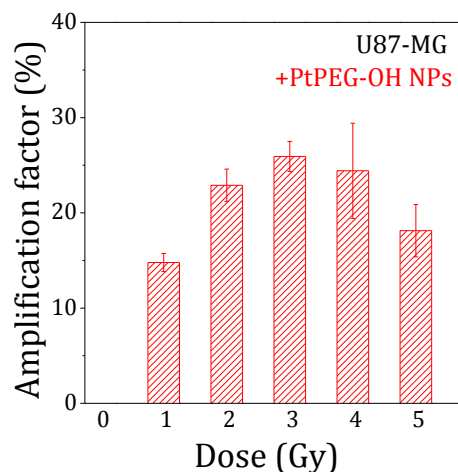


Figure III - 29. Amplification factor of PtPEG-OH NPs as function of the dose.

Complementary studies in different human cancer cell lines are being conducted in the group to evaluate the potentialities of both nanoparticles to improve the performance of hadrontherapy.

2.2.3 Conclusion

The main results, illustrated in **Figure III - 30**, and conclusions on the REE of PtPEG-OH NPs in combination with γ -rays and carbon ions are enlisted below:

- i) PtPEG-OH NPs amplify the biological effects of ionizing radiations (high energy photons and carbon ions).
- ii) The REE of NPs is stronger when carbon ions are used as incident radiation.
- iii) The combination of Pt NPs with carbon ions radiation is presented as a promising approach to improve the performance of hadrontherapy.
- iv) The unique property of PtPEG-OH NPs to amplify exclusively the induction of directly lethal damages was here demonstrated for the first time. These results open new perspectives on improving radiation tumor targeting.
- v) Metallic NPs (Pt and Au) enhance the effect of γ -rays.
- vi) Pt and Au NPs strongly increased the lethality of γ -rays, a very advantageous approach in the treatment of glioblastomas (shown in the U87-MG model).
- vii) Metallic NPs were found very promising for fractionated radiotherapy protocols.

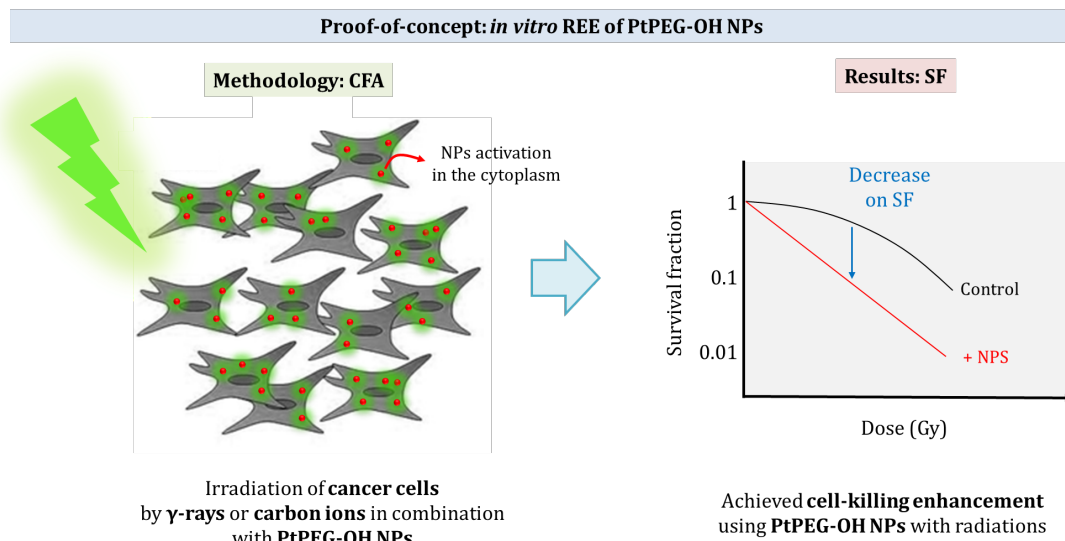


Figure III - 30. Schematic representation of the radio-enhancing cell killing effect of PtPEG-OH NPs.

2.3 Proof of principle: enhancement on the radio-induced nanosize damage

The interaction of ionizing radiation with biomolecules such as DNA, lipids and proteins leads to bond cleavages that may be repaired or not by living cells. It is commonly accepted that single bond breaks are little toxic for living organisms whilst complex bond breaks are difficult to repair and might induce cell killing.

In this work, we used a molecular bio-nanoprobe to quantify the effect at the nanoscale, particularly the damage that corresponds to nanosize lesions which are the most lethal for cells. In this purpose we used plasmid DNA as probes to quantify double strand breaks (DSB), which is the signature of molecular nanosize damage, lesions being separated by 2 nm minimum (distance between the two strands). Therefore, we present and discuss below the quantification of radio-induced nanosize breaks induced by γ -rays and the effect of NPs. The experimental method is described in **Chapter II – Section 4.2**.

2.3.1 Effect of PtPEG-OH NPs on the induction of nanometer size damages

Figure III - 31 shows the average number of DSBs induced in pure plasmids (control) and in plasmids in the presence of PtPEG-OH NPs. The ratio, nanoparticles per plasmid, is close to 4:1. The effect of the NPs concentration on the induction of nanosize damage is presented and discussed on **Appendix B**. In **Figure III - 31**, the nanosize breaks per plasmid are plotted as function of the irradiation dose.

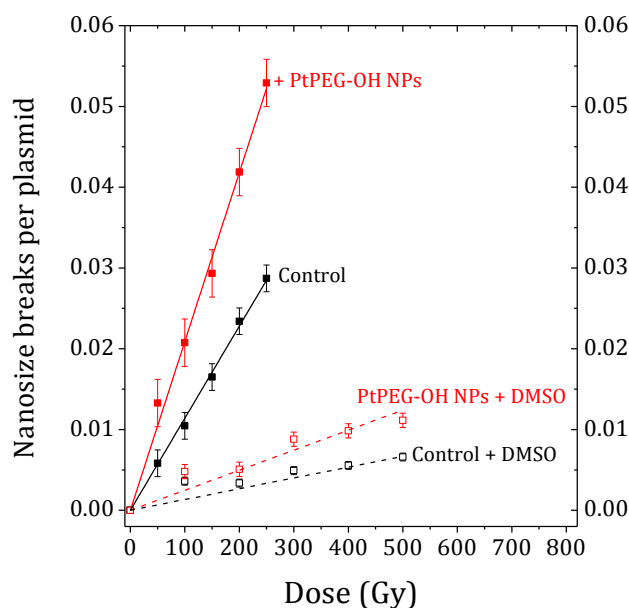


Figure III - 31. Nanosize damage induced by γ -rays in plasmids loaded with PtPEG-OH NPs (■) and in the control (■) as function of the irradiation dose. DMSO effect in plasmids loaded with PtPEG-OH NPs (□) and in the control (□).

We observe that the radio-induction of nanosize damage in the controls and in the PtPEG-OH NPs-loaded bio-nanoprobes increases linearly with the irradiation dose. This indicates single ionizing events [63]. In the presence of NPs, we observe that the induction of nanosize damages is strongly amplified (red line).

In some experiments, DMSO was added to investigate the effect of water radicals. We observe that the induction of nanosize damage sharply decrease in presence of DMSO (dotted lines). This effect is in agreement with previous studies performed with Pt-PAA NPs and GBNs activated not only by photons [64] but also by incident ions [65] [66] [67].

2.3.2 Amplification efficiency of molecular nanosize damage

The efficiency of PtPEG-OH NPs to amplify the induction of nanometer size damages was quantified using the amplification factor (AF) defined as:

$$AF = \frac{\text{yield}_{\text{control}} - \text{yield}_{\text{PtPEG-OH NPs}}}{\text{yield}_{\text{control}}} \times 100 \quad \text{Equation III - 18}$$

The yield is defined as the number of DSBs induced per plasmid and per Gy. It corresponds to the slope of the dose response curve. The values are reported in **Table III - 14**.

Table III - 14. Yields of controls and plasmids loaded with PtPEG-OH NPs with a NP:plasmid ratio close 4:1. DMSO was added in some experiments. The AFs are also reported.

Sample	NPs per plasmid	Nanosize breaks/plasmid/Gy x10 ⁻⁵	AF (%)	OH effect (%)
Control	0:1	11.40 ± 0.25	-	-
+PtPEG-OH NPs	4:1	20.90 ± 0.21	83 ± 4	-
Control + DMSO	0:1	1.34 ± 0.18	-	88 ± 1
PtPEG-OH NPs + DMSO	4:1	2.48 ± 0.11	85 ± 15	88 ± 1
Control + PEG-OH	0:1*	12.41 ± 0.22	9 ± 1	-

*sample prepared with a PEG-OH concentration estimated to be similar to the grafting of PEG in a Pt NP.

We observe that in the presence of PtPEG-OH NPs the induction of nanosize damage is enhanced by a factor of 83%. The nanosize damage yield increased from 11.4 to 20.9x10⁻⁵ breaks per plasmid per Gy. This result may well explain the enhancement of cell-killing in

[63] Śmiałek M A *et al.* (2009) *Radiat. Res.* **172** 529–36

[64] Porcel E *et al.* (2012) *J. Phys. Conf. Ser.* **373** 012006

[65] Porcel E *et al.* (2010) *Nanotechnology* **21** 85103

[66] Porcel E *et al.* (2014) *Nanomedicine* **10** 1601–8

[67] Schlatholter T *et al.* (2016) *Int. J. Nanomedicine* **11** 1549

the presence of PtPEG-OH NPs which is due to the increase on the induction of directly lethal damages.

2.3.3 Insight in mechanisms: the effect of OH[•] radicals

We investigated the effect of OH[•] free radicals by performing experiments in the presence of DMSO (see materials and methods **Chapter II -Section 4.2.1**). The results were presented in **Figure III - 31**.

In **Figure III - 31** we observe that the dose response curves drops drastically in presence of DMSO. The yields are reported in **Table III - 14**. The yield in the presence of DMSO decreased from 20.90 to 2.48×10^{-5} in plasmids loaded with PtPEG-OH NPs. This study clearly indicates that the amplification effects are mediated by water radicals for more than 88%. Surprisingly, we observe (**Table III - 14** - column 4) that the direct and indirect effects of radiation are amplified in the same proportion in the presence of NPs.

This ability of platinum nanoparticles to amplify nanosize molecular damage has been ascribed to a sequence of physical and chemical processes that take place at early stage in confined space [65] [61].

Briefly, incident highly energetic photons and secondary electrons produced along the track ionize platinum atoms. Deexcitation processes such as Auger relaxation (when inner shells are ionized) [68], plasmons deexcitation [69], electron capture [70] [71] take place. Deexcitation processes consecutively increase the number of emitted electrons leading to the ionization of the surrounding medium (water molecules and in biomolecules) and production of clustered free radicals and ROS. These species are highly toxic causing bond cleavages in biomolecules and ultimately cell death. In summary, platinum nanoparticles are responsible for the local enhancement of the ionization density that increases of radiation effects because of the spatial confinement of the resulting highly reactive cluster. This specific nanoscale effect may be of major interest for cancer radiotherapy in combination with nano-agents.

[61] McMahon S J *et al.* (2011) *Radiother. Oncol.* **100** 412–6

[65] Porcel E *et al.* (2010) *Nanotechnology* **21** 85103

[68] Kobayashi K *et al.* (2010) *Mutat. Res.* **704** 123–31

[69] Verkhovtsev A V *et al.* (2015) *J. Phys. Chem. C* **119** 11000–13

[70] Pešić Z D *et al.* (2009) *J. Phys. B At. Mol. Opt. Phys.* **42** 235202

[71] Stumpf H (1971) *Phys. der Kondens. Mater.* **13** 101–17

2.4 Conclusion: Multi-scale study

In this multi-scale study, we attribute the REE of PtPEG-OH NPS to the enhanced induction of nanoscopic bond breaks trigger on the cytosol, where biomolecules, such as proteins and lipids, can be lethally perturbed inhibiting the cell repairation pathways to lately cause cell death.

For instance, proteins are the major target for biological oxidants. The basic principles on the oxidation of proteins by irradiation-generated ROS were established in the pioneering studies of Garrison [72] [73], Swallow [74] and Schuessler and Schilling [75] who characterized reaction products formed when proteins were exposed to γ -rays under conditions where only OH^\cdot , $\text{O}_2^{\cdot-}$, or a mixture of both were presented. Results of these studies demonstrated that the modification of proteins is initiated mainly by reactions with OH^\cdot . This oxidation may adversely affect protein's activity resulting in an inadequate cell functional regulation, *e.g.* alteration on the activity of DNA repair proteins (γH2aX), and thus cell death.

Another biomolecule target of ionizing radiation is the lipid bilayer within cell membranes, which can be damaged *via* ROS. Lipid peroxidation by ROS was found as the main damage to the membranes, leading to an increase in membrane permeability and other transmembrane processes [76] [77]. For instance, studies of cell membrane irradiation have shown the induction of cell apoptosis. This effect was also observed in cells without a nucleus, confirming another pathway of cell-killing independently of nucleic acid damage [78].

Therefore, it is concluded (as illustrated in Figure III - 32) that PtPEG-OH NPs are excellent agents to increase the production of free radicals (demonstrated in experiments performed with the bio-nanoprobe in the presence of DMSO) inside cells (imaging results) enhancing the induction of nanosize damages and cell killing.

[72] Garrison W M *et al.* (1962) *Radiat. Res.* **16** 483–502

[73] Garrison W M *et al.* (1970) *J. Phys. Chem.* **74** 4506–9

[74] Swallow A J (1960) *Radiation Chemistry of Organic Compounds* pp 211–24

[75] Schuessler H and Schilling K (1984) *Int. J. Radiat. Biol. Relat. Stud. Physics, Chem. Med.* **45** 267–81

[76] Corre I *et al.* (2010) *Mutat. Res.* **704** 61–7

[77] Wong-Ekkabut J *et al.* (2007) *Biophys. J.* **93** 4225–36

[78] Haimovitz-Friedman A *et al.* (1994) *J. Exp. Med.* **180** 525–35

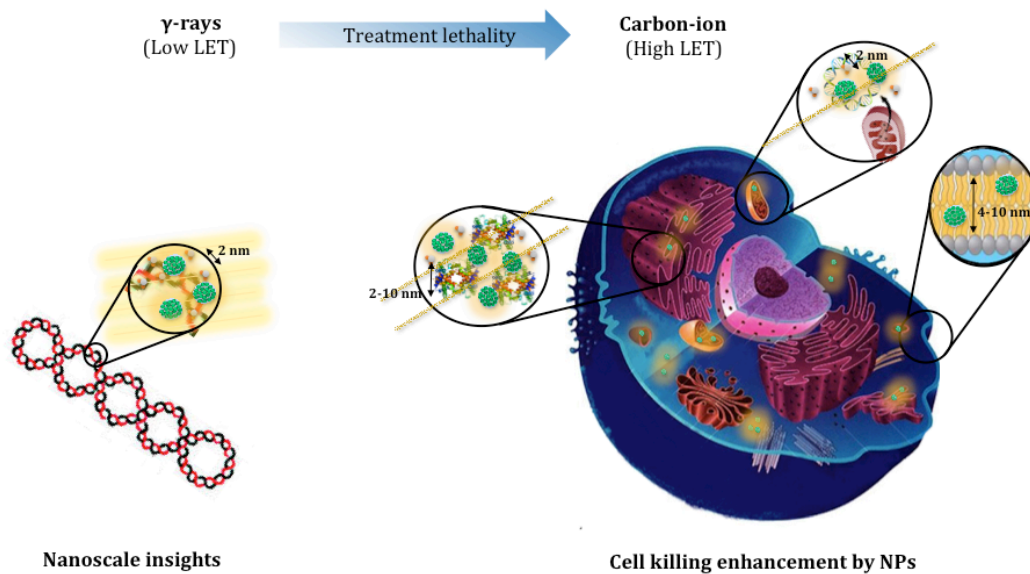


Figure III - 32. Multi-scale study: the radiation enhancing effect of PtPEG-OH NPs from the nanoscale to the cell.

3. References

- [1] Mie G 1908 Beiträge zur Optik trüber Medien, speziell kolloidaler Metallösungen *Ann. Phys.* **330** 377–445
- [2] Gharibshahi E and Saion E 2012 Influence of Dose on Particle Size and Optical Properties of Colloidal Platinum Nanoparticles *Int. J. Mol. Sci.* **13** 14723–41
- [3] Remita H, Lampre I, Mostafavi M, Balanzat E and Bouffard S 2005 Comparative study of metal clusters induced in aqueous solutions by γ -rays, electron or C6+ ion beam irradiation *Radiat. Phys. Chem.* **72** 575–86
- [4] Doane T L, Chuang C-H, Hill R J and Burda C 2012 Nanoparticle ζ -potentials. *Acc. Chem. Res.* **45** 317–26
- [5] Gilles M, Brun E and Sicard-Roselli C 2014 Gold nanoparticles functionalization notably decreases radiosensitization through hydroxyl radical production under ionizing radiation *Colloids Surfaces B Biointerfaces* **123** 770–7
- [6] Davey W P 1925 Precision Measurements of the Lattice Constants of Twelve Common Metals *Phys. Rev.* **25** 753–61
- [7] Kim K S, Winograd N and Davis R E 1971 Electron spectroscopy of platinum-oxygen surfaces and application to electrochemical studies *J. Am. Chem. Soc.* **93** 6296–7
- [8] Contour J P, Mouvier G, Hoogewys M and Leclere C 1977 X-ray photoelectron spectroscopy and electron microscopy of Pt-Rh gauzes used for catalytic oxidation of ammonia *J. Catal.* **48** 217–28
- [9] Barr T L 1978 An ESCA study of the termination of the passivation of elemental metals *J. Phys. Chem.* **82** 1801–10
- [10] Puglia C, Nilsson A, Hernnäs B, Karis O, Bennich P and Mårtensson N 1995 Physisorbed, chemisorbed and dissociated O₂ on Pt(111) studied by different core level spectroscopy methods *Surf. Sci.* **342** 119–33
- [11] Liu F, Zhao Z, Qiu L and Zhao L 2009 Applications of XPS on Nanoscale Material Research *J. Surf. Anal.* **15** 271–3
- [12] Fu X, Wang Y, Wu N, Gui L and Tang Y 2001 Surface Modification of Small Platinum Nanoclusters with Alkylamine and Alkylthiol: An XPS Study on the Influence of Organic Ligands on the Pt 4f Binding Energies of Small Platinum Nanoclusters *J. Colloid Interface Sci.* **243** 326–30
- [13] López G P, Castner D G and Ratner B D 1991 XPS O 1s binding energies for polymers containing hydroxyl, ether, ketone and ester groups *Surf. Interface Anal.* **17** 267–72
- [14] Truica-Marasescu F and Wertheimer M R 2008 Nitrogen-Rich Plasma-Polymer Films for Biomedical Applications *Plasma Process. Polym.* **5** 44–57
- [15] Contarini S, Howlett S P, Rizzo C and De Angelis B A 1991 XPS study on the dispersion of carbon additives in silicon carbide powders *Appl. Surf. Sci.* **51** 177–83
- [16] Hong R, Fischer N O, Emrick T and Rotello V M 2005 Surface PEGylation and Ligand Exchange Chemistry of FePt Nanoparticles for Biological Applications *Chem. Mater.* **17** 4617–21
- [17] Drummond I W, Robinson K S, Carrick A and Schmiedel H 1993 Practical polymer film characterisation using high performance XPS methods *Fresenius. J. Anal. Chem.* **346** 200–4
- [18] Pijpers A P, Berresheim K and Wilmers M 1993 Charge compensation for XPS on polymers *Fresenius. J. Anal. Chem.* **346** 104–9
- [19] Jansen R J J and van Bekkum H 1995 XPS of nitrogen-containing functional groups on activated carbon *Carbon N. Y.* **33** 1021–7
- [20] Deniau G, Azoulay L, Jégou P, Le Chevallier G and Palacin S 2006 Carbon-to-metal bonds: Electrochemical reduction of 2-butenenitrile *Surf. Sci.* **600** 675–84
- [21] Whelan C M, Ghijsen J, Pireaux J-J and Maex K 2004 Cu adsorption on carboxylic

- acid-terminated self-assembled monolayers: a high-resolution X-ray photoelectron spectroscopy study *Thin Solid Films* **464** 388–92
- [22] Crispin X, Lazzaroni R, Crispin A, Geskin V., Brédas J. and Salaneck W. 2001 Understanding the initial stages of polymer grafting on metals: a photoelectron spectroscopy study of acrylonitrile adsorption on transition metal surfaces *J. Electron Spectros. Relat. Phenomena* **121** 57–74
- [23] Forbes L M, O'Mahony A M, Sattayasamitsathit S, Wang J and Cha J N 2011 Polymer end-group mediated synthesis of well-defined catalytically active platinum nanoparticles *J. Mater. Chem.* **21** 15788
- [24] Forbes L M, Sattayasamitsathit S, Xu P F, O'Mahony A, Samek I A, Kaufmann K, Wang J and Cha J N 2013 Improved oxygen reduction reaction activities with amino acid R group functionalized PEG at platinum surfaces *J. Mater. Chem. A* **1** 10267–73
- [25] Silverstein R M, Bassler G C and Morrill T C 1991 *Spectrometric identification of organic compounds* (Wiley)
- [26] Lambert J B 1987 *Introduction to organic spectroscopy* (Macmillan)
- [27] Krishnan K and Krishnan R S 1966 Raman and infrared spectra of ethylene glycol *Proc. Indian Acad. Sci. - Sect. A* **64** 111–22
- [28] Nakamoto K 2009 *Infrared and Raman spectra of inorganic and coordination compounds. Part B: Applications in coordination, organometallic and bioinorganic chemistry* (Hoboken, New Jersey: John Wiley & Sons. Inc.)
- [29] Wysokiski R, Kuduk-Jaworska J and Michalska D 2006 Electronic structure, Raman and infrared spectra, and vibrational assignment of carboplatin. Density functional theory studies *J. Mol. Structure THEOCHEM* **758** 169–79
- [30] Glastrup J 1996 Degradation of polyethylene glycol. A study of the reaction mechanism in a model molecule: Tetraethylene glycol *Polym. Degrad. Stab.* **52** 217–22
- [31] Chibani S, Michel C, Delbecq F, Pinel C and Besson M 2013 On the key role of hydroxyl groups in platinum-catalysed alcohol oxidation in aqueous medium *Catal. Sci. Technol.* **3** 339–50
- [32] Mallat T and Baiker A 1994 Oxidation of alcohols with molecular oxygen on platinum metal catalysts in aqueous solutions *Catal. Today* **19** 247–83
- [33] Anderson R, Griffin K, Johnston P and Alsters P L 2003 Selective Oxidation of Alcohols to Carbonyl Compounds and Carboxylic Acids with Platinum Group Metal Catalysts *Adv. Synth. Catal.* **345** 517–23
- [34] Cox Gad S 2007 *Handbook of Pharmaceutical Biotechnology* ed S Cox Gad (John Wiley & Sons. Inc.)
- [35] Wand P, Bartl J D, Heiz U, Tschurl M and Cokoja M 2016 Functionalization of small platinum nanoparticles with amine and phosphines: Ligand binding modes and particle stability *J. Colloid Interface Sci.* **478** 72–80
- [36] Benyettou F, Hardouin J, Lecouvey M, Jouni H and Motte L 2012 Pegylated versus non-PEGylated $\gamma\text{Fe}_2\text{O}_3$ @ alendronate nanoparticles *J. Bioanal. Biomed.* **4** 39–44
- [37] Rima W, Sancey L, Aloy M-T, Armandy E, Alcantara G B, Epicier T, Malchère A, Joly-Pottuz L, Mowat P, Lux F, Tillement O, Burdin B, Rivoire A, Boulé C, Anselme-Bertrand I, Pourchez J, Cottier M, Roux S, Rodriguez-Lafrasse C and Perriat P 2013 Internalization pathways into cancer cells of gadolinium-based radiosensitizing nanoparticles *Biomaterials* **34** 181–95
- [38] Pfeiffer C, Rehbock C, Hühn D, Carrillo-Carrion C, de Aberasturi D J, Merk V, Barcikowski S, Parak W J, Huhn D, Carrillo-Carrion C, de Aberasturi D J, Merk V, Barcikowski S and Parak W J 2014 Interaction of colloidal nanoparticles with their local environment: the (ionic) nanoenvironment around nanoparticles is different from bulk and determines the physico-chemical properties of the nanoparticles *J. R. Soc. Interface* **11** 20130931–20130931
- [39] Usami N, Furusawa Y, Kobayashi K, Lacombe S, Reynaud-Angelin a, Sage E, Wu T-D,

- Croisy a, Guerquin-Kern J-L and Le Sech C 2008 Mammalian cells loaded with platinum-containing molecules are sensitized to fast atomic ions. *Int. J. Radiat. Biol.* **84** 603–11
- [40] Rima W, Sancey L, Aloy M-T, Armandy E, Alcantara G B, Epicier T, Malchère A, Joly-Pottuz L, Mowat P, Lux F, Tillement O, Burdin B, Rivoire A, Boulé C, Anselme-Bertrand I, Pourchez J, Cottier M, Roux S, Rodriguez-Lafrasse C and Perriat P 2013 Internalization pathways into cancer cells of gadolinium-based radiosensitizing nanoparticles. *Biomaterials* **34** 181–95
- [41] Jain S, Coulter J A, Hounsell A R, Butterworth K T, McMahon S J, Hyland W B, Muir M F, Dickson G R, Prise K M, Currell F J, O'Sullivan J M and Hirst D G 2011 Cell-specific radiosensitization by gold nanoparticles at megavoltage radiation energies. *Int. J. Radiat. Oncol. Biol. Phys.* **79** 531–9
- [42] Shah N B, Dong J and Bischof J C 2011 Cellular Uptake and Nanoscale Localization of Gold Nanoparticles in Cancer Using Label-Free Confocal Raman Microscopy *Mol. Pharm.* **8** 176–84
- [43] Romer W, Wu T-D, Duchambon P, Amessou M, Carrez D, Johannes L and Guerquin-Kern J-L 2006 Sub-cellular localisation of a ¹⁵N-labelled peptide vector using NanoSIMS imaging *Appl. Surf. Sci.* **252** 6925–30
- [44] Mao Z, Zhou X and Gao C 2013 Influence of structure and properties of colloidal biomaterials on cellular uptake and cell functions *Biomater. Sci.* **1** 896–911
- [45] Bandyopadhyay A, Das T and Yeasmin S 2015 *Nanoparticles in Lung Cancer Therapy - Recent Trends* (New Delhi: Springer India)
- [46] Marsh M and Marsh M 2001 *Endocytosis* (Oxford University Press)
- [47] Falcone S, Cocucci E, Podini P, Kirchhausen T, Clementi E and Meldolesi J 2006 Macropinocytosis: regulated coordination of endocytic and exocytic membrane traffic events. *J. Cell Sci.* **119** 4758–69
- [48] Gruenberg J and Maxfield F R 1995 Membrane transport in the endocytic pathway *Curr. Opin. Cell Biol.* **7** 552–63
- [49] Fernandez S, Jannin V, Rodier J-D, Ritter N, Mahler B and Carrière F 2007 Comparative study on digestive lipase activities on the self emulsifying excipient Labrasol®, medium chain glycerides and PEG esters *Biochim. Biophys. Acta - Mol. Cell Biol. Lipids* **1771** 633–40
- [50] Kou L, Sun J, Zhai Y and He Z 2013 The endocytosis and intracellular fate of nanomedicines: Implication for rational design *Asian J. Pharm. Sci.* **8** 1–10
- [51] Leys S P and Eerkes-Medrano D I 2006 Feeding in a calcareous sponge: particle uptake by pseudopodia. *Biol. Bull.* **211** 157–71
- [52] Stefančíková L, Porcel E, Eustache P, Li S, Salado D, Marco S, Guerquin-Kern J-L, Réfrégiers M, Tillement O, Lux F and Lacombe S 2014 Cell localisation of gadolinium-based nanoparticles and related radiosensitising efficacy in glioblastoma cells. *Cancer Nanotechnol.* **5** 6
- [53] Tubiana M, Dutreix J and Wambersie A 1986 Effects cellulaires des rayonnements ionisants. Les courbes de survie cellulaire *Radiobiologie* (Paris: Hermann, éditeurs des sciences et des arts) pp 73–104
- [54] Douglas B G and Fowler J F 1976 The Effect of Multiple Small Doses of X Rays on Skin Reactions in the Mouse and a Basic Interpretation *Radiat. Res.* **66** 401–26
- [55] Suzuki M, Kase Y, Yamaguchi H, Kanai T and Ando K 2000 Relative biological effectiveness for cell-killing effect on various human cell lines irradiated with heavy-ion medical accelerator in Chiba (HIMAC) carbon-ion beams *Int. J. Radiat. Oncol.* **48** 241–50
- [56] Nogier T and Regaud C 1914 Decroissance de la radiosensibilité des tumeurs malignes traitées par des doses successives et convenablement espacées des rayons X; autoimmunization contre les rayons *Compt. Rend. Acad. Sci. Paris* **58** 1711–4
- [57] Taggart L E, McMahon S J, Currell F J, Prise K M and Butterworth K T 2014 The role

- of mitochondrial function in gold nanoparticle mediated radiosensitisation *Cancer Nanotechnol.* **5** 5
- [58] International Commission on Radiological Protection 1963 Report of the RBE Subcommittee to the International Commission on Radiological Protection and the International Commission on Radiation Units and Measurements *Health Phys.* **9** 357–86
- [59] IAEA and ICRU 2008 Relative Biological Effectiveness in Ion Beam Therapy **461**
- [60] Kaur H, Pujari G, Semwal M K, Sarma A and Avasthi D K 2013 In vitro studies on radiosensitization effect of glucose capped gold nanoparticles in photon and ion irradiation of HeLa cells *Nucl. Instruments Methods Phys. Res. Sect. B Beam Interact. with Mater. Atoms* **301** 7–11
- [61] McMahon S J, Hyland W B, Muir M F, Coulter J A, Jain S, Butterworth K T, Schettino G, Dickson G R, Hounsell A R, O'Sullivan J M, Prise K M, Hirst D G and Currell F J 2011 Nanodosimetric effects of gold nanoparticles in megavoltage radiation therapy *Radiother. Oncol.* **100** 412–6
- [62] McMahon S J, Hyland W B, Muir M F, Coulter J a, Jain S, Butterworth K T, Schettino G, Dickson G R, Hounsell A R, O'Sullivan J M, Prise K M, Hirst D G and Currell F J 2011 Biological consequences of nanoscale energy deposition near irradiated heavy atom nanoparticles. *Sci. Rep.* **1** 18
- [63] Śmiałek M A, Moore S A, Mason N J and Shuker D E G 2009 Quantification of Radiation-Induced Single-Strand Breaks in Plasmid DNA using a TUNEL/ELISA-Based Assay *Radiat. Res.* **172** 529–36
- [64] Porcel E, Li S, Usami N, Remita H, Furusawa Y, Kobayashi K, Sech C Le and Lacombe S 2012 Nano-Sensitization under gamma rays and fast ion radiation *J. Phys. Conf. Ser.* **373** 012006
- [65] Porcel E, Liehn S, Remita H, Usami N, Kobayashi K, Furusawa Y, Le Sech C and Lacombe S 2010 Platinum nanoparticles: a promising material for future cancer therapy? *Nanotechnology* **21** 85103
- [66] Porcel E, Tillement O, Lux F, Mowat P, Usami N, Kobayashi K, Furusawa Y, Le Sech C, Li S and Lacombe S 2014 Gadolinium-based nanoparticles to improve the hadrontherapy performances. *Nanomedicine* **10** 1601–8
- [67] Schlatholter, Lacombe S, Eustache P, Porcel E, Salado D, Stefancikova L, Tillement O, Lux F, Mowat P, van Goethem M-J, Remita H and Biegun A 2016 Improving proton therapy by metal-containing nanoparticles: nanoscale insights *Int. J. Nanomedicine Volume* **11** 1549
- [68] Kobayashi K, Usami N, Porcel E, Lacombe S and Le Sech C 2010 Enhancement of radiation effect by heavy elements. *Mutat. Res.* **704** 123–31
- [69] Verkhovtsev A V., Korol A V. and Solov'yov A V. 2015 Electron Production by Sensitizing Gold Nanoparticles Irradiated by Fast Ions *J. Phys. Chem. C* **119** 11000–13
- [70] Pešić Z D, Hellhammer R, Sulik B and Stolterfoht N 2009 Strong anisotropy in the proton emission following fragmentation of H₂O molecules by impact with slow, highly charged Xenon ions *J. Phys. B At. Mol. Opt. Phys.* **42** 235202
- [71] Stumpf H 1971 On the theory of electronic processes in ionic crystal semiconductors *Phys. der Kondens. Mater.* **13** 101–17
- [72] Garrison W M, Jayko M E and BENNETT W 1962 Radiation-induced oxidation of protein in aqueous solution. *Radiat. Res.* **16** 483–502
- [73] Garrison W M, Kland-English M J, Sokol H A and Jayko M E 1970 Radiolytic degradation of the peptide main chain in dilute aqueous solution containing oxygen *J. Phys. Chem.* **74** 4506–9
- [74] Swallow A J 1960 Effect of ionizing radiation on proteins, RCO groups, peptide bond cleavage inactivation. -SH Oxidation *Radiation Chemistry of Organic Compounds* ed A J Swallow (New York: Pergamon Press) pp 211–24

- [75] Schuessler H and Schilling K 1984 Oxygen Effect in the Radiolysis of Proteins *Int. J. Radiat. Biol. Relat. Stud. Physics, Chem. Med.* **45** 267–81
- [76] Corre I, Niaudet C and Paris F 2010 Plasma membrane signaling induced by ionizing radiation. *Mutat. Res.* **704** 61–7
- [77] Wong-Ekkabut J, Xu Z, Triampo W, Tang I-M, Tieleman D P and Monticelli L 2007 Effect of lipid peroxidation on the properties of lipid bilayers: a molecular dynamics study. *Biophys. J.* **93** 4225–36
- [78] Haimovitz-Friedman A, Kan C C, Ehleiter D, Persaud R S, McLoughlin M, Fuks Z and Kolesnick R N 1994 Ionizing radiation acts on cellular membranes to generate ceramide and initiate apoptosis. *J. Exp. Med.* **180** 525–35

Chapter IV: RESULTS AND DISCUSSION
Mono- and bimetallic PEGylated gold-platinum nanoparticles

1	Nanoparticles characterization.....	165
1.1	Characterization of by spectrophotometry UV-Vis, TEM and DLS.....	165
1.1.1	Gold PEG-diamine nanoparticles	165
1.1.1.1	Characterization by UV-Vis absorption spectroscopy	165
1.1.1.2	Size estimation from UV-Vis spectra	168
1.1.1.3	Size and morphology determination by TEM and DLS.....	170
1.1.2	Platinum PEG-diamine nanoparticles	171
1.1.2.1	Characterization by UV-Vis absorption spectroscopy	171
1.1.2.2	Size and morphology determination by TEM and DLS.....	172
1.1.2.3	Proposed nanoparticles formation mechanism.....	173
1.1.3	Bimetallic gold-platinum PEG-diamine nanoparticles	176
1.1.3.1	Characterization by UV-Vis absorption spectroscopy	176
1.1.3.2	Size and morphology determination by TEM and DLS.....	177
1.2	Chemical composition	179
1.2.1	Oxidation state and chemical composition by XPS.....	179
1.2.1.1	Gold PEG-diamine nanoparticles	179
1.2.1.2	Platinum PEG-diamine nanoparticles	182
1.2.1.3	Bimetallic gold-platinum PEG-diamine nanoparticles.....	185
1.2.2	Functional characterization by FTIR.....	189
1.3	Conclusion	191

2	Proof of principle: enhancement on the radio-induced nanosize damage	193
3	References.....	197

Chapter IV: RESULTS AND DISCUSSION

Mono- and bimetallic PEGylated gold-platinum nanoparticles

In this chapter we present the characterization and molecular scale analysis of mono-gold, mono-platinum and bimetallic gold-platinum nanoparticles prepared by radiolysis and stabilized by PEG-diamine (PEG-2NH₂). The characterization of the nanoparticles is presented in **Section 1**. The radio-enhancement effect of these nanoparticles is shown and discussed in **Section 2**.

1 Nanoparticles characterization

The mono- and bimetallic PEGylated gold-platinum nanoparticles were characterized following the approach developed in this work to characterize the physico-chemical properties of PEGylated NPs (see **Chapter II- Section 2**).

In **Section 1.1**, a UV-Vis spectrophotometric analysis of nanoparticles colloids is presented. The nanoparticles size distribution was determined by TEM and DLS. The chemical composition of the nanoparticles was evaluated by XPS (**Section 1.2.1**) and FTIR (**Section 1.2.2**).

1.1 Characterization of by spectrophotometry UV-Vis, TEM and DLS

We followed the reduction of metal ions and nanoparticles formation by UV-Vis absorption spectroscopy. The size of mono- and bimetallic nanoparticles was determined by TEM and DLS. The TEM micrographs were obtained with the JEOL 100CXII microscope. In the particular case of gold nanoparticles, we also estimated their size by a simple method based on the UV-Vis data (using the maximum of the plasmon band).

1.1.1 Gold PEG-diamine nanoparticles

1.1.1.1 Characterization by UV-Vis absorption spectroscopy

Figure IV - 1 shows the UV-visible absorption spectra of controls consisting on aqueous solutions containing the precursor Au^{III}Cl₄⁻ (10⁻³ mol.L⁻¹) and the different PEG-2NH₂ (PEG-2000, Mw= 2000 g.mol⁻¹ and PEG-3000, Mw= 3000 g.mol⁻¹), as well as the mixtures Au^{III}Cl₄⁻/PEG-diamine 2000 and 3000 before irradiation.

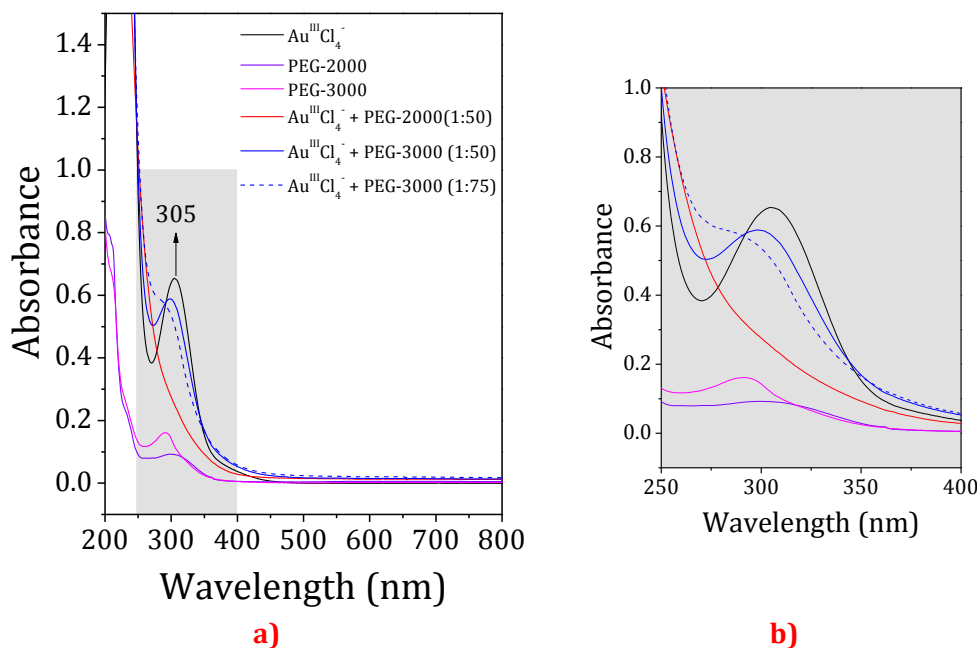


Figure IV - 1. UV-Vis absorption spectra (optical path= 2 mm) of control solutions containing 10^{-3} mol.L⁻¹ Au^{III}Cl₄⁻ and PEG-2NH₂ before irradiation (a). Panel (b) corresponds to the absorption spectra of samples shown in (a) but in a wavelength range from 250 to 400 nm.

In **Figure IV - 1a**, the absorption peak around 305 nm is the characteristic LMCT band of Au^{III}Cl₄⁻ ions, which correspond to the well-known ligand (chloro) to metal (gold) charge transfer.[1] [2] [3]. PEG-diamine at 5×10^{-2} mol.L⁻¹, presented an absorption peak around 290 nm (not observed for PEG-OH **Chapter III - Section 1.1**) and an increasing absorption signal at lower wavelengths. These features are attributed to the $n \rightarrow \sigma^*$ transition of aliphatic amines [4], not observed at lower PEG-diamine concentrations [5]. When gold ions are in the presence of PEG-diamine 2000, a complete disappearance of the LMCT is observed, which might indicate the formation of a complex Au^{III}-PEG-diamine 2000 before irradiation (intermediated species). In contrast, at the same molar ratio, PEG-3000 does not react with Au^{III}Cl₄⁻ and the LMCT is not quenched. By increasing the molar ratio to *ca.* 75 and thus amine groups (spectrum --- in **Figure IV - 1a** and **b**), the LMCT starts to disappear, indicating complexation of gold ions with the amine end-group of PEG. For all controls, no absorption signal is observed in the visible spectral region, indicating neither reduction of metal ions nor metal nuclei formation prior irradiation. Moreover, these solutions containing Au^{III}Cl₄⁻ ions (complexed by PEG or not) and PEGs are stable before irradiation.

[1] Remita S *et al.* (1999) *Radiat. Phys. Chem.* **54** 463–73

[2] Esumi K *et al.* (2000) *Langmuir* **16** 2604–8

[3] Kim Y-G *et al.* (2004) *Chem. Mater.* **16** 167–72

[4] Guedira F *Application de la Spectroscopie UV-Visible* Université Mohammed V-Agdal

[5] Fernandez-Fernandez A *et al.* (2014) *Int. J. Nanomedicine* **9** 4631–48

Figure IV - 2 shows the absorption spectra of solutions containing Au^{III}Cl₄⁻ and PEG-diamine after irradiation. **Figure IV - 2a** corresponds to irradiated samples containing Au^{III}Cl₄⁻ and PEG-2000. **Figure IV - 2b** corresponds to irradiated solutions containing Au^{III}Cl₄⁻ and PEG-3000. The samples were irradiated at different radiation doses to follow the radiolytic reduction of Au^{III} and nanoparticles formation.

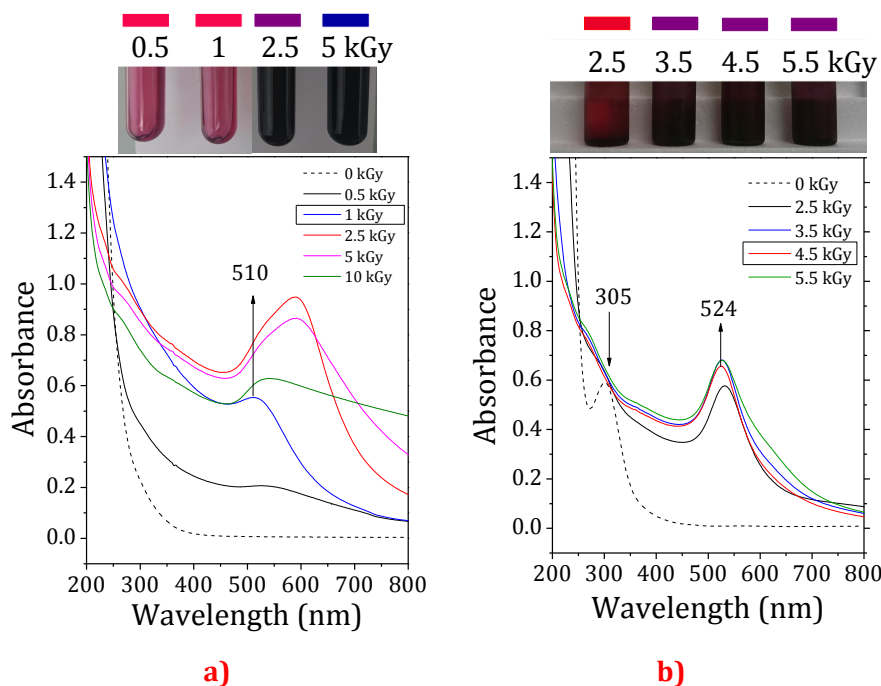


Figure IV - 2. UV-Vis absorption spectra (optical path= 2 mm) of samples containing 10^{-3} mol.L⁻¹ Au^{III}Cl₄⁻, PEG-2000 (a) or PEG-3000 (b) as function of the irradiation dose. Samples were prepared with a molar ratio PEG-2NH₂:Au of ca. 50. Inserted pictures show colloids after different irradiation doses.

After the deposition of 1 kGy to the mixture containing Au^{III}Cl₄⁻ and PEG-2000 (**Figure IV - 2a** in blue), the appearance of a well-defined plasmon band around 510 nm is observed, which is characteristic of a homogeneous colloidal solution composed of small gold nanospheres in water solution (<10 nm) [6]. At this dose, the colloidal solution displays a red colour [7]. For higher doses, the spectra display a broaden absorption plasmon band shifted to larger wavelengths and important scattering of light is observed. This, together with the new purple and blue reflected colours, suggests the formation of large nanoparticles with variable size and shapes [7] [8]. This effect at higher doses might indicate that PEG-2NH₂ is acting as an electron donor by essentially reducing ions adsorbed on the initial nuclei generated by radiolysis [9]. Summarizing, the AuPEG-2000

[6] Polte J *et al.* (2010) *J. Am. Chem. Soc.* **132** 1296–301

[7] NanoEurope Composix “Gold Nanoparticles: Optical Properties”

[8] Kim F *et al.* (2002) *J. Am. Chem. Soc.* **124** 14316–7

[9] *Physico-chimie* (1989) **34** 605–17

NPs colloidal solution obtained after 1 kGy radiation dose is the most homogeneous solution, which remains stable for several months when stored at 4 °C.

Figure IV - 2b corresponds to samples prepared using PEG-2NH₂ with Mw= 3000 g.mol⁻¹. After irradiation the LMCT signals disappears and the gold SPR band raises around 524 nm, which in comparison with AuPEG-2000 NPs corresponds to larger nanoparticles [6]. These colloidal AuPEG-3000 NPs were less stable than AuPEG-2000 NPs and precipitated approximately one week after synthesis. Notably, by keeping a molar ratio PEG-2NH₂:Au of *ca.* 50, which is based on the monomeric unit, the mixture Au^{III}Cl₄⁻ with PEG-3000, contains ~33% less amine groups than the mixture Au^{III}Cl₄⁻ with PEG-2000. This might explain an unsaturated coordination before irradiation, and thus the colloidal instability.

The synthesis of gold nanoparticles by radiolysis has been already investigated [10] [11]. In my work, I demonstrated the feasibility to synthesize AuNPs coated with PEG-diamine in a biocompatible medium (water) using a one-step radiolytic process. This study has shown the strong dependence of synthesis efficiency as a function of the PEG-diamine molecular weight, more particularly as function of the amines concentration. Finally, the NPs composed of PEG-2000 were found more stable than the ones coated with PEG-3000. AuPEG-2000 NPs remained stable for several months (up to a year) at 4 °C.

1.1.1.2 Size estimation from UV-Vis spectra

In 2007, Haiss and co-workers proposed a model to determine the size and concentration of spherical gold nanoparticles from the UV-Vis absorption spectra [12]. This method gives a quantitative description of gold nanoparticles absorbance in a size range from 5 up to 100 nm. We applied this method to get initial estimation about the nanoparticles size before TEM measurements. For small nanoparticles, the absorbance ratio of **Table IV - 1** was used to determine the size of gold nanoparticles.

[6] Polte J *et al.* (2010) *J. Am. Chem. Soc.* **132** 1296–301

[10] Gachard E *et al.* (1998) *New J. Chem.* **22** 1257–65

[11] Abidi W and Remita H (2010) *Recent Patents Eng.* **4** 170–88

[12] Haiss W *et al.* (2007) *Anal. Chem.* **79** 4215–21

Table IV - 1. Ratio of absorbance of gold nanoparticles at the surface plasmon resonance peak (A_{SPR}) to the absorbance at 450 nm (A_{450}) as function of the particle diameter [12].

A_{SPR}/A_{450}	d/nm	A_{SPR}/A_{450}	d/nm
1.10	3	1.56	12
1.19	4	1.61	14
1.27	5	1.65	16
1.33	6	1.69	18
1.38	7	1.73	20
1.42	8	1.80	25
1.46	9	1.86	30
1.50	10	1.92	35

The estimated sizes of AuPEG-2000 (1 kGy) and AuPEG-3000 (4.5 kGy) NPs are summarized in **Table IV - 2**.

Table IV - 2. Nanoparticles size determination by the model reported by Haiss *et al.*

Nanoparticle	λ_{SPR}	A_{SPR}	A_{450}	A_{SPR}/A_{450}	Size determination (nm)
AuPEG-2000 (1 kGy)	510	0.55	0.53	1.04	~3
AuPEG-3000 (4.5 kGy)	524	0.66	0.42	1.57	~12

This method gives size evaluation of 3 nm for gold nanoparticles synthesized with PEG-2000 and 12 nm for those synthesized with PEG-3000. For particle diameters smaller than 10 nm, the reported values should only be considered as estimation.

1.1.1.3 Size and morphology determination by TEM and DLS

Figure IV - 3 shows TEM micrographs of AuPEG-2000 NPs synthesized with a total radiation dose of 1 kGy, as well as, their core diameter size distribution.

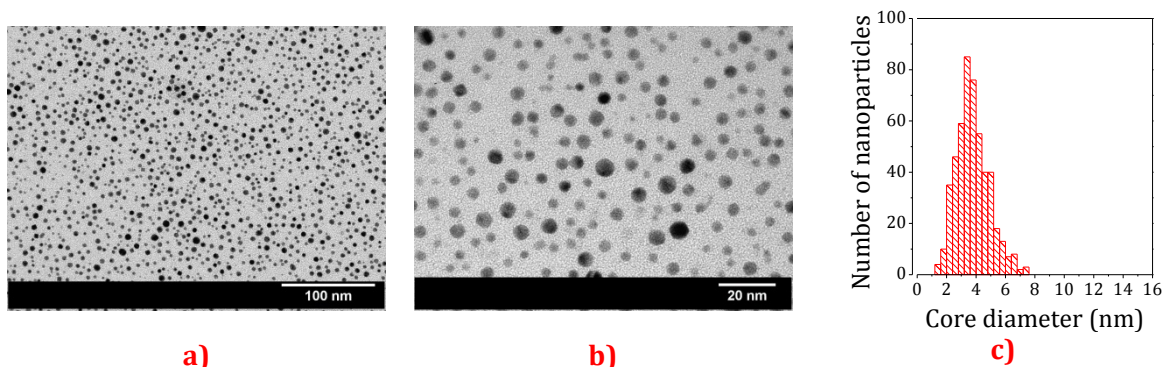


Figure IV - 3. TEM micrographs (a) of AuPEG-2000 NPs synthesized at 10^{-3} mol.L⁻¹ with a PEG-2NH₂:Au molar ratio of *ca.* 50 with a total dose of 1 kGy. (b) Magnified image of AuPEG-2000 NPs. (c) Core size distribution.

We observe well dispersed gold nanoparticles in panel **(a)**. The magnified image in panel **(b)** displays mainly spherical nanoparticles. These as-synthesized AuPEG-2000 NPs have an average core diameter of 3.8 ± 1.1 nm **(c)** and an hydrodynamic diameter of about 10.3 ± 2.7 nm (PDI= 0.290 ± 0.003).

Figure IV - 4 shows TEM micrographs of fresh AuPEG-3000 NPs synthesized with a total radiation dose of 4.5 kGy, as well as, their diameter size distribution.

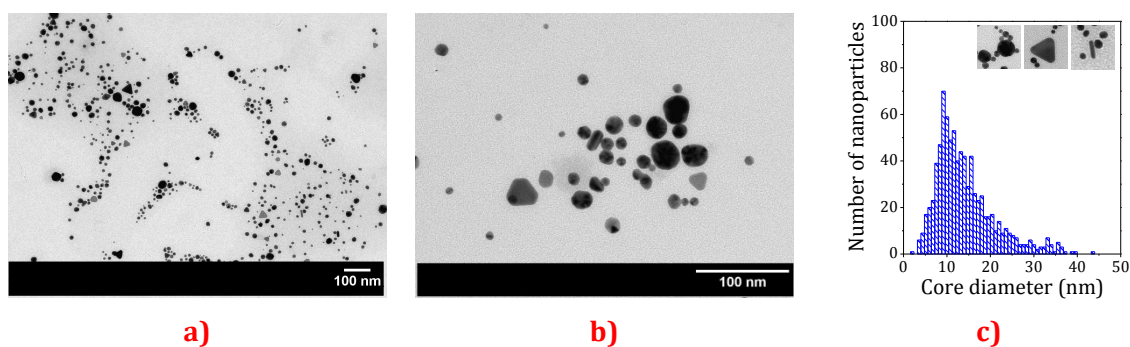


Figure IV - 4. TEM micrographs (a) of AuPEG-3000 NPs synthesized at 10^{-3} mol.L⁻¹ with a PEG-2NH₂:Au molar ratio of *ca.* 50. (b). Magnified image of AuPEG-3000 NPs. The core size distribution is shown in (c).

In contrast with AuPEG-2000 NPs, we observe higher polydispersity. We found nanospheres, squares, triangles and rods. Spherical particles have an average size of 14.2 ± 7.1 nm **(Figure IV - 4c)**. DLS measurements were not performed due to this high polydispersity. TEM measurements confirmed the difference of size and shape homogeneity of NPs as function of the polymeric chain length and the amine content.

In this work, we chose to further focus on the smallest and more stable Au NPs coated with PEG-2NH₂ Mw=2000 g.mol⁻¹ (PEG-2NH₂:Au molar ratio of *ca.* 50, D= 1kGy). In the next sections, these nanoparticles are simply named AuPEG-2NH₂ NPs.

1.1.2 Platinum PEG-diamine nanoparticles

1.1.2.1 Characterization by UV-Vis absorption spectroscopy

Figure IV - 5 shows the absorption spectra of aqueous solutions containing 10⁻³ mol.L⁻¹ (Pt(NH₃)₄)²⁺ and PEG-2NH₂ (Mw= 2000 g.mol⁻¹) before and after increasing irradiation doses. The maximum radiation dose was fixed to 10 kGy, which is the required dose for total platinum reduction in the presence of PEG-OH (Mw= 1000 g.mol⁻¹) (see results by XPS in **Chapter III – Section 1.3.2**). The solutions were prepared with a molar ratio PEG-2NH₂:Pt of *ca.* 50. These solutions remained stable prior irradiation.

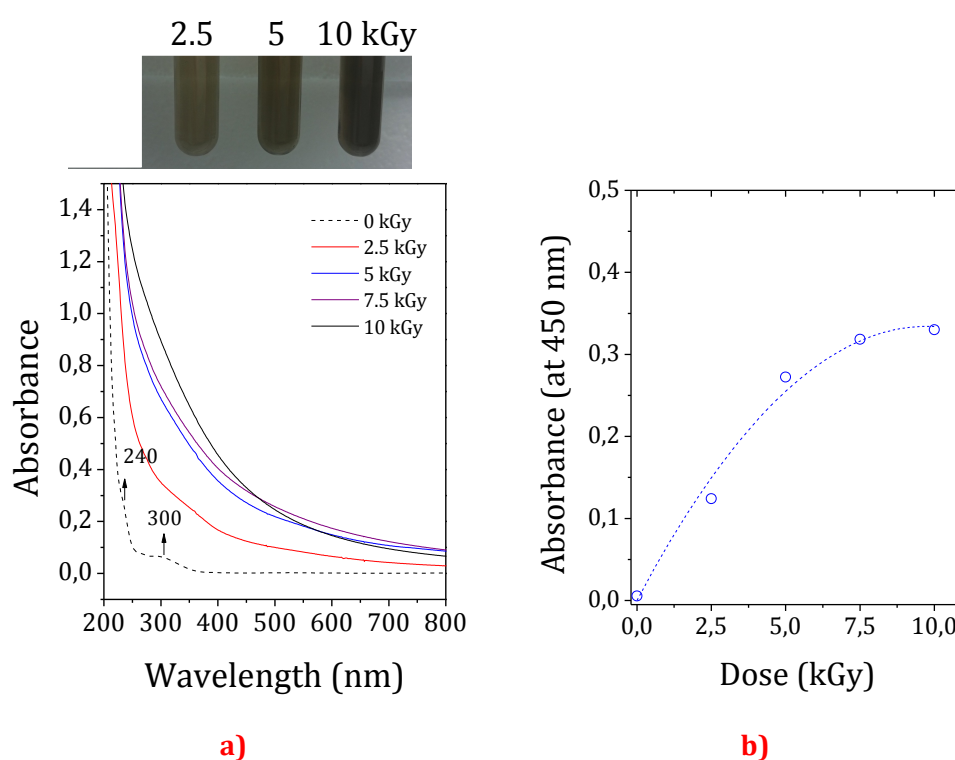


Figure IV - 5. (a) UV-Vis absorption spectra (optical path= 2 mm) of samples containing 10⁻³ mol.L⁻¹ (Pt(NH₃)₄)²⁺ and PEG-2000 as function of the irradiation dose. Samples were prepared with a molar ratio PEG-2NH₂:Pt of *ca.* 50. (b) Evolution of the absorbance at 450 nm as function of the irradiation dose.

The absorption spectrum before irradiation reveals an absorption peak around 300 nm and a small shoulder around 240 nm (**Figure IV - 5a**), which are similar to those steady signals identified before the radiolytic synthesis of PtPEG-OH NPs. These absorptions correspond to the LMCT band of platinum complexes (Pt(NH₃)₄)²⁺ (see the case of PtPEG-OH NPs in **Chapter III– Section 1.1**). After irradiation, we observed the disappearance of

these two absorption peaks and the appearance of the characteristic stretched absorption spectra in the visible region, suggesting the formation of platinum nanoparticles [13]. The inserted picture in **Figure IV - 5a**, shows colloidal solutions containing Pt after irradiation at doses of 2.5, 5 and 10 kGy. These display the solution colour change, from light to darker brown, which is a qualitative evidence for nanoparticles formation, and thus the increasing nanoparticles concentration as function of the dose. **Figure IV - 5b** shows the evolution of the absorbance in the visible region (at $\lambda = 450$ nm) when increasing the dose. An absorbance plateau is reached after 10 kGy suggesting the total reduction of Pt^{II} ions.

The platinum nanoparticles here presented remain stable at 4°C for several months (verified by UV-Vis spectrophotometry and DLS). We further characterized those nanoparticles obtained after 2.5 and 10 kGy by TEM.

1.1.2.2 Size and morphology determination by TEM and DLS

For comparison, **Figure IV - 6** shows TEM micrographs of PtPEG-2NH₂ NPs prepared at 10⁻³ mol.L⁻¹ after 2.5 kGy (**a**) and 10 kGy (**b**).

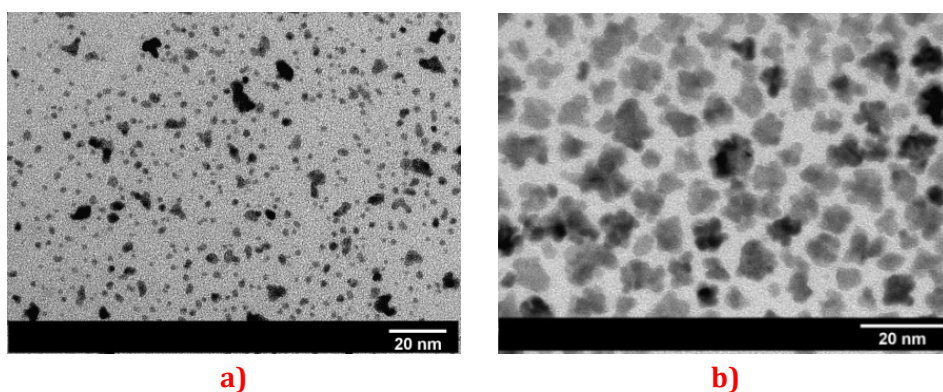


Figure IV - 6. TEM micrograph of PtPEG-2NH₂ NPs at 10⁻³ mol.L⁻¹ prepared with a total dose of 2.5 kGy (a) and 10 kGy (b).

We observe high polydispersity in the sample prepared with a radiation dose of 2.5 kGy (**Figure IV - 6a**). It contains discrete spherical particles of about 2.3 ± 0.9 nm in diameter and nanoparticles aggregates with variable shapes. On the other hand, after 10 kGy we mostly observe nanoparticles aggregates having an average diameter of 4.9 ± 2.7 nm (**Figure IV - 6b**).

[13] Henglein A *et al.* (1995) *J. Phys. Chem.* **99** 14129–36

The synthesis of PtPEG-2NH₂ NPs was also performed at 5×10^{-3} mol.L⁻¹ (PEG-2NH₂:Pt *ca.* 50, 50 kGy). **Figure IV - 7** shows TEM micrographs of these as-synthesized PtPEG-2NH₂ NPs, as well as, their size distribution.

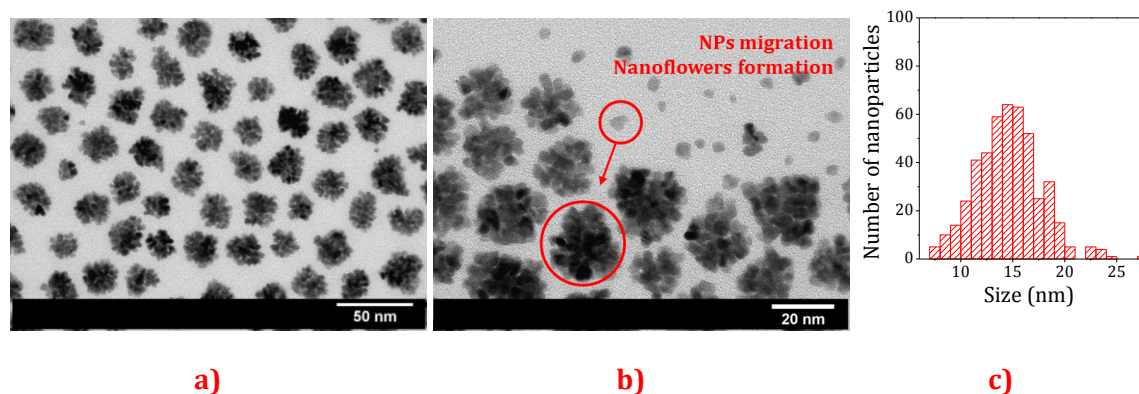


Figure IV - 7. TEM micrographs at two different magnifications of PtPEG-2NH₂ NPs synthesized at 5×10^{-3} mol.L⁻¹ prepared with a total dose of 50 kGy (a) and (b). PtPEG-2NH₂ NPs size distribution (c).

At these conditions, the nanoparticles were homogeneously formed as aggregates of about 14.6 ± 7.4 nm. This morphology is commonly named as nanoflowers (Pt NFs) [14]. These Pt NFs consist of discrete nanoparticles with an average diameter size of 3.2 ± 1.6 nm, which is equivalent to the size of the individual PtPEG-OH NPs (see size distribution in **Chapter III – Section 1.2**). Platinum nanoflowers colloids have an average hydrodynamic diameter of about 16.1 ± 4.6 nm (PDI= 0.115 ± 0.004).

1.1.2.3 Proposed nanoparticles formation mechanism

We attribute the formation of platinum nanoflowers to an intra-molecular cross-linking induced by radiolysis [15]. In the cross-linking process (see irradiation of polymers in **Chapter I – Section 1.1.2.4**), the polymeric chains are oxidized and macroradicals (polymer radicals) are produced to later form a polymer matrix.

The primary products of radiolysis have different rates of reaction with hydrophilic polymers [16] [17]. The rate of reaction of solvated electrons, entities that in the present case will preferentially reduce metal ions to neutral atoms, is relatively low in the presence of polymers. Solvated electrons have a rate constant within the range of 10^6 dm³.mol⁻¹.s⁻¹ [17]. In contrast, the rate constant of hydroxyl radicals is higher with a value

[14] Dandapat A *et al.* (2013) *Nanomater. Nanotechnol.* **3**

[15] Jovanović Ž *et al.* (2011) *Radiat. Phys. Chem.* **80** 1208–15

[16] Rosiak J M *et al.* (1995) *Radiat. Phys. Chem.* **46** 161–8

[17] Rosiak J M and Ulański P (1999) *Radiat. Phys. Chem.* **55** 139–51

in the range of $10^8 \text{ dm}^3 \text{ mol}^{-1} \text{ s}^{-1}$ [17]. Thus, OH· radicals are the main species of water radiolysis that react with polymer chains.

In the case of poly (ethylene oxide) chains, all the hydrogen atoms in the polymer are equivalent (-CH₂). Therefore, only one type of macroradicals can be formed upon OH· radicals' attack, which is localized on carbon atoms (**Figure IV - 8**, [18]). This structure of the carbon-centered polymer radicals is the great importance for the process of crosslinking. The concentration and molecular weight of the polymer are also important aspects that determine the crosslinking and competing reactions yields [17].

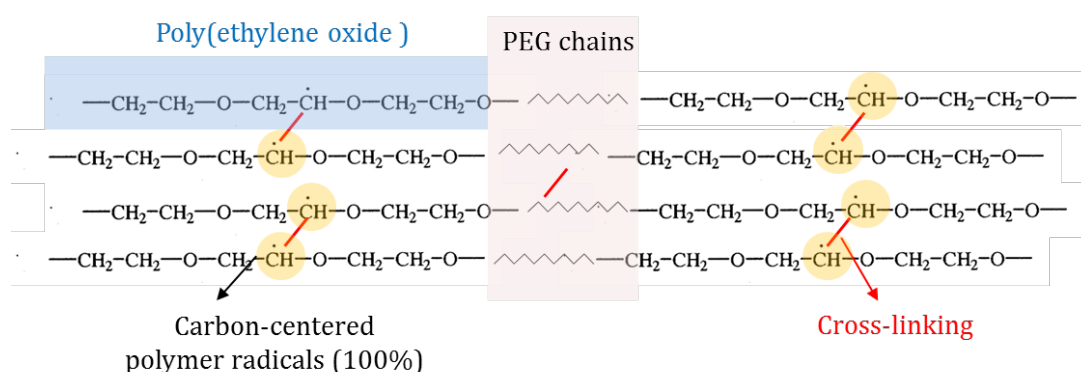


Figure IV - 8. Cross-linking process and structure of the poly (ethylene oxide) radical formed upon irradiation in aqueous solution.

It is suggested that the cross-linking occurs due to the absence of the intermediated species created using PEG-OH (see discussion **Chapter III - Section 1.4**). Before irradiation, the amine end-groups of PEG do not interact with the platinum complex, $(\text{Pt}(\text{NH}_3)_4)^{2+}$, contrary to the hydroxyl end-groups of PEG.

In the present case, the synthesis of nanoflowers might be understood considering two main simultaneous reactions: i) direct oxidation of PEG chains (macroradicals formation) and ii) reduction of the metal precursor. The formation of nanoflowers might be attributed to the induction of a slight swelling, facilitating discrete metal species to migrate and aggregate (**Figure IV - 7b**). This migration has been already observed during hydrogel preparation by radiolysis [15]. The proposed mechanism of platinum nanoflowers' formation is illustrated in **Figure IV - 9**.

[15] Jovanović Ž *et al.* (2011) *Radiat. Phys. Chem.* **80** 1208–15

[17] Rosiak J M and Ulański P (1999) *Radiat. Phys. Chem.* **55** 139–51

[18] Rosiak J M *et al.* (2002) *IAEA-TECDOC-1324*

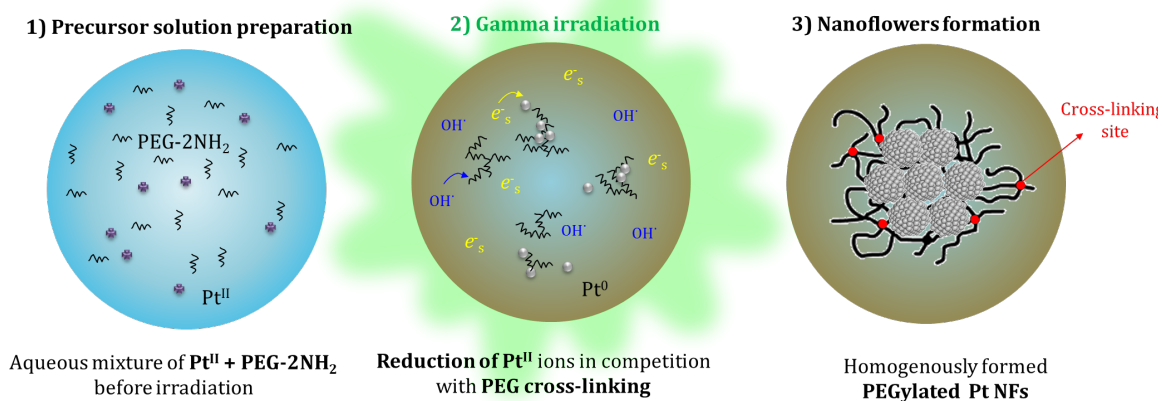


Figure IV - 9. Schematic synthesis of PtPEG-2NH₂ NPs (Pt NFs) by the proposed mechanism involving free Pt^{II} ions in the presence of free PEG-2NH₂ before irradiation (1), the radiolytic reduction of metal ions in competition with the polymer cross-linking process (2) and the homogenous formation of Pt NFs embedded into the PEG matrix (3).

By TEM, we observed that this last process is dose dependent (**Figure IV - 6**). At lower doses (as shown for 2.5 kGy), it is suggested that neither the metal ions reduction nor cross-linking processes are completed. At higher doses, it is expected total reduction (**Figure IV - 5b**).

We used the PtPEG-2NH₂ NPs synthesized at 5x10⁻³ mol.L⁻¹ (50 kGy) for all further characterization (XPS and FTIR presented in Section 1.2). The synthesis of these nanoparticles was reproducible. They were found stable for months (up to a year) when stored at 4°C (verified by UV-vis spectrophotometry and DLS). In particular, diluted solutions of PtPEG-2NH₂ NPs were used to elucidate their radiation enhancing effect on the induction of nanosize molecular damage (see results in **Section 2**).

1.1.3 Bimetallic gold-platinum PEG-diamine nanoparticles

1.1.3.1 Characterization by UV-Vis absorption spectroscopy

Figure IV - 10 shows the absorption spectra of aqueous solutions containing (Pt(NH₃)₄)²⁺ and Au^{III}Cl₄⁻ in the presence of PEG-2NH₂ (Mw= 2000 g.mol⁻¹) before (controls **(a)**) and after exposure to increasing irradiation doses **(b)**. Bimetallic nanoparticles were synthesized with a Pt:Au molar ratio of 1:1 and by keeping a PEG-2NH₂:metal molar ratio of *ca.* 50 (see experimental conditions in **Chapter II – Section 1.2**). Before irradiation the precursor solutions were found stable.

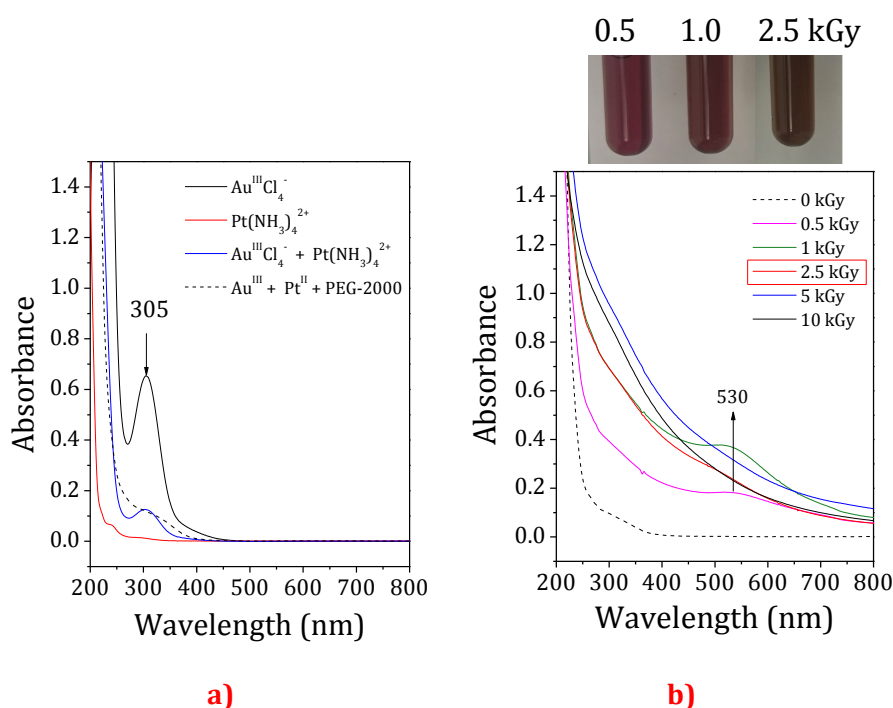


Figure IV - 10. UV-Vis absorption spectra (optical path= 2 mm) of controls before irradiation (a) and samples containing 5x10⁻⁴ mol.L⁻¹ Au^{III}Cl₄⁻, 5x10⁻⁴ mol.L⁻¹ Pt(NH₃)₄²⁺ and 5x10⁻² PEG-2NH₂ (Mw= 2000 g.mol⁻¹) as function of the irradiation dose (b). Inserted pictures in (b) show colloids after different irradiation doses.

Before irradiation, the absorption spectrum of the mixture Au^{III}Cl₄⁻ / (Pt(NH₃)₄)²⁺ in water (**Figure IV - 10a** (—)) displays the LMCT of the Au^{III}Cl₄⁻ ions at 305 nm. This signal disappears in the presence of PEG-2NH₂ (Mw= 2000 g.mol⁻¹) confirming the complexation between gold ions and PEG-2NH₂. By irradiating (**Figure IV - 10b**), a rising band around 530 nm is observed. This band corresponds to the SPR of gold, which indicates that gold ions are reduced and coalesced into atomic nanoclusters.

By increasing the radiation dose, the SPR of gold disappears and we observe the appearance of the stretched absorption spectra characteristic of pure colloidal Pt NPs. This

spectral evolution has already been described [19] [20] and corresponds to the formation of bilayered Au_{core}-Pt_{shell} nanoparticles. A complete disappearance of the SPR of gold was identified after 2.5 kGy irradiation, suggesting complete reduction of the auric ions and formation of platinum coating.

The inserted picture in **Figure IV - 10b** reveals the colour transition from red (gold) to brown (platinum), which suggests the bilayered gold-platinum structure. When Pt^{II} is used, only Au_{core}/Pt_{shell} particles might be obtained [11]. This structure is explained by early electron transfer from Pt complexes or nascent Pt⁰ to gold complexes (Au^{III} and intermediated Au^I species), which leads to a faster gold reduction forming small nuclei prior the creation of the Pt shell (**Figure IV - 11**).

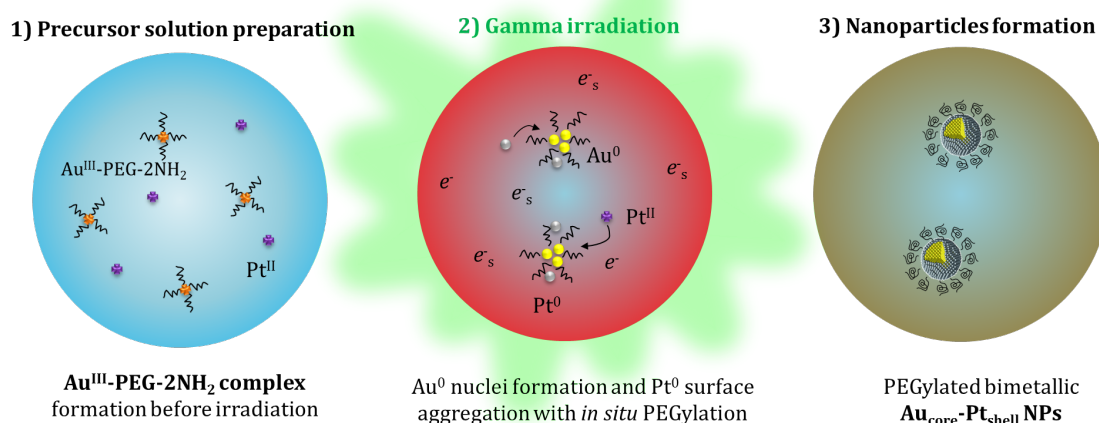


Figure IV - 11. Schematic synthesis of Au:PtPEG-2NH₂ NPs by the formation of an Au^{III}-PEG-2NH₂ complex (1), the radiolytic reduction of metal ions and early electron transfer from Pt to Au (2) and formation of Au_{core}-Pt_{shell} structured nanoparticles stabilized by PEG-2NH₂ (3).

In conclusion, I managed to produce biocompatible bimetallic gold-platinum nanoparticles stabilized by PEG for biomedical concerns. These Au:PtPEG-2NH₂ NPs remain stable for several months (up to a year) at 4 °C.

1.1.3.2 Size and morphology determination by TEM and DLS

Figure IV - 12 shows TEM micrographs of Au:PtPEG-2NH₂ NPs synthesized with a total radiation dose of 2.5 kGy.

[11] Abidi W and Remita H (2010) *Recent Patents Eng.* **4** 170–88

[19] Mirdamadi-Esfahani M *et al.* (2010) *Gold Bull.* **43** 49–56

[20] Remita H *et al.* (2005) *Radiat. Phys. Chem.* **72** 575–86

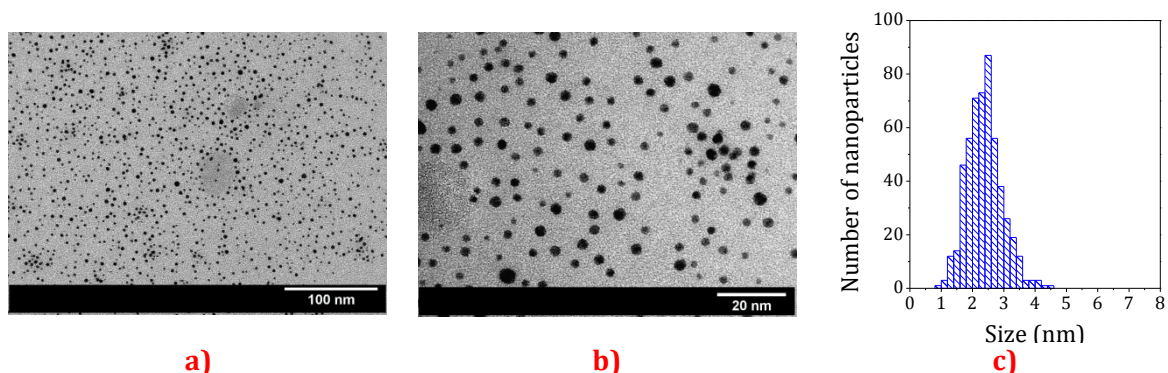


Figure IV - 12. TEM micrographs of Au:PtPEG-2NH₂ NPs synthesized at 10^{-3} mol.L⁻¹ with a PEG-2NH₂:M_T molar ratio of *ca.* 50 (a). Magnified image of Au:PtPEG-2NH₂ NPs (b), The core size distribution is shown in (c).

We observe well dispersed nanoparticles. They are homogeneous in size and shape having an average spherical core diameter of 2.4 ± 0.6 nm (c) and an d_H of 9.3 ± 3.0 nm (Pdl = 0.258 ± 0.085).

1.2 Chemical composition

We evaluated the oxidation state and chemical composition of the mono- and bimetallic gold-platinum PEGylated nanoparticles by XPS and FTIR spectroscopy.

1.2.1 Oxidation state and chemical composition by XPS

Figure IV - 13 shows the survey XPS spectra of the mono and bimetallic nanoparticles. Only the characteristic binding energies of Au, Pt, C, O, N and Cl were observed.

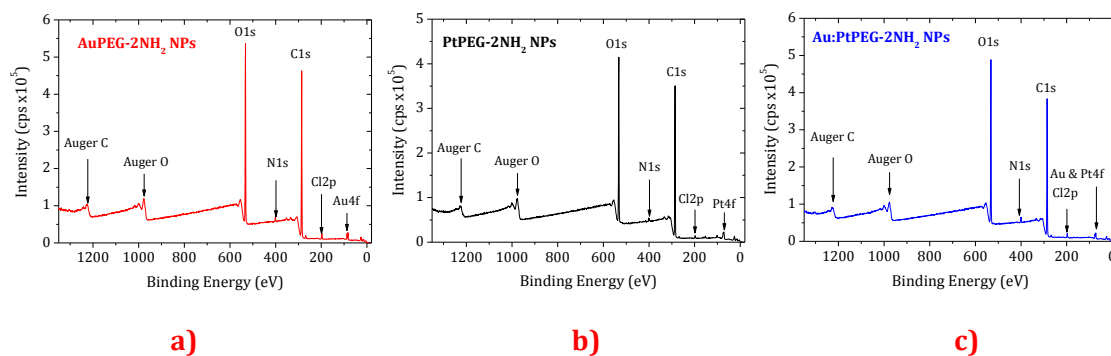


Figure IV - 13. Survey XPS spectra of the as-synthesized PtPEG-2NH₂, AuPEG-2NH₂ and Au:PtPEG-2NH₂ NPs.

1.2.1.1 Gold PEG-diamine nanoparticles

Figure IV - 14 shows the high-resolution XPS spectra of a metallic gold surface (bulk Au⁰ control) and AuPEG-2NH₂ NPs (D=1 kGy) at the Au-4f core level region.

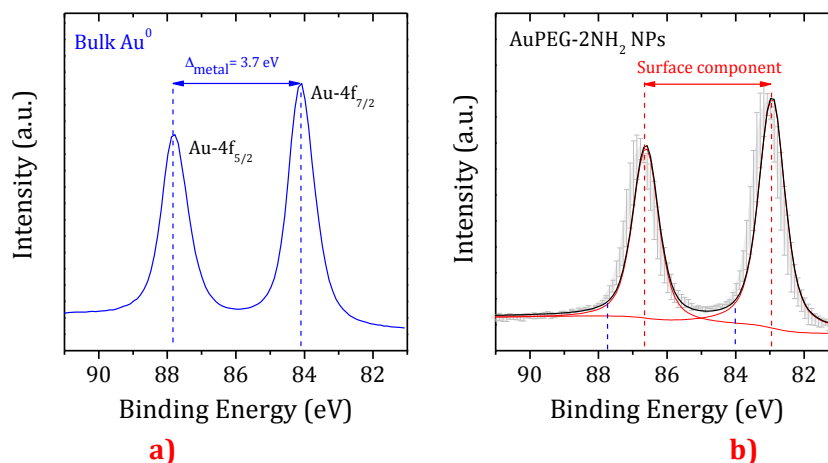


Figure IV - 14. XPS spectra corresponding to the Au-4f core level region of gold on (a) a metallic gold film and (b) on AuPEG-2NH₂ NPs.

In agreement with literature [21], the characteristic Au-4f_{7/2} and Au-4f_{5/2} spin-orbit components of metallic Au ($\Delta_{\text{metal}} \sim 3.7$ eV) were measured at 84.1 and 87.8 eV respectively on the metallic gold surface (**Figure IV - 14a**). The binding energy of Au⁰ nanoparticles (**Figure IV - 14b**) is observed ~ 1.2 eV below that for bulk, consistent with that expected for Au surface state [22]. At the Au-4f core level AuPEG-2NH₂ NPs have BEs of ~ 82.9 and 86.6 eV.

The C-1s, O-1s and N-1s XPS spectra of AuPEG-2NH₂ NPs are shown in **Figure IV - 15**. The inserted vertical dotted lines indicate the BE position of the control (pure PEG-2NH₂ – upper spectra).

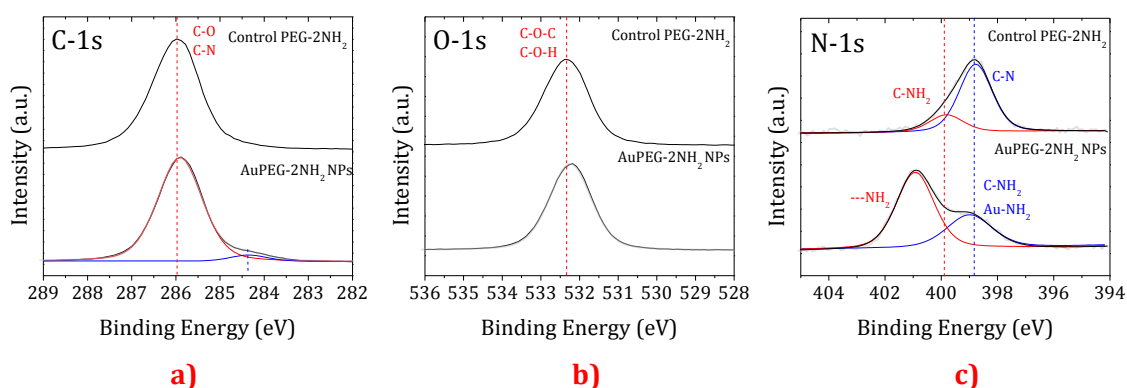


Figure IV - 15. XPS spectra of AuPEG-2NH₂ NPs at the C-1s (a), O-1s (b) and N-1s (c) regions.

The XPS measured binding energies, assignments and FWHM of controls (the metallic gold surface and PEG-2NH₂) and nanoparticles at the Au-4f, C-1s, O-1s and N-1s core levels are listed below in **Table IV - 3**.

The binding energies at the C-1s and O-1s core levels of AuPEG-2NH₂ NPs are identical to those of the native PEG-2NH₂. This has been already observed, indicating that the poly(ethylene oxide) chains keep their native chemical structure and may dominate a monolayer configuration [23]. We also observe in **Table IV - 3** that, at the C-1s and O-1s core levels, the FWHM values of AuPEG-2NH₂ NPs are identical to those of the control (≤ 0.2 eV), which is an additional indication of a perpendicular grafting of PEG molecules [24]. The small shoulder observed at lower BE at the C-1s region (**Figure IV - 15a**), which was also observed in the case of PtPEG-OH NPs (see results in **Chapter III - Section 1.3.3**), may be attributed to the C-C bonding [23]. The appearance and intensity of this

[21] Moulder J F *et al.* (1992) *Handbook of X-ray Photoelectron Spectroscopy*

[22] Citrin P H *et al.* (1983) *Phys. Rev. B* **27** 3160–75

[23] Hong R *et al.* (2005) *Chem. Mater.* **17** 4617–21

[24] Crispin X *et al.* (2001) *J. Electron Spectros. Relat. Phenomena* **121** 57–74

peak depends on the samples preparation protocol. PEG-2NH₂ was measured as powder (directly from the supplier) and nanoparticles as colloids after drop casting and natural drying. This variance may induce a different interaction between the PEG and the substratum (glass coverslip) [25].

Table IV - 3. XPS data summary: binding energy, assignment and FWHM of AuPEG-2NH₂ NPs.

Compound	Atomic core level	BE (eV)	Assignment	FWHM (eV)
PEG-2NH ₂	C-1s	285.9	C-O & C-N	1.3
	O-1s	532.4	C-O-HC-O-C	1.4
	N-1s	398.8	C-N	1.4
	N-1s	399.8	C-NH ₂	1.4
Au ⁰ solid	Au-4f _{7/2}	84.1	Au ⁰	0.9
	Au-4f _{5/2}	87.8	Au ⁰	0.9
AuPEG-2NH ₂ NPs	Au-4f _{7/2} surf.	82.9	Au ⁰	0.8
	Au-4f _{5/2} surf.	86.6	Au ⁰	0.8
	C-1s	285.9	C-O & C-N	1.2
	C-1s	284.4	-	1.0
	O-1s	532.2	C-O-H C-O-C	1.3
	N-1s	399.0	C-NH ₂ Au-NH ₂	1.9
	N-1s	400.9	---NH ₂	1.6

At the N-1s core level (**Figure IV - 15c**), the control sample presents two N-1s contributions around 398.8 and 399.8 eV. These BEs are characteristic of the primary amine end-group of PEG [21]. For nanoparticles, the N-1s spectrum contains two steady peaks at 399.0 and 400.9 eV, which are attributed to non-protonated and protonated amines, respectively. In agreement with other works [26], the lower binding energy component is particularly assigned to nitrogen in the pendant amine groups directly bond to gold nanoparticles. We also observe a broadening of about 36%, from 1.4 to 1.9 eV at this BE, which confirms the Au-N binding [26] [24]. The higher binding energy component

[21] Moulder J F *et al.* (1992) *Handbook of X-ray Photoelectron Spectroscopy*

[24] Crispin X *et al.* (2001) *J. Electron Spectros. Relat. Phenomena* **121** 57-74

[25] Kovach K M *et al.* (2014) *J. Biomed. Mater. Res. A* **102** 4195-205

[26] Kumar R *et al.* (2004) *Nanotechnology in Catalysis* Kluwer Academic/Plenum Publishers

also suggest the presence of hydrogen bonded amines (---NH_2), which might be consequence of a high graft density [27].

In conclusion, AuPEG-2NH₂ NPs consist on Au⁰ atoms only. It is suggested that PEG-2NH₂ chains are grafted perpendicularly [24] to the NP surface and that amine groups are directly bonded to nanoparticles [26].

1.2.1.2 Platinum PEG-diamine nanoparticles

Figure IV - 16 shows the high-resolution XPS spectrum of the PtPEG-2NH₂ NPs (D= 10 kGy) at the Pt-4f core level region. The spectrum deconvolution shows two contributions, one at 72.0 and 75.3 eV (in blue) and another at 70.4 and 73.7 eV (in red). These BEs correspond the Pt-4f_{7/2} and Pt-4f_{5/2} spin-orbit components of platinum [21]. At lower BEs it is clearly observed the surface component of Pt⁰ [28].

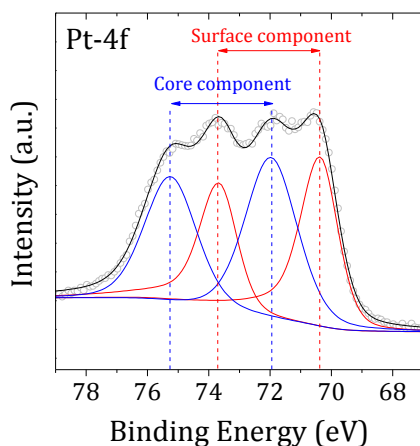


Figure IV - 16. XPS spectrum of PtPEG-2NH₂ NPs at the Pt-4f core level region.

The peaks at 72.0 and 75.3 eV are attributed to the core component of Pt⁰. This statement was confirmed by performing XPS analysis in samples prepared with an irradiation dose of 2.5 kGy. Those platinum nanoparticles (see **Figure IV - 6a**) were not completely reduced as we observed a main contribution of the intermediated Pt^I around 72.6 eV (XPS spectrum not presented here).

[21] Moulder J F *et al.* (1992) *Handbook of X-ray Photoelectron Spectroscopy*

[24] Crispin X *et al.* (2001) *J. Electron Spectros. Relat. Phenomena* **121** 57–74

[26] Kumar R *et al.* (2004) *Nanotechnology in Catalysis* Kluwer Academic/Plenum Publishers

[27] Graf N *et al.* (2009) *Surf. Sci.* **603** 2849–60

[28] Puglia C *et al.* (1995) *Surf. Sci.* **342** 119–33

The intensity ratio between the two platinum contributions was not consistent, even for different replicates of the same sample likely due to the heterogeneous NPs layer, which was prepared from colloidal solutions by drop casting and natural drying (see method **Chapter II – Section 2.5.2**). However, more important, the BEs were found at the same position for all the independent batches, confirming the presence of both steady Pt components.

In comparison with PtPEG-OH NPs (presented in **Chapter III – Section 1.3.2**), the BEs at the Pt-4f core level is shifted by about 1 eV, which is attributed to a chemical shift [29]. This suggests a strong interaction between the Pt⁰ nanoflowers and the PEG matrix by chemisorption of PEG molecules in the surface of the Pt NFs (Pt-O interaction) [30] [31].

We also investigated the C-1s, O-1s and N-1s core level BEs of nanoparticles to better elucidate the chemical configuration of the polymeric matrix. The C-1s, O-1s and N-1s XPS spectra of PtPEG-2NH₂ NPs are shown in **Figure IV - 17**.

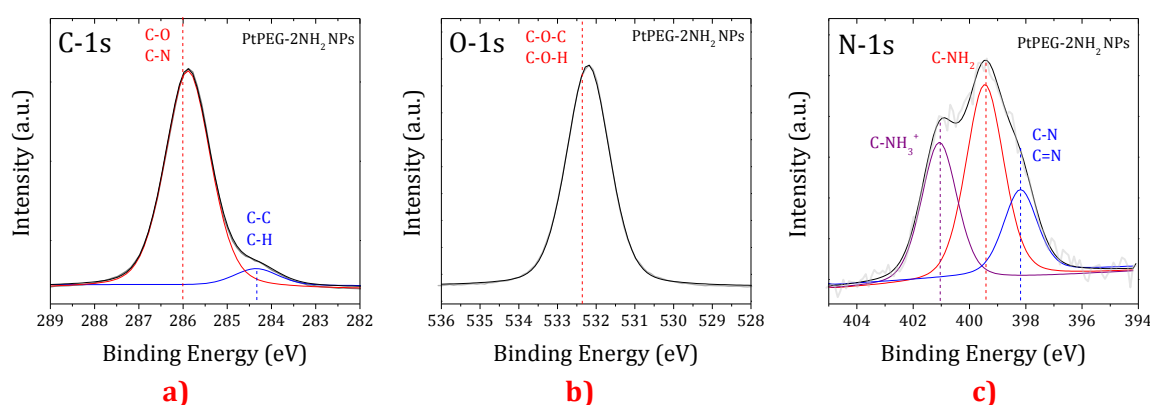


Figure IV - 17. XPS spectra of a control consisting on pure PEG-2NH₂ and PtPEG-2NH₂ NPs at the C-1s (a), O-1s (b) and N-1s (c) regions.

At the C-1s and O-1s core levels (**Figure IV - 17a and b**), the characteristic binding energies of PEG around 286.0 and 532.3 eV [32] were observed. These results indicate that the poly (ethylene oxide) chains of PEG-2NH₂ conserve their native C-O, C-N, C-O-C and C-O-H chemical structure after cross-linking [33] [34]. The C-1s signal observed at lower binding energy is assigned to C-C chemical structures, which might characterize the

[29] Feldman L C and Mayer J W (1986) X-ray photoelectron spectroscopy *Fundamentals of surface and thin film analysis* p 224

[30] Ono L K *et al.* (2010) *J. Phys. Chem. C* **114** 22119–33

[31] Parmigiani F *et al.* (1990) *J. Electron Spectros. Relat. Phenomena* **50** 39–46

[32] Beamson G and Briggs D (1992) *High resolution XPS of organic polymers, the scienta ESCA300 database*

[33] Truica-Marasescu F and Wertheimer M R (2008) *Plasma Process. Polym.* **5** 44–57

[34] Jansen R J J and van Bekkum H (1995) *Carbon N. Y.* **33** 1021–7

cross-linking process as illustrated in **Figure IV - 8**. This signal was clearly more intense than that of AuPEG-2NH₂ NPs (background due to interaction with the substratum). For instance, for one measured point, the area of the C-1s peak (cps/eV) increased from 3795.2 (AuPEG-2NH₂ NPs) to 7869.1 (PtPEG-2NH₂ NPs).

Remarkably, the XPS spectrum of nanoparticles at the N-1s core level differs greatly from the control (see upper spectrum **Figure IV - 15c**) and three stable components were detected. The XPS peak around 401.1 eV is assigned to the protonated form of alkylamines (C-NH₃⁺) [33] [21] while the contribution at ~399.5 eV is assigned to non-protonated alkylamines (-NH₂) both species may originate from radiolysis and the *in situ* cross-linking process. More interestingly, the shoulder observed around 398.2 eV may overlap the C-N and C=N chemical structures. This result also suggests a grafting polymerization (see irradiation of polymer described in **Chapter I - Section 1.1.2.4**) between the polymeric radicals induced by radiation and the amine end-groups of PEG. The N-1s binding energy of aliphatic C=N species are commonly found in a BE interval from 397.8 to 399.0 eV [33] [35]. Non-significant broadening was observed (± 0.2 eV) at the N-1s core level.

The XPS measured binding energies, assignments and FWHM of PtPEG-2NH₂ NPs at the Pt-4f, C-1s, O-1s and N-1s core levels are summarized in **Table IV - 4**.

We observed in **Table IV - 4** that the FWHM of PtPEG-2NH₂ NPs, at the Pt-4f core level, increased in about 43%, from ~1.4 to ~2.0. This broadening confirms the interaction of Pt NPs with PEG suggesting as well a flat PEG grafting [24].

[21] Moulder J F *et al.* (1992) *Handbook of X-ray Photoelectron Spectroscopy*

[24] Crispin X *et al.* (2001) *J. Electron Spectros. Relat. Phenomena* **121** 57-74

[33] Truica-Marasescu F and Wertheimer M R (2008) *Plasma Process. Polym.* **5** 44-57

[35] Rangan S *et al.* (2005) *J. Phys. Chem. B* **109** 12899-908

Table IV - 4. XPS data summary: binding energy, assignment and FWHM of the control (pure PEG-2NH₂) and PtPEG-2NH₂ NPs.

Compound	Atomic core level	BE (eV)	Assignment	FWHM (eV)
PtPEG-2NH ₂ NPs	Pt-4f _{7/2} surf.	70.4	Pt ⁰	1.4
	Pt-4f _{5/2} surf.	73.7	Pt ⁰	1.4
	Pt-4f _{7/2} core	72.0	*PtO	2.0
	Pt-4f _{5/2} core	75.3	*PtO	2.0
	C-1s	285.9	C-O & C-N	1.2
	C-1s	284.4	C-H & C-C	1.2
	O-1s	532.2	C-O-H C-O-C	1.3
	N-1s	399.5	C-NH ₂	1.6
	N-1s	401.1	C-NH ₃ ⁺	1.5
N-1s	398.2	C-N & C=N	1.4	

*chemisorbed oxygen [28] [31]

In conclusion, these XPS results show that PtPEG-2NH₂ NPs consist in Pt⁰ atoms, which might strongly interact with the formed polymeric matrix by chemisorption of PEG molecules on the surface of the Pt NFs. At the C-1s and O-1s core levels we observed that the poly(ethylene oxide) chains keep their chemical structure. Finally, at the N-1s core level we observed the presence of three different nitrogen species, which might also indicate the formation of intra-molecular C-C bonds (cross-linking) and C=N bonds (grafting polymerization).

1.2.1.3 Bimetallic gold-platinum PEG-diamine nanoparticles

Figure IV - 18 shows the high-resolution XPS spectra of bimetallic Au:PtPEG-2NH₂ NPs (D= 2.5 kGy) at the Au and Pt-4f core levels.

[28] Puglia C et al. (1995) *Surf. Sci.* 342 119–33

[31] Parmigiani F et al. (1990) *J. Electron Spectros. Relat. Phenomena* 50 39–46

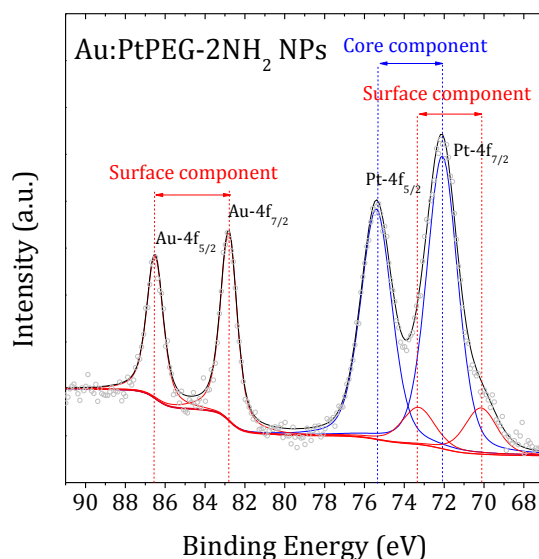


Figure IV - 18. XPS spectrum corresponding to the Au and Pt-4f core level region of bimetallic PEG-diamine nanoparticles.

In **Figure IV - 18**, the presence of both metals at their respective core level regions is observed. Quantitative estimates of Au/Pt ratio using XPS revealed ~ 3 times more detected platinum than gold, from 22 (Au) to 78 (Pt) atomic %, which indicate surface segregation of Pt atoms in gold seeds and thus a core/shell structure.

Different signal intensities (Au/Pt) were measured for different replicates resulting from the sample deposition protocol. However, gold and platinum BEs were found at the same positions in all replicates. Moreover, we consistently observed a higher contribution from the core component of platinum, observed at higher BEs. This result might suggest not only the presence of Pt⁰ but also the presence of the intermediated Pt^I indicating uncompleted radiolytic reduction of the platinum complex. The presence of Pt^I is not clear at this stage because Pt⁰ has been already characterized at this BE in bimetallic systems [36] [37]. The binding energies of the Au-4f spin-orbit components are observed at 82.8 and 86.5 eV. This agrees with the gold surface type also observed in the monometallic AuPEG-2NH₂ NPs.

Figure IV - 19 shows the XPS spectra of bimetallic nanoparticles at the C-1s, O-1s and N-1s core levels region.

[36] Li S *et al.* (2013) *Int. J. Electrochem. Sci.* **8** 8662–8

[37] Ilayaraja N *et al.* (2013) *J. Mater. Chem. A* **1** 4048–56

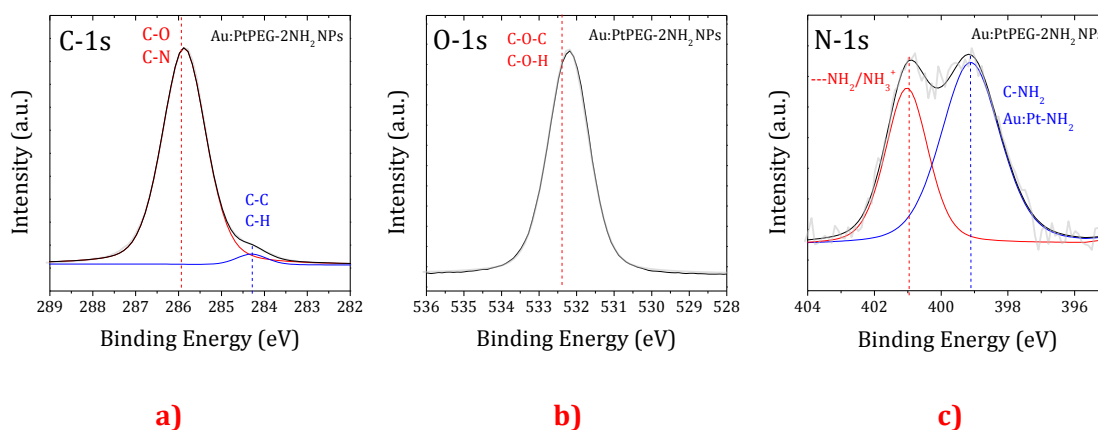


Figure IV - 19. XPS spectra of Au:PtPEG-2NH₂ NPs corresponding to the C-1s (a), O-1s (b) and N-1s (c) core levels regions.

The C-1s and O-1s signals are observed at the same binding energies of the native PEG. The FWHM at this core levels do not present any broadening. These nanoparticles present at the N-1s core level region two main contributions. The lower BE at 399.1 eV corresponds to the direct binding of nanoparticles with the amine end-group of PEG. This is confirmed by the broadening in about 50%, from 1.4 to 2.1, of the N-1s peak and of about 58%, from 1.2 (Pt⁰ metallic surface) to ~1.9, at the Pt-4f core level of nanoparticles. The measured XPS binding energies, assignments and FWHM of bimetallic nanoparticles at the Au and Pt-4f, C-1s, O-1s and N-1s core levels are summarized in **Table IV - 5**.

Table IV - 5. XPS data summary: binding energy, assignment and FWHM of Au:PtPEG-2NH₂ NPs.

Compound	Atomic core level	BE (eV)	Assignment	FWHM (eV)
Au:PtPEG-2NH ₂ NPs	Au-4f _{7/2} surf.	82.8	Au ⁰	1.0
	Au-4f _{5/2} surf.	86.5	Au ⁰	1.0
	Pt-4f _{7/2} surf.	70.2	Pt ⁰	1.9
	Pt-4f _{5/2} surf.	73.5	Pt ⁰	1.9
	Pt-4f _{7/2} core	72.1	Pt ⁰ /Pt ^I	1.8
	Pt-4f _{5/2} core	75.4	Pt ⁰ /Pt ^I	1.8
	C-1s	285.9	C-H & C-N	1.2
	C-1s	284.3	C-C	0.9
	O-1s	532.2	C-O-C	1.3
	N-1s	399.1	C-NH ₂ Au:Pt-NH ₂	2.1
N-1s	401.0	---NH ₂ /NH ₃ ⁺	1.5	

In summary, Au:PtPEG-2NH₂ NPs consist in Au⁰ atoms in the core and Pt in the shell as Pt⁰ and Pt^I. It is suggested that PEG chains are grafted perpendicularly [24] to the NPs surface and that amine groups are directly bonded to nanoparticles.

[24] Crispin X et al. (2001) *J. Electron Spectros. Relat. Phenomena* **121** 57–74

1.2.2 Functional characterization by FTIR

Figure IV - 20 shows the FTIR spectra of **(a)** the native PEG-2NH₂ (Mw= 2000 g.mol⁻¹), **(b)** the as-synthesized AuPEG-2NH₂ NPs after 1 kGy, **(c)** the PtPEG-2NH₂ NPs obtained after 10 kGy (nanoflowers) and **(d)** the Au:PtPEG-2NH₂ NPs obtained after 2.5 kGy. We highlight in red new IR bands in spectra **(b)**, **(c)** and **(d)**.

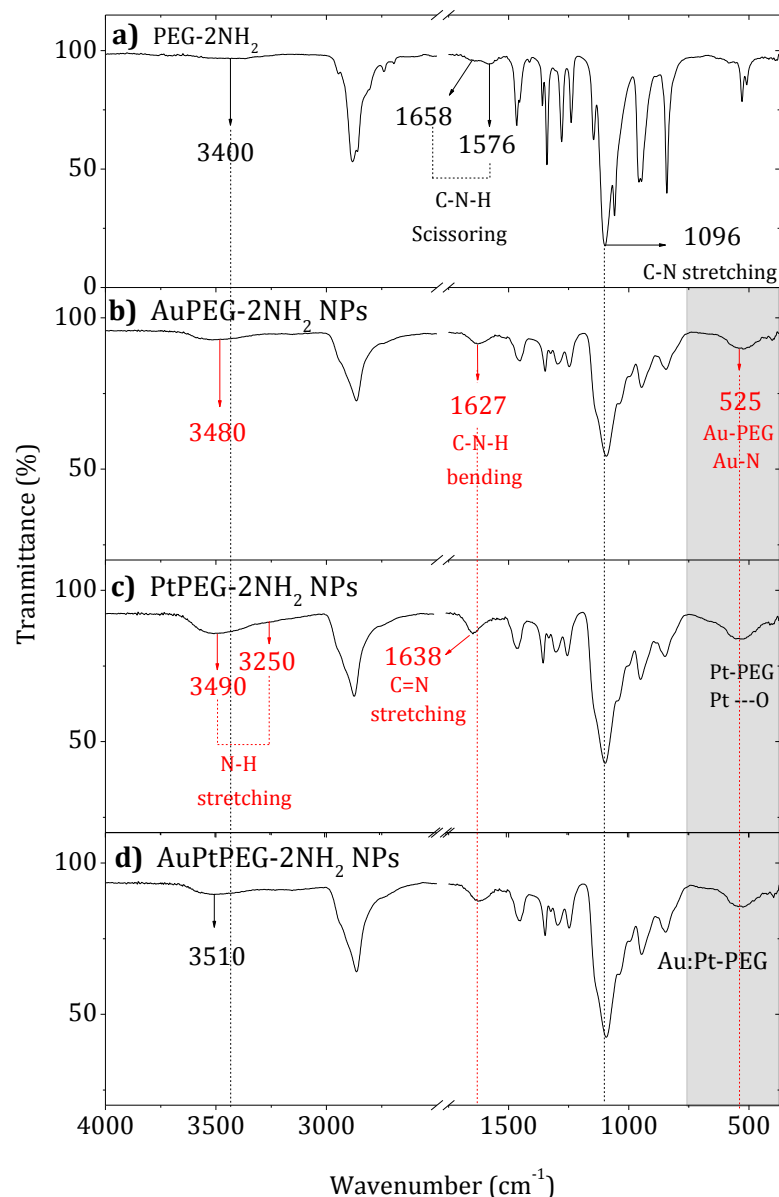


Figure IV - 20. FTIR spectra of (a) PEG-2NH₂, (b) AuPEG-2NH₂ NPs, (c) PtPEG-2NH₂ NPs and (d) Au:PtPEG-2NH₂ NPs obtained by radiolysis.

Figure IV - 20a shows the IR spectrum of the native PEG-2NH₂. This spectrum is very similar to that of the standard PEG-OH, which has been already described in **Chapter III - Section 1.4**. In particular, the IR bands centered at 1658 and 1576 cm⁻¹ are attributed to

the C-N-H scissoring mode that characterizes the amine end-group of PEG. At the same time, the C-N stretching mode is observed at 1096 cm⁻¹, signal that overlaps the ν_{C-O} vibrational mode of ether groups in PEG. The very weak signal around 3400 cm⁻¹ is attributed to the N-H stretching mode of primary amines.

Figure IV - 20b displays the IR spectrum of AuPEG-2NH₂ NPs. We observe the N-H stretching vibrational frequency at ~3480 cm⁻¹. The IR band at 1627 cm⁻¹ is attributed to the N-H bending vibration of the amine group while the broad peak centered around 525 cm⁻¹ corresponds to the gold-polymer interactions, mainly Au-N. In conclusion, this IR analysis indicated the presence of amine groups. This result is in agreement with XPS measurements suggesting the presence of different aliphatic amine species and the direct bonding to gold nanoparticles.

Figure IV - 20c corresponds to the infrared spectrum of the PtPEG-2NH₂ nanoflowers. In comparison with the native PEG-2NH₂, we identified three main new signals around 3490, 1638 and ~525 cm⁻¹. The new broadening band at 3490 cm⁻¹ is attributed to the asymmetrical N-H stretching mode of primary amines while the weak shoulder observed around 3250 cm⁻¹ corresponds to their symmetrical N-H stretching mode [38]. At 1638 cm⁻¹ we identify the C=N stretching band for imines (-N=C-) that occurs in the region from 1690 to 1620 cm⁻¹ [39]. In agreement with the literature, the conjugation of C=N containing systems, for instance with PEG molecules, produce a decrease in the C=N stretching frequency [39]. This signal is different to that observed in AuPEG-2NH₂ NPs as ATR-FTIR measurements were performed with a 4 cm⁻¹ spectral resolution (ALPHA-P with diamond ATR - Bruker). This IR band also supports (as shown by XPS) the hypothesis that the intra-molecular cross-linking process is accompanied by a simultaneous grafting polymerization and the formation of imine groups between the polymer radical -O-CH₂-ĊH-O-CH₂-CH₂- and the amine end-group of PEG (**Figure IV - 21**). Finally, the IR signal centered at ~525 cm⁻¹ corresponds to the platinum-PEG vibrational frequency.

[38] Silverstein R M *et al.* (1991) *Spectrometric identification of organic compounds* (Wiley)

[39] Socrates G (2001) *Infrared and Raman Characteristic Group Frequencies: Tables and Charts*

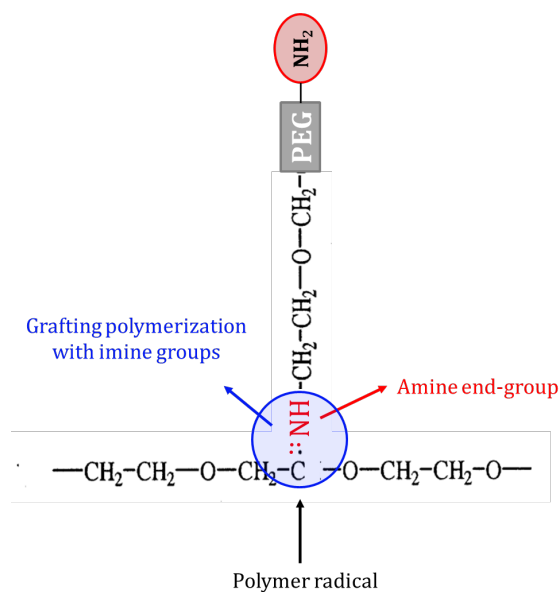


Figure IV - 21. Proposed configuration of the radiolysis induced grafting polymerization of PEG-2NH₂ chains.

In summary, this IR analysis shows that the cross-linking process is accompanied by the *in situ* formation of imines during radiolysis. It confirms the attribution of the N-1s XPS signal observed at 398.2 eV to the presence of C=N chemical species in PtPEG-2NH₂ NPs.

Finally, in **Figure IV - 20d** we observed that Au:PtPEG-2NH₂ NPs present very similar IR frequencies as those of AuPEG-2NH₂ NPs. At the lower spectral range frequencies, the metal-polymer interaction is observed.

Complementary FTIR measurements using the precursors' mixtures before irradiation are in process to investigate the formation of any intermediated specie, expected in the case of monometallic gold and bimetallic gold-platinum PEGylated nanoparticles. Far-infrared measurements are proposed to better elucidate the metallic functional groups formed during nanoparticles synthesis (Pt-O, Au-N, Au/Pt-N).

1.3 Conclusion

The optimal radiolytic conditions used to synthesize stable, biocompatible and ready-to-use mono- and bimetallic gold-platinum PEG-diamine nanoparticles were presented. The performed characterization allowed describing the mechanism of nanoparticles formation.

We stated that the radiolytic synthesis of mono- and bimetallic Au:Pt nanoparticles in the presence of PEG-2NH₂ is strongly influenced by the metal complex / PEG interaction prior irradiation, amine group content and PEG chain lengths (UV-Vis spectroscopy). The

PEGylation process is performed through two mechanisms; polymeric matrix formation and the direct bonding of PEG chains with the metal (coordination saturation).

PtPEG-2NH₂ NPs were obtained as aggregated nanoparticles, named nanoflowers, resulting from an *in situ* intra-molecular PEG cross-linking process. Platinum nanoflowers are stabilized by the flat interaction between platinum cores and the PEG matrix. AuPEG-2NH₂ and Au:PtPEG-2NH₂ NPs were obtained as well dispersed spherical nanoparticles suggesting initial complexation of gold ions by PEG. When the precursor solution contains gold (mono- and bimetallic developments), PEG is grafted perpendicularly to the metal in a monolayer conformation. **Figure IV - 22** summarizes these statements.

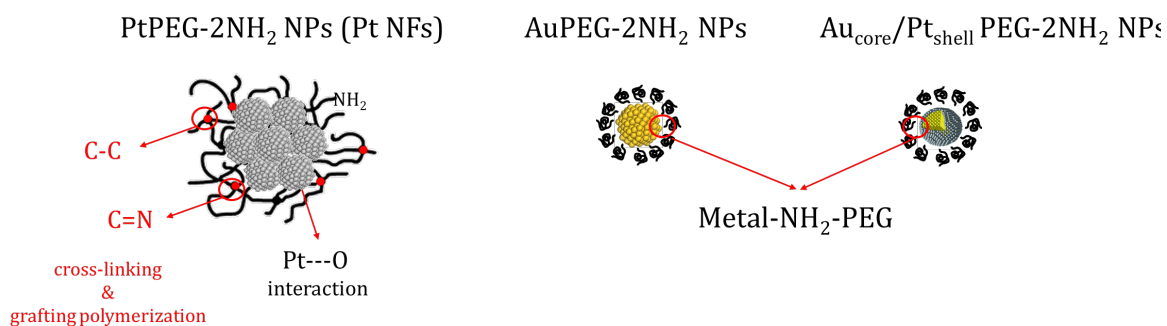


Figure IV - 22. Schematic representation of mono and bimetallic gold-platinum PEGylated nanoparticles.

2 Proof of principle: enhancement on the radio-induced nanosize damage

In this work, we used the molecular bio-nanoprobe to quantify the radio-induction of nanosize damage. The method is described in **Chapter II – Section 4.2**.

Figure IV - 23 shows the average number of DSBs induced in pure DNA plasmids (control) and in DNA plasmids loaded with PtPEG-2NH₂, AuPEG-2NH₂ and Au:PtPEG-2NH₂ NPs with a ratio that corresponds to 1 nanoparticle per 2 plasmids [1:2]. This molecular nanosize damage is here plotted as function of the irradiation dose.

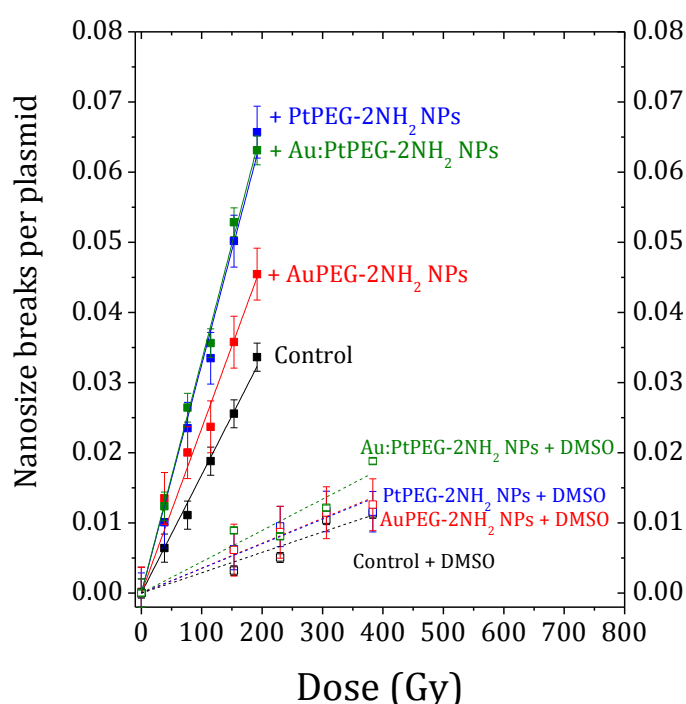


Figure IV - 23. Induced molecular nanosize damage in the control (■) and in plasmids loaded with PtPEG-2NH₂ NPs (■), AuPEG-2NH₂ NPs (■) and Au:PtPEG-2NH₂ NPs (■) as function of the irradiation dose. DMSO effect in the control (□) and in plasmids loaded with PtPEG-2NH₂ NPs (□), AuPEG-2NH₂ NPs (□) and Au:PtPEG-2NH₂ NPs (□).

As already observed for PtPEG-OH NPs (see results **Chapter III – Section 2.2.1**), we found that the radio-induction of nanosize damage, in the controls and in plasmids loaded with NPs, increases linearly with the irradiation dose. More interestingly, in the presence of nanoparticles, the induction of nanosize damages is strongly amplified. We also observed that the induction of nanosize damage sharply decreases in the presence of DMSO (dotted lines).

The efficiency of mono and bimetallic core/shell nanoparticles to amplify the induction of nanometer size damages was quantified through the amplification factor (AF) previously described (see definition in **Chapter III – Equation III-18**). **Table IV - 6** summarizes this

quantitative analysis. It enlists the yields (nanosize breaks / plasmid / Gy) of controls and plasmids loaded with NPs, the AFs and 'OH radicals' effect.

Table IV - 6. Yields of the control and plasmids loaded with mono- and bimetallic gold-platinum NPs ([2:1 ratio]). The AFs and DMSO effect are also reported.

Sample	Nanosize breaks/plasmid/Gy (x10 ⁻⁵)	AF (%)	OH effect (%)
Control	17.47 ± 0.51	-	-
PtPEG-2NH ₂ NPs	32.59 ± 0.92	87 ± 1	-
AuPEG-2NH ₂ NPs	23.49 ± 0.94	34 ± 2	-
Pt:AuPEG-2NH ₂ NPs	33.18 ± 0.54	90 ± 2	-
Control + DMSO	2.91 ± 0.22	-	83 ± 1
Pt NPs + DMSO	3.52 ± 0.23	21 ± 1	89 ± 1
Au NPs + DMSO	3.56 ± 0.13	22 ± 4	85 ± 1
Pt:Au NPs + DMSO	4.14 ± 0.36	42 ± 2	86 ± 1

These results show that in the presence of PEGylated (PEG-2NH₂) NPs the induction of nanosize damage is strongly enhanced. AuPEG-2NH₂ NPs are the less efficient nano-agents with an amplification factor of about 34%. We observe that platinum atoms at the NPs surface induced higher nanoscopic damage (PtPEG-2NH₂ NPs and bilayered Au_{core}-Pt_{shell} PEG-2NH₂ NPs). Platinum based nanoparticles have very similar amplification factors, of about 87% for monometallic Pt NPs and of about 90% for bimetallic Au_{core}/Pt_{shell} NPs.

In **Figure IV - 23**, we observe that the dose response curves drops drastically in presence of DMSO (see yields in **Table IV - 6**). This study indicates that water radicals mediate the amplification effect for more than 85%. In comparison with PtPEG-OH NPs (see results in **Chapter III - Section 2.3.3**), we observe (**Table IV - 6** - column 3) that the direct effects of radiation are less amplified in the presence of these three NPs.

The amplification effect of metallic NPs can be explained as due to early stage mechanisms of individual and collective electronic excitations [40] [41], which might depend on the thickness of the outer platinum shell and the overall size of metallic nanoparticles [42].

[40] Verkhovtsev A V *et al.* (2015) *J. Phys. Chem. C* **119** 11000–13

[41] Verkhovtsev A V *et al.* (2015) *Phys. Rev. Lett.* **114** 063401

[42] Karam T E *et al.* (2015) *J. Phys. Chem.* **119** 18573–80

Interestingly, in order to explain the enhancing effect of bimetallic systems, XPS inputs (see results **Section 1.2.1.3**) such as the ratio of the normalized integrated intensities (NPs shell/core) and the relative electron attenuation lengths may allow determining the thickness of the metallic overlayers [43], and thus the modeling of electron energy loss and secondary electron emission. This modeling is very important in the understanding of physical processes involved in the REE of metallic nanoparticles in biological systems. New collaborations have been established to perform these calculations to better elucidate the enhancing mechanisms.

An interesting hypothesis, which may explain the experimental results, has been recently proposed by Verkhovtsev *et al.* They demonstrated that the surface plasmon gives the dominating contribution to the electron production by metallic NPs such as Au and Pt exceeding that of the volume plasmon or individual atomic excitations (5d electrons). For instance, it was shown that Pt nanoclusters (~1 nm) are more efficient for electron production than Au (**Figure IV - 24**), effect that strongly depends on the nanocluster size [40].

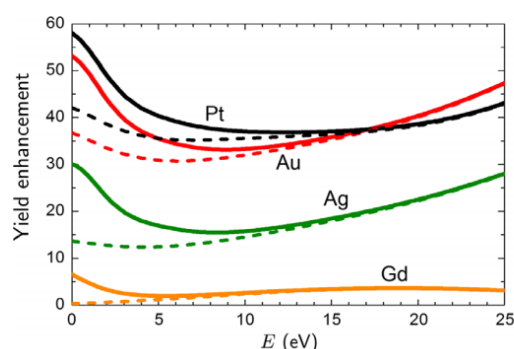


Figure IV - 24. Yield enhancement from 1 nm metallic NPs. Dashed lines show the contribution of individual atomic excitations while solid lines show the resulting sum of the individual and plasmonic excitations (from [41]).

When irradiating pure water, an important enhancement of the electron yield (of about one order of magnitude) may be expected in the presence of metallic NPs. Higher the electron production, higher the production of free radicals and ROS, which may increase the nanosize molecular damage and cell killing. The plasmon effect of metallic nanoparticles in biomolecules is illustrated in **Figure IV - 25**.

[40] Verkhovtsev A V *et al.* (2015) *J. Phys. Chem. C* **119** 11000–13

[41] Verkhovtsev A V *et al.* (2015) *Phys. Rev. Lett.* **114** 063401

[43] Shard A G (2012) *J. Phys. Chem. C* **116** 16806–13

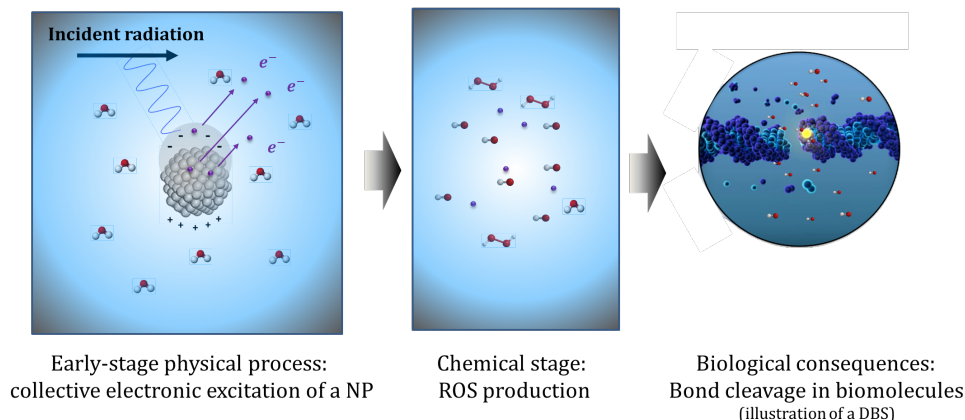


Figure IV - 25. The radiation enhancement mechanism of metallic nanoparticles. Representation of the early-stage physical processes: collective electronic excitation, follow by the chemical stage consisting on ROS production that ends with bond cleavage in biomolecules, which might induce cell death.

Notably to point, at the same experimental conditions (platinum concentration), this exploratory study showed that PtPEG-2NH₂ nanoflowers are ~ 2 times more efficient, from $42 \pm 2\%$ to $87 \pm 1\%$, than discrete PtPEG-OH NPs (see results at ratio 1:2 for PtPEG-OH NPs in **Appendix B**), which may be explained as an enhanced cross-section. In the present case, the REE of mono- and bimetallic NPs, which were synthesized at the same experimental conditions (total metal content and PEG-2NH₂:M ratios), might also be attributed to the presence of free Cl⁻ ions in the NPs solution. Indeed, halides are known by scavenging solvated electrons [44] resulting on less ROS production.

In conclusion, the quantification of the radio-induced nanosize damage using the bio-nanoprobe opened new perspectives to enhance the cell killing efficiency of platinum based nanoparticles. We suggest a main contribution of the platinum plasmon on the enhancing mechanism by comparing similar nanosize particles, the monometallic gold and bimetallic gold-platinum nanoparticles. Currently, different studies at cellular level are been performed in the group using these well stable and biocompatible PEGylated metallic nanoparticles.

[44] Buxton G V (2008) An overview of the radiation chemistry of liquids *Radiation Chemistry*

3 References

- [1] Remita S, Picq G, Khatouri J and Mostafavi M 1999 Radiolytic formation of bilayered Ptcore/Aushell and Auore/Ptshell clusters in aqueous solution *Radiat. Phys. Chem.* **54** 463–73
- [2] Esumi K, Suzuki A, Yamahira A and Torigoe K 2000 Role of Poly(amidoamine) Dendrimers for Preparing Nanoparticles of Gold, Platinum, and Silver *Langmuir* **16** 2604–8
- [3] Kim Y-G, Oh S-K and Crooks R M 2004 Preparation and Characterization of 1–2 nm Dendrimer-Encapsulated Gold Nanoparticles Having Very Narrow Size Distributions *Chem. Mater.* **16** 167–72
- [4] Guedira F Application de la Spectroscopie UV-Visible *Université Mohammed V-Agdal /FSR/ Master de sciences analytiques/ M9/ cours de Spectroscopie Ultraviolette*
- [5] Fernandez-Fernandez A, Manchanda R, Carvajal D A, Lei T, Srinivasan S and McGoron A J 2014 Covalent IR820-PEG-diamine nanoconjugates for theranostic applications in cancer. *Int. J. Nanomedicine* **9** 4631–48
- [6] Polte J, Ahner T T, Delissen F, Sokolov S, Emmerling F, Thünemann A F and Kraehnert R 2010 Mechanism of Gold Nanoparticle Formation in the Classical Citrate Synthesis Method Derived from Coupled In Situ XANES and SAXS Evaluation *J. Am. Chem. Soc.* **132** 1296–301
- [7] NanoEurope Composix Gold Nanoparticles: Optical Properties
- [8] Kim F, Song J H and Yang P 2002 Photochemical Synthesis of Gold Nanorods *J. Am. Chem. Soc.* **124** 14316–7
- [9] Physico-chimie L De, Cnrs R--ua and Paris-sud U 1989 Nucleation dynamics of silver aggregates simulation of photographic development processes **34** 605–17
- [10] Gachard E, Remita H, Khatouri J, Keita B, Nadjo L and Belloni J 1998 Radiation-induced and chemical formation of gold clusters *New J. Chem.* **22** 1257–65
- [11] Abidi W and Remita H 2010 Gold based Nanoparticles Generated by Radiolytic and Photolytic Methods *Recent Patents Eng.* **4** 170–88
- [12] Haiss W, Thanh N T K, Aveyard J and Fernig D G 2007 Determination of Size and Concentration of Gold Nanoparticles from UV–Vis Spectra *Anal. Chem.* **79** 4215–21
- [13] Henglein A, Ershov B G and Malow M 1995 Absorption Spectrum and Some Chemical Reactions of Colloidal Platinum in Aqueous Solution *J. Phys. Chem.* **99** 14129–36
- [14] Dandapat A, Mitra A, Gautam P K and De G 2013 Nanomaterials and Nanotechnology A Facile Synthesis of Pt Nanoflowers Composed of an Ordered Array of Nanoparticles Invited Article *Nanomater. Nanotechnol.* **3**
- [15] Jovanović Ž, Krklješ A, Stojkowska J, Tomić S, Obradović B, Mišković-Stanković V and Kačarević-Popović Z 2011 Synthesis and characterization of silver/poly(N-vinyl-2-pyrrolidone) hydrogel nanocomposite obtained by in situ radiolytic method *Radiat. Phys. Chem.* **80** 1208–15
- [16] Rosiak J M, Ulański P, Pajewski L A, Yoshii F and Makuuchi K 1995 Radiation formation of hydrogels for biomedical purposes. Some remarks and comments *Radiat. Phys. Chem.* **46** 161–8
- [17] Rosiak J M and Ulański P 1999 Synthesis of hydrogels by irradiation of polymers in aqueous solution *Radiat. Phys. Chem.* **55** 139–51
- [18] Rosiak J M, Janik I, Kadlubowski S, Kozicki M, Kujawa P, Stasica P and Ulanski P 2002 Radiation formation of hydrogels for biomedical application *IAEA-TECDOC-1324*
- [19] Mirdamadi-Esfahani M, Mostafavi M, Keita B, Nadjo L, Kooyman P and Remita H 2010 Bimetallic Au-Pt nanoparticles synthesized by radiolysis: Application in electro-catalysis *Gold Bull.* **43** 49–56
- [20] Remita H, Lampre I, Mostafavi M, Balanzat E and Bouffard S 2005 Comparative

- study of metal clusters induced in aqueous solutions by γ -rays, electron or C₆⁺ ion beam irradiation *Radiat. Phys. Chem.* **72** 575–86
- [21] Moulder J F, Stickle W F, Sobol P E and Bomben K D 1992 *Handbook of X-ray Photoelectron Spectroscopy* ed J Chastain (Minnesota, United States of America: Perkin-Elmer Corporation)
- [22] Citrin P H, Wertheim G K and Baer Y 1983 Surface-atom x-ray photoemission from clean metals: Cu, Ag, and Au *Phys. Rev. B* **27** 3160–75
- [23] Hong R, Fischer N O, Emrick T and Rotello V M 2005 Surface PEGylation and Ligand Exchange Chemistry of FePt Nanoparticles for Biological Applications *Chem. Mater.* **17** 4617–21
- [24] Crispin X, Lazzaroni R, Crispin A, Geskin V., Brédas J. and Salaneck W. 2001 Understanding the initial stages of polymer grafting on metals: a photoelectron spectroscopy study of acrylonitrile adsorption on transition metal surfaces *J. Electron Spectros. Relat. Phenomena* **121** 57–74
- [25] Kovach K M, Capadona J R, Gupta A Sen and Potkay J A 2014 The effects of PEG-based surface modification of PDMS microchannels on long-term hemocompatibility. *J. Biomed. Mater. Res. A* **102** 4195–205
- [26] Kumar R, Ghosh A, Patra C R, Mukherjee P and Sastry M 2004 Gold nanoparticles formed within ordered mesoporous silica and on amorphous silica *Nanotechnology in Catalysis* ed B Zhou, S Hermans and G A Somorjai (New York: Kluwer Academic / Plenum Publishers) pp 111–36
- [27] Graf N, Yegen E, Gross T, Lippitz A, Weigel W, Krakert S, Terfort A and Unger W E S 2009 XPS and NEXAFS studies of aliphatic and aromatic amine species on functionalized surfaces *Surf. Sci.* **603** 2849–60
- [28] Puglia C, Nilsson A, Hernnäs B, Karis O, Bennich P and Mårtensson N 1995 Physisorbed, chemisorbed and dissociated O₂ on Pt(111) studied by different core level spectroscopy methods *Surf. Sci.* **342** 119–33
- [29] Feldman L C and Mayer J W 1986 X-ray photoelectron spectroscopy *Fundamentals of surface and thin film analysis* (New York: Elsevier Science Publishing Co., Inc.) p 224
- [30] Ono L K, Yuan B, Heinrich H and Cuenya B R 2010 Formation and Thermal Stability of Platinum Oxides on Size-Selected Platinum Nanoparticles: Support Effects *J. Phys. Chem. C* **114** 22119–33
- [31] Parmigiani F, Kay E and Bagus P S 1990 Anomalous oxidation of platinum clusters studied by X-ray photoelectron spectroscopy *J. Electron Spectros. Relat. Phenomena* **50** 39–46
- [32] Beamson G and Briggs D 1992 *High resolution XPS of organic polymers, the scienta ESCA300 database*. (John Wiley and Sons Ltd)
- [33] Truica-Marasescu F and Wertheimer M R 2008 Nitrogen-Rich Plasma-Polymer Films for Biomedical Applications *Plasma Process. Polym.* **5** 44–57
- [34] Jansen R J J and van Bekkum H 1995 XPS of nitrogen-containing functional groups on activated carbon *Carbon N. Y.* **33** 1021–7
- [35] Rangan S, Bournel F, Gallet J-J, Kubsky S, Le Guen K, Dufour G, Rochet F, Sirotti F, Piaszenski G, Funke R, Kneppel M and Köhler U 2005 Surface Reactions of 3-Butenenitrile on the Si(001)-2 × 1 Surface at Room Temperature *J. Phys. Chem. B* **109** 12899–908
- [36] Li S, Dong Y, Bi X and Tang M 2013 Synthesis of Au @ Pt Core-Shell Nanoparticles with High Electro-catalytic Activity of Methanol Oxidation by Photochemical Seeding Growth *Int. J. Electrochem. Sci.* **8** 8662–8
- [37] Ilayaraja N, Prabu N, Lakshminarasimhan N, Murugan P and Jeyakumar D 2013 Au-Pt graded nano-alloy formation and its manifestation in small organics oxidation reaction *J. Mater. Chem. A* **1** 4048–56
- [38] Silverstein R M, Bassler G C and Morrill T C 1991 *Spectrometric identification of*

- organic compounds* (Wiley)
- [39] Socrates G 2001 *Infrared and Raman Characteristic Group Frequencies: Tables and Charts* (Chichester: John Wiley & Sons, LTD)
- [40] Verkhovtsev A V., Korol A V. and Solov'yov A V. 2015 Electron Production by Sensitizing Gold Nanoparticles Irradiated by Fast Ions *J. Phys. Chem. C* **119** 11000–13
- [41] Verkhovtsev A V., Korol A V. and Solov'yov A V. 2015 Revealing the Mechanism of the Low-Energy Electron Yield Enhancement from Sensitizing Nanoparticles *Phys. Rev. Lett.* **114** 063401
- [42] Karam T E, Smith H T and Haber L H 2015 Enhanced Photothermal Effects and Excited-State Dynamics of Plasmonic Size-Controlled Gold-Silver-Gold Core-Shell Nanoparticles *J. Phys. Chem.* **119** 18573–80
- [43] Shard A G 2012 A Straightforward Method For Interpreting XPS Data From Core-Shell Nanoparticles *J. Phys. Chem. C* **116** 16806–13
- [44] Buxton G V 2008 An overview of the radiation chemistry of liquids *Radiation Chemistry* ed M Spothem-Maurizot, M Mostafavi, T Douki and J Belloni (Les Ulis Cedex: EDP Sciences)

CONCLUSIONS

The main goal of my PhD was to develop new platinum based nanoparticles, stable and biocompatible, able to enhance the biological impact of ionizing radiations which includes NPs toxicity, uptake, localization and enhancing effect in combination with radiations (called radio-enhancement).

In this perspective:

- i) I optimized a new method of nanoparticle synthesis by radiolysis and I produced different kind of platinum core nanoparticles as well as bimetallic nanoparticles.
- ii) The radio-enhancing properties of nanoparticles were probed on cellular models, to characterize the biological impact, and experiments with a bio-nanoprobe were performed to characterize the molecular scale mechanisms of radio-enhancement.

1) Summary on the synthesis and characterization of nanoparticles

Biocompatible Pt NPs were prepared using a unique environmental friendly method. This last consisted on the reduction of metal complexes *via* water radiolysis in combination with *in situ* PEGylation. This new one-step synthesis allows the production of homogeneous in size and stable biocompatible nanoparticles. The final solution, which is sterilized by radiation, is ready-to-use for adding to biological systems.

In this work, I developed four nanoparticles, PtPEG-OH, PtPEG-2NH₂, AuPEG-2NH₂ and Au:PtPEG-2NH₂. Complementary techniques were used to describe the size, shape, chemical composition and stability of the nanoparticles. My work was focused on the characterization of PtPEG-OH essentially.

The main findings concerning the different nanoparticles I developed are summarized below.

- PtPEG-OH NPs

The PtPEG-OH NPs are small spherical nanoparticles (~3 nm). They are composed of a platinum core coated with biocompatible PEG-OH molecules. They have a hydrodynamic

diameter of about 9 nm and ζ -potential of about -16 mV at the pH range of physiological fluids.

The stability of the nanoparticles depends on the PEG-OH:Pt molar ratio used during the synthesis. The remarkable colloidal stability (stable up to 3 months when stored at 4°C) was attributed to the strong interaction between platinum and PEG-OH coating. The production of a strong binding was confirmed by the shift of the nitrogen peak observed in the XPS measurements. Interestingly, the creation of an intermediated amide takes place before the radiolysis. The complementary spectrometric methods suggested that PEG molecules interact with the platinum cores by keeping their chemical structure, which was interpreted as the presence of a perpendicular monolayer of PEG molecules at the platinum surface. These NPs were found non-toxic at an incubation molar concentration of 5×10^{-4} mol.L⁻¹.

- PtPEG-2NH₂ NPs

PtPEG-2NH₂ NPs have different size and shape than PtPEG-OH NPs. They formed platinum nanoflowers of ~15 nm, which are composed of aggregated ~3 nm metallic platinum NPs. Their synthesis consists on the reduction of the Pt complex simultaneously with PEG cross-linking. Pt NFs have remarkable stability up to a year. Their PEG coating was attributed to the chemisorption of PEG molecules at the nanoparticles surface. Preliminary results, not discussed in this manuscript, showed that these nanoparticles are **non-toxic** in human cell lines and are internalized. It is noteworthy to mention that the presence of an amine group offers the perspectives to graft new molecules at the surface such as a fluorescent tag. This would be the first time in the case of platinum nanoparticles. This has been initiated at the end of my PhD and is not presented here.

- AuPEG-2NH₂ NPs

The AuPEG-2NH₂ NPs are small spherical nanoparticles (~3 nm) with a gold core coated with PEG diamine. The stability and homogeneity of these nanoparticles strongly depended on the concentration of the amine end-groups of PEG in the precursor mixture and the length of the PEG chain. In this case, it was suggested the presence of intermediated species leading to a perpendicular grafting of PEG-2NH₂ and well stabilized colloids. The cytotoxicity evaluation of these NPs is in process.

- Au:PtPEG-2NH₂ NPs

The Au:PtPEG-2NH₂ NPs are small spherical nanoparticles (~3 nm) composed of two metals and covalently bonded to PEG (as in the case of the monometallic gold). These NPs presented a core-shell structure with Au at the centre and Pt at the periphery. This was explained in terms of redox potentials of each precursor compound. It was suggested the presence of intermediated species formed by the interaction between the gold precursor and the PEG-2NH₂, leading to a perpendicular grafting of the polymer at the bimetallic nanoparticle surface.

These results and optimized method opens new perspectives in the group to the preparation of multimodal bimetallic NPs by radiolysis.

2) Summary on the biological impact of PtPEG-OH NPs

In the frame of my PhD, the biological impact of only PtPEG-OH NPs was evaluated. Two human cancer cell lines, HeLa and U87-MG, were chosen as cellular models. Nanoparticles were not toxic in the experimental conditions used in this work (5×10^{-4} mol.L⁻¹ in Pt, 6 h).

First, we found that the NPs uptake is cell dependent. In particular, U87-MG cells internalize of about 5 times more NPs than HeLa cells. As expected from previous studies, the PtPEG-OH NPs were found located in the cytoplasm exclusively. Interestingly, the internalization pathways for the two cell lines were different: NPs enter in HeLa *via* passive diffusion while they enter in U87-MG *via* endocytosis.

Second, it was demonstrated that the combination of PtPEG-OH NPs with γ -rays or carbon ions strongly amplifies cancer cell killing. In particular, it was found that PtPEG-OH NPs amplify by 44% the cell killing of HeLa cells treated by carbon ions. This effect was attributed to the induction of directly lethal damages. This result is a major finding, which demonstrates that Pt NPs may strongly improve the performance of hadrontherapy.

A significant increase of radiation effects was also observed in the case of U87-MG cells treated by γ -rays, with an amplification factor of 20% at 2 Gy. By performing radiation experiments with the bio-nanoprobe, it was shown that NPs are responsible for the increase of nanosize molecular damage. This phenomenon is attributed to the electronic activation followed by re-neutralisation of the NP, which generates a large perturbation in the surrounding nanometer volume and thus the production of highly reactive and toxic free radical clusters. Other collective process such as the plasmon excitation and also charge transfer with water molecules may contribute to this process. Finally, the

amplification of cell killing is attributed to the induction of this highly local and strong perturbation that is initiated in the cytoplasm of the cells. The study of the biological response is still in progress.

In conclusion, the goal of my project was fully achieved and new biocompatible Pt NPs were successfully prepared, characterized and evaluated in different bio-systems under γ -rays and carbon ions irradiation. Last but not least, this work at the interface of physics, chemistry and biology shows the high potentialities of platinum based nanoparticles to improve radiation therapies.

1. Transmission Electron Microscopy (TEM)

The transmission electron microscope is a powerful tool used in material science. It uses a focused beam of high energy electrons (in the range of kV) that allows the imaging and analysis of specimens in the sub-micrometer (10^{-6} m) range. Because the wavelength of electrons is much smaller than that of light, the resolution attainable for TEM images is many orders of magnitude better than that from a light microscope. For this reason, TEM finds application in nanoscience research.

Electrons have both wave and particle properties as theorized by Louis-Victor de Broglie in 1924 [1]. The wavelength of electrons is related to their kinetic energy via the de Broglie equation:

$$\lambda_e = \frac{h}{\sqrt{2m_0E(1+\frac{E}{2m_0c^2})}} \quad \text{Equation A - 1}$$

where h is Planck's constant, m_0 is the rest mass of an electron, E is the energy of the accelerated electron and c is the speed of light. For instance, the wavelength of electrons in a 200 kV TEM is 2.5 pm. Thus, the use of electrons leads on a detailed structural examination through high-resolution and high-magnification imaging, which in particular cases allow the visualization of individual atoms.

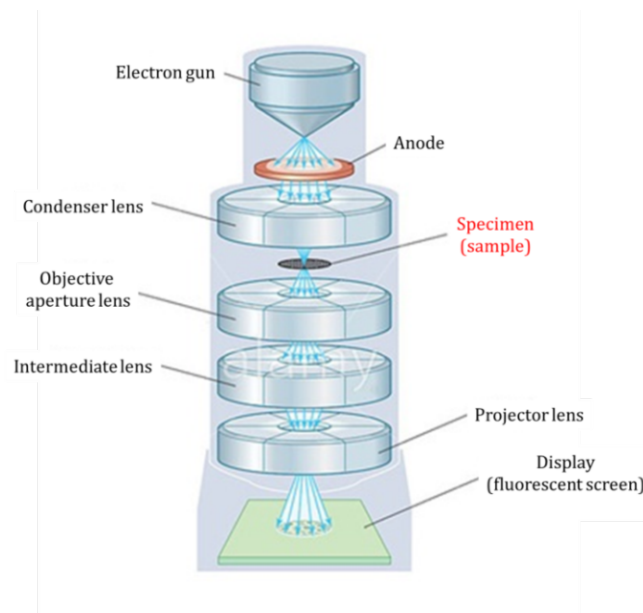


Figure A - 1. Typical TEM configuration (Encyclopædia Britannica, Inc).

[1] De Broglie L (1924) Thèse: Recherches sur la théorie des Quanta

Figure A - 1 illustrates the components of a basic TEM. From the top down, a TEM consists mainly on the source, the optics and the display.

The electron gun is usually a tungsten filament connected to a high voltage source in a typical range from ~100 to 300 kV that provides sufficient current to emit electrons either by thermionic or field electron emission into the vacuum. High vacuum (10^{-7} mbar) is used mainly to avoid collisions of electrons with gas atoms and thus accurately focus the electron beam into the sample by the use of electrostatic and electromagnetic lenses. The lensing stages in a standard TEM allow to form the beam (condenser lenses), to focus the beam (objective lenses) and to expand the beam onto the imaging device (projector lenses).

The transmitted beam, after electrons interaction with the sample, contains information about electron density, phase and periodicity which is used to form the image. TEM also enables the investigation of crystal structures, through an electron diffraction pattern, and the chemical composition of phases by X-ray and electron-energy analysis.

2. Dynamic Light Scattering (DLS)

Dynamic Light Scattering (DLS) is used to characterize particles, emulsions or molecules, which have been dispersed or dissolved in a solvent. The Brownian motion of particles in suspension induces scattering of the incident laser light (commonly 633 nm) at different intensities. The analysis on the intensity fluctuations yields the velocity of the Brownian motion (the larger the particles, the slower the Brownian motion). The particle size is determined by the following Stokes-Einstein relationship [2]:

$$d_H = \frac{kT}{3\pi\eta D} \quad \text{Equation A - 2}$$

where d_H = hydrodynamic diameter, D = translational diffusion coefficient, k = Boltzmann's constant, T = absolute temperature and η = viscosity.

Figure A - 2a shows the fundamental principle of DLS and **Figure A - 2b** represents the hydrodynamic diameter in a metal nanoparticle.

[2] Malvern Instruments (2014) Dynamic Light Scattering: An introduction in 30 minutes (Note technique)

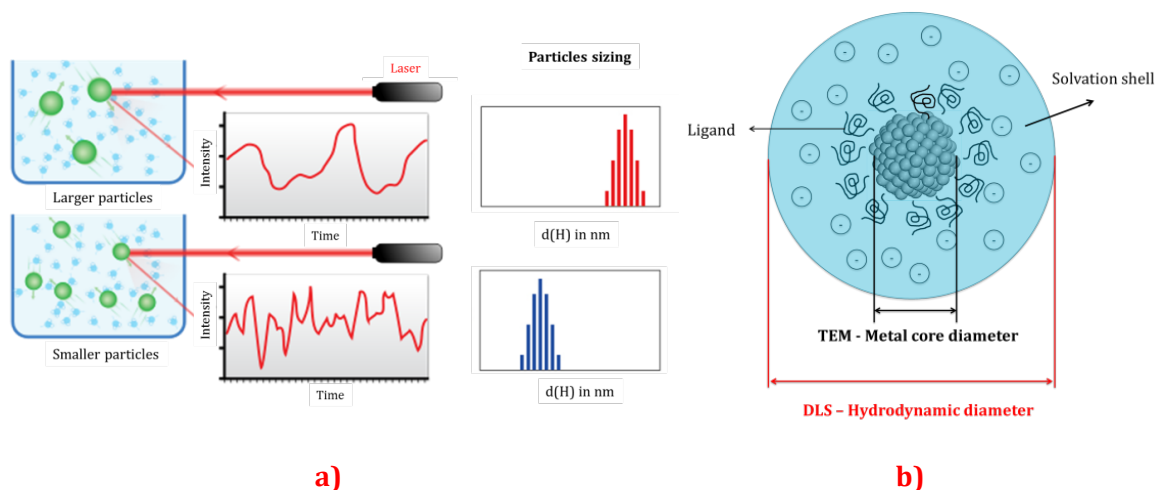


Figure A - 2. Schematic representation of the fundamental principle of DLS (a) and the hydrodynamic diameter of a metal nanoparticle (b). Adapted from https://en.wikipedia.org/wiki/Dynamic_light_scattering.

The Zetasizer Nano-ZS™ (Malvern Instruments Ltd) used in this work allows to characterize nanoparticles, polymer and protein solutions. Sizes ranging from 0.3 nm to 10 μm can be determined at temperatures ranging from 0 to 90°C.

3. Zeta potential

The zeta potential, also namely ζ -potential, is defined as the surface charge acquired by a particle or molecule in a given medium. The electronic properties of the liquid layer surrounding the particle are described as a double shell. It consists in an inner region (stern layer) where the ions are strongly bound and an outer (diffuse layer) region where ions are less associated to the core [3].

In the diffuse layer, there is a hypothetical boundary inside which particles are stable. When a particle moves, ions inside the boundary move with it. When a particles moves, ions beyond the boundary stay with the bulk fluid (commonly water). The potential at this boundary (surface of hydrodynamic shear) is called zeta potential. **Figure A - 3** shows the schematic description of ζ -potential.

[3] Malvern I (2015) Zeta potential - An introduction in 30 minutes 1-15

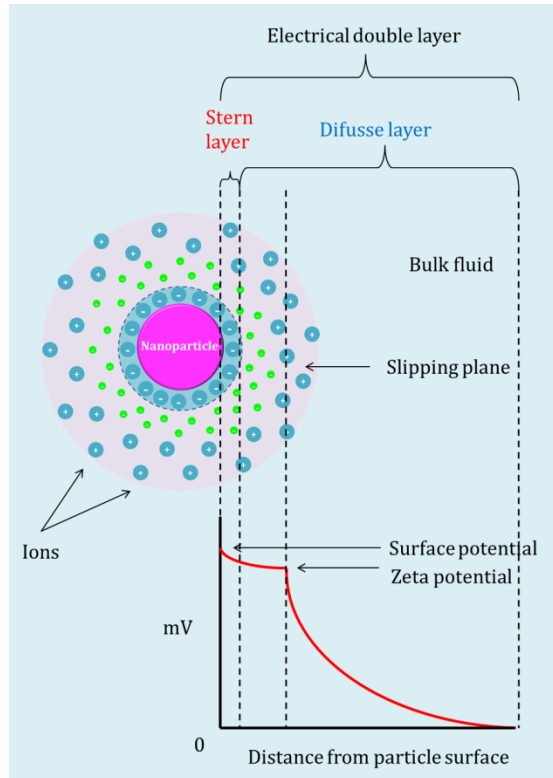


Figure A - 3. Schematic representation of the fundamental principle of the zeta potential.

The ζ -potential of particles in suspension is determined by electrophoresis. The velocity of suspended colloidal particles is measured while they migrate across an electrolyte subjected to an electric field. Viscous forces (η_F) acting on the particles tend to limit their movement until reaching equilibrium and thus constant velocity (V_E). This velocity depends on the strength of the electric field (E), the dielectric constant (ϵ) and the zeta potential. Thus, the electrophoretic mobility (U_E) is given by:

$$U_E = \frac{V_E}{E} \quad \text{Equation A - 3}$$

and the ζ -potential is determined by the Henry law as follow:

$$U_E = \frac{\epsilon \zeta f(\kappa a)}{6\pi\eta_F} \quad \text{Equation A - 4}$$

where $f(\kappa a)$ = Henry's function.

The ζ -potential strongly depends on the composition of the particles suspensions. It is mainly affected by:

- ionic concentration,
- type of ions,

- presence of surfactants or polyelectrolytes
- pH

In this work, we determined the ζ -potential of colloidal nanoparticles using the Zetasizer Nano-ZS already described. In **Figure A - 4**, we present the optical configuration of the Zetasizer Nano-ZS used to perform ζ -potential measurements.

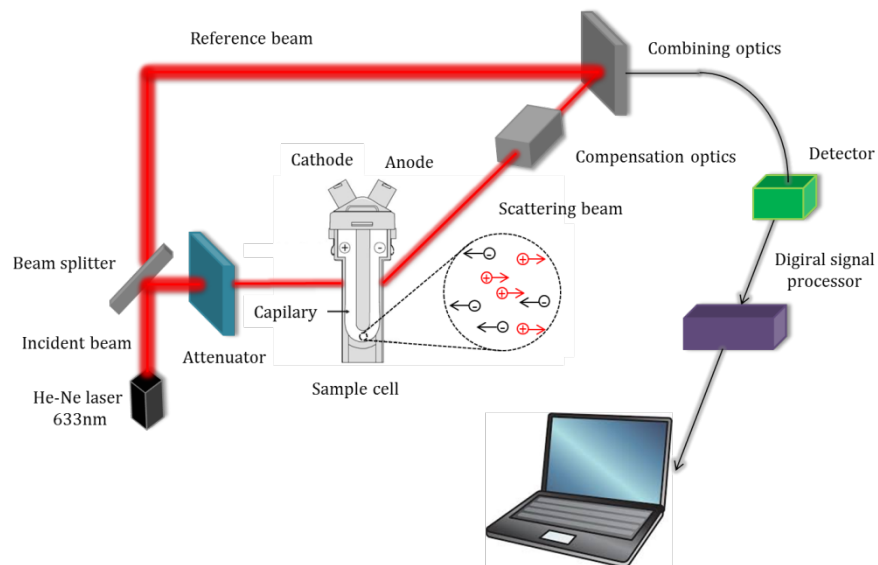


Figure A - 4. Optical configuration of the Zetasizer Nano-ZS for zeta potential measurements.

4. X-ray Photoelectron Spectroscopy (XPS)

X-ray Photoelectron Spectroscopy (XPS) is based on the photoelectric effect. Each atom has core electrons with characteristic binding energies (E_B , also referred as BE). These E_B are conceptually equal to the ionizing energy of the core electrons. They thus describe the electronic environment and the atomic species to which the electron is bound [4].

If the energy of the incident photon ($h\nu$) is large enough, the core electron escapes from the atom and emits out of the material surface with a kinetic energy E_k . The binding energy of that electron is determined by:

$$h\nu = E_B + E_k + \phi_s \quad \text{Equation A - 5}$$

where $h\nu$ is the incident X-ray photon energy (Mg $K\alpha$: 1253.6 eV or Al $K\alpha$: 1486.6 eV), E_k is the kinetic energy of the photoelectron, which is measured by the energy analyser, and ϕ_s is the photometer work function induced by the analyser. Since the work function can be compensated artificially, it is eliminated, giving the E_B as follow:

$$E_B = h\nu - E_k \quad \text{Equation A - 6}$$

Figure A - 5 illustrates the physical principle of XPS in a model atom.

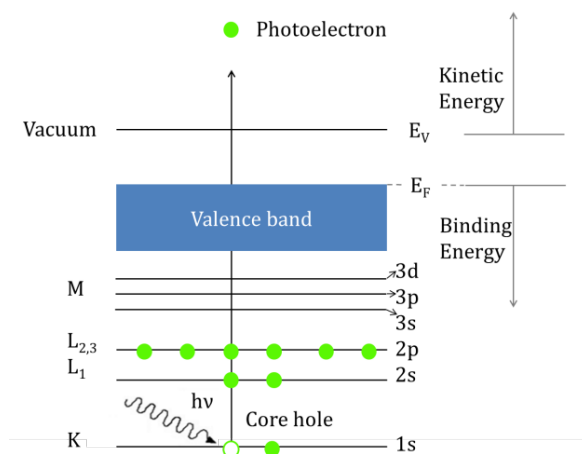


Figure A - 5. XPS principle: energy band structure and emission process for a model atom.

In a typical XPS spectrum the number of detected electrons is plotted as function of their binding energy in a range from 0 to $h\nu$. Each element is directly identified by its characteristic XPS peaks. These characteristic spectral peaks correspond to the electron

[4] Moulder J F et al. (1992) *Handbook of X-ray Photoelectron Spectroscopy* Perkin-Elmer Corporation

configuration of the atoms, *e.g.* 1s, 2s, 2p, 3s, etc. The number of detected electrons is proportional to the amount of element within the XPS sampling volume.

5. Fourier Transform Infrared (FTIR) spectroscopy

Infrared (IR) spectroscopy, also called vibrational spectroscopy, is an analytical tool largely used to determine the chemical structure and functional groups present in organic and inorganic compounds.

Infrared is electromagnetic radiation with longer wavelengths than those of visible light. It extends from the nominal red edge of the visible spectrum at 700 nm (1.24 meV) to 1 mm (1.7 eV). Photons within this range are not enough energetic to excite electrons, however, they induce vibrational excitation of covalently bonded atoms and groups through a change in the dipole moment of a molecule. With exception of diatomic homonuclear molecules, such as O₂, N₂, Cl₂ *etc.*, all molecules absorb IR light, which makes this technique one of the most used in analytical chemistry.

In IR spectroscopy molecules absorb specific IR frequencies which are characteristic to their structure. These absorptions are resonant frequencies which mainly depend on the masses of the atoms and their associated vibronic coupling. For instance, a molecule can vibrate in many ways called vibrational modes. Molecules with N number of atoms have 3N degrees of freedom, six of which are translations and rotations of the molecule itself. This leaves 3N-6 degrees of vibrational freedom (3N-5 if the molecule is linear). Vibrational modes are often given by descriptive names, such as stretching, bending, scissoring, rocking and twisting. **Figure A - 6** illustrates the IR region and vibrational modes.

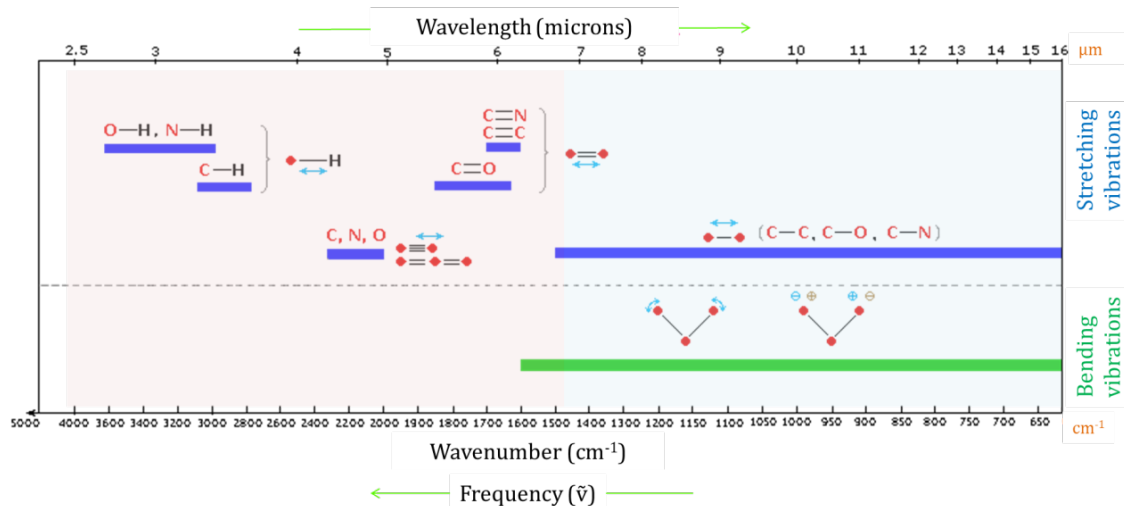


Figure A - 6. IR region and vibrational modes [5].

The blue colored sections above the dashed line refer to stretching vibrations and the green colored band below the line refers to bending vibrations. The infrared region from 1450 to 600 cm^{-1} is often called the fingerprint region. Absorption bands in the 4000 to 1450 cm^{-1} region are usually due to stretching vibrations of diatomic units and this is often called the group frequency region. In general:

- Stretching frequencies are higher than corresponding bending frequencies.
- Bonds to hydrogen have higher stretching frequencies than those to heavier atoms.
- Triple bonds have higher stretching frequencies than corresponding double bonds, which in turn have higher frequencies than single bonds.

In FTIR spectroscopy, the IR light is guided through an interferometer and then through the sample. In principle, a moving mirror inside the system alters the distribution of IR light that passes through the interferometer. The signal directly recorded from the interferometer build what is called an interferogram which represents light output as a function of the mirror position. This raw data is then mathematically processed using the Fourier Transform to obtain the commonly known FTIR spectrum [6]. A basic FTIR spectrum is essentially a graph of infrared light absorbance or transmittance on the vertical axis as function of the frequency, wavelength or wavenumber on the horizontal axis. **Figure A - 7** illustrates a classical FTIR spectrometer within its data processing.

[5] Reusch W Infrared Spectroscopy <https://www2.chemistry.msu.edu>

[6] Griffiths P R and De Haseth J A (2007) *Fourier Transform Infrared Spectrometry* (Wiley)

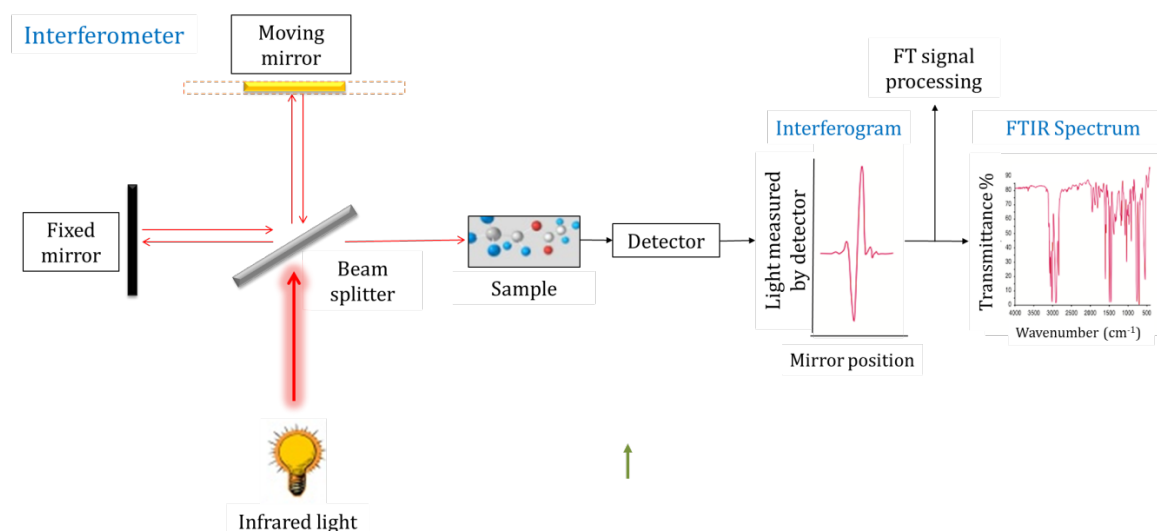


Figure A - 7. Schematically representation of a FTIR spectrometer and signal processing.

In the Attenuated Total Reflection (ATR) IR mode, the changes occurring when the IR beam is internally reflected by a crystal and the sample are measured (**Figure A - 8**). Briefly, an IR beam is directed onto an optically dense crystal (commonly a diamond) with a high refractive index at a certain angle. This internal reflectance creates an evanescent wave that extends beyond the surface of the crystal into the sample held in contact with the crystal. The attenuated energy from each evanescent wave is passed back to the IR beam, which then exits the opposite end of the crystal and is passed to the detector in the IR spectrometer.

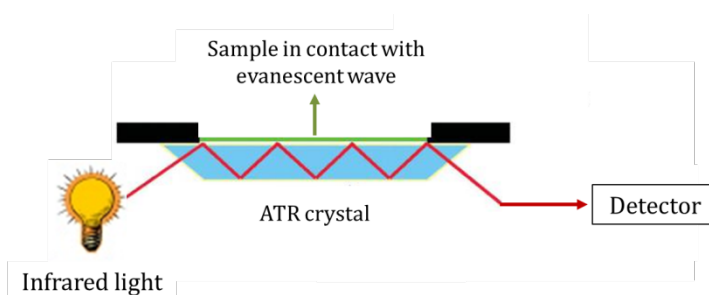


Figure A - 8. Principle of ATR infrared (adapted from http://las.perkinelmer.com/content/TechnicalInfo/TCH_FTIRATR.pdf).

6. Inductively Coupled Plasma Spectroscopy (ICP-OES and ICP-MS)

Inductively Coupled Plasma - Optical Emission Spectroscopy (ICP-OES) is a type of emission spectroscopy that uses inductively coupled plasma to produce excited atoms and ions that emit electromagnetic radiation at the characteristic wavelengths of elements.

The ICP generates a temperature in a range from 6000 to 10000 K to thermally excite all the elements presented in liquid samples. The photon emission is then collected by the spectrophotometer, diffracted and amplified to yield an intensity which can be converted to an elemental concentration by comparing with calibration standards.

In plasma mass spectroscopy (ICP-MS), the ICP is as well used as the excitation source. However, in contrast with the emission spectroscopy, the plasma in ICP-MS is used to generate ions that are then redirected to the mass analyser. These ions are finally separated and collected according to their mass to charge ratios (GC). Thus, all the constituents of samples can be identify and measured. ICP-MS offers higher sensitivity to detect a wider range of elements compared to ICP-OES.

7. References

- [1] De Broglie L 1924 *Recherches sur la théorie des Quanta* (Sorbonne)
- [2] Malvern I 2014 *Dynamic Light Scattering: An introduction in 30 minutes* 1–15
- [3] Malvern I 2015 *Zeta potential - An introduction in 30 minutes* 1–15
- [4] Moulder J F, Stickle W F, Sobol P E and Bomben K D 1992 *Handbook of X-ray Photoelectron Spectroscopy* ed J Chastain (Minnesota, United States of America: Perkin-Elmer Corporation)
- [5] Reusch W *Infrared Spectroscopy* <https://www2.chemistry.msu.edu>
- [6] Griffiths P R and De Haseth J A 2007 *Fourier Transform Infrared Spectrometry* (Hoboken, New Jersey: John Wiley & Sons Inc.)

Influence of platinum concentration

We evaluated the radio-enhancement effect as a function of the PtPEG-OH NPs concentration. Different concentrations, from 0.5 up to 8 NPs per plasmid, were studied. For better clarity, the set of dose response curves are not presented here.

Table B - 1 summarizes the quantitative analysis of the curves. It enlists the yields (nanosize breaks / plasmid / Gy) of controls and plasmids loaded with PtPEG NPs and the AFs. **Figure B - 1** shows the variation of the AF as function of the nanoparticles concentration.

Table B - 1. The yields of controls and plasmids loaded with PtPEG NPs at different concentrations. DMSO was added in some experiments. The AFs are also reported.

Sample	NPs per plasmid	Nanosize breaks/plasmid/Gy $\times 10^{-5}$	FA (%)
Control	0:1	11.40 \pm 0.25	-
Pt NPs-1	0.5:1	14.49 \pm 0.25	27 \pm 1
Pt NPs-2	1:1	15.10 \pm 0.40	32 \pm 1
Pt NPs-3	2:1	16.16 \pm 0.23	42 \pm 2
Pt NPs-4	4:1	20.90 \pm 0.21	83 \pm 4
Pt NPs-5	8:1	18.31 \pm 0.24	61 \pm 3
Control + DMSO	0:1	1.34 \pm 0.18	-
Pt NPs-4 + DMSO	4:1	2.48 \pm 0.11	85 \pm 15
Control + PEG	0:1	12.41 \pm 0.22	9 \pm 1

These results show that in presence of PtPEG NPs the induction of nanosize damage is enhanced from 27 up to 83 %. In addition, we observed that the induction of simple molecular breaks (not presented) remains constant in the presence of PtPEG NPs. A negligible amplification of 3% was observed for simple molecular damage (SSBs).

We also observe in **Table B - 1** (Control + PEG) that PEG chains enhanced by about 9% the induction of nanosize damage. It is attributed to the length of the PEG chain and thus to presence of a high number of ether groups, which cause an oxygen enhancement effect.

This result points out the unique property of PtPEG NPs to specifically amplify nanometer size damage, which confirms the property of NPs to amplify directly lethal damages (results in cells **Chapter III**).

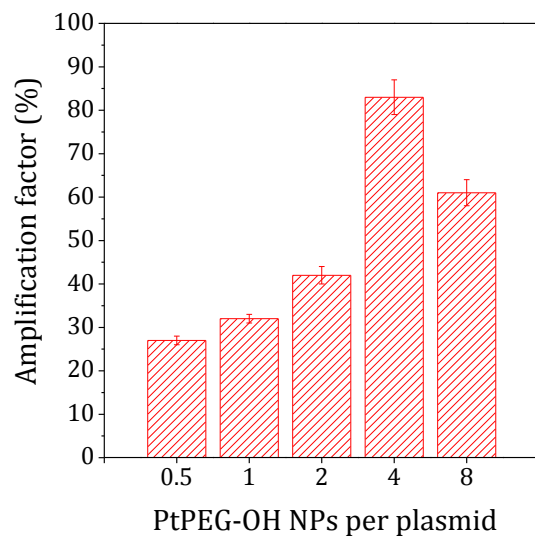


Figure B - 1. Amplification factor of nanosize damage by PtPEG NPs as function of concentration.

The effect was maximum at a concentration of 4 NPs per 1 plasmid (results presented in **Chapter III – Section 2.3**). At higher NPs concentration the AF decreases, it is ascribed to a saturation effect.